Biomaterials: Advances and Applications

Lead Guest Editor: Hamdy Doweidar
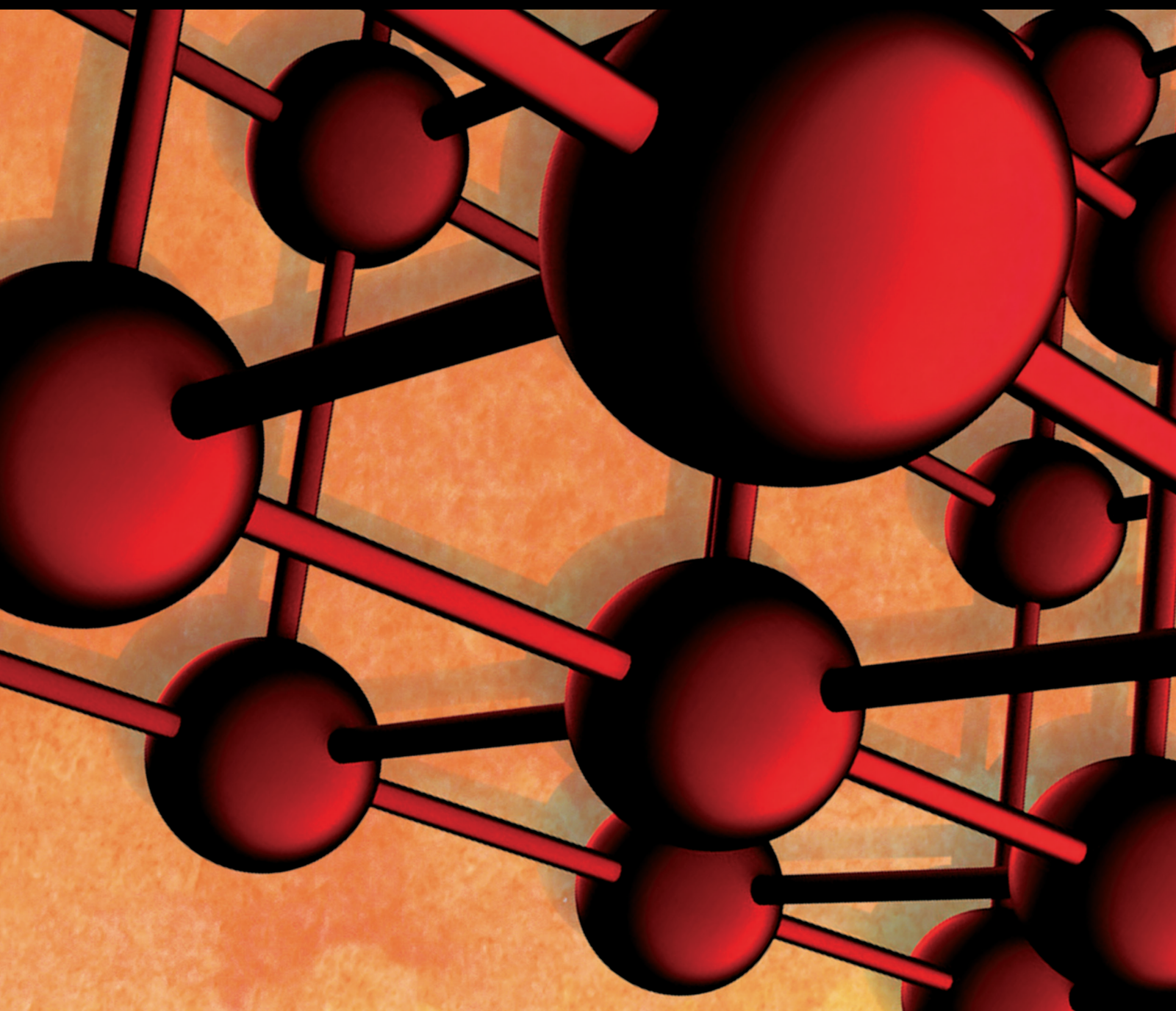Guest Editors: Toshihiro Kasuga, Gomaa El-Damrawi, and Delia Brauer

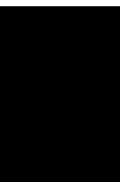# Biomaterials: Advances and Applications

Biomaterials: Advances and Applications

Lead Guest Editor: Hamdy Doweidar
Guest Editors: Toshihiro Kasuga, Gomaa El-Damrawi, and Delia Brauer

Achraf Ghorbal , Tunisia
Georgios I. Giannopoulos , Greece
Ivan Giorgio , Italy
Andrea Grilli , Italy
Vincenzo Guarino , Italy
Daniel Guay, Canada
Jenö Gubicza , Hungary
Xuchun Gui , China
Benoit Guiffard , France
Zhixing Guo, China
Ivan Gutierrez-Urrutia , Japan
Weiwei Han , Republic of Korea
Simo-Pekka Hannula, Finland
A. M. Hassan , Egypt
Akbar Heidarzadeh, Iran
Yi Huang , United Kingdom
Joshua Ighalo, Nigeria
Saliha Ilican , Turkey
Md Mainul Islam , Australia
Ilia Ivanov , USA
Jijo James , India
Hafsa Jamshaid , Pakistan
Hom Kandel , USA
Kenji Kaneko, Japan
Rajesh Kannan A , Democratic People's
Republic of Korea
Mehran Khan , Hong Kong
Akihiko Kimura, Japan
Ling B. Kong , Singapore
Pramod Koshy, Australia
Hongchao Kou , China
Alexander Kromka, Czech Republic
Abhinay Kumar, India
Avvaru Praveen Kumar , Ethiopia
Sachin Kumar, India
Paweł Kłosowski , Poland
Wing-Fu Lai , Hong Kong
Luciano Lamberti, Italy
Fulvio Lavecchia , Italy
Laurent Lebrun , France
Joon-Hyung Lee , Republic of Korea
Cristina Leonelli, Italy
Chenggao Li , China
Rongrong Li , China
Yuanshi Li, Canada

Guang-xing Liang , China
Barbara Liguori , Italy
Jun Liu , China
Yunqi Liu, China
Rong Lu, China
Zhiping Luo , USA
Fernando Lusquiños , Spain
Himadri Majumder , India
Dimitrios E. Manolakos , Greece
Necmettin Maraşlı , Turkey
Alessandro Martucci , Italy
Roshan Mayadunne , Australia
Mamoun Medraj , Canada
Shazim A. Memon , Kazakhstan
Pratima Meshram , India
Mohsen Mhadhbi , Tunisia
Philippe Miele, France
Andrey E. Miroshnichenko, Australia
Ajay Kumar Mishra , South Africa
Hossein Moayedi , Vietnam
Dhanesh G. Mohan , United Kingdom
Sakar Mohan , India
Namdev More, USA
Tahir Muhmood , China
Faisal Mukhtar , Pakistan
Dr. Tauseef Munawar , Pakistan
Roger Narayan , USA
Saleem Nasir , Pakistan
Elango Natarajan, Malaysia
Rufino M. Navarro, Spain
Miguel Navarro-Cia , United Kingdom
Behzad Nematollahi , Australia
Peter Niemz, Switzerland
Hiroshi Noguchi, Japan
Dariusz Oleszak , Poland
Laurent Orgéas , France
Togay Ozbakkaloglu, United Kingdom
Marián Palcut , Slovakia
Davide Palumbo , Italy
Gianfranco Palumbo , Italy
Murlidhar Patel, India
Zbyšek Pavlík , Czech Republic
Alessandro Pegoretti , Italy
Gianluca Percoco , Italy
Andrea Petrella, Italy

Claudio Pettinari (iD), Italy
Giorgio Pia (iD), Italy
Candido Fabrizio Pirri, Italy
Marinos Pitsikalis (iD), Greece
Alain Portavoce (iD), France
Simon C. Potter, Canada
Ulrich Prahl, Germany
Veena Ragupathi (iD), India
Kawaljit singh Randhawa (iD), India
Baskaran Rangasamy (iD), Zambia
Paulo Reis (iD), Portugal
Hilda E. Reynel-Avila (iD), Mexico
Yuri Ribakov (iD), Israel
Aniello Riccio (iD), Italy
Anna Richelli (iD), Italy
Antonio Riveiro (iD), Spain
Marco Rossi (iD), Italy
Fernando Rubio-Marcos (iD), Spain
Francesco Ruffino (iD), Italy
Giuseppe Ruta (iD), Italy
Sachin Salunkhe (iD), India
P Sangeetha (iD), India
Carlo Santulli, Italy
Fabrizio Sarasini (iD), Italy
Senthil Kumaran Selvaraj (iD), India
Raffaele Sepe (iD), Italy
Aabid H Shalla, India
Poorva Sharma (iD), China
Mercedes Solla, Spain
Tushar Sonar (iD), Russia
Donato Sorgente (iD), Italy
Charles C. Sorrell (iD), Australia
Damien Soulat (iD), France
Adolfo Speghini (iD), Italy
Antonino Squillace (iD), Italy
Koichi Sugimoto, Japan
Jirapornchai Suksaeree (iD), Thailand
Baozhong Sun, China
Sam-Shajing Sun (iD), USA
Xiaolong Sun, China
Yongding Tian (iD), China
Hao Tong, China
Achim Trampert, Germany
Tomasz Trzepieciński (iD), Poland
Kavimani V (iD), India

Matjaz Valant (iD), Slovenia
Mostafa Vamegh, Iran
Lijing Wang (iD), Australia
Jörg M. K. Wiezorek (iD), USA
Guosong Wu, China
Junhui Xiao (iD), China
Guoqiang Xie (iD), China
YASHPAL YASHPAL, India
Anil Singh Yadav (iD), India
Yee-wen Yen, Taiwan
Hao Yi (iD), China
Wenbin Yi, China
Tetsu Yonezawa, Japan
Hiroshi Yoshihara (iD), Japan
Bin Yu (iD), China
Rahadian Zainul (iD), Indonesia
Lenka Zaji#c#kova# (iD), Czech Republic
Zhigang Zang (iD), China
Michele Zappalorto (iD), Italy
Gang Zhang, Singapore
Jinghuai Zhang, China
Zengping Zhang, China
You Zhou (iD), Japan
Robert Černý (iD), Czech Republic

Contents

Research Article

Evidence of a Lead Metathesis Product from Calcium Hydroxyapatite Dissolution in Lead Nitrate Solution

Oratai Saisa-ard,[1] Weenawan Somphon,[2] Winya Dungkaew,[3] and Kenneth J. Haller[3]

[1] *Chemistry Program, Faculty of Science, Ubon Ratchathani Rajabhat University, Ubon Ratchathani 34000, Thailand*

[2] *Chemistry Department, Faculty of Liberal Arts and Science, Kasetsart University Kamphaeng Saen Campus,*
 Nakhon Pathom 73140, Thailand

[3] *School of Chemistry, Institute of Science, Suranaree University of Technology, Nakhon Ratchasima 30000, Thailand*

Correspondence should be addressed to Oratai Saisa-ard; oratai_phasai@yahoo.com and Kenneth J. Haller; ken.haller@gmail.com

Calcium hydroxyapatite, CaHAp, synthesized by the precipitation method, was utilized to study the calcium-lead metathesis reaction on dissolution in a lead nitrate solution under reflux conditions to prepare larger lead hydroxyapatite, PbHAp, crystals from CaHAp. SEM images show development of crystalline PbHAp on the surfaces of CaHAp. The needle-like crystal morphology observed for PbHAp after 24 h reaction time developed into hexagonal-rod crystal morphology within 48 h reaction time. The largest PbHAp crystals obtained from 48 h reaction time have approximate size of $10 \times 10 \times 40\ \mu$m. Powder X-ray diffraction results show mixed phases of CaHAp and PbHAp due to difficulty in separating the PbHAp product from the CaHAp substrate. The PbHAp peaks observed after 24 h of reaction sharpen and increase in intensity after 48 h of reaction confirming that the PbHAp phase is the major product for the 48 h reaction time. EDX results of the crystalline products show high intensity Pb peaks with lead to phosphorous ratio (5 : 3) as expected for PbHAp. Lower intensity Ca peaks are also observed, consistent with incomplete coverage of the CaHAp growth substrate.

1. Introduction

Calcium hydroxyapatite, $Ca_5(PO_4)_3(OH)$, CaHAp, the prototype structure of the apatite series, is the dominant component in biological hard tissues such as bones (about 69 wt% CaHAp) and teeth (about 95 wt% CaHAp) [1]. The structure belongs to space group $P6_3/m$ and is susceptible to ionic substitution in both anion and cation sites. Ca^{2+} can be replaced by various divalent cations including Fe^{2+}, Cr^{2+}, Zn^{2+}, Mg^{2+}, Cd^{2+}, Sr^{2+}, or Pb^{2+} [2–6], PO_4^{3-} can be replaced by AsO_4^{3-} or VO_4^{3-}, and OH^- can be replaced by F^- or Cl^- [7–10].

Complete substitution of Pb^{2+} ions into CaHAp structure results in the isostructural lead hydroxyapatite, sometimes called hydroxypyromorphite, $Pb_5(PO_4)_3(OH)$, PbHAp, which has been studied, including its structure [11, 12] and solubility properties [13], partly because the accumulation of Pb^{2+} in bones accompanies bone diseases. Chronic exposure to lead has been shown to inhibit skeletal development [14]

and/or can lead to osteoporosis [15] as the lead localizes in the area of bone formation and resorption, respectively. It is possible that this is a consequence of the lower solubility of PbHAp ($pK_{SP} = 62.79$) [16] compared to CaHAp ($pK_{SP} = 53.28$) [17]. Thus, the relationship between CaHAp and PbHAp in terms of their structure and properties as well as their potential interconversions might provide important keys in the understanding of the accumulation of Pb^{2+} in bone.

Studies on the mechanism and phase evolution of Pb^{2+} immobilization by synthetic CaHAp have been reported [18, 19] and show dissolution of CaHAp in Pb^{2+} solution and then concomitant crystallization of PbHAp in the system. The mechanism of PbHAp formation in acidic conditions has been proposed [20, 21] as follows.

Dissolution of CaHAp:

$$Ca_5(PO_4)_3(OH) + 7H^+ \longrightarrow 5Ca^{2+} + 3H_2PO_4^- + H_2O \quad (1)$$

Precipitation of PbHAp:

$$5Pb^{2+} + 3H_2PO_4^- + H_2O \longrightarrow Pb_5(PO_4)_3(OH) + 7H^+ \quad (2)$$
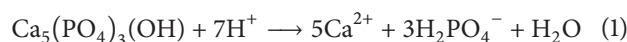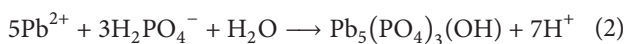
Earlier studies of Pb^{2+} immobilization by hydroxyapatite in the absence of potential substitution ions [22], in the presence of potential substitution anions [23], and in the presence of potential substitution cations [24] show the same dissolution/precipitation mechanism. While the Ca^{2+} and Pb^{2+} compounds are isostructural, they are in separate series due to the difficulty of substituting Pb for Ca in the apatite series or of substituting Ca for Pb in the pyromorphite series [25].

This work reports preparation of CaHAp and its X-ray absorption spectroscopy (XAS) spectrum to characterize the short-range environment around Ca absorbing atoms of the precipitate product. A reflux method was used to increase the CaHAp dissolution rate and thus the PbHAp crystallization rate in the metathesis reaction of CaHAp in lead nitrate solution. The relationship between reaction times and crystal morphologies of products is discussed.

2. Materials and Methods

2.1. Preparation of CaHAp Material. Phosphate and calcium solutions for preparation of CaHAp were prepared by dissolving 7.92 g (60 mmol) diammonium hydrogen phosphate, $(NH_4)_2HPO_4$ (Ajax Finechem, AR grade), in 100 mL deionized water and dissolving 23.60 g (100 mmol) calcium nitrate, $Ca(NO_3)_2 \cdot 4H_2O$ (Ajax Finechem, AR grade), in 100 mL deionized water. CaHAp was prepared by dropwise addition of phosphate solution into calcium solution, while stirring at room temperature and maintaining the solution pH at 11 with 1.0 M NaOH. After addition of the phosphate solution, the suspension was stirred continuously for 30 min and the precipitate was separated by filtration, washed with deionized water three times, and dried at 100°C for 24 h.

2.2. Preparation of PbHAp by Reflux Method. Excess CaHAp, 0.20 g (3.98 mmol), was ground in an agate mortar and added into a solution prepared by dissolving 0.0733 g (0.22 mmol) lead nitrate, $Pb(NO_3)_2$ (Ajax Finechem, AR grade), in 80 mL deionized water and refluxed for 24 h and 48 h. The white precipitates were separated by filtration, washed with deionized water three times, and dried at 100°C for 24 h.

2.3. Characterization. Crystal morphologies were observed by scanning electron microscopy (SEM) using a JSM 6400 electron microscope (JEOL, Japan) equipped with a Microspec model WDX-100 energy dispersive X-ray fluorescence (EDX) detector. IR spectra were acquired on a Perkin-Elmer model Spectrum GX Fourier transform infrared spectrophotometer in wavenumber range 400–4000 cm^{-1} from KBr pellets.

Powder X-ray diffraction (XRD) scans were acquired for the 2θ range 10–55° on a Bruker Analytical X-ray Systems D5005 diffractometer equipped with a Cu Kα sealed tube X-radiation source operating at 40 kV and 40 mA. Comparison with ICDD JCPDS files [26] was utilized for phase identification of products.

X-ray absorption spectroscopy (XAS) experiments were conducted at the BL-8 beamline at the Siam Photon Laboratory of the National Synchrotron Research Center of Thailand (Nakhon Ratchasima, Thailand) with the electron storage ring operated at 1.2 GeV with an average beam current of ~100 mA. A monochromatic beam was obtained by means of a Si(111) double crystal monochromator. Experiments were performed at the Ca K-edge in transmission mode. The gas ionization chamber was filled with N_2 (~400 mbar), and XAS spectra of $CaCl_2 \cdot 2H_2O$ were used for a standard energy calibration (4042 eV). Extended X-ray absorption fine structure, EXAFS, spectra were collected in an energy range between 3970 and 4750 eV, with energy steps of 1 eV. Samples and reference compounds were ground in an agate mortar in air until uniform and were sealed between layers of Kapton tape on the sample holder and then brought to the beam. EXAFS fitting was carried out using the IFEFFIT library [27] within the ATHENA XAS data processing suite [28], and interatomic distance estimates were obtained from the ATHENA suite [29].

3. Results and Discussion

CaHAp structure has been reported [30, 31]. It consists of metal atoms located on two crystallographically different sites: f sites (identified as Ca(I)) and h sites (identified as Ca(II)) as shown in Figure 1. Two metal ions at the Ca(I) sites are coordinated with nine O atoms (six shorter bonds to three O(1) and three O(2) phosphate oxygen atoms on Ca(I) sites define a twisted trigonal prism, and three longer bonds to O(3) atoms extend through the prism faces), and three metal ions at the Ca(II) sites are coordinated with seven O atoms (one O(1), one O(2), and four general O(3) atoms from PO_4^{3-} groups and one O(4) atom from an OH$^-$ group).

EXAFS fitting for CaHAp used the crystallographic parameters for ideally crystalline CaHAp taken from Posner et al. [30]. EXAFS data were Fourier-transformed in the k range 2–10.5 Å^{-1} using k^3-weighting of data and fit in real space in the range of 1–6 Å of the Ca local environment. Figure 2 shows EXAFS of (a) the k^3-weighted raw and fitted χ (chi) functions of the samples and (b) Fourier transformations of k^3-weighted EXAFS spectra. This is the best fit for these available EXAFS spectra. The distances displayed on the x-axis are not corrected for phase shifts and appear offset by about 0.3 Å. The coordination number that is detected by EXAFS spectroscopy is composed of the weighted sum of Ca(I) and Ca(II) sites. Higher shells of light backscattering atoms were omitted due to small intensity, and shells in very close neighborhood were combined in order to keep the number of fit parameters manageable and mathematically significant. Multiple scattering pathways were of negligible magnitude. These results show an average bond distance of all atoms surrounding Ca atoms, Ca–O#1 = 2.41 Å (for Ca–6O), Ca–P#2 = 3.22 Å (Ca–2.4P), Ca–P#3 = 3.59 Å (Ca–2.4P), Ca(I)–Ca(II)#4 = 3.95 Å (Ca–6Ca), Ca(I)–Ca(II)#5 = 4.03 Å (Ca–2.4Ca), and Ca(I)–Ca(I)#6 = 5.45 Å (Ca–3.6Ca).

(a)

(b)
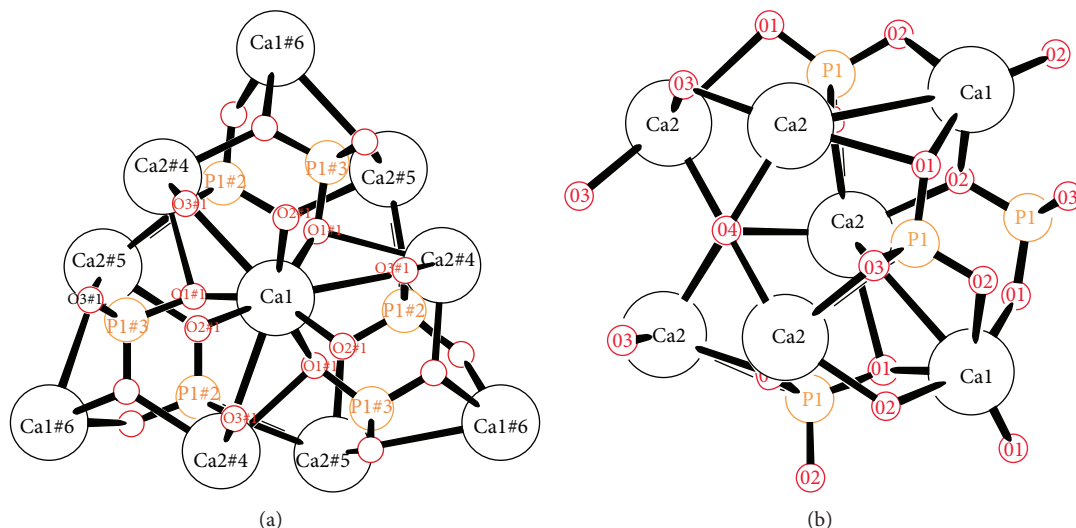
FIGURE 1: Projection drawings down [001] of (a) Ca(I) site and (b) the Ca(II) site in CaHAp.

(a)

(b)
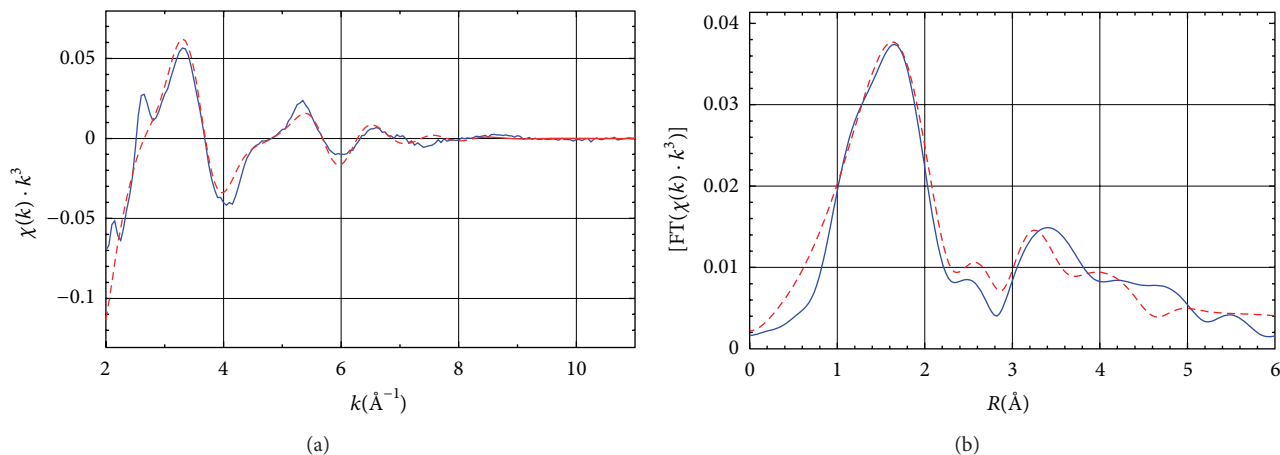
FIGURE 2: Ca K-edge EXAFS data of CaHAp experiment (solid lines) and fit to data (dashed lines). (a) The k^3-weighted $\chi(k)$ and (b) Fourier transformations of the k^3-weighted EXAFS spectra. Radial distribution functions were not corrected for phase shift (shorter distances by 0.3-0.4 Å with respect to crystallographic values). Note: the dotted lines are best fits.

The SEM images of CaHAp before and after refluxing in lead nitrate solution are shown in Figure 3. Crystalline product after refluxing for 24 h exhibits needle-like crystal morphology on the surface of the CaHAp substrate (Figure 3(b)) while the crystalline product after refluxing for 48 h exhibits hexagonal-rod crystal morphology (Figure 3(c)). The product crystal size increased with increasing reaction time; the largest crystal size observed is about $10 \times 10 \times 40\,\mu$m. The finely divided PbHAp phase could not be easily separated from the CaHAp substrate.

EDX spectra of products and the substrate after refluxing in lead nitrate solution are shown in Figure 4. The EDX spectrum of the post reaction CaHAp substrate (Figure 4(a)) shows high intensity Ca peaks with calcium to phosphorous ratio of about 5 : 3 as expected for CaHAp (but no evidence of Pb peaks), while the spectrum of crystalline product region (Figure 4(b)) shows high intensity Pb peaks with lead

to phosphorous ratio of 5 : 3 as expected for PbHAp. Low intensity Ca peaks are also observed in the product spectra, consistent with incomplete coverage of the CaHAp growth substrate. Similar spectra (not shown) were observed for the CaHAp substrate and PbHAp product areas after refluxing for 48 h. These spectra support the dissolution/precipitation mechanism previously proposed [20, 21] and do not give any suggestion of substitution of Ca^{2+} by Pb^{2+} in the CaHAp substrate to form a solid solution under the mild conditions of refluxing in H_2O.

XRD patterns of products after refluxing for 24 h and 48 h also show mixed PbHAp (JCPDS number 08-0259) and CaHAp (JCPDS number 09-0432) phases as shown in Figure 5.

The XRD pattern of the product after 48 h reflux clearly shows the PbHAp phase as the major product phase with the intensity of PbHAp peaks considerably increased, indicating
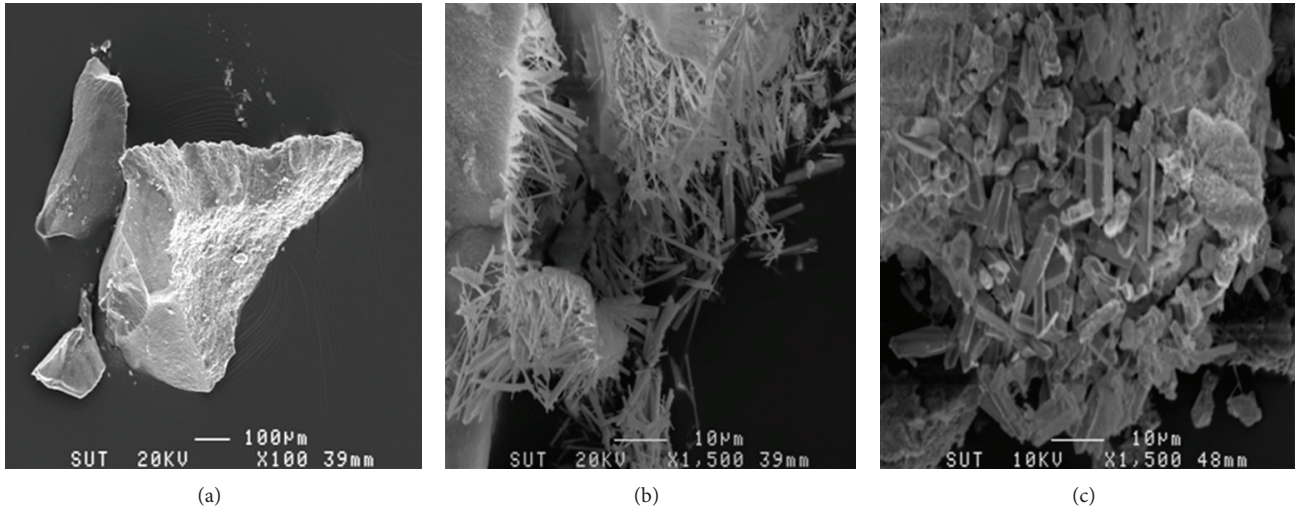
FIGURE 3: SEM images of (a) CaHAp before refluxing, (b) after refluxing in lead nitrate solution (917 mg/L) for 24 h, and (c) after refluxing for 48 h.
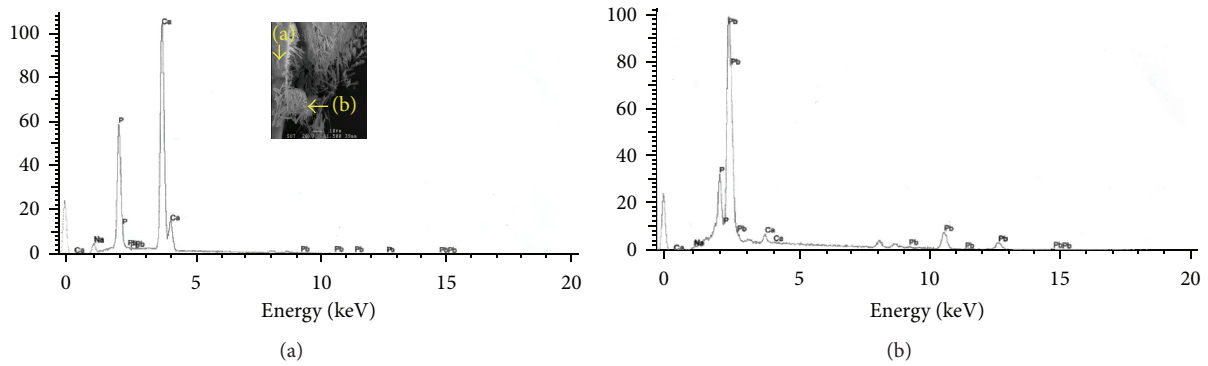
FIGURE 4: EDX spectra of products after refluxing in lead nitrate solution (917 mg/L) for 24 h. (a) CaHAp substrate and (b) PbHAp needle-like crystal product region. The inset shows the locations sampled for the spectra.
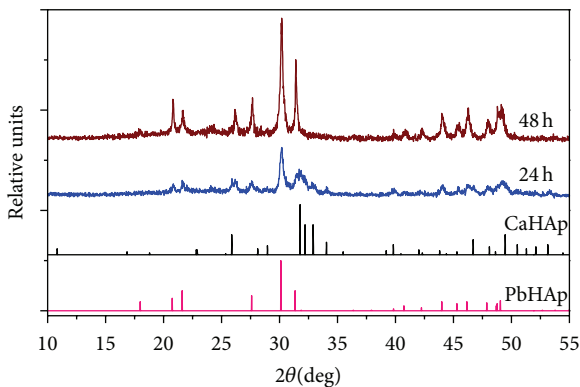
FIGURE 5: XRD patterns of products after refluxing in lead nitrate solution (917 mg/L) for 24 h and 48 h.

that formation of PbHAp phase increased with increased reaction time which is in agreement with previous work [18]. PbHAp crystal product is present as hexagonal rod-shaped crystals as shown in **Figure 3(c)**. The presence of both phases results from difficulty separating the finely divided PbHAp phase from the approximately 20-fold excess CaHAp reactant substrate phase.

IR spectra of CaHAp and products after refluxing in the presence of Pb^{+2} (**Figure 6**) show bands in the appropriate regions: $v_{1(P-O)}$ and $v_{3(P-O)}$ PO_4^{3-} stretching modes in the 961–1095 cm^{-1} region, $v_{2(O-P-O)}$ bending mode in the 467–473 cm^{-1} region, and the $v_{4(O-P-O)}$ bending mode in the 562–632 cm^{-1} region, consistent with previous reports for CaHAp [32, 33] and PbHAp [34].

The CaHAp reactant material was not calcined and shows broad water O–H stretching vibrational bands centered about 3468 cm^{-1} in the CaHAp spectrum with the v_{OH} apatite band as a shoulder at 3568 cm^{-1}, similar to reported values of 3573 [32] and 3569 cm^{-1} [33]. A small sharp O–H stretching mode appears at 3571 cm^{-1} in the product spectra, which compares favorably with the apatite bands and the reported [34] v_{OH} vibrational stretching band for pure PbHAp at 3560 cm^{-1}. A broad band in the 3000–3700 cm^{-1} region and a weak
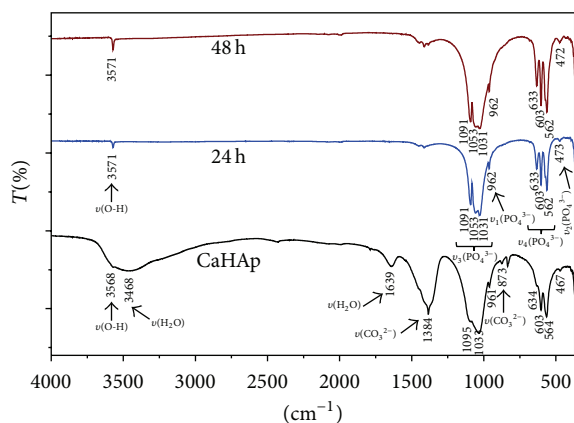
FIGURE 6: IR spectra of CaHAp before refluxing and after refluxing in lead nitrate solution (917 mg/L) for 24 h and 48 h.

peak at $1639 \, cm^{-1}$ in the CaHAp spectrum are consistent with absorbed H_2O on the KBr pellet or associated with the reactant substrate phase. As all the IR spectroscopy samples were prepared in the same manner, loss of these broad peaks on refluxing indicates that they are due to water associated with the reactant substrate phase.

The IR spectrum of CaHAp also shows bands of CO_3^{2-} stretching at $1384 \, cm^{-1}$ and CO_3^{2-} bending at $873 \, cm^{-1}$ in agreement with previous work [35]. The carbonate may come from the incorporation of atmospheric CO_2 through equilibrium with the alkaline reaction solution during the synthesis step. The incorporation of CO_3^{2-} into CaHAp materials has been suggested to increase the solubility of CaHAp [36].

4. Conclusion

The reflux method of CaHAp dissolution to provide phosphate anion in the presence of lead cation succeeds for producing larger sized crystals of the less soluble PbHAp from the aqueous solution. Hexagonal rod-shaped crystals of PbHAp formed and product crystal size increased with increasing reflux-reaction time. EDX results are consistent with the XRD results and show mixed phases of PbHAp and substrate CaHAp, but no evidence of Pb substitution into the CaHAp substrate phase. IR results indicate the incorporation of carbonate in the CaHAp substrate resulting in increased solubility of this material, but the carbonate anion does not appear to carry over into the PbHAp product crystals.

Conflict of Interests

The authors declare that there is no conflict of interests regarding the publication of this paper.

References

[1] R. Z. LeGeros, *Calcium Phosphates in Oral Biology and Medicine*, Karger, San Francisco, Calif, USA, 1st edition, 1991.

[2] T. Moriguchil, S. Nakagawa, and F. Kaji, "Reaction of Ca-deficient hydroxyapatite with heavy metal ions along with metal substitution," *Phosphorus Research Bulletin*, vol. 22, pp. 54–60, 2008.

[3] A. Yasukawa, T. Yokoyama, K. Kandori, and T. Ishikawa, "Reaction of calcium hydroxyapatite with Cd^{2+} and Pb^{2+} ions," *Colloids and Surfaces A*, vol. 299, no. 1–3, pp. 203–208, 2007.

[4] F. Ren, Y. Leng, R. Xin, and X. Ge, "Synthesis, characterization and ab initio simulation of magnesium-substituted hydroxyapatite," *Acta Biomaterialia*, vol. 6, no. 7, pp. 2787–2796, 2010.

[5] M. D. O'Donnell, Y. Fredholm, A. de Rouffignac, and R. G. Hill, "Structural analysis of a series of strontium-substituted apatites," *Acta Biomaterialia*, vol. 4, no. 5, pp. 1455–1464, 2008.

[6] H. Xu, L. Yang, P. Wang, Y. Liu, and M. Peng, "Removal mechanism of aqueous lead by a novel eco-material: carbonate hydroxyapatite," *Journal of Materials Science and Technology*, vol. 23, no. 3, pp. 417–422, 2007.

[7] Z. Dong, T. J. White, B. Wei, and K. Laursen, "Model apatite systems for the stabilization of toxic metals: I, calcium lead vanadate," *Journal of the American Ceramic Society*, vol. 85, no. 10, pp. 2515–2522, 2002.

[8] Y. Dai and M. J. Hughes, "Crystal structure refinements of vanadinite and pyromorphite," *Canadian Mineralogist*, vol. 27, pp. 189–192, 1989.

[9] W. Dungkaew, K. J. Haller, A. E. Flood, and J. F. Scamehorn, "Arsenic removal by precipitation with Calcium phosphate hydroxyapatite," *Advanced Materials Research*, vol. 506, pp. 413–416, 2012.

[10] T. Dordević, S. Šutović, J. Stojanović, and L. Karanović, "Sr, Ba and Cd arsenates with the apatite-type structure," *Acta Crystallographica C*, vol. 64, pp. i82–i86, 2008.

[11] S. Brückner, G. Lusvardi, L. Menabue, and M. Saladini, "Crystal structure of lead hydroxyapatite from powder X-ray diffraction data," *Inorganica Chimica Acta*, vol. 236, no. 1-2, pp. 209–212, 1995.

[12] J. Y. Kim, R. R. Fenton, B. A. Hunter, and B. J. Kennedy, "Powder diffraction studies of synthetic calcium and lead apatites," *Australian Journal of Chemistry*, vol. 53, no. 8, pp. 679–686, 2000.

[13] E. Valsami-Jones, K. V. Ragnarsdottir, A. Putnis, D. Bosbach, A. J. Kemp, and G. Cressey, "The dissolution of apatite in the presence of aqueous metal cations at pH 2-7," *Chemical Geology*, vol. 151, no. 1–4, pp. 215–233, 1998.

[14] J. D. Hamilton and E. J. O'Flaherty, "Influence of lead on mineralization during bone growth," *Fundamental and Applied Toxicology*, vol. 26, no. 2, pp. 265–271, 1995.

[15] H. E. Gruber, H. C. Gonick, F. Khalil-Manesh et al., "Osteopenia induced by long-term, low- and high-level exposure of the adult rat to lead," *Mineral and Electrolyte Metabolism*, vol. 23, no. 2, pp. 65–73, 1997.

[16] D. L. Parkhurst and C. A. J. Appelo, "PHREEQC (version 2) A computer program for speciation, batch-reaction, one-dimensional transport, and inverse geochemical calculations," U.S. Department of the Interior and U.S. Geological Survey, http://pfw.antipodes.nl/download.html, The minteq.v4.dat database accessed with the PHREEQC software, 1999, http://www.phreeplot.org/ppihtml/minteq.v4.dat.html.

[17] Y. Zhu, X. Zhang, Y. Chen et al., "A comparative study on the dissolution and solubility of hydroxylapatite and fluorapatite at 25°C and 45°C," *Chemical Geology*, vol. 268, no. 1-2, pp. 89–96, 2009.

[18] E. Mavropoulos, A. M. Rossi, A. M. Costa, C. A. C. Perez, J. C. Moreira, and M. Saldanha, "Studies on the mechanisms of lead immobilization by hydroxyapatite," *Environmental Science & Technology*, vol. 36, no. 7, pp. 1625–1629, 2002.

[19] E. Mavropoulos, N. C. C. Rocha, J. C. Moreira, A. M. Rossi, and G. A. Soares, "Characterization of phase evolution during lead immobilization by synthetic hydroxyapatite," *Materials Characterization*, vol. 53, no. 1, pp. 71–78, 2004.

[20] W. L. Lindsay, *Chemical Equilibria in Soils*, John Wiley & Sons, New York, NY, USA, 1979.

[21] L. Dong, Z. Zhu, Y. Qiu, and J. Zhao, "Removal of lead from aqueous solution by hydroxyapatite/magnetite composite adsorbent," *Chemical Engineering Journal*, vol. 165, no. 3, pp. 827–834, 2010.

[22] Q. Y. Ma, S. J. Traina, T. J. Logan, and J. A. Ryan, "In situ lead immobilization by apatite," *Environmental Science & Technology*, vol. 27, no. 9, pp. 1803–1810, 1993.

[23] Q. Y. M. Qi Ying Ma, S. J. Tralna, T. J. Logan, and J. A. Ryan, "Effects of aqueous Al, Cd, Cu, Fe(II), Ni, and Zn on Pb immobilization by hydroxyapatite," *Environmental Science & Technology*, vol. 28, no. 7, pp. 1219–1228, 1994.

[24] Q. Y. Ma, S. J. Traina, T. J. Logan, and J. A. Ryan, "Effects of NO_3^-, Cl^-, F^-, SO_4^{2-}, CO_3^{2-} on Pb2+ immobilization by hydroxyapatite," *Environmental Science & Technology*, vol. 28, pp. 408–418, 1994.

[25] J. R. van Wazer, *Phosphorus and Its Compounds*, Interscience, New York, NY, USA, 1958.

[26] ICDD, *Powder Diffraction Files (Database)*, International Center for Diffraction Data, Newtown Square, Pa, USA, 2007.

[27] M. Newville, "IFEFFIT: interactive XAFS analysis and FEFF fitting," *Journal of Synchrotron Radiation*, vol. 8, no. 2, pp. 322–324, 2001.

[28] B. Ravel and M. Newville, "ATHENA, ARTEMIS, HEPHAESTUS: data analysis for X-ray absorption spectroscopy using IFEFFIT," *Journal of Synchrotron Radiation*, vol. 12, no. 4, pp. 537–541, 2005.

[29] B. Ravel, *ATHENA User's Guide*, University of Chicago, 2009.

[30] A. S. Posner, A. Perloff, and A. F. Diorio, "Refinement of the hydroxyapatite structure," *Acta Crystallographica*, vol. 11, pp. 308–309, 1958.

[31] M. I. Kay, R. A. Young, and A. S. Posner, "Crystal structure of hydroxyapatite," *Nature*, vol. 204, no. 4963, pp. 1050–1052, 1964.

[32] M. Jevtić, M. Mitrić, S. Škapin, B. Jančar, N. Ignjatović, and D. Uskoković, "Crystal structure of hydroxyapatite nanorods synthesized by sonochemical homogeneous precipitation," *Crystal Growth and Design*, vol. 8, no. 7, pp. 2217–2222, 2008.

[33] S. Lazarević, I. Janković-Častvan, D. Tanasković, V. Pavićević, D. Janaćković, and R. Petrović, "Sorption of Pb^{2+}, Cd^{2+}, and Sr^{2+} ions on calcium hydroxyapatite powder obtained by the hydrothermal method," *Journal of Environmental Engineering*, vol. 134, pp. 683–688, 2008.

[34] V. Laperche and S. J. Traina, "Immobilization of Pb by hydroxyapatite," in *Adsorption of Metals By Geomedia*, E. A. Jenne, Ed., pp. 255–277, Academic Press, San Diego, Calif, USA, 1998.

[35] S. M. Barinov, I. V. Fadeeva, D. Ferro et al., "Stabilization of carbonate hydroxyapatite by isomorphic substitutions of sodium for calcium," *Russian Journal of Inorganic Chemistry*, vol. 53, no. 2, pp. 164–168, 2008.

[36] S. Liao, F. Watari, G. Xu, M. Ngiam, S. Ramakrishna, and C. K. Chan, "Morphological effects of variant carbonates in biomimetic hydroxyapatite," *Materials Letters*, vol. 61, no. 17, pp. 3624–3628, 2007.

Research Article

Forecasting of Corrosion Properties of Steel Wires for Production of Guide Wires for Cardiological Treatment

J. Przondziono,[1] W. Walke,[2] E. Hadasik,[1] and R. Młynarski[3]

[1] *Faculty of Materials Engineering and Metallurgy, Silesian University of Technology, Krasińskiego 8, 40-019 Katowice, Poland*
[2] *Faculty of Biomedical Engineering, Silesian University of Technology, General de Gaulle'a 66, 41-800 Zabrze, Poland*
[3] *Department of Electrocardiology, Medical University of Silesia, Ziołowa 45/47, 40-635 Katowice, Poland*

Correspondence should be addressed to J. Przondziono; joanna.przondziono@polsl.pl

The study presents evaluation of the influence of strain in drawing process and of surface modification on resistance to electrochemical corrosion of wires made of stainless steel for production of guide wires used in invasive cardiology. The results of static tensile test enabled us to determine the course of flow curve of wires made of X10CrNi 18-8 steel as well as mathematical form of flow stress function. Resistance to electrochemical corrosion was evaluated on the ground of registered anodic polarisation curves by means of potentiodynamic method. The tests were performed in solution simulating human blood on samples that were electrolytically polished and samples that were polished and then chemically passivated. Exemplary anodic polarisation curves were given. It was proved that with the applied strain, corrosion properties decrease. It was found that chemical passivation improves wire corrosion characteristics. Statistical analysis showed that there is a significant dependence between corrosion properties (polarisation resistance R_p) and strain ε applied in drawing process. Functions that present the change $R_p = f(\varepsilon)$ were selected. The issue is of importance to guide wire manufacturers because application of the suggested methodology will enable us to forecast corrosion characteristics of wire with the required strength drawn with the applied strain.

1. Introduction

Guide wires are indispensable instruments used in low-invasive treatment. Guide wires were initially manufactured for vascular applications, but over time they became indispensable also in other branches of medicine. They can be used in treatment where percutaneous access inside blood vessels is required—in angioplasty, in electrocardiology, when inserting electrodes to the heart, and in endoscopic gastrostomy or endourology [1–3]. In the latter one they are used for two purposes: (1) they ensure access to specific parts of urinary system and (2) they are used as guide wires over which catheters and stents can be inserted.

Such a wide application spectrum determined production of many different types of guide wires. They differ from one another in construction, dimensions, material they are made of, and mechanical characteristics, including stiffness or resistance to cracking [1]. Manufacturers make guide wires in their own catalogue series of types. Most of them

feature elastic flexible tip and stiff or semistiff body. Elastic tip enables us to avoid tissue damage and perforation. Most frequently, guide wires have the form of long, thin straight wires or wires with "J"-shaped tip. Also guide wires with more complicated construction have found their application. For example, in endourological percutaneous nephrolithotripsy or ureterorenoscopy, guide wires consist of both round wires and springs in which there are thin round wires and flat wires [4–8].

In invasive cardiology, thanks to application of intravascular guide wires, it is possible to insert the required instruments into blood vessels or, for example, implants, stents used in angioplasty. During treatment there is no need to cut blood vessels. In electrotherapy, guide wires are used in two ways. The first one includes accessing the vein, thanks to which an electrode can be inserted. The second one includes stiffening of the electrode, which facilitates its insertion in the respective place inside the heart.

Guide wires must meet a number of requirements. Most of all, their application must be safe for the patient. They should feature high resistance to electrochemical corrosion in the environment of tissues and saline solutions. When coming into contact with blood, they cannot cause any reaction. Guide wires should also feature the required mechanical properties suitable for the respective application. Functional properties are dependent on, among other things, chemical composition of the material, its metallurgical purity, and technological parameters of wire production process. The question of determination of physical and chemical characteristics of guide wire surface is also vital. They should be adapted to the characteristics of human tissue environment.

In case of plastic working, the selection of optimum parameters of wire drawing process is influenced by proper characteristics of technological plasticity of the material. It conditions obtaining the structure susceptible to drawing process and obtaining a product that features the required functional characteristics. Plastic strain is accompanied by the phenomenon of work hardening that is connected with the increase of flow stress σ_p. Hardening causes increase of strength properties of wire and decrease of its plastic properties. Correct determination of parameters of plastic working and obtaining suitable final properties of products are connected with analysis of the course of function $\sigma_p = f(\varepsilon)$, where ε means strain expressed as a logarithm. Curves of flow stress change as the function of strain (so-called flow curves) enables us to forecast behaviour of the material during plastic working [9]. Strain applied in drawing process also has a significant influence on corrosion properties of wire used for production of guide wires [10, 11].

Proper solution to technological problems regarding production of guide wires conditions the success of performed treatment in invasive cardiology. Engineers make use of work-hardening curves in order to select such parameters of drawing so as to obtain wires with mechanical characteristics required for the respective application. This study is a proposal of a similar behaviour in order to forecast corrosion characteristics of wire depending on strain applied in drawing process. Methodology presented in this study will enable us to define corrosion properties featured by the wire with the required strength drawn with the selected strain.

Guide wires in commercial use are manufactured among other things from stainless steel of X10CrNi 18-8 grade. The study presents the course of flow curve of wires made of that steel and mathematical form of flow stress function. Resistance to corrosion was evaluated on the ground of registered anodic polarisation curves by means of potentiodynamic method. Tests were made in the solution simulating human blood on samples that were electrolytically polished and polished and then chemically passivated. Exemplary anodic polarisation curves were presented, as well as curves showing the relation between polarisation resistance as the function of strain applied in wire drawing process. Performed tests enabled us to determine both the effect of strain during cold working and the way of surface preparation on wire corrosion characteristics.

2. Materials and Methods

Initial material for tests consisted of annealed wire rod made of X10CrNi 18-8 steel with diameter of 5.65 mm. Wire rod was drawn to a diameter of 1.5 mm. Total logarithmic strain in drawing process was $\varepsilon = 2.65$. Wire work hardening took place during cold working. In the course of strain process samples for mechanical and corrosion tests were cut off.

Flow stress σ_p of drawn materials is determined on the ground of stress-strain curve in tension in the arrangement σ_r-ε, where σ_r is real stress and ε is strain expressed as a logarithm. In order to determine actual stress, it is necessary to calculate real cross-section of sample S loaded with force F. Calculation of real cross-section of sample requires determination of real diameter of sample d, which is subject to change due to present elastic and plastic elongation. For the load corresponding to proof stress, the value of real stress $\sigma_{r0.2}$ was calculated in accordance with the formula (1) [9]

$$\sigma_{r0.2} = \frac{R_{p0.2}}{\left[\sqrt{1/1.002} - \nu \cdot R_{p0.2}/E\right]^2}, \qquad (1)$$

where $R_{p0.2}$ is proof stress, ν is Poisson's ratio, and E is Young's modulus.

Strength properties, including proof stress, were determined in static uniaxial tension test on testing machine Instron of 1116 type. Next, the course of flow curve of the function $\sigma_p = f(\varepsilon)$ was determined.

Wires were then subject to surface modification. Wires electropolished as well as polished and then chemically passivated in 40% nitric acid surface were selected for tests. Passivation proceeded at the temperature of 65°C for 20–60 min. Prior to polishing and passivation, wires were grounded with abrasive paper with granulation from 80–1200. It enabled us to remove subgrease layers and grease that was left on the surface after drawing process. Figure 1 shows pictures of wire rod and wire with diameter of 1.5 mm after drawing. On the surface, there is a visible subgrease layer (wire rod) and a layer of grease (wires). If greases had been left there, it would preclude correct execution of electrochemical polishing and passivation. It would also cause deterioration of corrosion characteristics of wires. Pictures of wire surface after plastic working were taken with electron scanning microscope with field emission FE SEM S-4200 Hitachi.

Resistance to electrochemical corrosion was evaluated on the ground of registered anodic polarisation curves by means of potentiodynamic method [12, 13]. Potentiodynamic tests of wires were performed in artificial blood plasma solution. Stern method was used in order to determine polarisation resistance. Potentiodynamic tests were performed at the temperature of $T = 37 \pm 1°C$ and pH $= 7.0 \pm 0.2$. Saturated calomel electrode (SCE) of KP-113 type served as reference electrode, whereas platinum electrode PtP-201 was used as auxiliary electrode. Table 1 presents composition of artificial blood plasma.

(a)

(b)
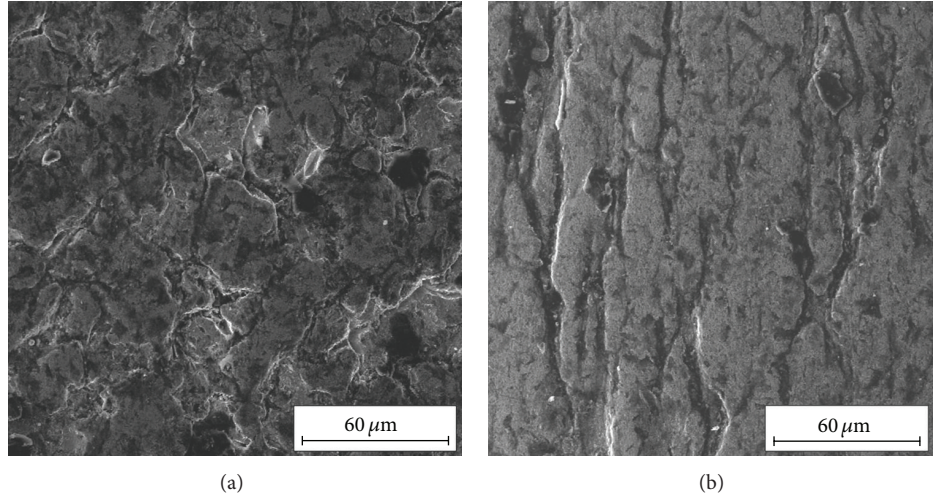
FIGURE 1: Surface of wire rod (a) and wire with diameter of 1.5 mm (b).

TABLE 1: Chemical composition of artificial blood plasma solution.

Chemical compound	Amount of distilled water, g/L
NaCl	6.8
$CaCl_2$	0.2
KCl	0.4
$MgSO_4$	0.1
$NaHCO_3$	2.2
Na_2HPO_4	0.126
NaH_2PO_4	0.026

3. Results

Table 2 presents strength properties of wires with selected diameters determined in tensile test.

Real stress values $\sigma_{r0.2}$ determined in tensile tests, corresponding to proof stress, served as the ground for making flow curve of tested wires and determination of mathematical form of flow stress function. The curve was approximated with function $\sigma_p = \sigma_{p0} + C\varepsilon^n$ that gives consideration to the value of stress for initial state (i.e., for annealed wire for drawing). Mathematical form of flow stress function for the tested steel is as follows:

$$\sigma_p = 253.1 + 894.6\varepsilon^{0.51}. \tag{2}$$

Figure 2 presents flow curve of wires made of X10CrNi 18-8 steel (ε means strain in drawing process expressed as a logarithm).

Potentiodynamic tests in artificial blood plasma enabled us to determine how wire resistance to electrochemical corrosion changes both in relation to strain applied in drawing process and to the way of wire surface preparation. OCP potential for all tested samples stabilised after 60 minutes. Corrosion test results are shown in Table 3. Figures 3 and 4 present selected anodic polarisation curves.

Next, it was determined whether there is a significant relation between corrosion properties and strain in drawing
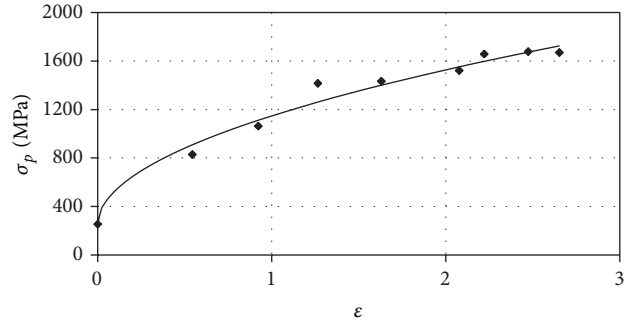
FIGURE 2: Flow curve of wire made of X10CrNi 18-8 steel.

process. Figure 5 shows curves obtained on the ground of selected results of corrosion tests, namely, the change of polarisation resistance R_p as the function of strain applied in drawing process ε. Functions presenting the change $R_p = f(\varepsilon)$ were selected. They look as follows:

(i) electrochemically polished wires

$$R_p = -118.4\varepsilon + 592.5, \quad R^2 = 0.886, \tag{3}$$

(ii) wires that were polished and chemically passivated

$$R_p = -444\varepsilon + 2057.5, \quad R^2 = 0.842. \tag{4}$$

Static analysis proved that significance level $P < 0.05$.

4. Discussion

Experimental determination of flow stress of the material is executed in one of basic tests: tensile, compression, or torsion. Indeed, static tensile test is accompanied by strain too small to be taken into consideration by engineers who design plastic forming processes; still it is the only possible one to be adopted in case of tests of thin wires. Performed mechanical

TABLE 2: Strength properties of wire.

Wire diameter d, mm	Logarithmic strain in the drawing process, ε	Tensile strength R_m, MPa	Proof stress $R_{p0.2}$, MPa
5.65	—	604	252
3.0	1.27	1607	1403
2.0	2.22	1827	1507
1.5	2.65	2178	1653

TABLE 3: Test results of pitting corrosion resistance.

Wire diameter d, mm	Strain in drawing process ε	Breakdown potential E_b, mV	Polarisation resistance R_p, kΩcm^2	Corrosion current density i_{corr}, μA/cm^2
Electrochemically polished wires				
5.6	0	+612	567	0.04
3.0	1.27	+510	459	0.10
1.5	2.65	+380	229	0.11
Electrochemically polished and chemically passivated wires				
5.6	0	+858	2220	0.012
3.0	1.27	+778	1230	0.021
1.5	2.65	+695	1070	0.024

properties tests enabled us to determine the course of flow curves and to select flow stress function of drawn wires made of X10CrNi 18-8 steel.

Performance of potentiodynamic tests enabled us to evaluate the impact of strain in drawing process on wire resistance to electrochemical corrosion artificial blood plasma solution. It was proved that with the applied strain, corrosion properties decrease. Perforation potential and polarisation resistance decrease, and anodic current density increases. That tendency applies both to electrolytically polished and polished and then chemically passivated wires.

Annealed wire rod with diameter of 5.65 mm featured the highest corrosion resistance, irrespective of the condition of the surface. Perforation potential of polished wire rod was $E_b = +612$ mV and, that of polished and passivated was $E_b = +858$ mV. The lowest perforation potential was observed in wire with diameter of 1.5 mm ($E_b = +380$ mV for polished wire and $E_b = +695$ mV for passivated wire). As strain increased, polarisation resistance also decreased. Polarisation resistance for polished wires was, respectively, $R_p = 576$ kΩcm^2 (wire rod) and $R_p = 229$ kΩcm^2 (wire with diameter of 1.5 mm). Polarisation resistance of polished and passivated wire rod was $R_p = 2220$ kΩcm^2 and of polished and passivated wire with diameter 1.5 mm was $R_p = 1070$ kΩcm^2.

Plastic strain in drawing process caused increase of corrosion current density for both types of wires, polished and polished and then passivated. Corrosion current density of polished wire rod was $i_{corr} = 0.04$ μA/cm^2 and of polished and passivated was $i_{corr} = 0.012$ μA/cm^2. Wire with diameter $d = 1.5$ mm featured the highest corrosion current density. It was $i_{corr} = 0.11$ μA/cm^2 for polished wire and $i_{corr} = 0.024$ μA/cm^2 for passivated wire.

Presented results show explicitly that chemical passivation substantially improved wire resistance to electrochemical corrosion in artificial blood plasma. Corrosion properties of passivated wires are higher than those of wires that were subject only to electrolytic polishing.

Static analysis showed that there is a significant dependence between corrosion properties (polarisation resistance) and strain applied in drawing process. Presented curves and functional relations give the ground to conclusions related to polarisation resistance of wire subject to surface treatment. The value of polarisation resistance shows that it was justifiable to use chemical passivation in case of wires for production of cardiologic guide made of X10CrNi 18-8 steel.

Presented curves represent correctly the results obtained experimentally. The greatest differences of polarisation resistance can be observed for wire with initial diameter. It must be highlighted that functions presented in the paper were elaborated for one heat. To transform them into universal relations for stainless steel X10CrNi 18-8, it is necessary to repeat the tests for a bigger number of heats.

5. Summary and Conclusions

The study proves that increase of strain in drawing process of wires made of stainless steel X10CrNi 18-8 causes decrease of their resistance to electrochemical corrosion in artificial blood plasma. Moreover, it was observed that chemical passivation improves wire corrosion characteristics.

Potentiodynamic test results also enabled us to obtain functional relations showing the influence of strain in drawing process on the change of polarisation resistance. It must

(a)

(b)
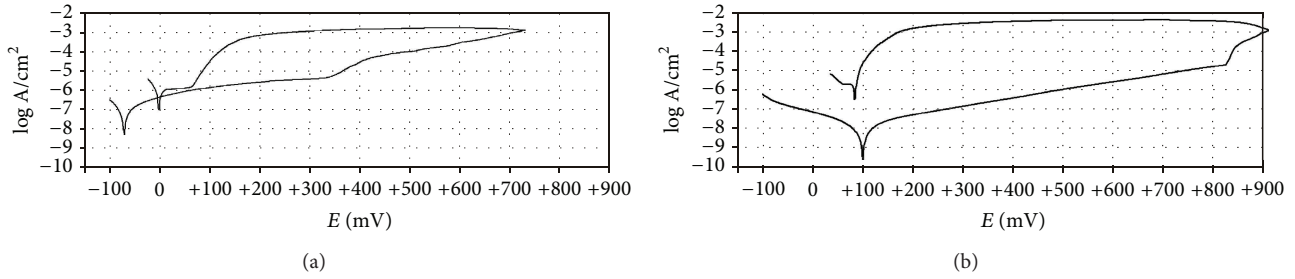
FIGURE 3: Anodic polarisation curve recorded for wire rod (d = 5.65 mm) electropolished (a) and passivated (b).

(a)

(b)
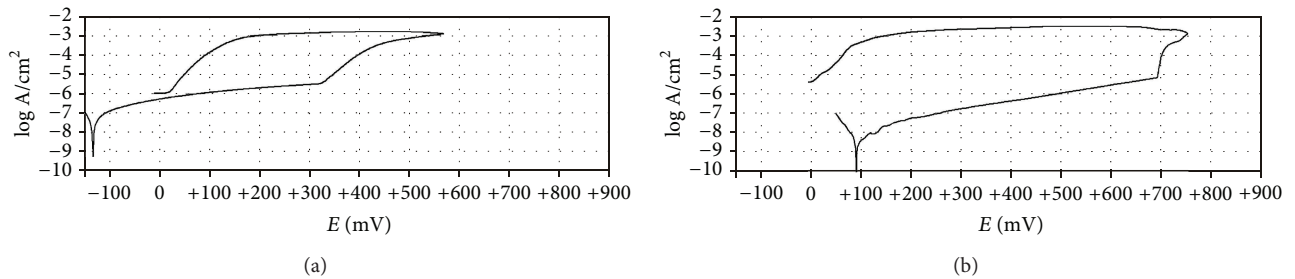
FIGURE 4: Anodic polarisation curve recorded for wire d = 1.5 mm electropolished (a) and passivated (b).

(a)

(b)
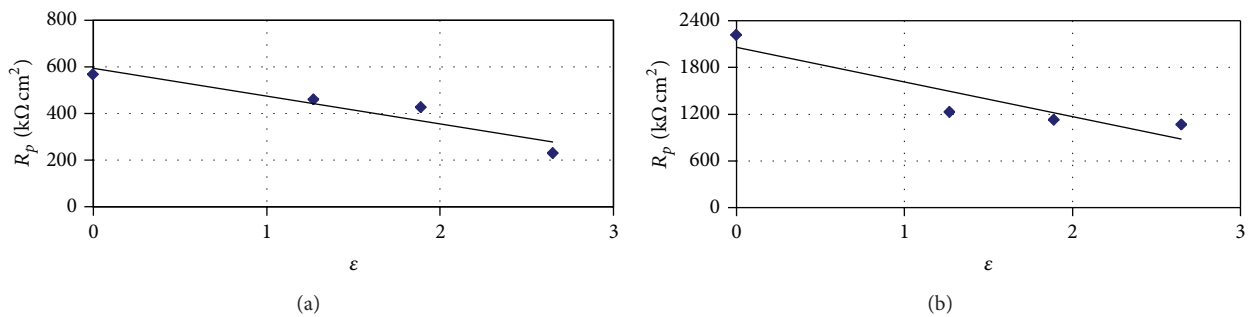
FIGURE 5: Dependence of polarisation resistance on strain in the drawing process: (a) of electrochemically polished wire and (b) of electrochemically polished and passivated wire.

be mentioned that presented functional relations are not of universal character and refer only to wires made of X10CrNi 18-8 steel tested in artificial blood plasma. If they are to be applied either to wires or other materials (e.g., other grades of steel, titanium alloys, cobalt alloys, alloys with elastic memory effect, and many other) or goods for other purposes, it is necessary to perform similar test for wires made of the respective material in another environment simulating human body saline (artificial urine solution, artificial saliva, and Tyrode or Ringer solution).

Problematic aspects presented in the study are crucial for process engineers who deal with designing wire drawing processes for medicine, as the issue of correct description of material plasticity is tightly connected with the selection of optimum parameters of wire production technological process. That issue is equally important to guide wire manufacturers, because if the respective curves or functions are to be applied, it is possible to forecast in advance corrosion characteristics of wire with the required strength drawn with the applied strain.

To sum up, it must be highlighted that proper description of flow stress function is one of the elements that determine acquisition of proper characteristics of technological plasticity of materials. These characteristics constitute currently the ground for databases for computer simulation of plastic working processes. Such bases could be completed with functional relations $R_p = f(\varepsilon)$ determined for various metallic biomaterials adjusted to human tissue environment in various body saline solutions. Then they could be used by process engineers and manufacturers of goods produced by means of cold working for various medical purposes. For example, when manufacturing a product (strip, bar, and wire, etc.) with the required mechanical characteristics, database will enable us to read both the value of necessary strain applied in processing and polarisation resistance corresponding to such strain that the respective biomaterial will feature.

That innovative proposal regarding creation of databases which take into account corrosive properties of metallic materials for medicine would make an extremely useful tool in designing technological processes of biomaterials.

Acknowledgment

References

[1] P. A. Schneider, *Endovascular Skills: Guidewire and Catheter Skills for Endovascular Surgery*, Informa Healthcare, New York, NY, USA, 2009.

[2] P. Fritzsche, M. Senac, and J. D. Moorhead, "Guide wire probe technique of the urinary tract," *RadioGraphics*, vol. 1, no. 2, pp. 38–48, 1981.

[3] A. Patriciu, D. Mazilu, H. S. Bagga, D. Petrisor, L. Kavoussi, and D. Stoianovici, "An evaluation method for the mechanical performance of guide-wires and catheters in accessing the upper urinary tract," *Medical Engineering and Physics*, vol. 29, no. 8, pp. 918–922, 2007.

[4] J. Przondziono, R. Młynarski, J. Szala, and A. Kur, "Characteristics of leaders used in heart pacemakers implantation," *Inżynieria Biomateriałów*, vol. 13, no. 100-101, pp. 56–58, 2010.

[5] J. Przondziono and W. Walke, "Potentiodynamic studies of stainless steel wire for endourology," *Archives of Materials Science and Engineering*, vol. 35, no. 1, pp. 21–28, 2009.

[6] J. Przondziono, J. Szala, and J. Kawecki, "Characteristics of guidewire used in percutaneous nephrolithotripsy," *Inżynieria Biomateriałów*, vol. 9, no. 58–60, pp. 178–180, 2006.

[7] E. Grzegorczyk, B. Młocek, A. Sołtysek, A. Szuła, and J. Przondziono, "Properties of wire used in ureterorenscopy," *Inżynieria Biomateriałów*, vol. 9, no. 58–60, pp. 181–183, 2006.

[8] F. Desgrandchamps, P. Pedron, P. Hoffmann, P. Teillac, and A. L. E. Duc, "A comparative study of guidewire electrical resistance," *British Journal of Urology*, vol. 80, no. 3, pp. 390–391, 1997.

[9] J. Przondziono, D. Halaczek, and J. Szymszal, "Determination of the flow curves of austenite steel wire in the drawing process," *Archives of Civil and Mechanical Engineering*, vol. 7, no. 1, pp. 85–91, 2007.

[10] W. Walke and J. Przondziono, "Influence of hardening and surface modification of endourological wires on corrosion resistance," *Acta of Bioengineering and Biomechanics*, vol. 14, no. 3, pp. 93–99, 2012.

[11] J. Przondziono, "The effect of strain hardening on resistance to electrochemical corrosion of wires used in cardiology," *Hutnik*, vol. 78, no. 8, pp. 663–666, 2011 (Polish).

[12] J. Szewczenko and J. Marciniak, "Corrosion of Cr-Ni-Mo steel implants electrically stimulated," *Journal of Materials Processing Technology*, vol. 175, no. 1-3, pp. 404–410, 2006.

[13] Z. Paszenda, "Application problems of implants used in interventional cardiology," *Advances in Soft Computing*, vol. 47, pp. 15–27, 2008.

Research Article

Aluminum Silicate Nanotube Modification of Cotton-Like Siloxane-poly(L-lactic acid)-vaterite Composites

Daiheon Lee,[1] Hirotaka Maeda,[2] Akiko Obata,[1] Keiichi Inukai,[3] Katsuya Kato,[4] and Toshihiro Kasuga[1]

[1] *Department of Frontier Materials, Nagoya Institute of Technology, Gokiso-cho, Showa-ku, Nagoya, Aichi 466-8555, Japan*

[2] *Center for Fostering Young and Innovative Researchers, Nagoya Institute of Technology, Gokiso-cho, Showa-ku, Nagoya 466-8555, Japan*

[3] *Ecological Ceramics Group, Materials Research Institute for Sustainable Development, National Institute of Advanced Industrial Science and Technology, Anagahora Shimo-Shidami, Moriyama-ku, Nagoya 463-8560, Japan*

[4] *Applied Technology with Traditional Ceramics Group, Advanced Manufacturing Research Institute, National Institute of Advanced Industrial Science and Technology, Anagahora Shimo-Shidami, Moriyama-ku, Nagoya 463-8560, Japan*

Correspondence should be addressed to Hirotaka Maeda; maeda.hirotaka@nitech.ac.jp
and Toshihiro Kasuga; kasuga.toshihiro@nitech.ac.jp

In our earlier work, a cotton-like biodegradable composite, consisting of poly(L-lactic acid) with siloxane-containing vaterite, has been prepared by electrospinning. In the present work, the fibers skeleton of the cotton-like composites was modified successfully with imogolite, which is hydrophilic and biocompatible, via a dip process using ethanol diluted solution to improve the cellular initial attachment. Almost no change in the fiber morphology after the surface modification was observed. The surface-modified composite showed the similar calcium and silicate ions releasabilities, for activating the osteoblasts, as an unmodified one. Cell culture tests showed that the initial adhesion of murine osteoblast-like cells on the surface of the fibers was enhanced by surface modification.

1. Introduction

Recently, the biodegradable polymers have attracted much attention as scaffolds [1, 2]. Poly(L-lactic acid) (PLLA), one of the common biodegradable polymers, has been reported as a scaffold material for bone reconstruction [3]. Several kinds of inorganic ions released from materials are reported to influence osteogenesis and angiogenesis [4]. Xynos et al. suggested that the ionic products, such as calcium and silicate ion released from Bioglass 45S5, have a stimulatory effect on osteoblast proliferation by increasing availability of insulin-like growth factor-II (IGF-II) [5]. The preparation of composites including inorganic materials, with calcium and silicate species releasing ability, in the biodegradable polymers is one of the important technologies for developing bone-forming biomaterials.

Our group has developed a polymer-ceramic composite material, PLLA/siloxane-containing vaterite (SiV) composite (PLLA/SiV), for the bone-filling material applications. The PLLA/SiV has the calcium and silicate ions releasing abilities derived from SiV [6]. In our earlier works, the PLLA/SiV fiber mats of ~300 μm in thickness, fabricated by electrospinning, showed bone formation by implanting the fiber mats on defects of 8 mm in diameter in the front midline of the calvaria in New Zealand rabbits [7, 8]. We also have prepared the cotton-like PLLA/SiV consisting of fibrous skeletons with open pore structure successfully by modified-electrospinning [9, 10]. The cells penetrated into the cotton-like PLLA/SiV and adhered on the fiber surface, resulting in proliferation inside of the cotton-like structure [10].

We believe that the enhancement of cell adhesion on the fiber surface is a critical factor for improving its biocompatibility. It has been widely accepted that the bone-forming cells prefer to attach on hydrophilic surface than hydrophobic one [11–13]. Nanometer-sized hydrous aluminum silicate, which

is called imogolite, $(HO)_3Al_2O_3Si(OH)$, has tubular structure of ~2.3 nm external and ~1.0 nm internal diameters [14], with up to several micrometers lengths. Imogolite nanotubes (INTs) have very hydrophilic surface owing to numerous hydroxyl groups on the surface. Ishikawa et al. reported that human and mouse osteoblast-like cells were widely spread on INTs coated on polystyrene cell culture dish, compared with the culture dish [15–17]. INT is one of the potential candidates to modify the fiber surface in the cotton-like PLLA/SiV for enhancing their cellular attachments.

The calcium and silicate ions releasing ability of PLLA/SiV, which has an effect on enhancing the cellular activity [18], is very important for accelerating bone formation on the material. Fujikura et al. suggested that the hydroxyapatite coating layer on fibers of the fiber mats, which were prepared by electrospinning, controlled calcium and silicate ions release from the fibers [19]. The influence of INT modification on the ions releasing ability of the cotton-like PLLA/SiV is considered to be examined.

In our previous report, it has been reported that the cell compatibility of PLLA/SiV fiber mats, especially at the early stage, was improved with INTs coating by electrophoretic deposition [20]. In our preliminary experiments, the electrophoretic deposition method has almost no effect on cotton-like PLLA/SiV. INTs would pass over the cotton-like PLLA/SiV because of the very high porosity of cotton-like structure. The aim of this work is to examine the effective way of PLLA/SiV surface modification with INTs. The PLLA/SiV has hydrophobic surface due to the matrix PLLA. INTs are dispersed in aqueous solution as a result of synthesis. It might lead to difficulty of coating on hydrophobic PLLA/SiV surface. It was considered that, by improving hydrophilicity of the fibrous PLLA/SiV surface temporarily, the modification using dip-coating would be able to be applied effectively. Our idea for improving the hydrophilicity is to treat the cotton-like PLLA/SiV with diluted ethanol. In the present work, the dip-coating method, one of the simplest ways, was investigated for INT modification of cotton-like PLLA/SiV to enhance the cellular attachment.

2. Materials and Methods

2.1. Preparation of Cotton-Like PLLA/SiV.
SiV particles, which were spherical particles of ~1 μm diameter, containing 2.6 wt% silicon, were prepared by a carbonation method using methanol and γ-aminopropyltriethoxysilane (APTES; Momentive Performance Materials, Japan). The detail of the preparation was described in our previous reports [7, 8, 18]. PLLA/SiV was prepared by kneading PLLA (LACIA; molecular weight = ~140 kDa, Mitsui Chemicals, Japan) with SiV particles at 200°C for 10 min. The weight ratio of PLLA : SiV was 7 : 3.

The PLLA/SiV solution for electrospinning was prepared using a chloroform as a solvent; PLLA weight ratio in the solution was 10 wt%. Following our previous report [9], cotton-like PLLA/SiV was prepared by electrospinning in ethanol (Wako Pure Chemicals, Japan) as a collector at room temperature. We have reported that PLLA fiber mats composed of the fiber skeleton ~10 μm in diameter allow cellular ingrowth into the gaps between them [21]. The fibers diameter was controlled by electrospun conditions as follows: impressed voltage: 15 kV, collector distance: 300 mm, and solution flow rate: 0.25 mL/min.

2.2. Preparation of INT-Dispersed Aqueous Solutions.
The preparation procedure of INTs was described in our previous report [20]. In brief, 18.47 g of aluminum chloride ($AlCl_3\cdot 6H_2O$; Wako Pure Chemicals, Japan) and 9.20 g sodium silicate ($Na_4SiO_4\cdot nH_2O$; Wako Pure Chemicals, Japan) were dissolved in 500 g of distilled water, respectively; Si/Al molar ratio of 0.41. sodium hydroxide (NaOH, 1 mol/L; Wako Pure Chemicals, Japan) aqueous solution was slowly added to the above described sodium silicate/aluminum chloride solution until pH of the solution reached 6.8. The resulting samples were separated by centrifugation, and the obtained precipitates were rinsed with distilled water. The centrifugation-rinsing process was repeated three times, and then the aluminum silicate precursors were dispersed in 12 L of distilled water by acidification with hydrochloric acid (HCl, 5 mol/L; Wako Pure Chemicals, Japan). The precursor solution was heated at 95°C for 4 days. Finally, the dispersed INTs in an aqueous solution with a concentration of 0.087 wt% were obtained.

2.3. INT Modification of the Cotton-Like PLLA/SiV by a Dip-Coating Method.
The INT-dispersed aqueous solution was diluted with ethanol to prepare the suspension for the dipping process. The weight ratio of INT-dispersed aqueous solution : ethanol was 10 : 90 or 50 : 50. It is well known that the vaterite of SiV is in the unstable phase in water and easily transforms into calcite [22, 23]. Ethanol was used for dilution because the vaterite is known to be more stable in ethanol than in water [24]. Cotton-like PLLA/SiV was dipped into the suspension and dried in a vacuum chamber at room temperature. The sample, which was modified using 50% diluted suspension, was denoted as PLLA/SiV-INT(50-1). In the case of 90% diluted suspension, the sample was prepared by the dipping process by repeating it 5 times and was denoted as PLLA/SiV-INT(10-5), hereafter.

2.4. Evaluation of INT-Modified Cotton-Like PLLA/SiV.
The morphology of cotton-like PLLA/SiV fibers was observed by field emission gun scanning electron microscopy (FE-SEM) (JSM-6301F, JEOL, Japan), incorporating energy dispersive X-ray spectroscopy (EDS) (Vantage, Noran, USA), after coating with amorphous osmium by plasma chemical vapor deposition.

The static water contact angles on the pressed samples, by uniaxial pressing under a pressure of 20 MPa for 5 sec, were measured with a CCD camera using SImage minisoftware. The contact angles were determined from the average of measurements at ten random points per sample (i.e., $n = 10$). The crystalline phases of calcium carbonates were analyzed with an X-ray diffractometer (XRD) (PANalytical X' pert-MPD, Netherlands; Cu Kα: 45 kV, 40 mA).

(a)

(b)

(c)
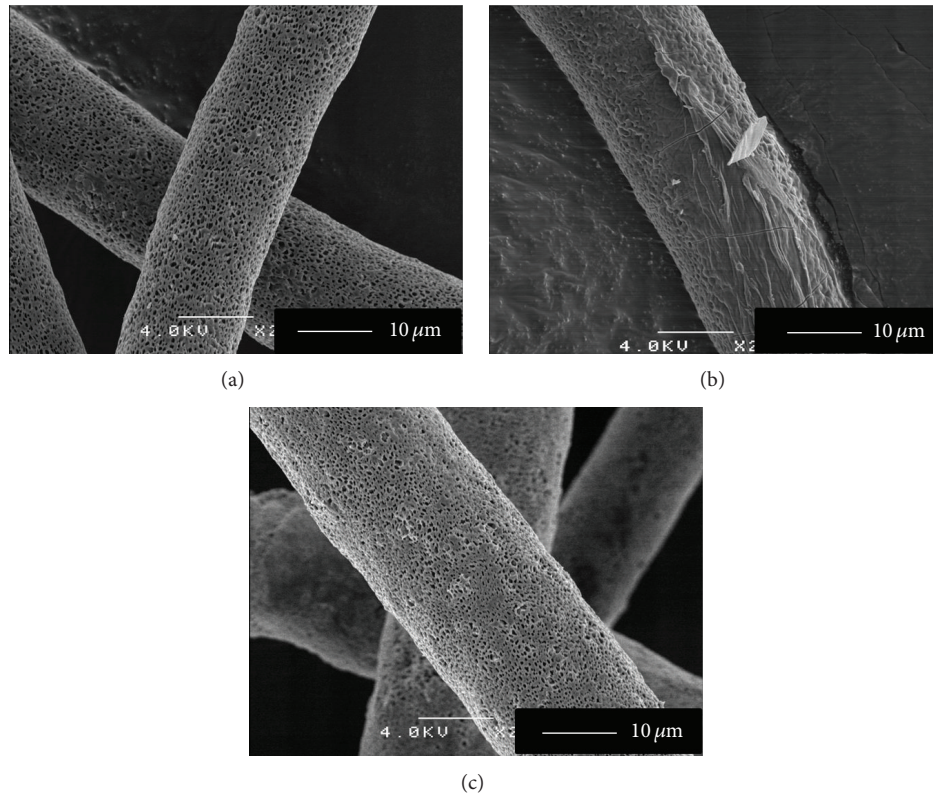
FIGURE 1: SEM images of (a) PLLA/SiV and ((b), (c)) INT-modified PLLA/SiV; (b) PLLA/SiV-INT(50-1) and (c) PLLA/SiV-INT(10-5).

Each sample of 10 mg was soaked in 10 mL of Tris buffer solution (pH ~7.4) at 37°C for 24 h. The released calcium and silicate ion amounts from samples were measured by inductively coupled plasma-atomic emission spectroscopy (ICP-AES) (ICPS-7000, Shimadzu, Japan). Three specimens at each point were measured (i.e., $n = 3$).

2.5. Cell Culture. Twenty milligrams of each sample was put in a well of 24-well plates and compressed with a silica glass tube of 15 mm outer diameter, 12 mm inner diameter, and 15 mm height. The resultant samples were sterilized using ethylene oxide gas. The samples were wetted by ethanol and then they were rinsed with a culture medium (alpha minimum essential medium, α-MEM) containing 10% fetal bovine serum. Murine osteoblast-like (MC3T3-E1) cells were seeded onto the samples with a density of 200,000 cells per well and incubated 3 h at 37°C in 5% CO_2 for evaluation of their initial attachment. After the incubation, the samples were rinsed with α-MEM and then incubated in the culture medium containing the reagent of the Cell Counting Kit-8 (CCK-8; Dojindo, Japan) at 37°C for 2 h. The attached cell number on samples was colorimetrically estimated by measuring the absorbance of the resulting medium at 450 nm ($n = 3$). Differences between the samples were determined by Student's t-test, with $P < 0.05$, which is considered to be statistically significant. The samples after 3 h of the incubation were fixed with 2.5% glutaraldehyde for 40 min at 4°C, dehydrated through a series of increasing concentrations

of ethanol, and finally dried with hexamethyldisilazane. The morphology of attached cells on samples was observed by FE-SEM.

3. Results and Discussion

Figure 1 shows the fiber morphologies of cotton-like PLLA/SiV before and after INT modification. The average and standard deviation of 100 parts of electrospun fiber diameters were 12 and 3 μm, respectively. Temperature and relative humidity are known as minor factors in the controlling of fiber diameter [25]. The temperature and relative humidity could affect the certain random fiber diameters of PLLA/SiV. As shown in Figure 1(a), the fibers have numerous pores of submicrometer diameter on their surfaces, due to the volatilization of the solvent during electrospinning. The fiber surface of PLLA/SiV-INT(50-1) was covered partially with the aggregated INTs, as shown in Figure 1(b). On the other hand, as shown in Figure 1(c), the numerous pores on the fiber surface of PLLA/SiV-INT(10-5) were observed; there was almost no change in the fiber morphology between the samples before and after 5 times of the dip-coating using highly diluted solution. INT-containing solution diluted with ethanol is considered to reduce the formation of INT aggregates. The aggregation rate of INTs maybe reduced in lower INTs concentration with an ethanol diluted solution. The EDS analysis (not shown here) exhibited the existence of aluminum, originated from INTs. The amount of detected

(a)

(b)
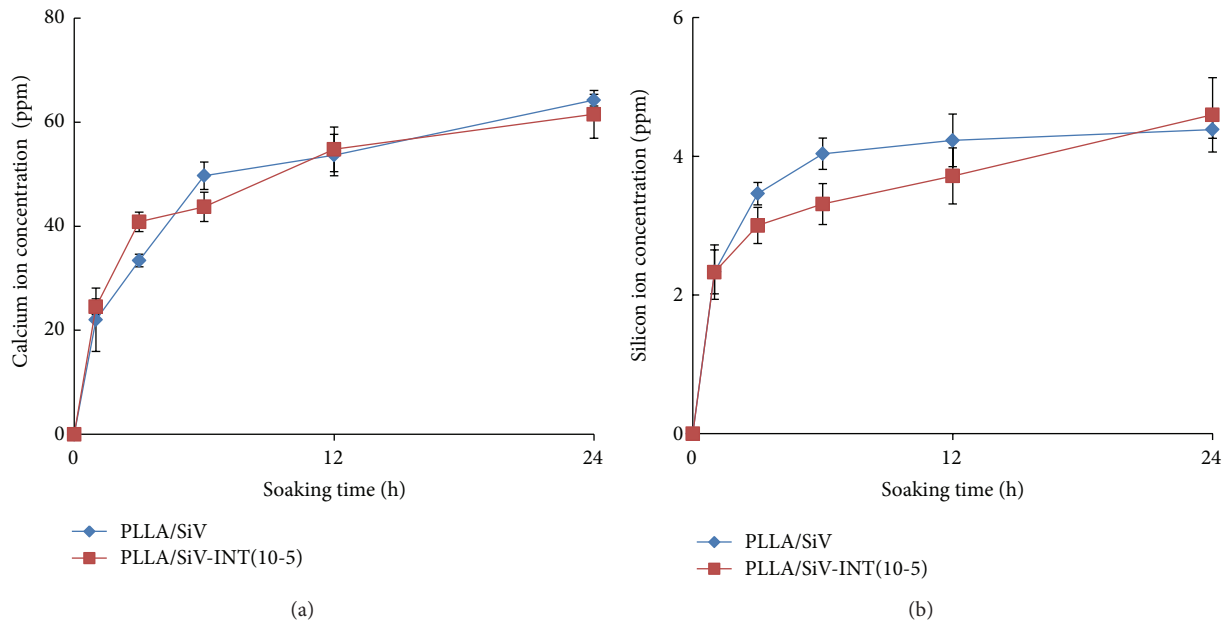
FIGURE 2: (a) Calcium and (b) silicon amounts released from PLLA/SiV and PLLA/SiV-INT(10-5) after soaking in Tris buffer solution. Circle: PLLA/SiV, diamond: PLLA/SiV-INT(10-5).

aluminum was ~5.0 ± 1.8 at % in PLLA/SiV-INT(10-5). This result indicated that INTs were coated on PLLA/SiV fiber surfaces by dip-coating. The crystalline phase of calcium carbonate (vaterite) in cotton-like PLLA/SiV was identified from XRD analysis; the peak of calcite did not appear. Almost no differences in the XRD patterns of between samples before and after the modification were observed. No conversion of vaterite into calcite occurred during the repeated dip-coating process.

In EDS analysis of our previous report, almost no Al was detected on the fiber of fiber mats by dipping [20]. The hydrophobic surface of PLLA/SiV could be a cause of the difficulty to INT modifying because the INTs dispersed solution was based in water. The surface tension is a decisive factor to determine the wettability of a liquid on the solid surface [26]. Vázquez et al. reported that surface tension of the ethanol aqueous solution decreased with increasing the ratio of ethanol [27]. In case of ethanol diluting, the INTs aqueous solution could get high wettability with PLLA/SiV fibers surface. Thus, dip-coating with ethanol diluted INTs solution could be a useful method for INT modifying of the surface of cotton-like PLLA/SiV.

In contact angle measurement, the water drop penetrated into the INT-modified samples, immediately. In contrast, the contact angle of PLLA/SiV was 105°. INT modification was found to have an excellent effect on the improvement of the fibers in the cotton-like PLLA/SiV, owing to high water-absorption ability of the nanotube structure [28, 29]. As a result, the INT-modification makes it easier for the cell suspension to penetrate into the matrix. That is, we believe that there is no difference in the hydrophilicity between the INT-modified samples. PLLA/SiV-INT(10-5) was discussed to compare it with PLLA/SiV, hereafter.
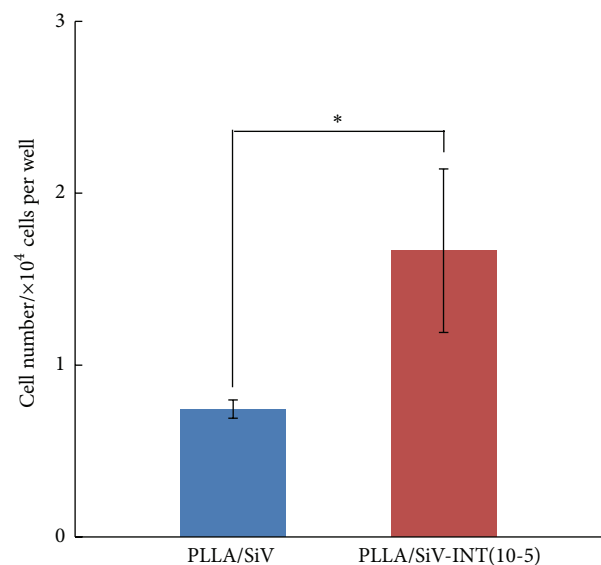
FIGURE 3: CCK-8 viability assay of MC3T3-E1 cells after 3 h of incubation on PLLA/SiV and PLLA/SiV-INT(10-5).

Figure 2 shows the released calcium and silicate ion amounts from samples. Both samples showed a similar trend on their releasing behaviors, independent of INT modification. It is supposed that the INT modification does not interrupt the calcium and silicate ions release from PLLA/SiV fibers.

Figure 3 shows attached cell numbers after 3 h of incubation on the samples. It is considerable that the great parts of seeded cells were passed through the cotton-like samples because the samples have very high porosity. The attached

(a)

(b)

(c)

(d)
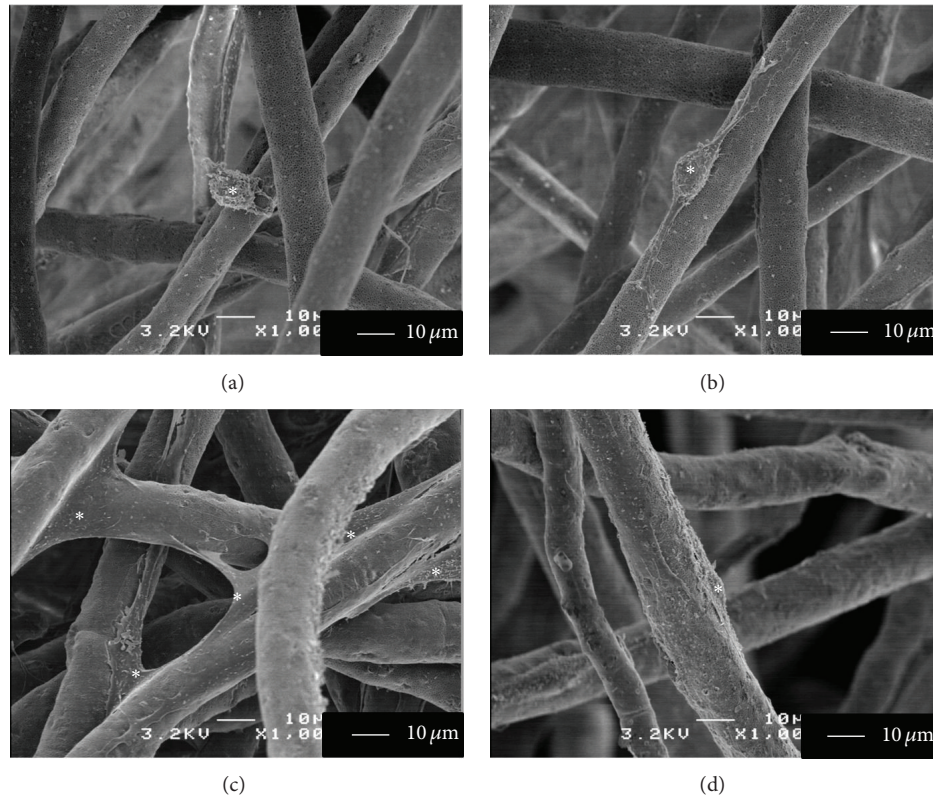
FIGURE 4: SEM images of MC3T3-E1 cells after 3 h of incubation on ((a), (b)) PLLA/SiV and ((c), (d)) PLLA/SiV-INT(10-5). Asterisk indicates the attached cells.

cell numbers on PLLA/SiV-INT(10-5) were almost twice of those on PLLA/SiV. Figure 4 exhibits the cell morphologies on the samples after 3 h of incubation. The cells on the PLLA/SiV were still spherical, as shown in Figures 4(a) and 4(b). In contrast, the cells on PLLA/SiV-INT(10-5) were more spread widely than those on PLLA/SiV. Some of them on PLLA/SiV-INT(10-5) were bridged between adjacent fibers. Aoki et al. reported that the well-spreaded cells adhered stronger and have more affinity to scaffold than round cells [30]. This suggests that the INT-modified cotton-like PLLA/SiV has more favorable surface for cell attachment than PLLA/SiV. Some reports suggest that the protein adsorption on the surface of materials contributes to cell adhesion [31, 32]. In our preliminary experiment, imogolite showed high adsorption ability with cell-adhesive proteins such as fibronectin or vitronectin. The cell-adhesive proteins might be more easily adsorbed on the fiber surfaces of INT-modified cotton-like PLLA/SiV than those of the PLLA/SiV. Therefore, the evaluation on protein adsorption ability of INT-modified cotton-like PLLA/SiV is currently in progress.

4. Conclusions

The fiber surface of cotton-like PLLA/SiV was modified successfully with imogolite nanotubes by a dip-process using ethanol-diluted aqueous solution. There was almost no change in the fiber morphology even after the surface modification. The calcium and silicate ions releasing behavior of the modified sample was almost the same as that of PLLA/SiV. The cell adhesion on PLLA/SiV was enhanced by surface modification with imogolite. Thus, the surface modification may be useful for improving cellular compatibility of biodegradable polymer materials.

Conflict of Interests

The authors declare no competing financial interests.

Acknowledgments

References

[1] J. C. Middleton and A. J. Tipton, "Synthetic biodegradable polymers as orthopedic devices," *Biomaterials*, vol. 21, no. 23, pp. 2335–2346, 2000.

[2] Y. Chen, S. Zhou, and Q. Li, "Microstructure design of biodegradable scaffold and its effect on tissue regeneration," *Biomaterials*, vol. 32, no. 22, pp. 5003–5014, 2011.

[3] P. Mainil-Varlet, B. Rahn, and S. Gogolewski, "Long-term in vivo degradation and bone reaction to various polylactides. 1. One-year results," *Biomaterials*, vol. 18, no. 3, pp. 257–266, 1997.

[4] A. Hoppe, N. S. Güldal, and A. R. Boccaccini, "A review of the biological response to ionic dissolution products from bioactive glasses and glass-ceramics," *Biomaterials*, vol. 32, no. 11, pp. 2757–2774, 2011.

[5] I. D. Xynos, A. J. Edgar, L. D. K. Buttery, L. L. Hench, and J. M. Polak, "Ionic products of bioactive glass dissolution increase proliferation of human osteoblasts and induce insulin-like growth factor II mRNA expression and protein synthesis," *Biochemical and Biophysical Research Communications*, vol. 276, no. 2, pp. 461–465, 2000.

[6] T. Wakita, J. Nakamura, Y. Ota, A. Obata, T. Kasuga, and S. Ban, "Effect of preparation route on the degradation behavior and ion releasability of siloxane-poly(lactic acid)-vaterite hybrid nonwoven fabrics for guided bone regeneration," *Dental Materials Journal*, vol. 30, no. 2, pp. 232–238, 2011.

[7] A. Obata, T. Hotta, T. Wakita, Y. Ota, and T. Kasuga, "Electrospun microfiber meshes of silicon-doped vaterite/poly(lactic acid) hybrid for guided bone regeneration," *Acta Biomaterialia*, vol. 6, no. 4, pp. 1248–1257, 2010.

[8] T. Wakita, A. Obata, G. Poologasundarampillai, J. R. Jones, and T. Kasuga, "Preparation of electrospun siloxane-poly(lactic acid)-vaterite hybrid fibrous membranes for guided bone regeneration," *Composites Science and Technology*, vol. 70, no. 13, pp. 1889–1893, 2010.

[9] T. Kasuga, A. Obata, H. Maeda, Y. Ota, X. Yao, and K. Oribe, "Siloxane-poly(lactic acid)-vaterite composites with 3D cotton-like structure," *Journal of Materials Science*, vol. 23, no. 10, pp. 2349–2357, 2012.

[10] A. Obata, H. Ozasa, T. Kasuga, and J. R. Jones, "Cotton wool-like poly (lactic acid)/vaterite composite scaffolds releasing soluble silica for bone tissue engineering," *Journal of Materials Science*, vol. 24, no. 7, pp. 1649–1658, 2013.

[11] P. B. Van Wachem, T. Beugeling, and J. Feijen, "Interaction of cultured human endothelial cells with polymeric surfaces of different wettabilities," *Biomaterials*, vol. 6, no. 6, pp. 403–408, 1985.

[12] Y. Tamada and Y. Ikada, "Cell adhesion to plasma-treated polymer surfaces," *Polymer*, vol. 34, no. 10, pp. 2208–2212, 1993.

[13] Y. Arima and H. Iwata, "Effect of wettability and surface functional groups on protein adsorption and cell adhesion using well-defined mixed self-assembled monolayers," *Biomaterials*, vol. 28, no. 20, pp. 3074–3082, 2007.

[14] P. Cradwick, V. Farmer, J. Russell, C. Masson, K. Wada, and N. Yoshinaga, "Imogolite, a hydrated aluminium silicate of tubular structure," *Nature*, vol. 240, no. 104, pp. 187–189, 1972.

[15] K. Ishikawa, S. Abe, Y. Yawaka, M. Suzuki, and F. Watari, "Osteoblastic cellular responses to aluminosilicate nanotubes, imogolite using Saos-2 and MC3T3-E1 cells," *Journal of the Ceramic Society of Japan*, vol. 118, no. 1378, pp. 516–520, 2010.

[16] K. Ishikawa, T. Akasaka, S. Abe, Y. Yawaka, M. Suzuki, and F. Watari, "Application of imogolite, almino-silicate nanotube, as scaffold for the mineralization of osteoblasts," *Bioceramics Development and Applications*, vol. 1, pp. 1–3, 2011.

[17] K. Ishikawa, T. Akasaka, Y. Nodasaka et al., "Physical properties of aluminosilicate nanotubes, imogolite, as scaffold and effect on osteoblastic mineralization," *Nano Biomedicine*, vol. 1, no. 2, pp. 109–120, 2009.

[18] A. Obata, S. Tokuda, and T. Kasuga, "Enhanced in vitro cell activity on silicon-doped vaterite/poly(lactic acid) composites," *Acta Biomaterialia*, vol. 5, no. 1, pp. 57–62, 2009.

[19] K. Fujikura, S. Lin, J. Nakamura, A. Obata, and T. Kasuga, "Preparation of eletrospun fiber mats using siloxane-containing vaterite and biodegradable polymer hybrids for bone regeneration," *Journal of Biomedical Materials Research Part B*, 2013.

[20] S. Yamazaki, H. Maeda, A. Obata, K. Inukai, K. Kato, and T. Kasuga, "Aluminum silicate nanotube coating of siloxane-poly (lactic acid)-vaterite composite fibermats for bone regeneration," *Journal of Nanomaterials*, vol. 2012, Article ID 463768, 7 pages, 2012.

[21] K. Fujikura, A. Obata, and T. Kasuga, "Cellular migration to electrospun poly (lactic acid) fibermats," *Journal of Biomaterials Science, Polymer Edition*, vol. 23, no. 15, pp. 1939–1950, 2012.

[22] M. S. Rao, "Kinetics and mechanism of the transformation of vaterite to calcite," *Bulletin of the Chemical Society of Japan*, vol. 46, pp. 1414–1417, 1973.

[23] N. Spanos and P. G. Koutsoukos, "The transformation of vaterite to calcite: effect of the conditions of the solutions in contact with the mineral phase," *Journal of Crystal Growth*, vol. 191, no. 4, pp. 783–790, 1998.

[24] S.-F. Chen, S.-H. Yu, J. Hang, F. Li, and Y. Liu, "Polymorph discrimination of $CaCO_3$ mineral in an ethanol/water solution: formation of complex vaterite superstructures and aragonite rods," *Chemistry of Materials*, vol. 18, no. 1, pp. 115–122, 2006.

[25] S. De Vrieze, T. Van Camp, A. Nelvig, B. Hagström, P. Westbroek, and K. De Clerck, "The effect of temperature and humidity on electrospinning," *Journal of Materials Science*, vol. 44, no. 5, pp. 1357–1362, 2009.

[26] Y. Yuan and T. R. Lee, "Contact Angle and Wetting Properties," in *Surface Science Techniques*, G. Bracco and B. Holst, Eds., pp. 3–34, Springer, Berlin, Germany, 2013.

[27] G. Vázquez, E. Alvarez, and J. M. Navaza, "Surface tension of alcohol + water from 20 to 50°C," *Journal of Chemical and Engineering Data*, vol. 40, no. 3, pp. 611–614, 1995.

[28] V. C. Farmer, M. J. Adams, A. R. Fraser, and F. Palmieri, "Synthetic imogolite: properties, synthesis, and possible applications," *Clay Minerals*, vol. 18, no. 4, pp. 459–472, 1983.

[29] M. Suzuki, "Absorption properties and application of allophane and imogolite," *Journal of Clay Science Society of Japan*, vol. 42, no. 3, pp. 144–147, 2003 (Japanese).

[30] N. Aoki, A. Yokoyama, Y. Nodasaka et al., "Strikingly extended morphology of cells grown on carbon nanotubes," *Chemistry Letters*, vol. 35, no. 5, pp. 508–509, 2006.

[31] T. A. Horbett and M. B. Schway, "Correlations between mouse 3T3 cell spreading and serum fibronectin adsorption on glass and hydroxyethylmethacrylate-ethylmethacrylate copolymers," *Journal of Biomedical Materials Research*, vol. 22, no. 9, pp. 763–793, 1988.

[32] Y. Yang, R. Cavin, and J. L. Ong, "Protein adsorption on titanium surfaces and their effect on osteoblast attachment," *Journal of Biomedical Materials Research A*, vol. 67, no. 1, pp. 344–349, 2003.

Research Article

The Effect of Negative Poisson's Ratio Polyurethane Scaffolds for Articular Cartilage Tissue Engineering Applications

Yeong Jun Park and Jeong Koo Kim

Department of Biomedical Engineering, Graduate School, Inje University, Gimhae 621-749, Republic of Korea

Correspondence should be addressed to Jeong Koo Kim; jkkim@inje.ac.kr

An auxetic polyurethane (PU) scaffold was prepared to investigate chondrocyte proliferation under compressive stimulation for cartilage regeneration. To give a negative Poisson's ratio to the PU scaffold, volumetric compression with a 3 : 1 ratio was applied during heat treatment. For the control PU scaffold, the Poisson's ratio was 0.9 ± 0.25 with elongation at 20% of the strain range. Poisson's ratio for experimental specimens was approximately -0.4 ± 0.12 under the same conditions. In cell proliferation tests, cells were cultivated within the prepared scaffold under compression with a 20% strain range. With a 20% strain range elongation, the compressive load was approximately 0.3 N. The experimental group showed a 1.3 times higher cellular proliferation rate than that of the control group after 3 days in culture. At day 5 of culture, however, the rate of proliferation of the control group increased so that there was no significant difference between groups. However, collagen content (produced by the cells) in the cell-proliferated medium was 1.5 times higher in the experimental group after 5 days in culture. This may have been due to the effectiveness of the auxetic structure of the scaffold. An isotropic compressive load was transmitted to the cells due to the negative Poisson ratio of the scaffold.

1. Introduction

Bone and cartilage generation by autogenous cell/tissue transplantation is one of the most promising techniques in orthopedic surgery and biomedical engineering [1]. Due to the inability of avascular and aneural tissues to self-heal, even minor cartilage defects can result in mechanical joint instability and progressive damage, and cartilage damage is notoriously difficult to treat and cure [2]. Autologous cell-based tissue engineering using three-dimensional (3D) porous scaffolds has provided an option for the repair of full thickness defects in adult cartilage tissue [3]. The scaffold or 3D construct provides the necessary support for cells to proliferate and maintain their differentiated function, and its architecture defines the ultimate shape of the new bone and cartilage [4].

All these natural and artificial materials for 3D scaffolds have a convex cell shape and exhibit a positive Poisson's ratio, which is defined as the negative of the lateral strain divided by the longitudinal strain when a load is applied in the longitudinal direction [5]. On the other hand, materials or structures that contract in the transverse direction under uniaxial compression or expand laterally when stretched are said to have negative Poisson's ratios [6, 7]. This phenomenon is the opposite of the behavior of a positive Poisson's ratio due to the effect of the material structure. For negative Poisson's ratio material, the structures are commonly known as auxetic structures, which are similar to a reentrant honeycomb structure [8]. This reentrant shape is fabricated by transforming a conventional honeycomb shape into the concave structure that finally produces the auxetic structure. As shown in Figure 1, the reentrant structure unfolds under tension and gives rise to a negative Poisson's ratio. Usually, an allowable range of Poisson's ratio is −1.0 to 0.5 based on the thermodynamic consideration of strain energy in the theory of elasticity [9]. In the last two decades, the behavior of the negative Poisson's ratio was predicted, discovered, or deliberately introduced in various materials, such as foam and microstructure polymers [10, 11]. This sort of material is expected to have interesting mechanical properties, such

(a)

(b)
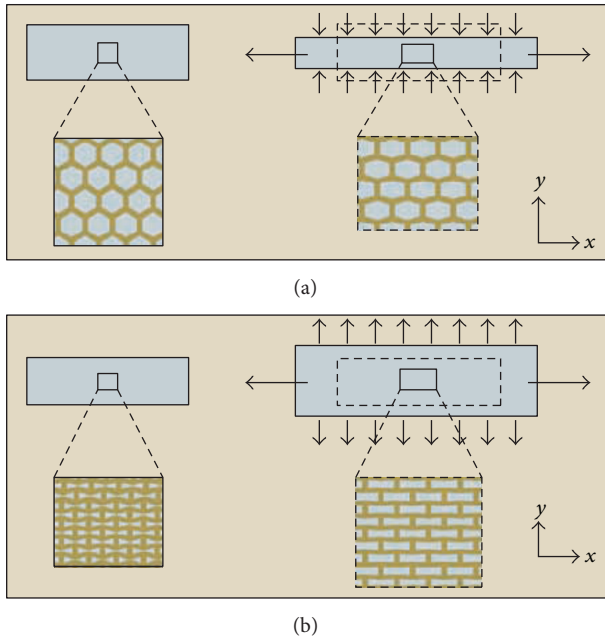
Figure 1: Behaviour of positive Poisson's ratio and negative Poisson's ratio when subjected to tensile loading. The pores have a rounder shape (a), while in (b), the pore space is larger, giving rise to a negative Poisson's ratio [11].

Figure 2: Schematic diagram of the preparation of an auxetic scaffold (compressive volume ratio = 2.5 ~ 3.0).

as high energy absorption, fracture toughness, indentation resistance, and enhanced shear moduli, which may be useful in some applications [6].

Auxetic materials are known to exhibit various enhanced physical characteristics over their conventional counterparts [10]. They show increased indentation resistance and improved acoustic damping properties. These enhanced characteristics make negative Poisson's ratio materials perform better in many practical applications; however, although these enhanced properties have been studied in industrial and academic fields, there have been few studies in tissue engineering. Fozdar et al. reported that there are possibilities to fabricate tunable negative Poisson's ratio scaffold by digital micromirror device projection printing for tissue engineering applications [12].

In cartilage tissue engineering, a focus has been on the relationship between chondrocyte response and physical properties of the scaffold (i.e., stiffness, hydrophilicity). However, knowledge is lacking about chondrocyte behavior with mechanical stimulation in a negative Poisson's ratio scaffold. Mechanical stimulation associated with normal body functions is crucial in properly reforming articular cartilage with tissue engineering [2].

In this study, we form an auxetic structural polyurethane (PU) scaffold for cartilage regeneration and investigate chondrocyte proliferation effectiveness within the auxetic scaffold under mechanical (compression) stimulation.

2. Materials and Methods

2.1. Specimen (Scaffold) Preparation. PU foam was purchased from Kumsung Sponge Co. (Seoul, Republic of Korea).

PU foams were treated with 70% ethanol for 30 min for sterilization.

Control specimens were prepared with 60 ppi PU foam. Pore size and shape of experimental specimens were controlled by heating and compression. A metal mold with dimensions of 5 cm × 5 cm × 7.5 cm was used to prepare specimens. To materialize the auxetic structure, the desired volumetric ratio was estimated as 3.0 based on a predetermined calculation. A schematic diagram of the process is presented in Figure 2. The initial sample size of the PU sample was cut to approximately 8 cm × 8 cm × 9 cm, giving an initial volume to final volume ratio of 1 : 3 after applying compression. The PU foam was then placed carefully into the mold, using a tongue depressor to prevent wrinkles. The foam was pulled and adjusted at each end to ensure that it fit the mold exactly. The metallic mold was then placed in the center of a furnace (preheated to 150°C) for 30 min at 200°C under triaxial compression in order to produce a reentrant structure of the PU foam. Then, the mold was cooled slowly to room temperature. The mold containing the PU foam was removed from the furnace, and the heat-treated PU foam was removed from the mold and cut into small cylindrical shapes.

2.2. Estimation of Poisson's Ratio. Poisson's ratio was estimated by image processing [13, 14]. A digital microscope (BX51; Olympus Corporation, Tokyo, Japan) was used to measure Poisson's ratio of the specimens. Compressive loading was applied to the specimens with a material testing machine (LRX-PLUS; Lloyd Instruments, West Sussex, UK). The experimental setup with the microscope for capturing the specimen while applying a load to measure the displacement of the specimen is shown in Figure 3. The relative positions of pointed marks were used to estimate the strain and Poisson's ratio. Images were processed with Photoshop 7.0. For each specimen, five measurements were taken from a 0.05 to 0.25 strain range, as shown in Figure 4. In-built tools of the digital microscope were used to measure the x-axis and y-axis displacements, which were then calculated using (1) to determine Poisson's ratio.
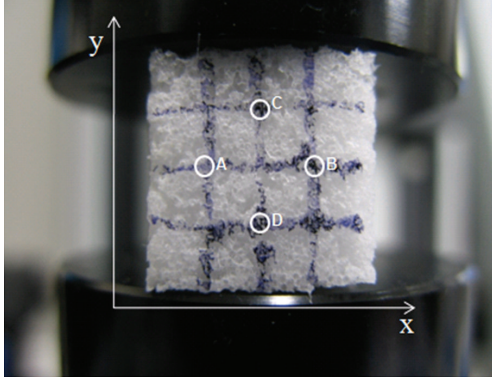
FIGURE 3: Experimental setup with microscope for capturing the specimen while applying a load to measure the displacement of the specimen with the points (A to D).
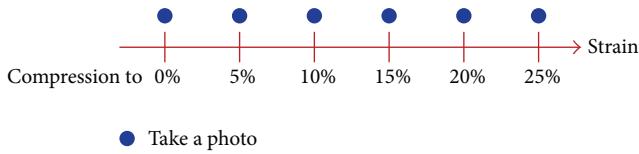
FIGURE 4: Strain intervals while applying load for taking photos to measure displacement of the prepared specimens.

In order to investigate pore shapes and distribution, a cross section of the scaffold was observed by Scanning Electron Microscope (S-4300DSE, HITACHI, Tokyo, Japan).

We have

$$\varepsilon_x = \frac{|A - B| - |A_0 - B_0|}{|A_0 - B_0|},$$

$$\varepsilon_y = \frac{|C - D| - |C_0 - D_0|}{|C_0 - D_0|}, \tag{1}$$

$$\nu = -\frac{\varepsilon_x}{\varepsilon_y},$$

where ε_x = strain of x-axis, ε_y = strain of y-axis, ν = material Poisson's ratio, A_0 to D_0 = initial point (load = 0), and A to D = moved point under load.

2.3. Chondrocyte Isolation and Culture. Porcine cartilage was harvested from the lateral and medial condyle of 6-month-old pig hinge legs. The obtained cartilage was chopped into small pieces with sterilized scissors. The cartilage was digested for 4 h in Dulbecco's Modified Eagle Medium (DMEM, Gibco) containing 2 mg/mL collagenase and filtered through a nylon sieve cell strainer (Falcon, New Jersey, USA) having an 80 μm pore size. The cells were rinsed with phosphate buffered saline (PBS) solution (Lonza, Walkersville, USA) and then centrifuged at 1500 rpm for 5 min. The centrifuged cell pellet was washed with PBS, and the number of cells was determined by using a hemocytometer. Chondrocytes were then cultured in cell culture flasks with DMEM supplemented with 10% fetal bovine serum (Gibco)

and 1% antibiotics (Gibco) in a humidified incubator with 5% CO_2 at 37°C. The media were exchanged every 3 days.

2.4. Cell Proliferation Estimation. For sterilization of the specimens in order to culture the prepared cells, all specimens were incubated with 70% ethanol for 1 h, followed by washing three times with PBS solution. For cell seeding, second to third passage chondrocytes were used. An initial cell density of 2.0×10^5 (cells/specimen) was seeded in a humidified incubator containing 5% CO_2 at 37°C. Cells were cultured in the prepared scaffold with static compression (compression with 20% strain). The exerted static load from 20% strain elongation of the prepared scaffold was about 0.3 N. The cellular proliferation rate was measured by using the Cell Counting Kit (CCK-8; Dojindo Molecular Technologies, Inc., Maryland, USA) and the Sircol collagen assay kit (Biocolor, Antrim, UK). Experiments were observed on days 1, 3, and 5. The absorbances of the CCK-8 solution (DMEM : CCK solution = 10 : 1) and Sircol collagen assay solution were measured by using a Fluorescence Multi-Detection Reader (Synergy HT, BIO-TEK Instruments, Inc., Vermont, USA) at 450 nm and 550 nm, respectively.

2.5. Statistical Analysis. Data were expressed as mean ± standard error for all comparisons. A t-test was used to evaluate differences between groups ($P < 0.05$).

3. Results and Discussion

A PU scaffold with a negative Poisson's ratio was formed by creating a reentrant cell structure inside the foam. The original microstructure of the PU foam is shown in Figure 5(a); the pores are well distributed and uniform in shape and size. For formation of negative Poisson's ratio scaffolds, a compressive load was applied with thermal treatment; this resulted in the transformation of the microstructure from a convex cell shape to a deformed cell shape as shown in Figure 5(b). The cell shapes were deformed and generated new bonding and debonding between the cells [15]. As a result, Poisson's ratio of the control group was estimated as 0.9 ± 0.25 on average with 20% strain elongation via compressive loading. In contrast, the experimental group had a Poisson's ratio of approximately −0.4 ± 0.12 with 20% strain elongation via compressive loading (Figure 6).

In the cellular proliferation test, the experimental group had a 1.3 times higher cellular proliferation rate compared to the control group 3 days after cell seeding. At day 5 in culture, the experimental group had a 1.2 times higher cellular proliferation rate, but there was no significant difference between groups, as shown in Figure 7. However, results of the Sircol collagen assay showed that the amount of collagen produced by the cells after 3 and 5 days in culture was about 1.5 times higher in the experimental group ($P < 0.05$), as shown in Figure 8. This is an important finding because collagen production is essential for proliferated cells to construct extracellular matrix in tissue engineering. The results suggest that isotropic compressive stimulation occurred due to the auxetic structure of the scaffold and isotropic mechanical stimulation was effectively transmitted to the cells through

(a)

(b)
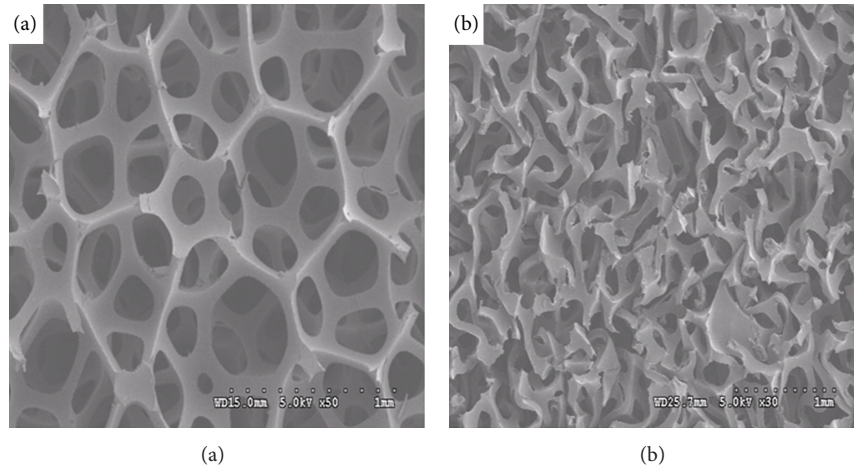
Figure 5: Microstructures of polyurethane scaffolds: (a) a control specimen and (b) an experimental specimen.
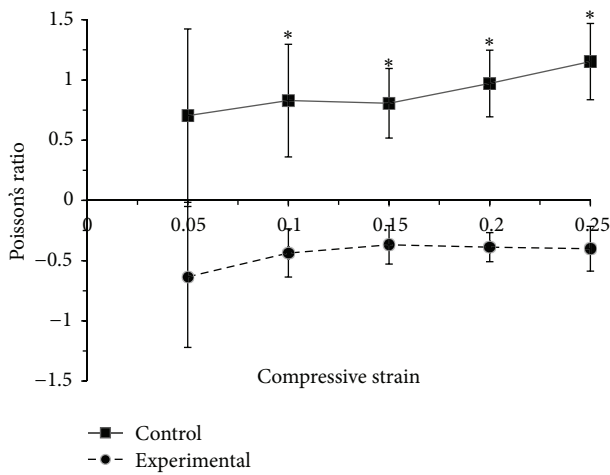
Figure 6: Poisson's ratio variation of prepared polyurethane scaffolds with strain ranges with compressive loading ($^*P < 0.05$, $n = 5$).
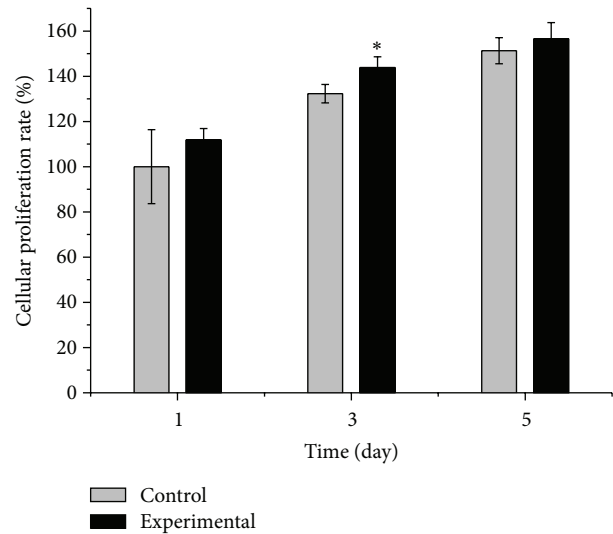
Figure 7: Chondrocyte proliferation rate on polyurethane scaffolds. Values were normalized ($n = 5$, $^*P < 0.05$).

the scaffold. Isotropic compressive stimulation was favorable for chondrocyte proliferation and collagen production. The results indicate that isotropic compressive stimulation could be more effective on collagen production during chondrocyte proliferation, which is a good indicator for the construction of extracellular matrix as well as cartilage tissue, and that chondrocytes preferentially proliferate on a negative Poisson's ratio PU scaffold rather than a conventional scaffold because of isotropic mechanical stimulation.

The cellular proliferation decrease after 5 days in culture could be affected by viscoelastic properties of the scaffold. The applied load to the scaffold would be transmitted sufficiently to the cells during the initial 3 days; however, on day 5, the compressive load should be decreased due to stress relaxation of the PU scaffold. Hence, it is inferred that the increase in cellular proliferation decreased at day 5 compared with the initial 3-day cultivation period.

4. Conclusions

It is well known that physical and/or chemical stimulation is effective for cellular proliferation during cell cultivation. We used PU foam to investigate the formation of an auxetic structural scaffold and the effectiveness of cell proliferation in the scaffold with mechanical stimulation. With compressive load stimulation, the auxetic PU scaffold successfully transferred the compressive load isotropically to the cells. Hence, the auxetic scaffold could be effective for chondrocyte proliferation with compressive load stimulation. From this study, we confirmed that mechanical stimulation is effective for chondrocytes proliferation and that isotropic stimulation could be more effective for collagen production from the cells.

Biodegradable polymeric scaffolds are widely used in tissue engineering, but there have been few studies related to auxetic biodegradable scaffolds. Hence, we suggest that
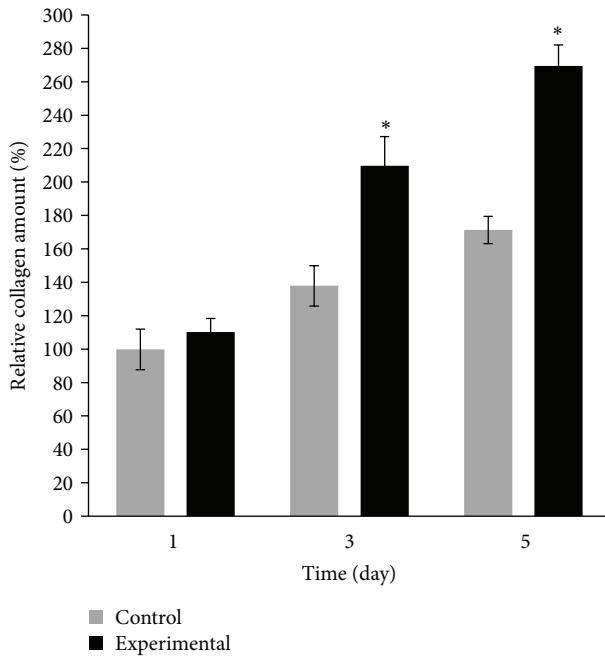
FIGURE 8: Relative amount of collagen within the PU scaffold during cell cultivation. Values were normalized ($n = 5$, $^*P < 0.05$).

biodegradable polymeric scaffolds should be considered for forming an auxetic structure as well as for isotropic mechanical stimulation in cartilage tissue engineering.

Acknowledgment

References

[1] C. W. Patrick Jr., A. G. Mikos, and L. V. McIntire, "Prospectus of tissue engineering," in *Frontiers in Tissue Engineering*, pp. 3–14, Elsevier Science, New York, NY, USA, 1998.

[2] Y. M. Jung, M. S. Park, J. W. Lee et al., "Cartilage regeneration with highly-elastic three-dimensional scaffolds prepared from biodegradable poly(l-lactide-co-ε-caprolactone)," *Biomaterials*, vol. 29, no. 35, pp. 4630–4636, 2008.

[3] Y. Wang, D. J. Blasioli, H. J. Kim, H. S. Kim, and D. L. Kaplan, "Cartilage tissue engineering with silk scaffolds and human articular chondrocytes," *Biomaterials*, vol. 27, no. 25, pp. 4434–4442, 2006.

[4] D. W. Hutmacher, "Scaffolds in tissue engineering bone and cartilage," *Biomaterials*, vol. 21, no. 24, pp. 2529–2543, 2000.

[5] J. B. Choi and R. S. Lakes, "Analysis of elastic modulus of conventional foams and of re-entrant foam materials with a negative Poisson's ratio," *International Journal of Mechanical Sciences*, vol. 37, no. 1, pp. 51–59, 1995.

[6] H. Wan, H. Ohtaki, S. Kotosaka, and G. Hu, "A study of negative Poisson's ratios in auxetic honeycombs based on a large deflection model," *European Journal of Mechanics, A/Solids*, vol. 23, no. 1, pp. 95–106, 2004.

[7] B. Brandel and R. S. Lakes, "Negative Poisson's ratio polyethylene foams," *Journal of Materials Science*, vol. 36, no. 24, pp. 5885–5893, 2001.

[8] D. Prall and R. S. Lakes, "Properties of a chiral honeycomb with a Poisson's ratio of -1," *International Journal of Mechanical Sciences*, vol. 39, no. 3, pp. 305–314, 1997.

[9] H. Ohtaki, G. Hu, Y. Nagasaka, and S. Kotosaka, "Analysis of negative Poisson's ratios of re-entrant honeycombs," *JSME International Journal A*, vol. 47, no. 2, pp. 113–121, 2004.

[10] J. N. Grima, R. Gatt, N. Ravirala, A. Alderson, and K. E. Evans, "Negative Poisson's ratios in cellular foam materials," *Materials Science and Engineering A*, vol. 423, no. 1-2, pp. 214–218, 2006.

[11] W. Yang, Z. M. Li, W. Shi, B. H. Xie, and M. B. Yang, "Review on auxetic materials," *Journal of Materials Science*, vol. 39, no. 10, pp. 3269–3279, 2004.

[12] D. Y. Fozdar, P. Soman, J. W. Lee, L.-H. Han, and S. Chen, "Three-dimensional polymer constructs exhibiting a tunable negative Poisson's ratio," *Advanced Functional Materials*, vol. 21, no. 14, pp. 2712–2720, 2011.

[13] J. B. Choi and R. S. Lakes, "Nonlinear properties of polymer cellular materials with a negative Poisson's ratio," *Journal of Materials Science*, vol. 27, no. 17, pp. 4678–4684, 1992.

[14] R. D. Widdle Jr., A. K. Bajaj, and P. Davies, "Measurement of the Poisson's ratio of flexible polyurethane foam and its influence on a uniaxial compression model," *International Journal of Engineering Science*, vol. 46, no. 1, pp. 31–49, 2008.

[15] A. Butenhoff, R. S. Lakes, and Y. C. Wang, "Influence of cell size on re-entrant transformation of negative Poisson's ratio reticulated polyurethane foams," *Cellular Polymers*, vol. 20, no. 4–6, pp. 373–385, 2001.

Research Article

Fibre Laser Cutting and Chemical Etching of AZ31 for Manufacturing Biodegradable Stents

Ali Gökhan Demir,[1] Barbara Previtali,[1] and Carlo Alberto Biffi[2]

[1] *Department of Mechanical Engineering, Politecnico di Milano, Via La Masa 1, 20156 Milan, Italy*
[2] *National Research Council, Institute for Energetics and Interphases, Corso Promessi Sposi 29, 23900 Lecco, Italy*

Correspondence should be addressed to Ali Gökhan Demir; aligokhan.demir@polimi.it

The use of magnesium-alloy stents shows promise as a less intrusive solution for the treatment of cardiovascular pathologies as a result of the high biocompatibility of the material and its intrinsic dissolution in body fluids. However, in addition to requiring innovative solutions in material choice and design, these stents also require a greater understanding of the manufacturing process to achieve the desired quality with improved productivity. The present study demonstrates the manufacturing steps for the realisation of biodegradable stents in AZ31 magnesium alloy. These steps include laser microcutting with a Q-switched fibre laser for the generation of the stent mesh and subsequent chemical etching for the cleaning of kerf and surface finish. Specifically, for the laser microcutting step, inert and reactive gas cutting conditions were compared. The effect of chemical etching on the reduction in material thickness, as well as on spatter removal, was also evaluated. Prototype stents were produced, and the material composition and surface quality were characterised. The potentialities of combining nanosecond laser microcutting and chemical etching are shown and discussed.

1. Introduction

As materials processing technology advances, advanced medical devices that depend on intrinsic material properties for their function have become available. The idea of using biocompatible and even biodegradable materials for biomedical implants has been a matter of historical discussion. The first use of Mg in a medical device, in the form of wire ligatures to stop bleeding in patients, was recorded as early as 1878 [1]. The development of high-precision micromachining technologies has enabled the use of advanced materials, realising a high precision in complex forms and small dimensions.

Biodegradability, referring to the dissolution of the medical device inside the human body once it fulfils its duty, has become one of the most attractive properties in cardiovascular stents. This property is crucial for the treatment of infant patients, because, the vessel grows as the patient grows older. Magnesium is both biocompatible and biodegradable and, as a metal, possesses mechanical properties that are superior to those of biodegradable polymers, both in terms of yield stress and maintaining the expanded shape without excessive recoil. As a result, Mg and its alloys have been receiving increased attention from the medical communities for various biomedical implant applications [2], including cardiovascular stents [3–6].

With an increasing demand in the market for stents, developing process cycles capable of maintaining high level of quality and increased productivity becomes essential. While various methods for stent manufacturing are available (such as braiding and knitting of wires, vapour deposition of the stent mesh, photochemical etching of sheets and tubes, water jet cutting of tubes, and electric discharge machining), the vast majority of the stents is produced via laser microcutting of hollow tubes [7–9]. Among these options, industrial solutions are being adapted for the laser microcutting of Mg stents, although limited information regarding the manufacturing conditions has been disclosed [5, 6, 10, 11]. On the other hand, photo-chemical machining has been demonstrated to be a suitable production method for magnesium-alloy stents [12, 13]. As the most commonly applied process in industrial

(a)

(b)
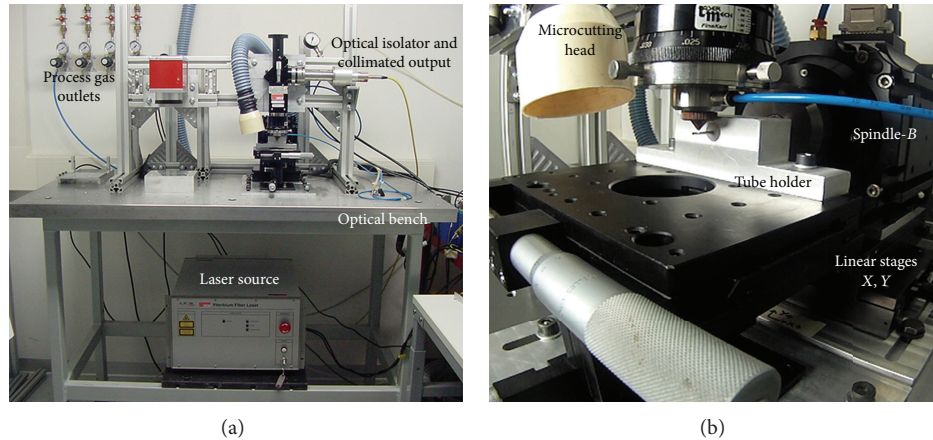
FIGURE 1: Laser microcutting setup used for the laser microcutting of AZ31 tubes.

stent production, laser microcutting provides a flexible solution for achieving complex geometries on a variety of materials without requiring the use of dedicated masks or dies. In the last decade, the introduction and rapid diffusion of fibre lasers into the market have resulted in their utilisation in microcutting applications that includes stent fabrication [14–16]. Ultra-fast lasers with ps to fs pulse durations have been applied to stent fabrication, providing improved cutting quality with limited thermal damage on the material [17–19]. These systems still require higher capital and maintenance costs than other laser systems. A balance between quality and productivity is essential, first to fulfil the market demand and subsequently to reduce production costs. This balance can be achieved by combining laser microcutting process characterised by a good balance between productivity and low thermal damage (as would be provided by ns-pulse lasers) and chemical cleaning processes and optimizing the overall process chain.

Laser processing of magnesium and its alloys has been explored sparingly. Literature dealing with the laser processing of magnesium alloys can be found mainly in the field of welding [20–22], and limited information is available in the case of laser cutting [23–25]. The existing studies describe laser cutting in the macrodimensional range, whereas limited information is available on the microcutting of these alloys [26]. Although biodegradable stents in Mg alloys are currently being developed industrially, with ongoing clinical trials, to authors' knowledge, there is no literature dealing with the manufacturing of these devices.

This study describes the manufacturing of biodegradable Mg stents in AZ31 alloy. The production cycle involves laser microcutting of small diameter tubes with a Q-switched fibre laser operating in ns-pulse regime, followed by a finishing operation of chemical etching with an HNO_3 ethanol solution. The morphological and material-related attributes of the manufactured stents were characterised extensively after each production step. The results imply that the production cycle employed in this work is suitable for manufacturing the complex shape of the stent mesh on AZ31 magnesium-alloy tubes with a high precision.

2. Experimental

In this section, the novel mesh design and material selection criteria are introduced. The manufacturing steps are then presented in sequential order: first, the incision of the stent mesh on tubular material, second, chemical etching as a finishing operation for cleaning the dross and oxidised zones around the cutting area and completing the material separation. Finally, methods for evaluating kerf quality and material composition are described.

2.1. Mesh Design and Material Selection. The mesh design development is not investigated in this work. The developed mesh resulted from design optimisation through a 2D morphing procedure to retain minimum strain with maximum mass [31]. Among a group of candidate magnesium alloys, AZ31 was found to be the most suitable, due to the higher availability of the alloying elements (i.e., the alloy does not include rare earth elements). Moreover, the formability of the alloy for extrusion of semi-finished hollow tubes was found to be better [32]. The AZ31 tubes used in stent fabrication were 2.5 mm in outer diameter and 0.2 mm in thickness.

2.2. Laser Microcutting. Laser microcutting was carried out using a Q-switched fibre laser system operating in the ns-pulse regime (IPG Photonics YLP-1/100/50/50). The laser was coupled to a microcutting head with a 60 mm focal lens and a coaxial nozzle with a 0.5 mm diameter for the addition of process gas (Laser Mech Fine Kerf). To control positioning, 2 linear axis stages (X- and Y-axis) and a spindle (B-axis), both using micrometric precision, were integrated (Aerotech ALS-130, ACS-150). The system was adaptable to both 2D-flat sheet and 3D-tubular cutting. To allow handling of the small tubes without deflections a tube-holding apparatus was adapted to the system. The details of the laser microcutting setup are described in Table 1, and the system components can be seen in Figure 1.

Compared to the laser microcutting of flat sheets, laser microcutting of small tubes has a narrower process parameter window, due to machining a close profile. When ns laser
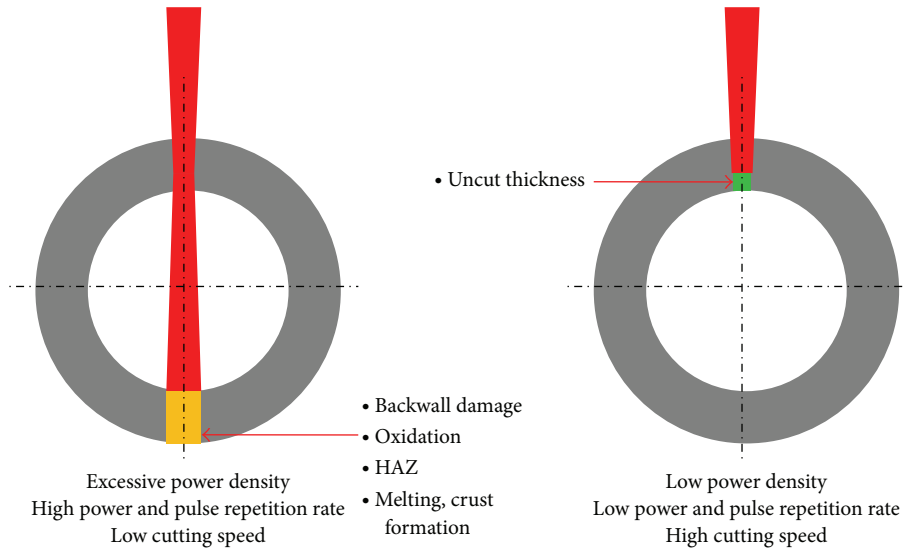
FIGURE 2: Common limitations in laser tube microcutting with ns-pulse laser sources.

TABLE 1: General specifications of the laser micromachining system used in the laser microcutting of AZ31 tubes.

IPG Photonics YLP-1/100/50/50 pulsed fibre laser	
Wavelength	1064 nm
Maximum average power	50 W
Maximum pulse energy	1 mJ
Minimum pulse duration (FWHM)	100 ns
Pulse repetition rate	20–80 kHz
Collimated beam diameter	5.9 mm
Beam quality factor (M^2)	1.7
Focused beam diameter	23 μm
High precision positioning system	
Spindle accuracy	±72.7 μrad
Linear axis accuracy	1 μm

TABLE 2: Processing conditions for laser microcutting of AZ31.

Average power	4.5–6.0–7.5 W
Pulse energy	0.18–0.24–0.30 mJ
Pulse repetition rate	25 kHz
Cutting speed	2 mm/s
Process gas type	Ar, O_2
Process gas pressure	7 bar
Focal position	0 mm

pulses are used, the mechanisms of material removal become a mixture of ablation from the top side of the kerf and melt expulsion from the bottom of the kerf as it is opened to its fully cut thickness. Thus, low power density conditions generate blind grooves on the material without generating a fully open kerf, while high power density conditions can machine beyond the side of the tube on which the beam is projected and cause damage to the backside (see Figure 2). Accordingly, the allowable range for the laser microcutting parameters was determined by preliminary experiments on flat AZ31 sheets with 200 μm to achieve cutting conditions suitable for generating the fine mesh geometry. Average power of the laser was varied between 4.5–7.5 W, while pulse repetition rate was fixed as 25 kHz. Cutting speed of 2 mm/s was used to allow the positioning system to operate in the correct regime within the complicated mesh trajectory. Regarding the process gas, literature pertaining to the laser cutting of Mg alloys describes the issues of dross formation and related limitations in the quality of the cut kerf. One proposed method for dealing with

these issues involves the use of multiple assist gas nozzles and the manipulation of the gas flow to facilitate the movement of molten material [23]. Due to dimensional restrictions, these considerations were not applicable in this study. Instead, two different process gas conditions for microcutting were studied: an inert gas condition using Ar (purity 99.998%) and a reactive-cutting condition using O_2 (purity 99.95%) in which the oxidation enthalpy is combined with the laser energy. Both conditions were applied at a pressure of 7 bar. This intermediate value was chosen, because higher pressures can cause material deflection throughout the laser micro-cutting operation. Although lower pressures can be prefer-able for reactive gas cutting involving O_2, in this case, an intermediate pressure was chosen to include the mechanical ejection of material from the bottom of the opened kerf. The laser microcutting conditions are summarised in Table 2. Chemical etching was employed on the stent mesh cut on flat sheets until separation was achieved or 25% of the material thickness was lost. The conditions were compared in terms of full separation after chemical etching, and parameter sets were determined for tube cutting.

On the tubular material, first, linear incisions were made along the tube axis to characterise the kerf quality after laser microcutting and chemical etching. The same conditions were used for the laser microcutting of the stent mesh on the tubes.
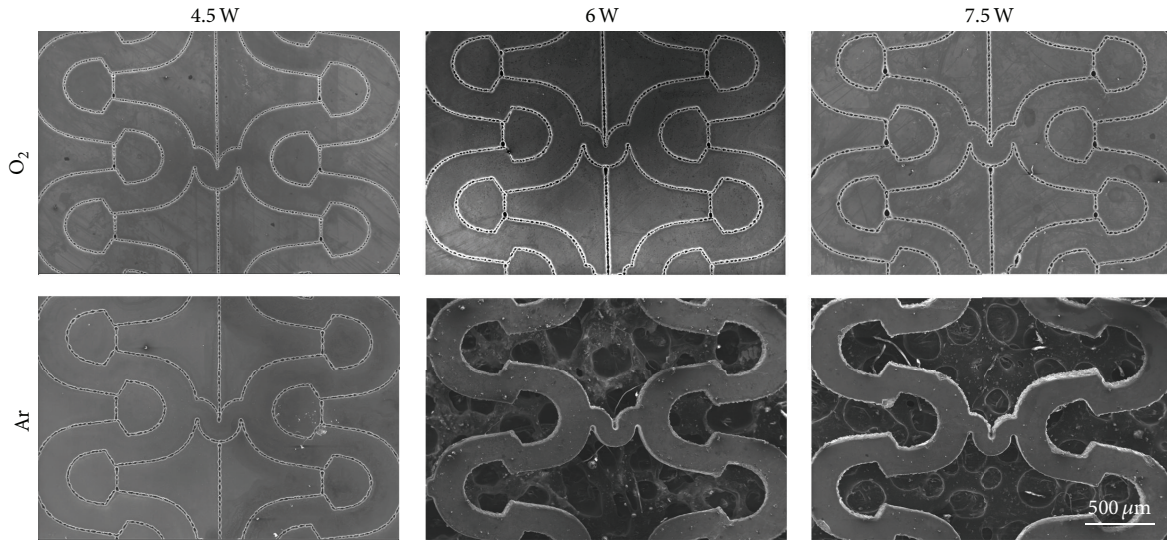
FIGURE 3: Laser cutting of stent mesh with different power and process gas conditions on flat AZ31. Samples show results after chemical etching. The non-separated specimens were etched until the sheet thickness was reduced to 0.16 mm.

2.3. Chemical Etching. A solution consisting of 10 mL HNO_3 and 90 mL ethanol was employed, based on an etchant used for magnesium polishing [33]. Chemical etching was applied at room temperature, and after immersion in the etching solution, the samples were rinsed with water, cleaned in an ultrasonic bath, while being submerged in ethanol, and then dried in ambient air. Each set of samples was etched in 50 mL of fresh etchant. Although the etching step is intended to remove the dross and recast areas around the cutting zone, it is possible that the solution may also significantly etch the stent body, causing a reduction in both weight and thickness [34]. Thus, the effect of the etching solution in reducing the thickness of the material was first studied on 0.4 mm thick AZ31 flat sheets. When samples were immersed for less than 5 seconds, etching did not activate, no cleaning effect was observed, and no significant thickness reduction was measured. The etching duration was thus varied between 5–600 seconds. Specimens were photographed before and after chemical etching using an optical microscope (Leitz Ergolux 200), and the thicknesses were measured using image processing software (Leica IM50). Using these measurements, a regression model was derived to predict the thickness reduction (Δr [μm]) as a function of etching time (t [s]) for etching durations ranging between 5–600 seconds. This model was used to determine the limiting etching duration that would generate a 20 μm thickness reduction, which corresponds to 10% of the tube thickness used for stent manufacturing. Chemical etching was then applied to the laser microcut stents, for this determined duration to reveal the efficacy of the process in removing the dross and completing the kerf separation.

2.4. Methods and Instruments for the Evaluation of Kerf Quality. Scanning electron microscopy (SEM) was applied to capture morphological images of the linear cuts after the laser microcutting and chemical etching steps to assess their geometrical attributes (Zeiss LEO 1430). Spatter height was also measured from the SEM images, with 4 replications taken along the cutting axis. The incisions on the tubes were sectioned after chemical etching to reveal the kerf geometry. The kerf width was measured at the laser entrance and exit sides on the transverse sections of the cuts, with 4 replications. SEM images were also obtained for the laser microcut stents after each processing step for qualitative morphological analysis.

The chemical composition of the final stent produced with the chosen processing conditions was also characterised. Energy-dispersive X-ray spectroscopy (EDS) was used to identify material chemical composition after each manufacturing step, which was compared to the initial composition. Three measurements were taken at two distinct positions, as follows.

(i) The stent wall: the side of the laser-microcut kerf that remains on the stent body.

(ii) The external surface of the stent: the part of stent that does not interact directly with the laser beam, which is the contour defined by the outer diameter of the tubular raw material.

Imaging with back scattered electrons was also employed to reveal differences in elemental mass and thereby revealing the oxidation zones. Surface roughness measurements were carried out on the stent wall with focus-variation-based optical imaging (Alicona Infinite Focus).

3. Results

3.1. Laser Microcutting. The initial cuts made on the flat sheets revealed the strong influence of the process gas, as complete separation after chemical etching was only possible in the case of cuts made with Ar (see Figure 3). In this case the minimum average power level for complete separation

Ar O$_2$
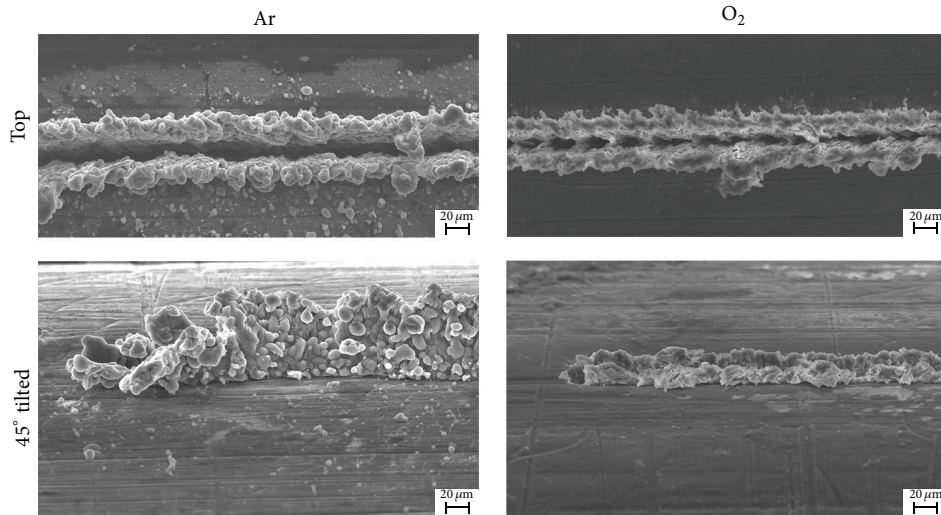
FIGURE 4: SEM images of the linear incisions on the AZ31 tube obtained with Ar and O$_2$ process gasses.

after chemical etching was 6 W. The stent meshes cut with O$_2$ were not separable from the scrap in any of the experimented conditions, and the chemical etching was stopped when the thickness of the flat sheets was reduced to 0.16 mm. Although in this initial phase reactive gas cutting with O$_2$ was found to not be suitable for the microcutting of AZ31, it was retained in the further study for a better comprehension of the effect of the process gas. Two conditions using the same average power at 7.5 W and pulse repetition rate at 25 kHz with O$_2$ and Ar as the process gas were selected for further analysis. With these selected conditions linear incisions and stent mesh were generated on the tubular material to understand better the mechanisms governing the difference in the cutting conditions with the different process gasses.

The linear incisions showed the presence of spatter around the cut kerf for both process gas conditions. However, the SEM images revealed different spatter characteristics in terms of the amount and morphology for the two cases (see Figure 4). The spatter height was estimated to be $84.6 \pm 11.6\,\mu$m for the cuts made using Ar as the process gas and $26.4 \pm 6.8\,\mu$m for the cuts made using O$_2$. A granular spatter structure with droplets around the kerf is visible on the cuts made with Ar. This observation suggests that material is ejected in the form of droplets. It can be hypothesised that explosive behaviour occurs, ejecting a portion of the material upwards, while the remaining material runs out from the lower end of the open kerf. This behaviour would be induced by ablation conditions yielding sufficiently high local temperatures to allow explosive boiling, that is, generating bubble formation, which then collapse. The splashing material is also pushed laterally with respect to the cutting direction by the process gas pressure. In contrast, the reactive cutting conditions using O$_2$ as the process gas show a reduced volume of spatter and an amorphous morphology, with no droplets around the cutting area. This observation suggests that the spatter was deposited from the liquid phase. Thus, the quantity of spatter generation is limited compared to the inert gas conditions. However,

top-view images show an irregular and narrow kerf, suggesting that molten material is also deposited inside the kerf.

Figure 5 shows the stents cut using the different process gas conditions. The integrated machining system was able to generate the complex form of the stent, and the scrap material was kept intact on the tube. The spatter characteristics observed for the linear cuts were replicated in the production of the complicated stent mesh trajectory. Due to the increased length of the cuts, the spatter deposited in the form of droplets is more visible in the case of Ar processing. The stents cut with O$_2$ are overall cleaner on the surface; however, the kerf is evidently narrower. This observed narrower kerf is hypothesised to result from the formation of MgO, which possesses a high melting temperature, around the cut area. Thus, even with the increased available energy provided by the enthalpy of oxidation, kerf expansion in the lateral direction relative to the cutting front is interrupted once the MgO layer is formed.

3.2. Chemical Etching. Figure 6 reports the measured reduction values and the fitted model for the initial phase of the chemical etching study. A linear model was found to be adequate across the experimental interval. It should be noted that the regression model cannot be applied to predict thickness reduction for etching durations under 5 seconds, as the nature of the etching process changes in this regime. It can be seen that the cleaning range is limited to the first few seconds after the activation of the etching process, as half of the thickness of AZ31 sheets is removed after approximately 9 minutes of etching. An etching duration of 10 seconds was found to be the limiting duration for stent cleaning to maintain a thickness reduction no larger than 10%. This etching duration is predicted by the fitted regression model to affect a reduction of $18.8 \pm 7.4\,\mu$m (95% confidence interval for the mean). However, it must be noted that the etching of tubular material in this dimension range is expected to differ from the etching of a sheet due to capillary effects inside the tube and different microstructures generated during the manufacturing processes (i.e., cold rolling for flat sheets and
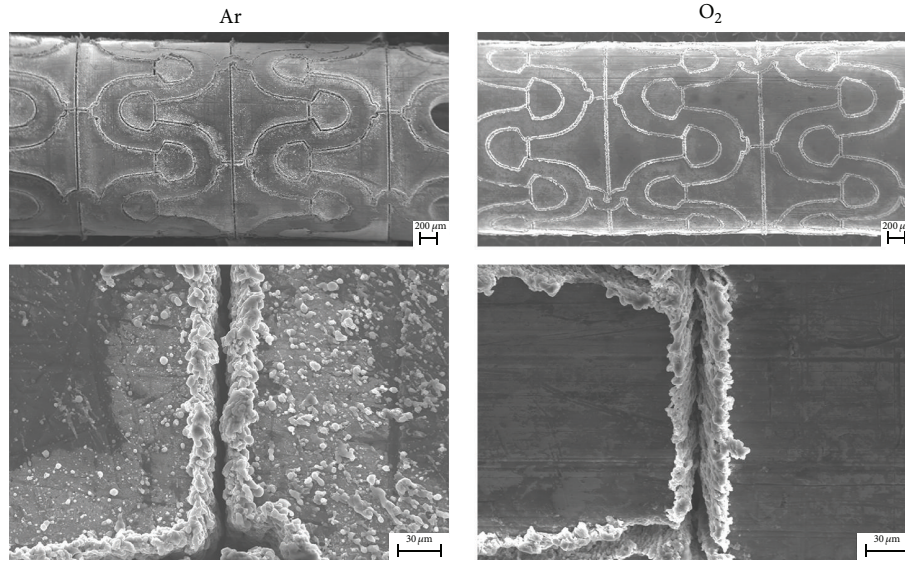
FIGURE 5: SEM images of the laser microcut stents produced using Ar and O_2.

Measured
$\Delta r \ (\mu m) = 15.24 + 0.3574\, t \ (s) \ (R_{adj}^2 = 98\%)$
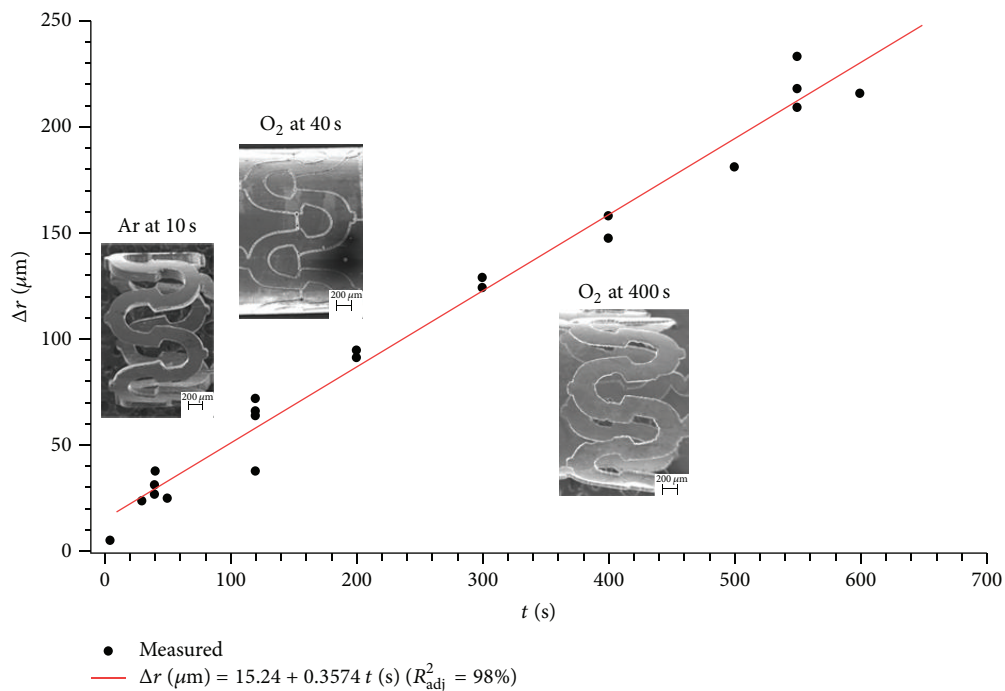
FIGURE 6: Thickness reduction of AZ31 sheets as a function of etching time, along with the etched stents from different process gas and etching conditions.

extrusion for the tubes). But the main purpose of this study is to reveal the material response to the etchant and to determine the processing range for cleaning laser microcut stent.

The stents cut with different process gas conditions, after their chemical etching, are shown in Figure 7. Although spatter on the surface was removed in both cases, the complete separation of the scrap from the stent was not possible in the case of reactive O_2 cutting, even after a prolonged etching duration of 40 seconds. This inability is due to the irregular

kerf, along which loss-of-cut points can be observed. The uncut section in the deeper regions is hypothesised to be the result of interruptions caused by MgO formation, as observed also in the narrower kerf width after laser microcutting with O_2 process gas. Although chemical etching can preferentially remove the dross and oxidised zones, it does not provide complete separation at points where the process energy could not penetrate to induce cutting conditions. Further chemical etching removes the uncut sections at the same rate at which the whole stent body is reduced in thickness. Figure 8 shows

Ar at 10 s   O₂ at 40 s
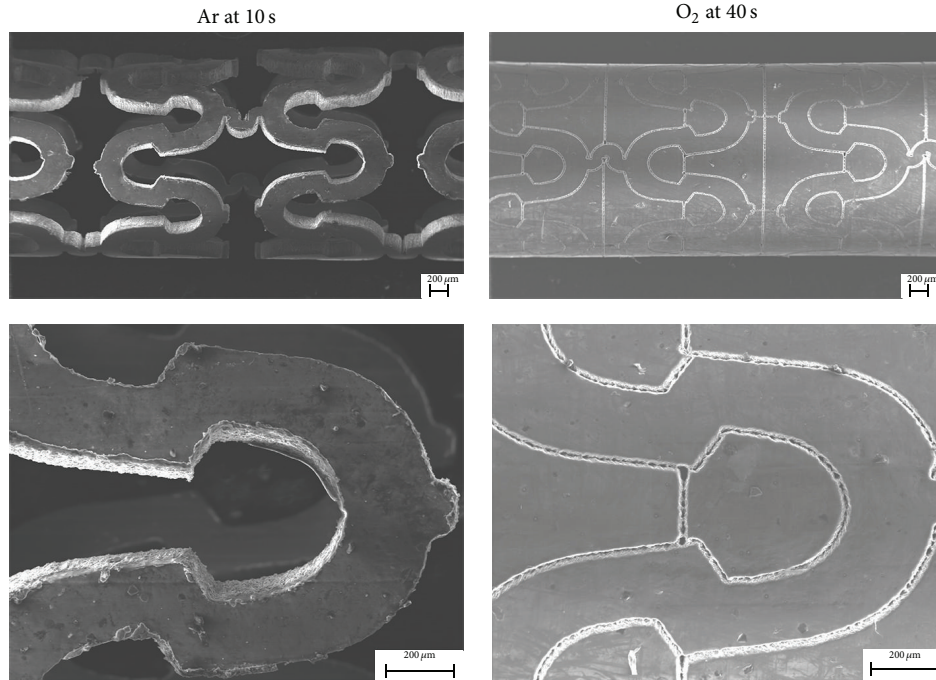
FIGURE 7: SEM images of the laser microcut stents using Ar and O₂, after chemical etching.
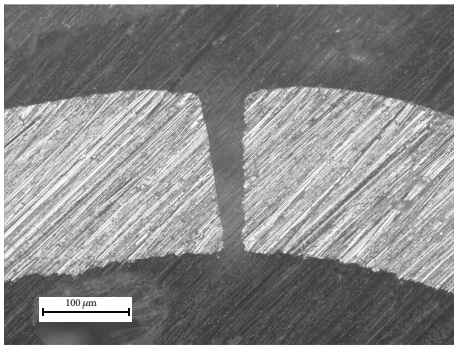
FIGURE 8: Cross-section of a linear incision produced using Ar as the assist gas, after chemical etching.

a cross-section of an incision made using Ar as the assist gas following its chemical etching. The cut kerf is completely clean and shows a conical form, with a kerf width of $54.8 \pm 2.6\,\mu m$ on top and $28.9 \pm 3.8\,\mu m$ on the bottom side. A cross-section of the incisions made with O_2 as the assist gas could not be obtained due to the closed kerf.

The losses of cut are observed when O_2 is used as the assist gas can be better understood by comparing the physical properties of the Mg alloy to those of the traditional stent material, stainless steel, which is commonly cut with O_2 [8, 9, 13]. Table 3 reports the physical properties of AZ31 and AISI 316L stainless steel, along with those of their main oxide components, which are MgO and FeO, respectively. In comparison to stainless steel, AZ31 has twice the oxidation enthalpy, 10 times the thermal diffusivity, and a viscosity almost 5 times lower. Although physical properties of AZ31 would appear to facilitate the generation of a higher

processing energy with a more mobile molten phase, its oxide, MgO behaves as a refractory layer, preventing the processing energy from penetrating into the material. After the generation of an MgO layer inside the kerf, the primary role of O_2 is its mechanical action, pushing the generated melt out of the kerf. At this point, due to the higher melting temperature and relatively lower viscosity and thermal conductivity of MgO, the process comes to a halt locally. In the case of stainless steel, the generation of FeO does not induce such a refractory layer. Due to its low melting temperature, FeO remains in liquid form within the cut front. Furthermore, at the cutting temperatures induced (>2000 K), the Fe/FeO mixture exhibits lower viscosity than does the molten Fe (<5 mPa·s) [27]. For these reasons, complete separation of the stents cut with O_2 was only possible after longer etching: up to 400 seconds of immersion in the etchant, with excessive thickness reductions up to $160\,\mu m$ (see Figure 6).

Complete separation is achievable under the inert gas cutting conditions after the previously determined 10 second chemical etching period. Using Ar as an assist gas provides shielding from excessive oxidation and also pushes the melt out of the kerf; thus, the loss of cut resulting from MgO generation is avoided. In fact, the advantages of the low melting temperature of AZ31 and the lower viscosity of Mg are exploited at these conditions, allowing a comparably low processing energy in the absence of an enthalpy of oxidation. The thickness reduction for the etched stent cut with Ar after 10 seconds of etching was measured to be $25\,\mu m$, which is slightly higher than the set limiting condition of $20\,\mu m$ but within the confidence interval predicted by the regression model. In this case, the stent is free of the adhered dross on the surface, the wall quality is improved, and the edges are rounded. However, the walls require further electrochemical

TABLE 3: Physical properties of the biodegradable stent material AZ31, the traditional stent material AISI 316L, and the oxides of their main alloying components, MgO and FeO [27–30].

		AZ31	AISI 316L	MgO	FeO
Density	ρ (kg/m^3)	1770	8000	3580	5700
Heat capacity	c_p (J/kgK)	1020	500	920	803
Melting temperature	T_m (K)	905	1723	3098	1643
Boiling temperature	T_b (K)	1363	3273	3533	N/A
Thermal conductivity	K (W/mK)	96	21.5	50	10
Thermal diffusivity	α (m^2/s)	$5.32 \cdot 10^{-5}$	$0.54 \cdot 10^{-5}$	$1.52 \cdot 10^{-5}$	$0.22 \cdot 10^{-5}$
Oxidation enthalpy	ΔH (kJ/mol)	−602 (Mg)	−260 (Fe)	N/A	N/A
Viscosity at T_m	η (mPa s)	1.25 (Mg)	6	1.41	40

TABLE 4: Chemical composition of the semi-finished hollow tubes in comparison with the stents laser microcut using Ar, before and after chemical etching.

wt %	Semi-finished hollow tube	After laser microcutting with Ar		After chemical etching	
	External surface	External surface	Wall	External surface	Wall
Al	3.88	1.9 ± 0.4	1.3 ± 0.6	4.2 ± 0.8	2.1 ± 0.3
Zn	0.98	0	0	1.4 ± 0.2	0.3 ± 0.4
Mg	95.14	98.1 ± 0.4	98.7 ± 0.6	94.4 ± 0.6	97.6 ± 0.1

polishing to achieve the quality required for an implant-grade stent. This guideline has not been strictly considered in this study.

At this point, it can be concluded that the use of O_2 for the microcutting of biodegradable stents produced from AZ31 is inadequate. Thus, the final stent manufacturing process involves the use of Ar as the process gas, followed by 10 seconds of chemical etching with the ethanol HNO$_3$ solution.

3.3. Characterisation of the Final Stent. In Table 4, the chemical composition measurements for the final stent, produced by laser microcutting with Ar as the assist gas, are reported. Notably, most of the Al and all of the Zn are lost after laser microcutting. The complete loss of Zn within the alloy is a result of its low melting and boiling points (T_m = 693 K, T_b = 1179 K), which result in its instantaneous vaporisation during cutting. Aluminium is less prone to such vaporisation loss due to its higher boiling temperature (T_m = 933.4 K, T_b = 2767 K). The material seems to retain its chemical composition after chemical etching, as the observed values are close to the nominal composition. In the stent wall, the chemical composition differs slightly from the nominal composition due to increased thermal effects in the vicinity of the cut kerf. As a result of the thermal laser process, alloying elements are partially lost in a superficial layer, and following the removal of this layer via chemical etching, the initial alloy composition is retained.

Figure 9 presents SEM images, taken in imaging mode with back scattered electrons, of the stent after laser microcutting and after chemical etching. The darker areas in Figure 9 result from oxidised zones near the cut kerf. It is apparent that despite the fact the cutting was performed with Ar, an inert gas, surface oxidation is still present due to the high reactivity of Mg. On the other hand, after chemical etching, such zones are mostly removed.

Figure 10 reports the surface quality of the stent after laser microcutting under inert gas conditions and after chemical etching. The SEM images suggest a visible improvement in the surface roughness of the stent after chemical etching. As the spatter around the stent wall is removed, the edges are also rounded due to the polishing effect of the chemical etching. The stent roughness was R_a = 1.42 μm after the laser microcutting and R_a = 1.26 μm after the chemical etching. It is difficult to compare these roughness values with those presented in the literature because each case of material and laser source couple constitutes a completely different machining condition. However, if a comparison should be made with data available in the literature for similar cases, the measured roughness was lower than that observed for fibre laser cutting of AZ31 with a continuous wave system (R_a = 2–10 μm) [22]; slightly higher than that observed for fibre laser cutting of stainless steel with an ms-pulse system (R_a = 0.35–1 μm) [8]; similar to that observed for cutting nitinol (R_a = 1.34 μm) and higher than that observed for cutting of a platinum alloy with a ps-pulse system (R_a = 0.49 μm) [16]; and in a similar range to that observed for cutting nitinol with fs-pulse system (R_a = 0.26–2.4 μm) [17].

4. Conclusions

The present study demonstrates laser microcutting of AZ31 tubes with an ns-pulse fibre laser followed by chemical etching for biodegradable stent fabrication. The primary results obtained by this study can be summarised as follows.

(i) Laser microcutting with fibre lasers operating in the ns-regime is a feasible solution for the manufacturing of Mg alloy biodegradable stents. The advantages provided by fibre laser technology should allow further industrialisation and simplify the production of next generation stents.

(a)

(b)
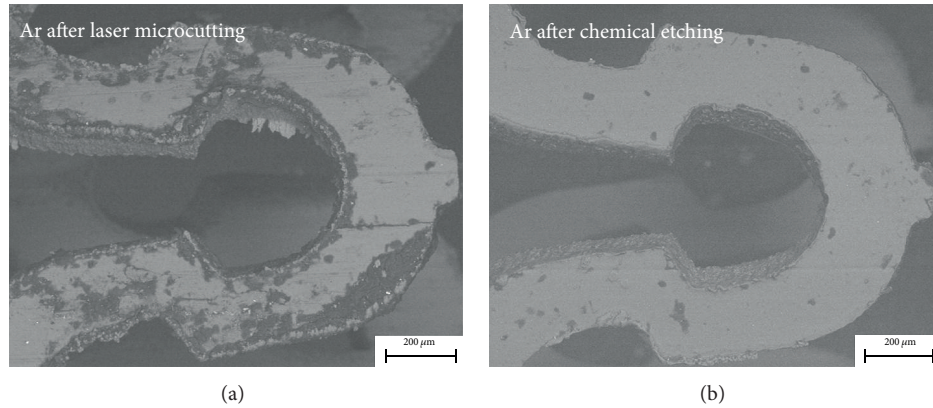
FIGURE 9: SEM images of stents cut with Ar, taken in back scattered electron mode.

(a)

(b)

(c)

(d)
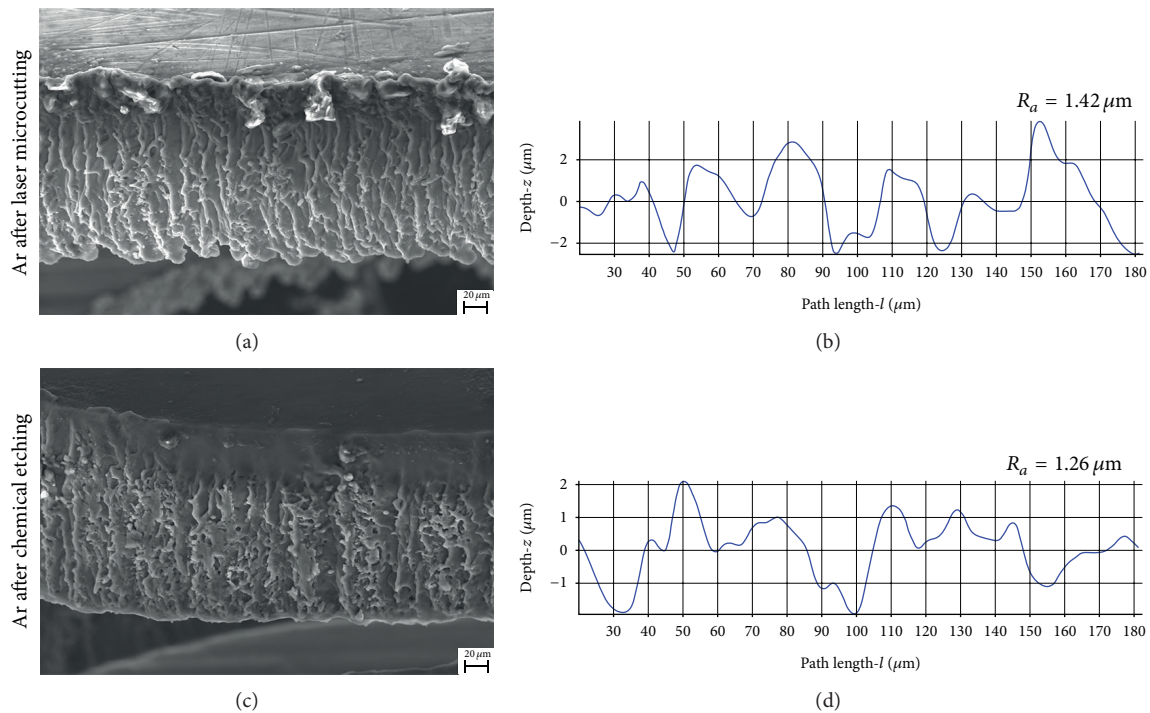
FIGURE 10: SEM images and roughness profiles of the stent after laser microcutting and chemical etching.

(ii) Laser microcutting of AZ31 Mg alloy requires inert gas conditions, rather than reactive cutting with O_2, which is the process gas used for microcutting with the traditional stent material, stainless steel. The use of O_2 results in MgO generation in the cut kerf. MgO, due to its high melting temperature, acts as a refractory layer, which precludes the cutting process from penetrating in the lateral and radial directions.

(iii) Chemical etching preferentially attacks the heat-affected and oxidised zones of laser microcut AZ31 alloy. However, thickness reduction is inevitable during the etching process. The limiting etching duration, under which thickness reduction was no more than 10% of the 200 μm thickness of the stent, was found to be 10 seconds.

(iv) Chemical etching as a finishing operation is required with laser microcutting. The applied HNO_3 ethanol solution cleaned the deposited spatter on the stent surface and cleaned the kerf in the case of stents cut with Ar. In the case of stents cut with O_2, the etchant was effective in cleaning the dross; however, kerf separation could not be completed without excessive etching durations that reduced the stent thickness to 20% of the initial thickness. After the initial removal of dross and the oxidised zone, preferential etching on the damaged zones no longer occurred and etching continued on the uncut sections of the base material as well as the stent body.

(v) The final processing path for stent manufacturing involved the use of Ar as the process gas for laser

microcutting and 10 seconds of chemical etching. Scrap parts were easily removed by chemical etching for this period of time. This etching time is shorter than a typical cleaning procedure in an isotonic bath, making this process a viable option for reducing postprocessing lead times.

(vi) The thermal laser process causes the loss of alloying compounds from the AZ31 alloy. It was possible to maintain the chemical composition of the produced stents by removing the oxidised zones with chemical etching.

(vii) The results reported here describe prototype level stents. To produce stents that are ready for implantation, electrochemical etching would be required to improve the surface quality, and surface coatings would be applied to control the biodegradation rate.

The diffusion of biodegradable and biocompatible stents in Mg alloys depends on a number of aspects that can render them competitive against the most widely used stent material, stainless steel. The control of material properties, corrosion rate, and manufacturability are the key issues, which require substantial accumulation of knowledge. Although laser microcutting of stents appears to be a widely explored field, in the case of Mg alloys, it still requires further attention. The future studies should be aimed to reveal advantages of different laser sources, not only in terms of pulse duration regime, but also in terms of different wavelengths. Although a universal laser source to fulfil all the different aspects seems still far from reality, potential solutions giving a good compromise can be identified. In this context, the ns-pulsed fibre laser sources demonstrate high flexibility, robustness, and productivity. However, the quality requirements are still challenged by the ultra-fast laser sources. Another important aspect that was not addressed in this study is the pulse shape, which is a highly influential factor on the machining quality. This factor can be the key to improve laser microcutting quality in ns-pulse regime. As a final remark, it should be noted that the use of laser beam permits more than cutting of the tubular precursor. The use of the same laser source to machine surfaces for drug insertion or biopolymer coating application, and to modify surface properties for slowing biodegradation rate, is included in the future studies.

Conflict of Interests

The authors declare that no competing and financial interests exist within the present work.

Acknowledgments

References

[1] F. Witte, "The history of biodegradable magnesium implants: a review," *Acta Biomaterialia*, vol. 6, no. 5, pp. 1680–1692, 2010.

[2] M. P. Staiger, A. M. Pietak, J. Huadmai, and G. Dias, "Magnesium and its alloys as orthopedic biomaterials: a review," *Biomaterials*, vol. 27, no. 9, pp. 1728–1734, 2006.

[3] G. Mani, M. D. Feldman, D. Patel, and C. M. Agrawal, "Coronary stents: a materials perspective," *Biomaterials*, vol. 28, no. 9, pp. 1689–1710, 2007.

[4] P. Erne, M. Schier, and T. J. Resink, "The road to bioabsorbable stents: reaching clinical reality?" *CardioVascular and Interventional Radiology*, vol. 29, no. 1, pp. 11–16, 2006.

[5] R. Waksman, R. Pakala, P. K. Kuchulakanti et al., "Safety and efficacy of bioabsorbable magnesium alloy stents in porcine coronary arteries," *Catheterization and Cardiovascular Interventions*, vol. 68, no. 4, pp. 607–617, 2006.

[6] P. Zartner, R. Cesnjevar, H. Singer, and M. Weyand, "First successful implantation of a biodegradable metal stent into the left pulmonary artery of a preterm baby," *Catheterization and Cardiovascular Interventions*, vol. 66, no. 4, pp. 590–594, 2005.

[7] D. Stoeckel, C. Bonsignore, and S. Duda, "A survey of stent designs," *Minimally Invasive Therapy and Allied Technologies*, vol. 11, no. 4, pp. 137–147, 2002.

[8] A. Raval, A. Choubey, C. Engineer, and D. Kothwala, "Development and assessment of 316LVM cardiovascular stents," *Materials Science and Engineering A*, vol. 386, no. 1-2, pp. 331–343, 2004.

[9] Y. P. Kathuria, "Laser microprocessing of metallic stent for medical therapy," *Journal of Materials Processing Technology*, vol. 170, no. 3, pp. 545–550, 2005.

[10] C. Di Mario, H. Griffiths, O. Goktekin et al., "Drug-eluting bioabsorbable magnesium stent," *Journal of Interventional Cardiology*, vol. 17, no. 6, pp. 391–395, 2004.

[11] R. Erbel, C. Di Mario, J. Bartunek et al., "Temporary scaffolding of coronary arteries with bioabsorbable magnesium stents: a prospective, non-randomised multicentre trial," *The Lancet*, vol. 369, no. 9576, pp. 1869–1875, 2007.

[12] D. M. Allen, M. Simpkins, and H. Almond, "A novel photochemical machining process for magnesium aerospace and biomedical microengineering applications," *Journal of Micromechanics and Microengineering*, vol. 20, no. 10, Article ID 105010, 2010.

[13] D. M. Allen, G. Esho, and H. Almond, "Design and novel fabrication of cylindrical magnesium stents," in *Proceedings of the 1st International Conference on Design and Processes for Medical Devices*, pp. 1–6, 2012.

[14] K. F. Kleine, B. Whitney, and K. G. Wstkinds, "Use of fiber lasers for micro cutting applications in the medical device industry," in *Proceedings of the 21st International Congress on Applications of Laser and Electro-Optics (ICALEO '02)*, October 2002.

[15] H. Meng, J. Liao, Y. Zhou, and Q. Zhang, "Laser micro-processing of cardiovascular stent with fiber laser cutting system," *Optics and Laser Technology*, vol. 41, no. 3, pp. 300–302, 2009.

[16] N. Muhammad, D. Whitehead, A. Boor, and L. Li, "Comparison of dry and wet fibre laser profile cutting of thin 316L stainless steel tubes for medical device applications," *Journal of Materials Processing Technology*, vol. 210, no. 15, pp. 2261–2267, 2010.

[17] M. Mielke, D. Gaudiosi, K. Kim et al., "Ultrafast fiber laser platform for advanced materials processing," *Journal of Laser Micro Nanoengineering*, vol. 5, no. 1, pp. 53–58, 2010.

[18] N. Muhammad, D. Whitehead, A. Boor, W. Oppenlander, Z. Liu, and L. Li, "Picosecond laser micromachining of nitinol and platinum-iridium alloy for coronary stent applications," *Applied Physics A*, vol. 106, no. 3, pp. 607–617, 2012.

[19] N. Muhammad and L. Li, "Underwater femtosecond laser micromachining of thin nitinol tubes for medical coronary stent manufacture," *Applied Physics A*, vol. 107, no. 4, pp. 849–861, 2012.

[20] J. Zhu, L. Li, and Z. Liu, "CO_2 and diode laser welding of AZ31 magnesium alloy," *Applied Surface Science*, vol. 247, no. 1-4, pp. 300–306, 2005.

[21] S. M. Chowdhury, D. L. Chen, S. D. Bhole, E. Powidajko, D. C. Weckman, and Y. Zhou, "Microstructure and mechanical properties of fiber-laser-welded and diode-laser-welded AZ31 magnesium alloy," *Metallurgical and Materials Transactions A*, vol. 42, no. 7, pp. 1974–1989, 2011.

[22] L. D. Scintilla, L. Tricarico, M. Brandizzi, and A. A. Satriano, "Nd:YAG laser weldability and mechanical properties of AZ31 magnesium alloy butt joints," *Journal of Materials Processing Technology*, vol. 210, no. 15, pp. 2206–2214, 2010.

[23] T. Fushimi, M. Kitazawa, M. Endo, S. Yamaguchi, K. Nanri, and T. Fujioka, "Parametric studies on improved laser cutting performance of magnesium alloy with two flow nozzles," *Japanese Journal of Applied Physics*, vol. 43, no. 8 A, pp. 5347–5351, 2004.

[24] A. Kratky, D. Schuöcker, and G. Liedl, "Processing with kW fibre lasers—advantages and limits," in *Proceedings of the SPIE XVII International Symposium on Gas Flow, Chemical Lasers, and High-Power Lasers*, 2009.

[25] L. D. Scintilla and L. Tricarico, "Experimental investigation on fiber and CO_2 inert gas fusion cutting of AZ31 magnesium alloy sheets," *Optics & Laser Technology*, vol. 46, pp. 42–52, 2013.

[26] A. G. Demir, B. Previtali, D. Colombo et al., "Fiber laser micromachining of magnesium alloy tubes for biocompatible and biodegradable cardiovascular stents," in *Proceedings of the Fiber Lasers IX: Technology, Systems, and Applications*, January 2012.

[27] J. Powell, D. Petring, R. V. Kumar, S. O. Al-Mashikhi, A. F. H. Kaplan, and K. T. Voisey, "Laser-oxygen cutting of mild steel: the thermodynamics of the oxidation reaction," *Journal of Physics D*, vol. 42, no. 1, Article ID 015504, 2009.

[28] ASM Handbook, American Society for Metals, Metals Park, http://products.asminternational.org/hbk/index.jsp, 2013.

[29] A. Leu, S. Ma, and H. Eyring, "Properties of molten magnesium oxide," *Proceedings of the National Academy of Sciences of the United States of America*, vol. 72, no. 3, pp. 1026–1030, 1975.

[30] M. Takeda, T. Onishi, S. Nakakubo, and S. Fujimoto, "Physical properties of iron-oxide scales on Si-containing steels at high temperature," *Materials Transactions*, vol. 50, no. 9, pp. 2242–2246, 2009.

[31] W. Wu, L. Petrini, D. Gastaldi et al., "Finite element shape optimization for biodegradable magnesium alloy stents," *Annals of Biomedical Engineering*, vol. 38, no. 9, pp. 2829–2840, 2010.

[32] Q. Ge, M. Vedani, and G. Vimercati, "Extrusion of magnesium tubes for biodegradable stent precursors," *Materials and Manufacturing Processes*, vol. 27, no. 2, pp. 140–146, 2012.

[33] G. F. Vander Voort, *Metallography, Principles and Practice*, McGraw and Hill, New York, NY, USA, 1984.

[34] H. Zhao, R. Stalmans, J. Van Humbeeck, and I. De Scheerder, "Pickling of laser-cut NiTi slotted tube stents: effect on surface morphology, dimension changes and mechanical behaviour," in *Proceedings of the International Conference on Martensitic Transformations*, pp. 1125–1128, June 2002.

Research Article

Adhesion of *E. coli* Bacteria Cells to Prosthodontic Alloys Surfaces Modified by TiO$_2$ Sol-Gel Coatings

Katarzyna Banaszek,[1] Witold Szymanski,[2] Bożena Pietrzyk,[2] and Leszek Klimek[2,3]

[1] Medical University of Lodz, Department of General Dentistry, Chair of Restorative Dentistry, Pomorska 251, 92-213 Lodz, Poland
[2] Technical University of Lodz, Institute of Materials Science and Engineering, Stefanowskiego 1/15, 90-924 Lodz, Poland
[3] Medical University of Lodz, Department of Dental Technique, Pomorska 251, 92-213 Lodz, Poland

Correspondence should be addressed to Leszek Klimek; leszek.klimek@p.lodz.pl

The evaluation of the degree of bacteria *E. coli* adhesion to modified surfaces of the chosen prosthodontic alloys was presented. The study was carried out on Co-Cr (Wironit), Ni-Cr (Fantocer), and Fe-Cr-Ni (Magnum AN) alloys. Bare substrate as a control and titanium dioxide coated samples were used. The samples were placed for 24 hours in bacterial culture medium. After incubation period, a number of bacterial cells were evaluated by scanning electron microscope. The study revealed that modification of the alloy surfaces by titanium dioxide coating significantly decreases the amount of bacteria adhering to the surfaces and that additionally bare metal alloy substrates have a different degree of susceptibility to bacterial adhesion.

1. Introduction

In native physiological conditions of the healthy organism, the oral cavity contains opportunistic microorganisms, among which the most numerous are bacteria; however, fungi and protozoa can be also found. Moreover, the presence of viruses has been frequently confirmed in this environment. Bacteria colonize all natural structures (soft and hard tissue) of the oral cavity, that is, mucosa, gingivae, and teeth enamel. In the oral cavity, bacteria adhere easily to the hard structures, especially teeth, as well as prosthodontic appliances. Microorganisms which adhere to the natural and artificial surfaces and form colonies surrounded by polymeric extracellular matrix are called the biofilm or plaque. Biofilm can be formed on the teeth (as dental plaque), gingiva (as gingival plaque), and dentures (as denture plaque). The plaque composition and degree of colonization depend on its location in the patient's oral cavity, saliva composition, diet, natural cleansing mechanisms, and hygienic procedures.

Presence of the microorganisms in the oral cavity may lead to corrosive destruction (MIC—microbiologically influenced corrosion) [1] of metal prosthodontic restorative materials [2, 3]. Even titanium and its alloys, considered to be corrosion resistant, can be colonised by bacteria, which may initiate corrosion [2, 4]. The adhesion of microorganisms to natural and artificial surfaces and formation of the biofilm could be also responsible for the serious diseases [5].

Metabolic activity of microorganisms is associated with an initiation and/or an increase in electrochemical and chemical processes that lead to corrosive destruction of materials and their alloys. Metabolic activity may also cause modification of the surrounding environment resulting in physicochemical changes [6–8]. Due to this, when choosing alloys used in dentistry, it is necessary to evaluate their interactions with biological objects (bacteria, proteins) in the oral cavity environment.

Therefore, taking into consideration pathogenic features of the bacterial plaque and its influence on the homeostasis of the oral cavity, the degree of bacterial accumulation on metal alloys used in prosthodontics should be examined. This is of high significance for persons having tooth losses, particularly patients additionally suffering from periodontal and oral mucosa diseases.

In case of the lowered organism immunity, when the host does not have enough antibodies, bacterial flora finds ideal

TABLE 1: Chemical composition of alloys used for examinations.

| Alloy | Number of elements [%] wt. | | | | | | |
	Cr	Mo	Fe	Mn	Ni	Si	Co
Fantocer	24.79	8.89	1.33	0.12	63.13	1.57	0.17
Magnum AN	23.38	2.94	43.42	1.24	25.70	2.99	0.12
Wironit	30.52	4.73	0.11	1.56	0.06	0.82	62.21

conditions for excessive growth. This is of great importance for patients using dentures. For patients with partial tooth loss, some of the remaining parts of teeth are used as abutments for prosthodontic reconstruction and have to withstand a higher load induced by forces associated with chewing. The teeth are subjected to stresses and lateral movements, sometimes leading to overloading. The attachment apparatus, that is, the alveolar bone, the tooth, and periodontal ligaments supporting the tooth in the alveolus, has to withstand all these forces. This may be manifested by lengthening of the periodontal ligament, which results in the periodontal space widening. Bacteria accumulating around the abutment can contribute to the development of inflammation and additionally to the periodontal space widening, bone structure rarefaction, and finally to weakening of the attachment apparatus maintaining the tooth in the alveolus.

Metal alloys, with cobalt, nickel, chromium, and iron as basic components, are frequently used in prosthodontics. Although they possess a relatively low corrosive resistance as compared to noble metal alloys [9], they are widely applied due to economic reasons. To improve their corrosion resistance, different types of coatings (nitrides, carbides, oxides, carbonitrides, and others) are deposited on their surfaces [10–14]. Many scientific papers indicate that these coatings can decrease the bacterial adhesion to the alloy surface [15, 16]. The thickness and conditions of TiO_2 coating annealing can cause diffusion of alloy elements from the substrate to coatings, which can influence coating properties, that is, chemical and phase composition [17]. Thus, it seems reasonable to investigate how TiO_2 coatings affect the bacterial adhesion to the surfaces of biomaterials (e.g., different chemical compositions) commonly used in prosthodontic appliances.

2. Aim of the Study

The aim of this study was to determine the degree of bacterial adhesion to the modified surfaces of the chosen prosthodontic alloys coated with titanium dioxide by the sol-gel method.

3. Materials and Methods

Cylindrical samples of selected alloys (Table 1) with a diameter of 8 mm and 5 mm height were used as a substrate in this study.

Ten samples were made from each alloy. They were divided into two groups. The samples of the first group were left uncoated (control samples), whereas those in the second group were coated with titanium dioxide.

TiO_2 coatings were elaborated with the sol-gel method. Titania sol was prepared from titanium (IV) butoxide by mixing it with absolute ethanol, acetic acid, and distilled water in a proper ratio. The samples were coated with the sol using the dip-coating method. The substrate was dipped and emerged from the sol with the speed of 30 mm/min. The dip-coated film was dried at room temperature for at least 15 min. Next, the sample was annealed at 500°C for 15 min. The process of the film deposition was repeated three times. The thickness of obtained coatings was about 300 nm.

The surface morphology and chemical composition of the prepared samples were examined by a scanning electron microscopy (SEM) using Hitachi S3000N microscope equipped with a Noran X-ray energy dispersive spectroscopy detector (EDS). The crystalline phase composition of TiO_2 coatings was analysed with the scan step SIEMENS D-500 X-ray diffractometer (XRD) using Co Kα characteristic radiation and a graphite monochromator. An identification of phase composition was carried out with the use of the X-RAYAN computer software, supported with the ICDD database. For better clarity, XRD pattern of metallic substrate was subtracted from XRD pattern of TiO_2 coating.

E. coli bacterial cells (DH5α strain) were used as the biological material because E. coli is the most common microorganism used as a model organism. The investigation of bacterial surface colonization was carried out under flow condition of culture medium. The samples were ultrasonically cleaned. After that process, the samples were placed in a biological flow reactor chamber. An annular holder with holes was used to fix the samples. The rotational flow was forced by electromagnetic stirrer. The whole system with samples was steam autoclaved (Prestige Medical 2100 autoclave). Investigations were carried out at one level of rotational frequency of 150 rpm (150 rpm warranted laminar flow condition). At the next stage, the reactor was refilled with 200 mL of sterile culture medium. The Luria-Bertani (LB) medium was composed of Pepton G 0.5%, yeast extract 0.5%, and NaCl 1.0%. The samples were incubated for 24 h in a medium containing a standard number (340×10^6 per 1 mL) of E. coli (DH5α strain) at 37°C under flow condition. After incubation, they were extensively washed with deionised water. This procedure allowed removing bacteria, which were not strongly adhering to the surface [18]. The samples, after the incubation period, were fixed for 1 h at 4°C with 2.5% glutaraldehyde in water. The fixed samples were then dehydrated with gradient series of ethanol, air-dried, and finally coated with a 20–30 nm-thick gold film in a sputtering apparatus (JEE-4X Jeol). Observations were made to count bacteria adhering to the sample surfaces. Scanning electron microscope was used to examine the specimens at magnification of 1000x and voltage of 5 kV. Thirty observation places were selected from each group of the studied samples, and the number of bacteria was evaluated for them. All procedures were repeated five times. The average cell number and standard deviation observed on the surfaces were used for the evaluation of colonization degree. The statistical parametric analysis based on small samples was applied to assess statistical significance of the results.
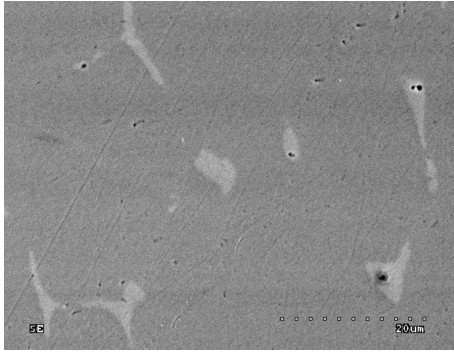
FIGURE 1: SEM image of TiO_2 coating on Magnum AN alloy.
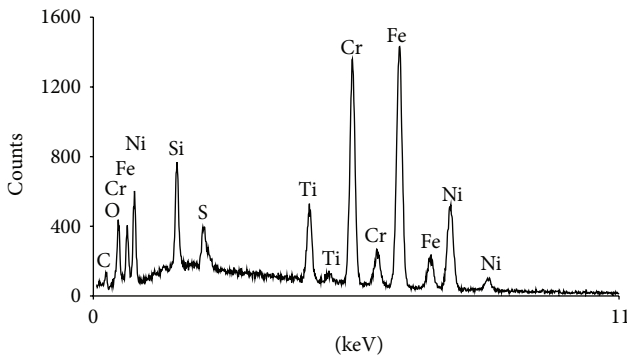
FIGURE 2: EDS analysis of TiO_2 coating on Magnum AN alloy.

— 04–0477 TiO_2 titanium oxide/anatase syn.

FIGURE 3: XRD pattern of TiO_2 coating.

4. Results and Discussion

The morphology of sol-gel TiO_2 coating on the dental alloy (Magnum AN) is shown in Figure 1. It can be observed that the coating well reproduced the microstructure of the metallic substrate surface. All investigated coatings were homogeneous with no visible signs of delamination, cracks, or flaking.

The spectrum of EDS elemental analysis of the previously-mentioned coating is shown in Figure 2. It contains elements originated from the substrate as well as titanium and oxygen originated from the coating, with the atomic ratio O/Ti = 2.

TiO_2 can exist as amorphous form or in several crystalline structures such as rutile, anatase, and brookite. The X-ray diffraction patterns of the TiO_2 sol-gel coating is shown in Figure 3. It was found that according to ICDD card 04-0477, TiO_2 revealed crystalline structure of anatase.

The example images obtained in the scanning electron microscope are shown in Figures 4(a) and 4(f). Figure 5 shows the chart presenting calculations of the number of bacteria adhered to the investigated surfaces. The data presented in Figure 5 demonstrate that the greatest amount of bacteria adhered to the unmodified alloy surfaces, amongst which Wironit alloy showed the higher amount of bacteria, while the lowest one was estimated in case of Fantocer. The additional relationship between nickel concentration in the alloy and the number of bacterial cells adhered to the surfaces

was observed. Studied alloys evidently differed in the nickel content (Table 1). The negative correlation was found between the number of bacteria and nickel concentration (Figure 6). However, the similar amount of bacteria was detected on the surfaces of alloys coated with TiO_2. Analogous results were found by Ciston et al. for zirconia ultrafiltration membranes coated with TiO_2 where the reduction in bacterial adhesion to the surface varied between 12 and 47% as compared to control samples [19].

Based on the ANOVA test and calculations of the number of bacteria adhering to particular samples, statistically significant differences ($P < 0.0001$) between the groups were observed. The Bonferroni statistical test was used for evaluation of the statistical significance between all pairs of groups ($P < 0.05$). However, there were no significant differences found in the number of bacteria that adhered to the surfaces of different alloys with deposited TiO_2 coatings (Table 2). Moreover, the number of adhered bacteria to the alloy surfaces with different Ni content was also statistically significant.

Titanium dioxide coatings have been found to reduce the number of bacteria adhered to their surfaces of about 37%–70% (compared to the bare substrates). Comparing the obtained results for TiO_2 coatings with those of alloy surfaces coated with titanium nitrides and carbonitrides [16], it can be stated that titanium dioxide coatings are not as efficient as TiN_x and TiC_xN_y, regarding their resistance to bacterial surface accumulation. The amount of bacteria adhering to the surface was considerably lower for these coatings and equalled 0.7 per 1000 μm^2 for TiN, 1.9 per 1000 μm^2 for TiCN (containing 4% of carbon wt), and 2.4 per 1000 μm^2 for TiCN (containing 15% of carbon wt). However, it is difficult to univocally state that TiO_2 coatings are worse than titanium nitrides and carbonitrides regarding the resistance to the bacterial adhesion. Different conditions of performing experiments (TiO_2—the flow culture, TiN, and TiCN—the stationary culture) might be the reason for such great differences. The culture in hydrodynamic conditions can better reflect the environment of the oral cavity. Moreover, the flow conditions allow better culture oxygenation and more even distribution of nutrients in the surrounding medium.

(a)

(b)

(c)

(d)

(e)

(f)
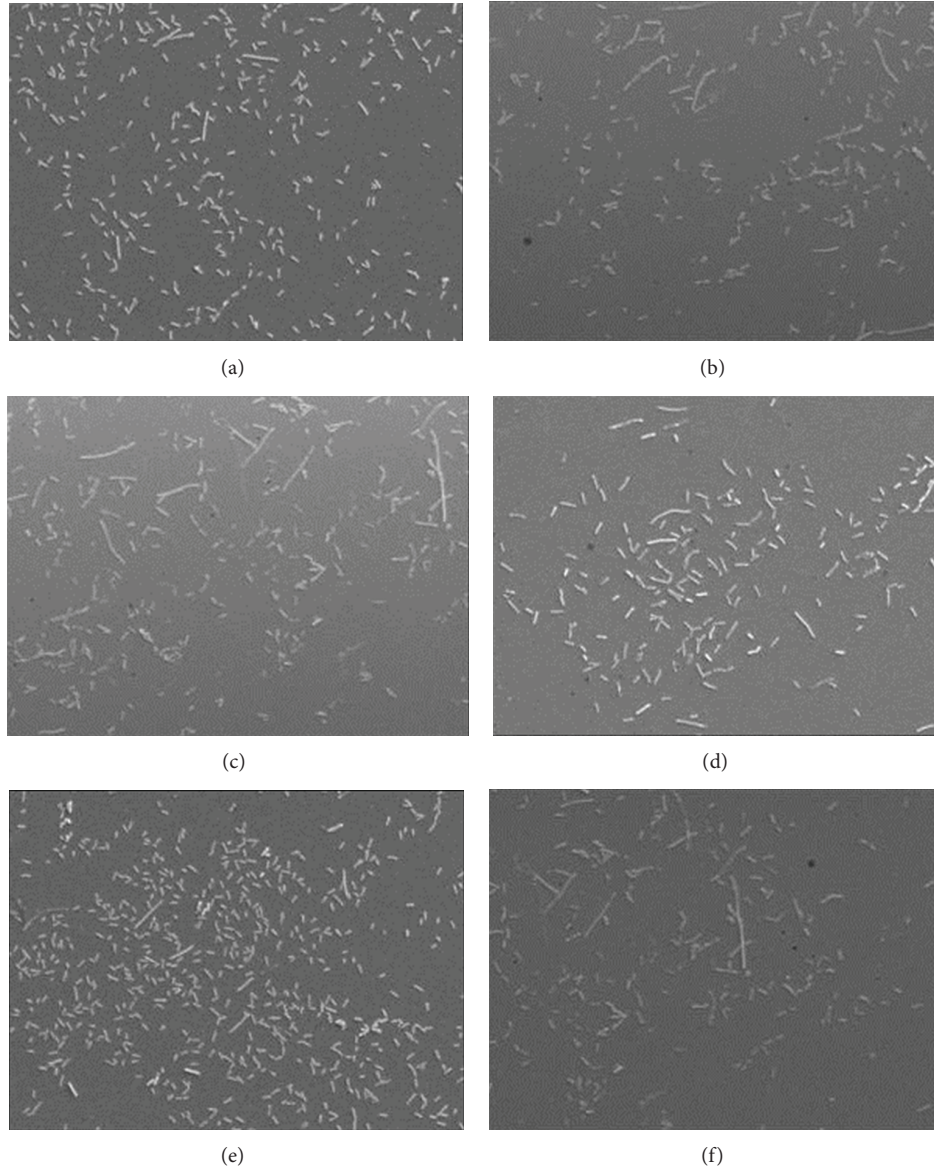
FIGURE 4: SEM pictures of the examined sample surface; (a) Fantocer; (b) Fantocer with TiO_2 coating; (c) Magnum AN; (d) Magnum AN with TiO_2 coating; (e) Wironit; (f) Wironit with TiO_2 coating.

TABLE 2: The Bonferroni test between all pairs of tested groups ($P < 0.05$).

Samples	Magnum AN	Fantocer	Wironit	Magnum AN with TiO_2 coating	Fantocer with TiO_2 coating	Wironit with TiO_2 coating
Magnum AN	−	+	+	+	+	+
Fantocer		−	+	+	+	+
Wironit			−	+	+	+
Magnum AN with TiO_2 coating				−	−	−
Fantocer with TiO_2 coating					−	−
Wironit with TiO_2 coating						−

Symbol "+" denotes results with statistical significance between couples of samples.
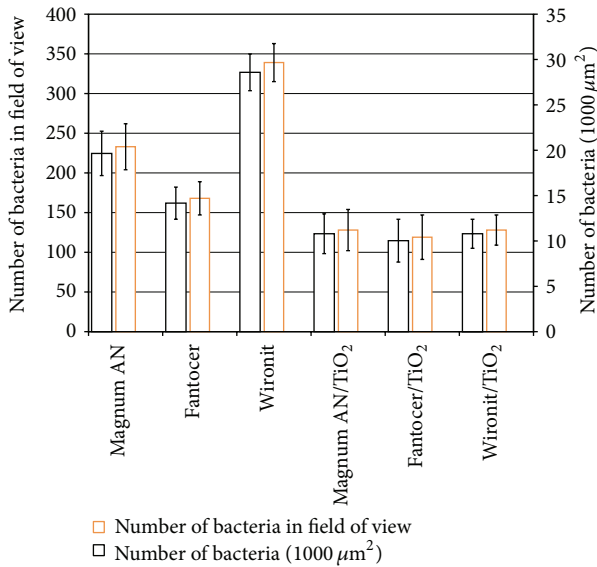
Figure 5: Number of bacteria adhered to the examined sample surfaces.
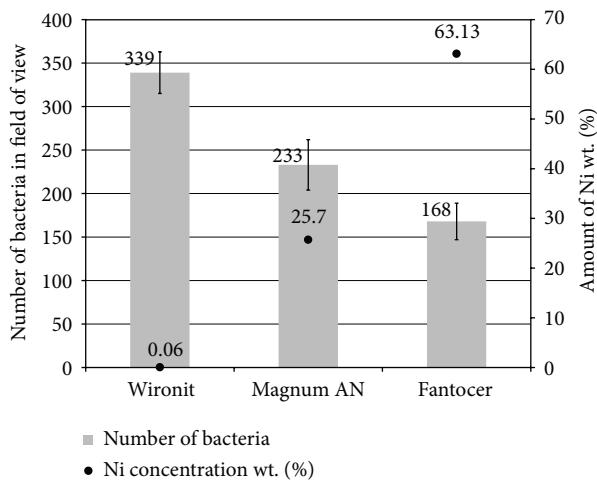
Figure 6: Relationship between the number of bacteria and nickel content in the alloy.

Better environmental conditions can induce intensification of bacterial adhesion.

TiO$_2$ coatings applied in different conditions may more effectively reduce microorganism adhesion due to their photocatalytic properties which cause the coatings to become bactericidal after ultraviolet radiation [19, 20]. The photocatalysis phenomenon might be applied in sterilization of medical instruments as well as during water and air purification [12–23]. However, this phenomenon is not significant in case of prosthodontic materials because of the way of their usage. These materials are kept in the oral cavity for a relatively long time, and free radicals formed due to the layer irradiation may lead to the impairment of cellular membranes, RNA and DNA [24].

Despite the fact that nickel reduces the number of bacteria accumulating on the alloy surfaces, it may induce allergic reactions of patients sensitive to nickel. Therefore, the deposition of protective coatings on alloy surfaces has a beneficial effect on the reduction of nickel ion release to the oral cavity tissues and the number of adhering bacteria.

5. Conclusions

(1) Modification of prosthodontic alloy surfaces by TiO$_2$ sol-gel coating limits the biofilm formation compared to bare substrate.

(2) Negative correlation between Ni content and bacterial colonization has been confirmed for selected alloys.

Authors' Contribution

All authors cooperated in categories: (A) the preparation of the research program, (B) the execution of research, (D) the interpretation of data, and (E) preparation of the paper. Additionally, K. Banaszek and W. Szymański contributed in category (C) the statistical analysis.

Acknowledgment

References

[1] I. B. Beech and C. C. Gaylarde, "Recent advances in the study of biocorrosion—an overview," *Revista de Microbiologia*, vol. 30, no. 3, pp. 177–190, 1999.

[2] J. H. Chern Lin, S. J. Lo, and C. P. Ju, "Biocorrosion study of titanium-nickel alloys," *Journal of Oral Rehabilitation*, vol. 23, no. 2, pp. 129–134, 1996.

[3] M. Wilson, H. Patel, H. Kpendema, J. H. Noar, N. P. Hunt, and N. J. Mordan, "Corrosion of intra-oral magnets by multi-species biofilms in the presence and absence of sucrose," *Biomaterials*, vol. 18, no. 1, pp. 53–57, 1997.

[4] L. Rimondini, S. Farè, E. Brambilla et al., "The effect of surface roughness on early in vivo plaque colonization on titanium," *Journal of Periodontology*, vol. 68, no. 6, pp. 556–562, 1997.

[5] W. Jakubowski, A. Ślósarczyk, Z. Paszkiewicz, W. Szymański, and B. Walkowiak, "Bacterial colonization of bioceramic surfaces," *Advances in Applied Ceramics*, vol. 107, pp. 217–221, 2008.

[6] E. Heitz, H. C. Flemming, and W. Sand, Eds., *Microbially Influenced Corrosion of Materials*, Springer, Berlin, Germany, 1996.

[7] B. J. Little, P. A. Wagner, and F. Mansfeld, *Microbiologically Influenced Corrosion*, NACE International, Houston, Tex, USA, 1997.

[8] A. K. Tiller, "Electrochemical aspects of microbial corrosion: an overview," in *Microbial Corrosion*, pp. 54–65, The Metals Society, London, UK, 1983.

[9] C. D. Peterson, B. M. Hillberry, and D. A. Heck, "Component wear of total knee prostheses using Ti-6Al-4V, titanium nitride coated Ti-6Al-4V, and cobalt-chromium-molybdenum femoral

components," *Journal of Biomedical Materials Research*, vol. 22, no. 10, pp. 887–903, 1988.

[10] L. Klimek, "Structure and corrosion resistance of the titanium nitrides and nitrocarbides layers on the WIRONIT dental alloy," *InżBiomater*, vol. 8, pp. 40–43, 2005.

[11] D. Rylska, L. Klimek, and J. Sokołowski, "Corrosion resistance investigations of prosthetic dental alloys coated by TiN," *Annals of Transplantation*, vol. 9, no. 1, supplement, pp. 104–108, 2004.

[12] B. Pietrzyk, S. Miszczak, Z. Gawroński, and J. Chęcmanowski, "The influence of deposition conditions of TiO_2 sol-gel coatings on properties of Co-Cr-Mo alloy," *Inżynieria Materiałowa*, vol. 25, pp. 284–286, 2004.

[13] A. Wisbey, P. J. Gregson, and M. Tuke, "Application of PVD TiN coating to Co-Cr-Mo based surgical implants," *Biomaterials*, vol. 8, no. 6, pp. 477–480, 1987.

[14] S. Miszczak, B. Pietrzyk, and Z. Gawronski, "Protective properties of composite oxide coatings deposited by sol-gel method," *Powder Metallurgy and Metal Ceramics*, vol. 50, no. 5-6, pp. 295–300, 2011.

[15] M. Kamińska, W. Okrój, W. Szymański et al., "Interaction of parylene C with biological objects," *Acta of Bioengineering and Biomechanics*, vol. 11, pp. 19–25, 2009.

[16] L. Klimek, "Adhesion of bacteria on modified surfaces of prosthodontic Co-Cr-Mo alloy. Initial examinations," *Surface Engineering*, vol. 4, pp. 64–68, 2006 (Polish).

[17] D. A. H. Hanaor and C. C. Sorrell, "Review of the anatase to rutile phase transformation," *Journal of Materials Science*, vol. 46, no. 4, pp. 855–874, 2011.

[18] W. Jakubowski, G. Bartosz, P. Niedzielski, W. Szymanski, and B. Walkowiak, "Nanocrystalline diamond surface is resistant to bacterial colonization," *Diamond and Related Materials*, vol. 13, no. 10, pp. 1761–1763, 2004.

[19] S. Ciston, R. M. Lueptow, and K. A. Gray, "Bacterial attachment on reactive ceramic ultrafiltration membranes," *Journal of Membrane Science*, vol. 320, no. 1-2, pp. 101–107, 2008.

[20] H. Szymanowski, A. Sobczyk-Guzenda, A. Rylski et al., "Photo-induced properties of thin TiO_2 films deposited using the radio frequency plasma enhanced chemical vapor deposition method," *Thin Solid Films*, vol. 515, no. 13, pp. 5275–5281, 2007.

[21] W. Kangwansupamonkon, V. Lauruengtana, S. Surassmo, and U. Ruktanonchai, "Antibacterial effect of apatite-coated titanium dioxide for textiles applications," *Nanomedicine*, vol. 5, no. 2, pp. 240–249, 2009.

[22] H. Yamashita, H. Nose, Y. Kuwahara, Y. Nishida, S. Yuan, and K. Mori, "TiO_2 photocatalyst loaded on hydrophobic Si_3N_4 support for efficient degradation of organics diluted in water," *Applied Catalysis A*, vol. 350, no. 2, pp. 164–168, 2008.

[23] R. Yuan, R. Guan, P. Liu, and J. Zheng, "Photocatalytic treatment of wastewater from paper mill by TiO_2 loaded on activated carbon fibers," *Colloids and Surfaces A*, vol. 293, no. 1–3, pp. 80–86, 2007.

[24] W. G. Wamer, J.-J. Yin, and R. R. Wei, "Oxidative damage to nucleic acids photosensitized by titanium dioxide," *Free Radical Biology and Medicine*, vol. 23, no. 6, pp. 851–858, 1997.

Review Article

Corrosion Protection and Surface Treatment of Magnesium Alloys Used for Orthopedic Applications

Nabil Nassif and Ibrahim Ghayad

Corrosion Control and Surface Protection Department, Central Metallurgical Research and Development Institute (CMRDI), P.O. Box 87, Helwan, Cairo, Egypt

Correspondence should be addressed to Ibrahim Ghayad; ighayad@yahoo.com

An overview is reported about the history of prevailing magnesium alloys as orthopedic biodegradable materials. Important features of the effect of alloying additions, along with surface treatments for corrosion protection of magnesium alloys, are described. Hydroxyapatite (HA), the promising coat deposited by different direct and electrochemical methods to tailor corrosion resistance and biocompatibility, is discussed. Surface modifications, such as microarc oxidation or anodization which lead to nanostructures fabricated to provide better adhesion for HA coatings, are presented.

1. Introduction

Metallic materials continue to play an essential role as biomaterials to assist with the repair or replacement of bone tissue that has become diseased or damaged [1]. Metals are more suitable for load-bearing applications compared with ceramics or polymeric materials due to their combination of high mechanical strength and fracture toughness. Currently approved and commonly used metallic biomaterials include stainless steels, titanium, and cobalt-chromium-based alloys. A limitation of these current metallic biomaterials is the possible release of toxic metallic ions and/or particles through corrosion or wear processes [2–6] that lead to inflammatory cascades which reduce biocompatibility and cause tissue loss [2, 4–13]. Moreover, the elastic moduli of these alloys are not well matched with that of natural bone tissue, resulting in stress shielding effects that can lead to reduced stimulation of new bone growth and remodeling which decreases implant stability [14]. Current metallic biomaterials are essentially neutral in vivo, remaining as permanent fixtures, which in the case of plates, screws, and pins used to secure serious fractures must be removed by a second surgical procedure after the tissue has healed sufficiently [15]. Repeat surgery increases costs to the health care system and further morbidity to the patient.

2. Magnesium Alloys as a Biodegradable Implant Material

Fortunately, magnesium, Mg, and its alloys which are chemically active can degrade naturally in the physiological environment by corrosion and are potential candidates in biodegradable hard-tissue implants. Mg^{2+} is the fourth most abundant cation in the human body and is largely stored mainly in bone tissues. It is vital to metabolism processes, a cofactor in many enzymes, and a key component of the ribosomal machinery that translates the genetic information encoded by mRNA into polypeptide structures [16–19]. Early clinical investigations and recent in vivo and in vitro studies suggest that Mg-based implants have good biocompatibility [20–22]. It has also been reported that Mg-based implants can stimulate the development of a hard callous at fracture sites [20, 23]. The unique mechanical properties of Mg alloys also render them desirable hard-tissue implants. Mg alloys possess a density of ≈ 1.7–$2.0\,\mathrm{g\,cm^{-3}}$ that is close to that of natural bones (1.8–$2.1\,\mathrm{g\,cm^{-3}}$), and the compressive strength and tensile strength are much higher than those of biodegradable polymers. Compared with Ti alloys (110–117 GPa), stainless steels (189–205 GPa), and Co-Cr alloys (230 GPa), the elastic modulus of Mg alloys (41–45 GPa) is closer to that of natural bones. Hence, the stress shielding effect can be mitigated [16].

However, the major drawback of Mg alloys is their low corrosion resistance in the body. In this respect, Mg is undesirable because it is very active chemically, with a standard potential ≈ -1.7 V (standard hydrogen potential). The native MgO and/or Mg(OH)$_2$ surface layers are loose in nature and cannot provide sufficient protection to resist corrosion encountered in the physiological environment which contains a large amount of chloride ions (~104 mmol/L) [24]. Chloride ions can convert the surface Mg(OH)$_2$ into more soluble MgCl$_2$, and dissolution of Mg(OH)$_2$ makes the surface more active, decreasing the protected area and promoting further dissolution of Mg. The reactions are summarized as follows [16, 24]:

$$Mg + 2Cl^- \longrightarrow MgCl_2 \qquad (1)$$

$$Mg(OH)_2 + 2Cl^- \longrightarrow MgCl_2 \qquad (2)$$
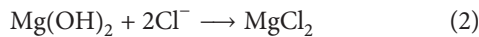
In addition, the high concentration of buffering agents in the body plasma is responsible for the high dissolution rate of Mg. When Mg is exposed to an aqueous solution, the following reaction takes place [24]:

$$Mg + 2H_2O \longrightarrow Mg^{2+} + 2OH^- + H_2 \qquad (3)$$
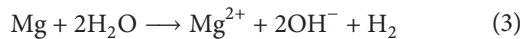
The buffering agents consume the generated OH$^-$ quickly in turn, expediting the conversion from Mg to Mg^{2+}. It has been demonstrated that inorganic components as well as proteins and amino acids influence the degradation rate. As a result, Mg-based biomedical implants can lose the necessary mechanical integrity before the tissue has sufficient time to heal completely. Hard-tissue repair typically requires implantation of the fixture for at least 12 weeks [16].

3. Corrosion Protection of Mg Alloys

Improvement of corrosion resistance of Mg alloys could be achieved via alloying [22, 25], use of composites [26], or surface treatment.

3.1. Effect of Alloying Elements. An appropriate alloying composition can improve the corrosion resistance, mechanical properties, and the ease of manufacture of Mg-based materials. Two primary groups of Mg-based alloys are those contain 2–10 wt% aluminum (Al) with trace additions of zinc (Zn) and manganese (Mn), demonstrate moderate corrosion resistance and improved mechanical properties [27]. The second group uses a mixture of rare earth (RE) elements in combination with another metal such as zinc, yttrium, or sliver and a small amount of zirconium which imparts a fine grain structure and enhanced mechanical properties [27]. As these materials are used in the body, care must be taken to choose alloying elements that are nontoxic. However, it is well known that Al is harmful to neurons [28] and osteoblasts [29] and is also associated with dementia and Alzheimer's disease [28]. The administration of RE (Pr, Ce, Y, etc.) could lead to hepatotoxicity [30]. Excessive Yttrium ions (Y^{+3}) have been shown to change the expression of some rat genes and to have adverse effects on DNA transcription factors [31]. This has led to a demand for the development of a novel biodegradable Mg

alloys in which Ca, Zn, Mn, and Si could be an appropriate alloying elements, such as:

Mg-xCa ($x = 1, 2, 3, 4, 5\cdots$) [32–34],

Mg-1Zn-1Ca [35],

Mg-2Zn-1.2Mn-1Ca [36],

Mg-Si (-Ca, Zn) [37],

Mg-xZn ($x = 1, 3, 6, 10$) [32, 38–40],

Mg-1Mn-1Zn [41],

Mg-1Mn [32].
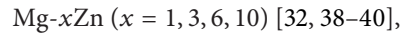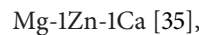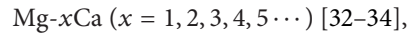
Ca or Zn is one of the most abundant nutritionally essential elements in the human body [34, 37, 42–45] and has basic safety for biomedical applications. Mn is an essential trace element (<0.8 mg/L in blood serum), but high concentration may induce neurotoxicity [46]. Zn and/or Mn helps to overcome the harmful corrosion effect of iron (Fe) and nickel (Ni) impurities that might be present in Mg alloys. Ca reduces oxidation in the molten condition and during heat treatment. It also improves the rollability [47]. Mg-1Zn produced less hydrogen than many other binary Mg alloys in simulated body fluid (SBF) [48]. Ca and Zn act as grain refining agents which improve both corrosion resistance and mechanical properties [49, 50]. With increasing Ca content, more and coarser Mg$_2$Ca phase precipitates are along grain boundaries, weakening both the mechanical property and corrosion resistance of as-cast Mg-Ca alloy [51]. An as-extruded Mg-4Zn-0.2Ca ternary alloy [52] exhibited excellent mechanical integrity during in vitro degradation. After 30 days immersion in simulated body fluid (SBF) solutions, the values of the yield strength, the ultimate tensile strength, the elongation, and the elastic modulus of the alloy were degraded to values which still enough for bone fixing [52]. Ca ion concentration up to 50 mg/L, Zn ion concentration up to 60 mg/L, and Mg ion concentration up to 1000 mg/L did not cause cell toxicity [37].

Strontium (Sr), along with Ca and Mg, shares similar chemical, biological, and metallurgical properties. There is about 140 mg Sr in the human body, and 99% of the body content of Sr is located in the bones. Proper addition of Sr can refine the grain size of Mg alloys and enhance the corrosion resistance. Gu et al. [53] prepared hot rolled Mg-Sr binary alloys with a Sr content ranging from 1 to 4 wt% and found that Mg-2Sr alloy exhibited the highest strength and the lowest corrosion rate. The in vivo results showed that the degrading as-rolled Mg-2Sr alloy promoted bone mineralization and peri-implant new bone formation without inducing any significant adverse effects [54]. Ternary alloys, Mg-Zn-Sr [54], and Mg-Ca-Sr [55] were also developed, both of which suggest that the presence of higher amount of secondary intermetallic phases leads to poorer corrosion resistance.

Silicon (Si) has been regarded recently as an essential mineral in the human body [56]. It plays an important role in aiding the healing process and helping to build the immune system [57]. Moreover, it may be important for the growth and development of bone and connective tissue [58]. Therefore, it is also possible for Mg-Si alloy to be a biodegradable bone implant material. Refinement of microstructure by Ca

is an effective way to improve mechanical and corrosion properties [49, 50]. It is worthy to note that heat treatment of these Mg alloys can improve both mechanical and corrosion properties [59, 60].

3.2. Surface Treatments of Mg Alloys.

Surface treatment of Mg alloys is of particular interest for degradable implants because the corrosion rate is intended to be low in the initial phase due to the modified surface layer and then returns to the normal value when the layer corrodes away. Such a degradation pattern is desirable since the loss of strength of the implant would mirror the increase in strength of the healing union by providing sufficient support in the initial phase [61]. A large body of methods in the surface treatment of Mg alloys for improving corrosion resistance has been reported in the literature [62]. However, these methods are intended for industrial applications and might contain materials that are toxic. For implant applications, several approaches have also been reported to optimize and tailor the corrosion behavior as well as the biocompatibility.

3.2.1. Hydroxyapatite (HA) Coatings.

For orthopedic applications, hydroxyapatite (HA) [25, 26, 43, 63–70] or other types of calcium phosphate (Ca-P) coatings are generally of high interest. Generally, the corrosion rate of Mg alloys is significantly decreased by different types of Ca-P coatings. As the detailed nature of the coatings studied varies over a wide range, of course also the measured degradation rates are different. From the preparation point of view, the most simple are Ca-P coatings that spontaneously form on Mg and Mg alloys upon exposure to simulated biofluids [71–74]. In addition to influencing the corrosion rate of Mg, Ca-P coating has been shown to be beneficial for biocompatibility [75, 76]. The layer that forms spontaneously on Mg alloys in SBF solution is not hydroxyapatite but instead an amorphous mixed (Mg, Ca)-phosphate (which can be carbonated and hydrated).

HA [$(Ca_{10}(PO_4)_6(OH)_2)$] is currently used as a biomedical material due to its excellent biocompatibility and bioactivity, attributed to its chemical and structural similarities to bone and tooth minerals [77]. On account of its low strength and high brittleness, an important use of HA is as a bioactive coating on metallic substrates. Many methods have already been developed to prepare HA coatings on metallic substrates, such as sol-gel process [78], electrophoretic deposition [79], sputtering process [80], laser surface melting [81], pulse laser deposition [82], physical vapor deposition (PVD) [83], plasma spraying [84], and biomimetic methods [85]. However, these cannot be used to deposit HA coating on Mg alloys because of its low melting point and poor heat resistance. It is well established that HA deposited from aqueous solution has a composition and structure more close to that of human bones and teeth [66, 68, 86]. Thus, chemical or electrochemical method [63, 73–77, 87, 88] is the proper way to prepare HA coating on Mg substrates.

Certainly, a single-step coating process using nontoxic aqueous solution without applying electrical current is the most preferable from the view point of product cost and environmental load. However, this direct synthesis of HA [66–68] on Mg alloys was, and still now, a scientific challenge because

Mg ions prevent HA crystallization with the substitution of Mg atom for the Ca atom in the HA structure. Subsequently, the HA structure is destabilized by a decrease in the atomic ratio of Ca/P; that is, Mg ions inhibit apatite nucleation and growth. However, calcium-phosphate apatites were detected on alkali and heat treated Mg after they had been soaked in SBF for 14 days [68]. Direct HA coating was successfully carried out on Mg alloys in aqueous solution by Hiromoto and Yamamoto [74], but the coating time is up to 24 h. An electroless method to prepare a stable HA-containing conversion coating on Mg was also reported [89]. The utility of an equilibrium diagram generated by the use of advanced software allowed for the conversion coating solution concentration and pH to be selected to optimize coating preparation, which was specifically Ca-deficient HA-Mg(OH)$_2$. To overcome Mg ions inhibition just mentioned, one approach uses optimized solution chemistry to produce poorly crystalline HA on Mg alloy AZ31 [90]. Another approach uses Ca-chelate compound [74, 91] and optimized solution chemistry and temperature to obtain dense and uniform HA coatings, on pure Mg, that takes less than 2 hours [91].

Electrochemical deposition (ED) of HA on Mg alloys also has unique advantages due to its capability of forming a uniform coating on a porous substrate or one with a complex shape, its controllability with regard to the thickness and chemical composition of the coating, and its low deposition temperature [63, 69]. It is thus recognized as one of the most promising techniques for degradable Mg alloys.

Nevertheless, in a traditional cathodic electrodeposition process, when a static potential is applied, loose, porous, and low adhesive coatings can easily develop. The main reasons are: first, a polarization in concentrations is formed, since the speed of ion diffusion from the main body of the solution to the surface of the metallic substrate is too slow, and secondly, H$_2$ is produced on the cathode due to the reduction of H$_2$O. To solve this problem, it is suggested that pulsed power (pulse reverse current, PRC) be used for depositing the adherent coating [92–95]. The PRC parameters are demonstrated in [35].

Pure HA coating suffers relatively high dissolution rate in the biological environment [95], which is unfavorable for long-term stability of the implant and makes the interface between bone and implant unstable [96, 97]. Recently, many researchers have focused on the application of fluorine-doped hydroxyapatite $Ca_{10}(PO4)_6(OH)_{2-x}F_x$ (FHA) as a bioactive coating to provide early stability and long-term performance [98, 99]. In comparison with pure HA coating, FHA coating could provide significant dissolution-resistant property, better apatite-like layer deposition, better protein adsorption, better cell attachment, and improved alkaline phosphataze activity in cell culture [98, 100]. Since FHA and Mg alloy are all degradable, Mg alloy with FHA coating has received more and more interest as biodegradable materials [66, 100]. Pulse reverse current (PRC) technique was also used to deposit FHA coating on Mg alloys [35]. Besides, H$_2$O$_2$, a strong oxidative reagent, was introduced into the electrolyte, which was first induced on cathode to only produce OH$^-$ ions during the electrodeposition process [101]. Therefore, H$_2$O$_2$ could reduce the effect of H$_2$ evolution on

the nucleation and growth of nano-FHA coating by PRC technique.

Microarc oxidation (MAO) [67, 102–106] followed by electrochemical deposition (ED) of HA is another attempt to overcome the single HA coating obtained through ED which has a low bonding [107, 108] strength (about 4–6 MPa) and may lead to peel off after implantation [107]. MAO, which is an electrolytic process, can fabricate porous ceramic coating with high adhesion to the substrate. It is outlined that this porous coating can be used as the intermediate layer for depositing HA because it can generate pinning force when HA is deposited in the pores [109] and enhance the corrosion resistance of the porous layer. At the same time, recent developments in biomineralization have already demonstrated that nanosized crystals and particles play an important role in the formation of hard tissues of animals [110]. As reported in [111, 112], mechanical properties, such as compressive strength, hardness, and indentation fracture toughness, of HA increased with a decrease in grain size, and the nanosized HA can promote bone cell adhesion and proliferation in comparison with microsized HA [111, 113]. Therefore fabricating a nanosized HA coating on the MAO coating may be a promising way to improve the biocompatibility and corrosion resistance of Mg alloys. The MAO coating is prepared under a pulse voltage mode, and the cell potential is increased gradually till 165–175 V; then the working electrode is oxidized for about 30 min. [67]. The electrolyte is prepared by dissolving 0.1 mol/L $Na_3PO_4\cdot12H_2O$, 0.028 mol/L $CH_{14}N_2Na_2O_8\cdot H_2O$, 0.01 mol/L $Na_2SiO_3\cdot9H_2O$, and 0.28 mol/L $KF\cdot2H_2O$ in distilled water. According to another publication [104], MAO was conducted at a fixed applied voltage in the range 360–400 V for 10 min to obtain promising results for the surface treatment of Mg-Ca alloys which exhibit good corrosion resistance and surface biocompatibility. The electrolyte was prepared from the solution of 10 g/L sodium silicate with 3.5 g/L sodium hydroxide. Shi et al. [106] performed MAO in 500 mL aqueous solution containing 50 g/L NaOH, 40 g/L Na_2SiO_3, 20 g/L $Na_2B_4O_7$, and 40 g/L $Na_3C_6H_5O_7$ at a constant potential of 90 V for 40 min.

Anodization is the third type of techniques to fabricate nanostructure coatings. It is also an electrolytic oxidation process in which the metal as anode is converted to oxide film having desirable corrosion protective, decorative, and functional properties [114–120]. Anodization can increase the film thickness, hardness, corrosion resistance, and wear resistance and provide better adhesion for primers than the bare metal. The anodizing behavior of Mg alloys is strongly influenced by the voltage or current applied. Different passive and active states can be found depending on the applied voltage/current, time, substrate, and electrolyte [121]. Studies have investigated many aspects of anodizing Mg, such as electrolyte composition [122–125], anodizing parameters such as constant voltage or constant current density control modes [120, 124, 126], substrate effects including substrate type, Mg purity, and alloying element concentration [38, 72, 120, 124, 127], and time of anodization [114]. Different electrolytes have been proposed: either an aqueous [114–116, 123–125, 128–132] or nonaqueous [119, 133] solutions. However, when anodization is used in the bioenvironment, there are certain requirements for the coating. The coating should be thick, strong, and nontoxic. That is to say electrolyte should be carefully designed.

Over the past decades, a variety of self-ordering electrochemical processes have been found to produce oxide nanostructures from aqueous or nonaqueous fluoride-containing solutions [134]. Under optimized conditions resulting surface features are regular tubular (nanotubular) or porous structures. There are many works reported in the literature on the formation of ordered porous oxides of metals including valve metals, such as Al [135, 136], Ta [137], Zr [138, 139], Nb [140, 141], Ti [142–144], and Hf [145], but only a few attempts can be found based on Mg and Mg alloys. Since Mg hardly forms defined oxide films in aqueous solution, it may be a promising approach to use nonaqueous solutions for anodization, particularly with the aim of reducing chemical dissolution during anodization. Brunner et al. [133] showed the formation of a black, porous oxide layer on Mg from water free methanol or ethanol electrolytes containing nitrate ions. Ono and Asoh [146] studied anodization of pure Mg in nonaqueous solutions where they showed the formation of a barrier layer in a solution consisting of a mixture of amine, ethylene glycol, and water. They also investigated the formation of anodic oxide films on Mg surfaces in alkaline-fluoride solutions [125] and for the first time, using alkaline aluminate solution, they reported formation of cylindrical cellular structures [124].

In order to optimize the biological performance, the corrosion behavior of the material as well as its interactions with cells needs to be tailored. For instance, in the case of Ti, drastic influence of nanotubular TiO_2 layers on the cell behavior has been reported as compared with compact TiO_2 layers [147]. Moreover, such nanotubular surface layers were found to enhance the formation of HA on the Ti surface [148]. In the case of Mg, electrochemical anodization approaches to achieve similar surface morphologies as reported for Ti have been explored, and even though nanoporous [133] as well as nanotubular [119] surface layer has been reported. These nanostructures until now show a poor order. Moreover, possible enhancement of biological functionalities by such nanostructured surface layer has not yet been explored.

3.2.2. Miscellaneous Coating Approaches. Apart from the above mentioned Ca-P coatings, many coating techniques have been developed to reduce the corrosion of Mg alloys, such as hydrogenated amorphous silicon [149], alkaline heat treatment [68, 150], carbonate treatment [151], fluoride conversion coatings [152–157], biodegradable polymers [158–160], or composite coatings of polymers and calcium phosphates [161–163]. Moreover, the degradation behavior of Mg alloys can be significantly influenced by self-assembled monolayers [164, 165] or by protein adsorption layers which can be covalently bound to Mg surface using silane coupling chemistry [166]. The latter approach may have the advantage that in addition to the demonstrated strong effects on Mg dissolution rate, binding of specific proteins on the surface prevents nonspecific adsorption from the body fluids and hence may offer a wide range of possibilities to tailor the biological performance to match the requirements of the specific application targeted.

Fluoride chemical conversion coatings own merits such as low cost and simplicity in operation [167]. Fluoride is one of the few known agents that can stimulate osteoblast proliferation and increase new mineral deposition in cancellous bones. It is essential in the diet of human beings and is thought to be required for normal dental and skeletal growths [168]. Fluoride incorporated into the bone increases the size and, thus, decreases the solubility of the bone apatite crystals [169].

4. Concluding Remarks

The key to develop Mg-based alloys that are suitable as biodegradable orthopedic implants is how to control their degradation rates and mechanical integrity in the physiological environment [35, 153]. That is to say, Mg alloys would remain in the body and maintain mechanical integrity over a time period of 6–12 weeks for upper limbs or 12–24 weeks for lower limbs [170, 171], 12–18 weeks [35], 12 weeks [45], or three phases: 3–7 days, 3-4 months, and months to years [170, 172], while the bone tissue heals, eventually are replaced by natural tissue. It is also important that the degradation products, such as, Mg^{2+}, H_2, and OH^- should be within the body's acceptable absorption levels [35]. If pH change and H_2 evolution increase are too drastic, cell death [118] and spalling off the coat as well as susceptibility to stress corrosion cracking and H_2-embrittlement [173, 174] of the implant material can take place. However, if the corrosion rate of Mg-implant can be controlled by developing novel alloys or surface modifications, the biological environment may be better able to deal with H_2-gas and OH^- ions generation.

Conflict of Interests

The authors hereby certify that there are no financial or competing interests that exist in this work.

References

[1] M. Niinomi, "Recent metallic materials for biomedical applications," *Metallurgical and Materials Transactions A*, vol. 33, pp. 477–486, 2002.

[2] D. A. Puleo and W. W. Huh, "Acute toxicity of metal ions in cultures of osteogenic cells derived from bone marrow stromal cells," *Journal of Applied Biomaterials*, vol. 6, no. 2, pp. 109–116, 1995.

[3] J. J. Jacobs, J. L. Gilbert, and R. M. Urban, "Corrosion of metal orthopaedic implants," *Journal of Bone and Joint Surgery A*, vol. 80, no. 2, pp. 268–282, 1998.

[4] C. Lhotka, T. Szekeres, I. Steffan, K. Zhuber, and K. Zweymüller, "Four-year study of cobalt and chromium blood levels in patients managed with two different metal-on-metal total hip replacements," *Journal of Orthopaedic Research*, vol. 21, no. 2, pp. 189–195, 2003.

[5] J. J. Jacobs, A. K. Skipor, L. M. Patterson et al., "Metal release in patients who have had a primary total hip arthroplasty: a prospective, controlled, longitudinal study," *Journal of Bone and Joint Surgery A*, vol. 80, no. 10, pp. 1447–1458, 1998.

[6] J. J. Jacobs, N. J. Hallab, A. K. Skipor, and R. M. Urban, "Metal degradation products: a cause for concern in metal-metal bearings?" *Clinical Orthopaedics and Related Research*, no. 417, pp. 139–147, 2003.

[7] D. Granchi, G. Ciapetti, S. Stea et al., "Cytokine release in mononuclear cells of patients with Co-Cr hip prosthesis," *Biomaterials*, vol. 20, no. 12, pp. 1079–1086, 1999.

[8] Y. Niki, H. Matsumoto, Y. Suda et al., "Metal ions induce bone-resorbing cytokine production through the redox pathway in synoviocytes and bone marrow macrophages," *Biomaterials*, vol. 24, no. 8, pp. 1447–1457, 2003.

[9] D. R. Haynes, S. J. Boyle, S. D. Rogers, D. W. Howie, and B. Vernon-Roberts, "Variation in cytokines induced by particles from different prosthetic materials," *Clinical Orthopaedics and Related Research*, no. 352, pp. 223–230, 1998.

[10] J. Y. Wang, B. H. Wicklund, R. B. Gustilo, and D. T. Tsukayama, "Titanium, chromium and cobalt ions modulate the release of bone-associated cytokines by human monocytes/macrophages in vitro," *Biomaterials*, vol. 17, no. 23, pp. 2233–2240, 1996.

[11] B. I. Yanming, R. R. Van De Motter, A. A. Ragab, V. M. Goldberg, J. M. Anderson, and E. M. Greenfield, "Titanium particles stimulate bone resorption by inducing differentiation of murine osteoclasts," *Journal of Bone and Joint Surgery A*, vol. 83, no. 4, pp. 501–508, 2001.

[12] M. J. Allen, B. J. Myer, P. J. Millett, and N. Rushton, "The effects of particulate cobalt, chromium and cobalt-chromium alloy on human osteoblast-like cells in vitro," *Journal of Bone and Joint Surgery B*, vol. 79, no. 3, pp. 475–482, 1997.

[13] M. L. Wang, L. J. Nesti, R. Tuli et al., "Titanium particles suppress expression of osteoblastic phenotype in human mesenchymal stem cells," *Journal of Orthopaedic Research*, vol. 20, no. 6, pp. 1175–1184, 2002.

[14] J. Nagels, M. Stokdijk, and P. M. Rozing, "Stress shielding and bone resorption in shoulder arthroplasty," *Journal of Shoulder and Elbow Surgery*, vol. 12, no. 1, pp. 35–39, 2003.

[15] J. B. Park and Y. K. Kim, "Metallic biomaterial," in *Biomaterials Principles and Application*, J. B. Park and J. D. Bronzino, Eds., CRC Press, Boca Raton, Fla, USA, 2003.

[16] M. P. Staiger, A. M. Pietak, J. Huadmai, and G. Dias, "Magnesium and its alloys as orthopedic biomaterials: a review," *Biomaterials*, vol. 27, no. 9, pp. 1728–1734, 2006.

[17] A. Hartwig, "Role of magnesium in genomic stability," *Mutation Research*, vol. 475, no. 1-2, pp. 113–121, 2001.

[18] F. I. Wolf and A. Cittadini, "Chemistry and biochemistry of magnesium," *Molecular Aspects of Medicine*, vol. 24, no. 1–3, pp. 3–9, 2003.

[19] J. Vormann, "Magnesium: nutrition and metabolism," *Molecular Aspects of Medicine*, vol. 24, no. 1–3, pp. 27–37, 2003.

[20] V. V. Troitskii and D. N. Tsitrin, "The resorbing metallic alloy "Osteosintezit" as material for fastening broken bone," *Khirurgiia*, vol. 8, pp. 41–44, 1944.

[21] E. D. McBride, "Absorbable metal in bone surgery. A further report on the use of magnesium alloys," *Journal of the American Medical Association*, vol. 111, pp. 2464–2467, 1938.

[22] F. Witte, V. Kaese, H. Haferkamp et al., "In vivo corrosion of four magnesium alloys and the associated bone response," *Biomaterials*, vol. 26, no. 17, pp. 3557–3563, 2005.

[23] R. Zeng, W. Dietzel, F. Witte, N. Hort, and C. Blawert, "Progress and challenge for magnesium alloys as biomaterials," *Advanced Engineering Materials*, vol. 10, no. 8, pp. B3–B14, 2008.

[24] G. Song and A. Atrens, "Understanding magnesium corrosion. A framework for improved alloy performance," *Advanced Engineering Materials*, vol. 5, no. 12, pp. 837–858, 2003.

[25] F. Witte, J. Fischer, J. Nellesen et al., "In vitro and in vivo corrosion measurements of magnesium alloys," *Biomaterials*, vol. 27, no. 7, pp. 1013–1018, 2006.

[26] F. Witte, F. Feyerabend, P. Maier et al., "Biodegradable magnesium-hydroxyapatite metal matrix composites," *Biomaterials*, vol. 28, no. 13, pp. 2163–2174, 2007.

[27] B. A. Shaw, "Corrosion resistance of magnesium alloys," in *ASM Handbook*, D. Stephen, Ed., vol. 13A of *Corrosion: Fundamentals, Testing and Protection*, ASM International, London, UK, 2003.

[28] S. S. A. El-Rahman, "Neuropathology of aluminum toxicity in rats (glutamate and GABA impairment)," *Pharmacological Research*, vol. 47, no. 3, pp. 189–194, 2003.

[29] C.-H. Ku, D. P. Pioletti, M. Browne, and P. J. Gregson, "Effect of different Ti-6Al-4V surface treatments on osteoblasts behaviour," *Biomaterials*, vol. 23, no. 6, pp. 1447–1454, 2002.

[30] Y. Nakamura, Y. Tsumura, Y. Tonogai, T. Shibata, and Y. Ito, "Differences in behavior among the chlorides of seven rare earth elements administered intravenously to rats," *Toxicological Sciences*, vol. 37, no. 2, pp. 106–116, 1997.

[31] W. Yang, P. Zhang, J. Liu, and Y. Xue, "Effect of long-term intake of Y^{+3} in drinking water on gene expression in brains of rats," *Journal of Rare Earths*, vol. 24, no. 3, pp. 369–373, 2006.

[32] N. T. Kirkland, J. Lespagnol, N. Birbilis, and M. P. Staiger, "A survey of bio-corrosion rates of magnesium alloys," *Corrosion Science*, vol. 52, no. 2, pp. 287–291, 2010.

[33] W.-C. Kim, J.-G. Kim, J.-Y. Lee, and H.-K. Seok, "Influence of Ca on the corrosion properties of magnesium for biomaterials," *Materials Letters*, vol. 62, no. 25, pp. 4146–4148, 2008.

[34] Y. Wan, G. Xiong, H. Luo, F. He, Y. Huang, and X. Zhou, "Preparation and characterization of a new biomedical magnesium-calcium alloy," *Materials and Design*, vol. 29, no. 10, pp. 2034–2037, 2008.

[35] H. X. Wang, S. K. Guan, X. Wang, C. X. Ren, and L. G. Wang, "In vitro degradation and mechanical integrity of Mg-Zn-Ca alloy coated with Ca-deficient hydroxyapatite by the pulse electrodeposition process," *Acta Biomaterialia*, vol. 6, no. 5, pp. 1743–1748, 2010.

[36] E. Zhang and L. Yang, "Microstructure, mechanical properties and bio-corrosion properties of Mg-Zn-Mn-Ca alloy for biomedical application," *Materials Science and Engineering A*, vol. 497, no. 1-2, pp. 111–118, 2008.

[37] E. Zhang, L. Yang, J. Xu, and H. Chen, "Microstructure, mechanical properties and bio-corrosion properties of Mg-Si(-Ca, Zn) alloy for biomedical application," *Acta Biomaterialia*, vol. 6, no. 5, pp. 1756–1762, 2010.

[38] G. Song, "Control of biodegradation of biocompatable magnesium alloys," *Corrosion Science*, vol. 49, no. 4, pp. 1696–1701, 2007.

[39] L. P. Xu, E. L. Zhang, D. S. Yin, S. Y. Zeng, and K. Yang, "In vitro corrosion behaviour of Mg alloys in a phosphate buffered solution for bone implant application," *Journal of Materials Science*, vol. 19, no. 3, pp. 1017–1025, 2008.

[40] S. Zhang, X. Zhang, C. Zhao et al., "Research on an Mg-Zn alloy as a degradable biomaterial," *Acta Biomaterialia*, vol. 6, no. 2, pp. 626–640, 2010.

[41] L. Yang and E. L. Zhang, "Biocorrosion behavior of magnesium alloy in different simulated fluids for biomedical application," *Materials Science and Engineering C*, vol. 29, pp. 1691–1696, 2009.

[42] S. Zhang, J. Li, Y. Song et al., "In vitro degradation, hemolysis and MC3T3-E1 cell adhesion of biodegradable Mg-Zn alloy," *Materials Science and Engineering C*, vol. 29, no. 6, pp. 1907–1912, 2009.

[43] Z. Li, X. Gu, S. Lou, and Y. Zheng, "The development of binary Mg-Ca alloys for use as biodegradable materials within bone," *Biomaterials*, vol. 29, no. 10, pp. 1329–1344, 2008.

[44] H. Tapiero and K. D. Tew, "Trace elements in human physiology and pathology: zinc and metallothioneins," *Biomedicine and Pharmacotherapy*, vol. 57, no. 9, pp. 399–411, 2003.

[45] Y. Xin, T. Hu, and P. K. Chu, "In vitro studies of biomedical magnesium alloys in a simulated physiological environment: a review," *Acta Biomaterialia*, vol. 7, no. 4, pp. 1452–1459, 2011.

[46] F. Witte, N. Hort, C. Vogt et al., "Degradable biomaterials based on magnesium corrosion," *Current Opinion in Solid State and Materials Science*, vol. 12, no. 5-6, pp. 63–72, 2008.

[47] J. Polmear, "Magnesium and magnesium alloys," in *ASM Specialty Handbook*, M. M. Avedesian and H. Baker, Eds., p. 14, ASM International, Materials Park, Ohio, USA, 1999.

[48] X. Gu, Y. Zheng, Y. Cheng, S. Zhong, and T. Xi, "In vitro corrosion and biocompatibility of binary magnesium alloys," *Biomaterials*, vol. 30, no. 4, pp. 484–498, 2009.

[49] G. Y. Yuan, Z. L. Liu, Q. D. Wang, and W. J. Ding, "Microstructure refinement of Mg-Al-Zn-Si alloys," *Materials Letters*, vol. 56, no. 1-2, pp. 53–58, 2002.

[50] A. Srinivasan, S. Ningshen, U. Kamachi Mudali, U. T. S. Pillai, and B. C. Pai, "Influence of Si and Sb additions on the corrosion behavior of AZ91 magnesium alloy," *Intermetallics*, vol. 15, no. 12, pp. 1511–1517, 2007.

[51] H. R. B. Rad, M. H. Idris, M. R. A. Kadir, and S. Farahany, "Microstructure analysis and corrosion behavior of biodegradable Mg-Ca implant alloys," *Materials and Design*, vol. 33, no. 1, pp. 88–97, 2012.

[52] Y. Sun, B. Zhang, Y. Wang, L. Geng, and X. Jiao, "Preparation and characterization of a new biomedical Mg-Zn-Ca alloy," *Materials and Design*, vol. 34, pp. 58–64, 2012.

[53] X. N. Gu, X. H. Xie, N. Li, Y. F. Zheng, and L. Qin, "In vitro and in vivo studies on a Mg-Sr binary alloy system developed as a new kind of biodegradable metal," *Acta Biomaterialia*, vol. 8, no. 6, pp. 2360–2374, 2012.

[54] H. S. Brar, J. Wong, and M. V. Manuel, "Investigation of the mechanical and degradation properties of Mg-Sr and Mg-Zn-Sr alloys for use as potential biodegradable implant materials," *Journal of the Mechanical Behavior of Biomedical Materials*, vol. 7, pp. 87–95, 2012.

[55] I. S. Berglund, H. S. Brar, N. Dolgova et al., "Synthesis and characterization of Mg-Ca-Sr alloys for biodegradable orthopedic implant applications," *Journal of Biomedical Materials Research B*, vol. 100, pp. 1524–1534, 2012.

[56] S. E. Whiting, "Not all Minerals Are Created Equal," http://www.healingwithnutrition.com/equalminerals.html.

[57] M. F. McCarty, "Reported antiatherosclerotic activity of silicon may reflect increased endothelial synthesis of heparan sulfate proteoglycans," *Medical Hypotheses*, vol. 49, no. 2, pp. 175–176, 1997.

[58] S. Sripanyakorn, R. Jugdaohsingh, H. Elliott et al., "The silicon content of beer and its bioavailability in healthy volunteers," *British Journal of Nutrition*, vol. 91, no. 3, pp. 403–409, 2004.

[59] Z. Xu, C. Smith, S. Chen, and J. Sankar, "Development and microstructural characterizations of Mg-Zn-Ca alloys for biomedical applications," *Materials Science and Engineering B*, vol. 176, no. 20, pp. 1660–1665, 2011.

[60] W. Zhou, T. Shen, and N. N. Aung, "Effect of heat treatment on corrosion behaviour of magnesium alloy AZ91D in simulated body fluid," *Corrosion Science*, vol. 52, no. 3, pp. 1035–1041, 2010.

[61] W. S. Pietrzak, D. Sarver, and M. Verstynen, "Bioresorbable implants—practical considerations," *Bone*, vol. 19, no. 1, pp. 109S–119S, 1996.

[62] J. E. Gray and B. Luan, "Protective coatings on magnesium and its alloys—a critical review," *Journal of Alloys and Compounds*, vol. 336, no. 1-2, pp. 88–113, 2002.

[63] C. Wen, S. Guan, L. Peng, C. Ren, X. Wang, and Z. Hu, "Characterization and degradation behavior of AZ31 alloy surface modified by bone-like hydroxyapatite for implant applications," *Applied Surface Science*, vol. 255, no. 13-14, pp. 6433–6438, 2009.

[64] J. D. Majumdar, U. Bhattacharyya, A. Biswas, and I. Manna, "Studies on thermal oxidation of Mg-alloy (AZ91) for improving corrosion and wear resistance," *Surface and Coatings Technology*, vol. 202, no. 15, pp. 3638–3642, 2008.

[65] L. Xu, G. Yu, E. Zhang, F. Pan, and K. Yang, "In vivo corrosion behavior of Mg-Mn-Zn alloy for bone implant application," *Journal of Biomedical Materials Research A*, vol. 83, no. 3, pp. 703–711, 2007.

[66] Y. Song, S. Zhang, J. Li, C. Zhao, and X. Zhang, "Electrodeposition of Ca-P coatings on biodegradable Mg alloy: in vitro biomineralization behavior," *Acta Biomaterialia*, vol. 6, no. 5, pp. 1736–1742, 2010.

[67] J. H. Gao, S. K. Guan, J. Chen et al., "Fabrication and characterization of rod-like nano-hydroxyapatite on MAO coating supported on Mg-Zn-Ca alloy," *Applied Surface Science*, vol. 257, no. 6, pp. 2231–2237, 2011.

[68] L. Li, J. Gao, and Y. Wang, "Evaluation of cyto-toxicity and corrosion behavior of alkali-heat-treated magnesium in simulated body fluid," *Surface and Coatings Technology*, vol. 185, pp. 92–98, 2004.

[69] Y. W. Song, D. Y. Shan, and E. H. Han, "Electrodeposition of hydroxyapatite coating on AZ91D magnesium alloy for biomaterial application," *Materials Letters*, vol. 62, no. 17-18, pp. 3276–3279, 2008.

[70] C.-Y. Zhang, R.-C. Zeng, R.-S. Chen, C.-L. Liu, and J.-C. Gao, "Preparation of calcium phosphate coatings on Mg-1.0Ca alloy," *Transactions of Nonferrous Metals Society of China*, vol. 20, no. 2, pp. s655–s659, 2010.

[71] R. Rettig and S. Virtanen, "Composition of corrosion layers on a magnesium rare-earth alloy in simulated body fluids," *Journal of Biomedical Materials Research A*, vol. 88, no. 2, pp. 359–369, 2009.

[72] S. Hiromoto, T. Shishido, A. Yamamoto, N. Maruyama, H. Somekawa, and T. Mukai, "Precipitation control of calcium phosphate on pure magnesium by anodization," *Corrosion Science*, vol. 50, no. 10, pp. 2906–2913, 2008.

[73] D. A. Cortés, H. Y. López, and D. Mantovani, "Spontaneous and biomimetic apatite formation on pure magnesium," *Materials Science Forum*, vol. 539-543, no. 1, pp. 589–594, 2007.

[74] S. Hiromoto and A. Yamamoto, "High corrosion resistance of magnesium coated with hydroxyapatite directly synthesized in an aqueous solution," *Electrochimica Acta*, vol. 54, no. 27, pp. 7085–7093, 2009.

[75] F. Geng, L. L. Tan, X. X. Jin, J. Y. Yang, and K. Yang, "The preparation, cytocompatibility, and in vitro biodegradation study of pure β-TCP on magnesium," *Journal of Materials Science*, vol. 20, no. 5, pp. 1149–1157, 2009.

[76] L. Xu, F. Pan, G. Yu, L. Yang, E. Zhang, and K. Yang, "In vitro and in vivo evaluation of the surface bioactivity of a calcium phosphate coated magnesium alloy," *Biomaterials*, vol. 30, no. 8, pp. 1512–1523, 2009.

[77] H. W. Denissen, K. De Groot, P. Ch. Makkes, A. Van Den Hoff, and P. J. Klopper, "Tissue response to dense apatite implants in rats," *Journal of Biomedical Materials Research*, vol. 14, no. 6, pp. 713–721, 1980.

[78] C. Wu, Y. Ramaswamy, D. Gale et al., "Novel sphene coatings on Ti-6Al-4V for orthopedic implants using sol-gel method," *Acta Biomaterialia*, vol. 4, no. 3, pp. 569–576, 2008.

[79] M. Javidi, S. Javadpour, M. E. Bahrololoom, and J. Ma, "Electrophoretic deposition of natural hydroxyapatite on medical grade 316L stainless steel," *Materials Science and Engineering C*, vol. 28, no. 8, pp. 1509–1515, 2008.

[80] Y. Yang, K.-H. Kim, and J. L. Ong, "A review on calcium phosphate coatings produced using a sputtering process—an alternative to plasma spraying," *Biomaterials*, vol. 26, no. 3, pp. 327–337, 2005.

[81] Y. C. Guan, W. Zhou, and H. Y. Zheng, "Effect of laser surface melting on corrosion behaviour of AZ91D Mg alloy in simulated-modified body fluid," *Journal of Applied Electrochemistry*, vol. 39, pp. 1457–1464, 2009.

[82] F. Garcia, J. L. Arias, B. Mayor et al., "Effect of heat treatment on pulsed laser deposited amorphous calcium phosphate coatings," *Journal of Biomedical Materials Research*, vol. 43, pp. 69–76, 1998.

[83] S. A. Hacking, M. Zuraw, E. J. Harvey, M. Tanzer, J. J. Krygier, and J. D. Bobyn, "A physical vapor deposition method for controlled evaluation of biological response to biomaterial chemistry and topography," *Journal of Biomedical Materials Research A*, vol. 82, no. 1, pp. 179–187, 2007.

[84] L.-M. Sun, C. C. Berndt, A. K. Gross, and A. Kucuk, "Material fundamentals and clinical performance of plasma-sprayed hydroxyapatite coatings: a review," *Journal of Biomedical Materials Research B*, vol. 58, pp. 570–592, 2001.

[85] E. L. Zhang, C. M. Zou, and S. Y. Zeng, "Preparation and characterization of silicon-substituted hydroxyapatite coating by a biomimetic process on titanium substrate," *Surface and Coatings Technology*, vol. 203, pp. 1075–1080, 2005.

[86] J. M. Zhang, C. J. Lin, Z. D. Feng, and Z. W. Tian, "Mechanistic studies of electrodeposition for bioceramic coatings of calcium phosphates by an in situ pH-microsensor technique," *Journal of Electroanalytical Chemistry*, vol. 452, no. 2, pp. 235–240, 1998.

[87] Y. Zhang, G. Zhang, and M. Wei, "Controlling the biodegradation rate of magnesium using biomimetic apatite coating," *Journal of Biomedical Materials Research B*, vol. 89, pp. 408–414, 2008.

[88] Y. Wang, M. Wei, and J. Gao, "Improve corrosion resistance of magnesium in simulated body fluid by dicalcium phosphate dihydrate coating," *Materials Science and Engineering C*, vol. 29, no. 4, pp. 1311–1316, 2009.

[89] X.-B. Chen, N. Birbilis, and T. B. Abbott, "A simple route towards a hydroxyapatite-Mg(OH)$_2$ conversion coating for magnesium," *Corrosion Science*, vol. 53, no. 6, pp. 2263–2268, 2011.

[90] J. E. Gray-Munro and M. Strong, "The mechanism of deposition of calcium phosphate coatings from solution onto magnesium alloy AZ31," *Journal of Biomedical Materials Research A*, vol. 90, pp. 339–350, 2009.

[91] M. Tomozawa, S. Hiromoto, and Y. Harada, "Microstructure of hydroxyapatite-coated magnesium prepared in aqueous solution," *Surface and Coatings Technology*, vol. 204, no. 20, pp. 3243–3247, 2010.

[92] M. S. Chandrasekar and M. Pushpavanam, "Pulse and pulse reverse plating-Conceptual, advantages and applications," *Electrochimica Acta*, vol. 53, no. 8, pp. 3313–3322, 2008.

[93] P. Peng, S. Kumar, N. H. Voelcker, E. Szili, R. S. C. Smart, and H. J. Griesser, "Thin calcium phosphate coatings on titanium by electrochemical deposition in modified simulated body fluid," *Journal of Biomedical Materials Research A*, vol. 76, no. 2, pp. 347–355, 2006.

[94] S. Lin, R. Z. LeGeros, and J. P. LeGeros, "Adherent octacalcium-phosphate coating on titanium alloy using modulated electrochemical deposition method," *Journal of Biomedical Materials Research A*, vol. 66, no. 4, pp. 819–828, 2003.

[95] E. C. Meng, S. K. Guan, H. X. Wang et al., "Effect of electrodeposition modes on surface characteristics and corrosion properties of fluorine-doped hydroxyapatite coatings on Mg-Zn-Ca alloy," *Applied Surface Science*, vol. 257, no. 11, pp. 4811–4816, 2011.

[96] K. Cheng, W. Weng, H. Wang, and S. Zhang, "In vitro behavior of osteoblast-like cells on fluoridated hydroxyapatite coatings," *Biomaterials*, vol. 26, no. 32, pp. 6288–6295, 2005.

[97] J. Wang, C. Huang, Q. Wan, Y. Chen, and Y. Chao, "Characterization of fluoridated hydroxyapatite/zirconia nano-composite coating deposited by a modified electrocodeposition technique," *Surface and Coatings Technology*, vol. 204, no. 16-17, pp. 2576–2582, 2010.

[98] J. Wang, Y. Chao, Q. Wan, Z. Zhu, and H. Yu, "Fluoridated hydroxyapatite coatings on titanium obtained by electrochemical deposition," *Acta Biomaterialia*, vol. 5, no. 5, pp. 1798–1807, 2009.

[99] Y. Wang, S. Z. Sam Zhang, X. Zeng, K. C. Kui Cheng, M. Q. Min Qian, and W. Weng, "In vitro behavior of fluoridated hydroxyapatite coatings in organic-containing simulated body fluid," *Materials Science and Engineering C*, vol. 27, no. 2, pp. 244–250, 2007.

[100] J. Li, Y. Song, S. Zhang et al., "In vitro responses of human bone marrow stromal cells to a fluoridated hydroxyapatite coated biodegradable Mg-Zn alloy," *Biomaterials*, vol. 31, no. 22, pp. 5782–5788, 2010.

[101] X. Y. Chen, Z. W. Zhao, A. L. Chen, and H. G. Li, "Pulsed electrodeposition of hydroxyapatite on titanium substrate in solution containing hydrogen peroxide," *Transactions of Nonferrous Metals Society of China*, vol. 17, no. 3, pp. 617–621, 2007.

[102] X. P. Zhang, Z. P. Zhao, F. M. Wu, Y. L. Wang, and J. Wu, "Corrosion and wear resistance of AZ91D magnesium alloy with and without microarc oxidation coating in Hank's solution," *Journal of Materials Science*, vol. 42, no. 20, pp. 8523–8528, 2007.

[103] Z. Yao, L. Li, and Z. Jiang, "Adjustment of the ratio of Ca/P in the ceramic coating on Mg alloy by plasma electrolytic oxidation," *Applied Surface Science*, vol. 255, no. 13-14, pp. 6724–6728, 2009.

[104] X. N. Gu, N. Li, W. R. Zhou et al., "Corrosion resistance and surface biocompatibility of a microarc oxidation coating on a Mg-Ca alloy," *Acta Biomaterialia*, vol. 7, no. 4, pp. 1880–1889, 2011.

[105] J. Liang, P. B. Srinivasan, C. Blawert, and W. Dietzel, "Influence of pH on the deterioration of plasma electrolytic oxidation coated AM50 magnesium alloy in NaCl solutions," *Corrosion Science*, vol. 52, no. 2, pp. 540–547, 2010.

[106] Y. Shi, M. Qi, Y. Chen, and P. Shi, "MAO-DCPD composite coating on Mg alloy for degradable implant applications," *Materials Letters*, vol. 65, no. 14, pp. 2201–2204, 2011.

[107] W. Shang, B. Chen, X. Shi, Y. Chen, and X. Xiao, "Electrochemical corrosion behavior of composite MAO/sol-gel coatings on magnesium alloy AZ91D using combined micro-arc oxidation and sol-gel technique," *Journal of Alloys and Compounds*, vol. 474, no. 1-2, pp. 541–545, 2009.

[108] S. Ban and J. Hasegawa, "Morphological regulation and crystal growth of hydrothermal-electrochemically deposited apatite," *Biomaterials*, vol. 23, no. 14, pp. 2965–2972, 2002.

[109] H. Duan, K. Du, C. Yan, and F. Wang, "Electrochemical corrosion behavior of composite coatings of sealed MAO film on magnesium alloy AZ91D," *Electrochimica Acta*, vol. 51, no. 14, pp. 2898–2908, 2006.

[110] S. V. Dorozhkin, "Nanosized and nanocrystalline calcium orthophosphates," *Acta Biomaterialia*, vol. 6, no. 3, pp. 715–734, 2010.

[111] S. S. Banerjee, S. Tarafder, N. M. Davies, A. Bandyopadhyay, and S. Bose, "Understanding the influence of MgO and SrO binary doping on the mechanical and biological properties of β-TCP ceramics," *Acta Biomaterialia*, vol. 6, no. 10, pp. 4167–4174, 2010.

[112] J. Wang and L. L. Shaw, "Nanocrystalline hydroxyapatite with simultaneous enhancements in hardness and toughness," *Biomaterials*, vol. 30, no. 34, pp. 6565–6572, 2009.

[113] Y.-P. Lu, Y.-M. Chen, S.-T. Li, and J.-H. Wang, "Surface nanocrystallization of hydroxyapatite coating," *Acta Biomaterialia*, vol. 4, no. 6, pp. 1865–1872, 2008.

[114] D. Xue, Y. Yun, M. J. Schulz, and V. Shanov, "Corrosion protection of biodegradable magnesium implants using anodization," *Materials Science and Engineering C*, vol. 31, no. 2, pp. 215–223, 2011.

[115] Y. Zhang, C. Yan, F. Wang, H. Lou, and C. Cao, "Study on the environmentally friendly anodizing of AZ91D magnesium alloy," *Surface and Coatings Technology*, vol. 161, no. 1, pp. 36–43, 2002.

[116] H. Ardelean and I. Frteur P Marcus, "Corrosion protection of magnesium alloys by Ce, Zr and Nb oxide layers," in *Passivation of Metals and Semiconductors, and Properties of Thin Oxide Layers*, P. Marcus and V. Maurice, Eds., Proceedings of the 9th International Symposium, Paris, France, July 2005, pp. 225–230, 2006.

[117] C. Ying-Liang, W. Hai-Lan, C. Hua et al., "Corrosion properties of AZ31 magnesium alloy and protective effects of chemical conversion layers and anodized coatings," *Transactions of Nonferrous Metals Society of China*, vol. 17, no. 3, pp. 502–508, 2007.

[118] S. Virtanen, "Biodegradable Mg and Mg alloys: corrosion and biocompatibility," *Materials Science and Engineering B*, vol. 176, no. 20, pp. 1600–1608, 2011.

[119] M. C. Turhan, R. P. Lynch, H. Jha, P. Schmuki, and S. Virtanen, "Anodic growth of self-ordered magnesium oxy-fluoride nano-porous/tubular layers on Mg alloy (WE43)," *Electrochemistry Communications*, vol. 12, no. 6, pp. 796–799, 2010.

[120] Y. Mizutani, S. J. Kim, R. Ichino, and M. Okido, "Anodizing of Mg alloys in alkaline solutions," *Surface and Coatings Technology*, vol. 169-170, pp. 143–146, 2003.

[121] A. L. Yerokhin, X. Nie, A. Leyland, A. Matthews, and S. J. Dowey, "Plasma electrolysis for surface engineering," *Surface and Coatings Technology*, vol. 122, no. 2-3, pp. 73–93, 1999.

[122] I. S. Park, Y. S. Jang, Y. K. Kim, M. H. Lee, J. M. Yoon, and T. S. Bae, "Surface characteristics of AZ91D alloy anodized with

various conditions," *Surface and Interface Analysis*, vol. 40, no. 9, pp. 1270–1277, 2008.

[123] H.-Y. Hsiao and W.-T. Tsai, "Characterization of anodic films formed on AZ91D magnesium alloy," *Surface and Coatings Technology*, vol. 190, no. 2-3, pp. 299–308, 2005.

[124] S. Ono, M. Miyake, and H. Asoh, "Effects of formation voltage and electrolyte ions concentration on the structure and passivity of anodic films on magnesium," *Journal of Japan Institute of Light Metals*, vol. 54, no. 11, pp. 544–550, 2004.

[125] S. Ono, H. Kijima, and N. Masuko, "Microstructure and voltage-current characteristics of anodic films formed on magnesium in fluoride electrolytes," *Journal of Japan Institute of Light Metals*, vol. 52, no. 3, pp. 115–121, 2002.

[126] L. L. Li, Y. L. Cheng, H. M. Wang, and Z. Zhang, "Anodization of AZ91 magnesium alloy in alkaline solution containing silicate and corrosion properties of anodized films," *Transactions of Nonferrous Metals Society of China*, vol. 18, pp. 722–727, 2008.

[127] O. Khaselev and J. Yahalom, "The anodic behavior of binary Mg-Al alloys in KOH-aluminate solutions," *Corrosion Science*, vol. 40, no. 7, pp. 1149–1160, 1998.

[128] Y. Zhang, C. Yan, F. Wang, and W. Li, "Electrochemical behavior of anodized Mg alloy AZ91D in chloride containing aqueous solution," *Corrosion Science*, vol. 47, no. 11, pp. 2816–2831, 2005.

[129] H. Fukuda and Y. Matsumoto, "Formation of Ti-Si composite oxide films on Mg-Al-Zn alloy by electrophoretic deposition and anodization," *Electrochimica Acta*, vol. 50, no. 27, pp. 5329–5333, 2005.

[130] H.-Y. Hsiao, H.-C. Tsung, and W.-T. Tsai, "Anodization of AZ91D magnesium alloy in silicate-containing electrolytes," *Surface and Coatings Technology*, vol. 199, no. 2-3, pp. 127–134, 2005.

[131] S. Verdier, M. Boinet, S. Maximovitch, and F. Dalard, "Formation, structure and composition of anodic films on AM60 magnesium alloy obtained by DC plasma anodising," *Corrosion Science*, vol. 47, no. 6, pp. 1429–1444, 2005.

[132] H. Fukuda and Y. Matsumoto, "Effects of Na_2SiO_3 on anodization of Mg-Al-Zn alloy in 3 M KOH solution," *Corrosion Science*, vol. 46, no. 9, pp. 2135–2142, 2004.

[133] J. G. Brunner, R. Hahn, J. Kunze, and S. Virtanen, "Porosity tailored growth of black anodic layers on magnesium in an organic electrolyte," *Journal of the Electrochemical Society*, vol. 156, no. 2, pp. C62–C66, 2009.

[134] A. Ghicav and P. Schmuki, "Self-ordering electrochemistry: a review on growth and functionality of TiO_2 nanotubes and other self-aligned MO_x structures," *Chemical Communications*, vol. 20, pp. 2791–2808, 2009.

[135] J. W. Diggle, T. C. Downie, and C. W. Goulding, "Anodic oxide films on aluminum," *Chemical Reviews*, vol. 69, no. 3, pp. 365–405, 1969.

[136] H. Masuda and K. Fukuda, "Ordered metal nanohole arrays made by a two-step replication of honeycomb structures of anodic alumina," *Science*, vol. 268, no. 5216, pp. 1466–1468, 1995.

[137] I. Sieber, B. Kannan, and P. Schmuki, "Self-assembled porous tantalum oxide prepared in H_2SO_4/HF electrolytes," *Electrochemical and Solid-State Letters*, vol. 8, no. 3, pp. J10–J12, 2005.

[138] H. Tsuchiya, J. M. MacAk, A. Ghicov, L. Taveira, and P. Schmuki, "Self-organized porous TiO_2 and ZrO_2 produced by anodization," *Corrosion Science*, vol. 47, no. 12, pp. 3324–3335, 2005.

[139] H. Tsuchiya, J. M. Macak, I. Sieber, and P. Schmuki, "Self-organized high-aspect-ratio nanoporous zirconium oxides prepared by electrochemical anodization," *Small*, vol. 1, no. 7, pp. 722–725, 2005.

[140] S. Ono, T. Nogasaka, H. Shimazaki, and H. Asoh, in *Proceedings of the 206th Meeting of the Electrochemical Society*, Meeting abstract, p. 788, Honolulu, Hawaii, USA, October 2004.

[141] I. Sieber, H. Hildebrand, A. Friedrich, and P. Schmuki, "Formation of self-organized niobium porous oxide on niobium," *Electrochemistry Communications*, vol. 7, no. 1, pp. 97–100, 2005.

[142] V. Zwilling, E. Darque-Ceretti, A. Boutry-Forveille, D. David, M. Y. Perrin, and M. Aucouturier, "Structure and physicochemistry of anodic oxide films on titanium and TA6V alloy," *Surface and Interface Analysis*, vol. 27, no. 7, pp. 629–637, 1999.

[143] J. M. Macak, H. Tsuchiya, and P. Schmuki, "High-aspect-ratio TiO_2 nanotubes by anodization of titanium," *Angewandte Chemie International Edition*, vol. 44, pp. 2100–2102, 2005.

[144] J. M. Macak, H. Tsuchiya, L. Taveira, S. Aldabergerova, and P. Schmuki, "Smooth anodic TiO_2 nanotubes," *Angewandte Chemie International Edition*, vol. 44, no. 45, pp. 7463–7465, 2005.

[145] H. Tsuchiya and P. Schmuki, "Self-organized high aspect ratio porous hafnium oxide prepared by electrochemical anodization," *Electrochemistry Communications*, vol. 7, no. 1, pp. 49–52, 2005.

[146] H. Asoh and S. Ono, "Anodizing of magnesium in amine-ethylene glycol electrolyte," *Materials Science Forum*, vol. 419-422, pp. 957–962, 2003.

[147] J. Park, S. Bauer, K. Von Der Mark, and P. Schmuki, "Nanosize and vitality: TiO_2 nanotube diameter directs cell fate," *Nano Letters*, vol. 7, no. 6, pp. 1686–1691, 2007.

[148] H. Tsuchiya, J. M. Macak, L. Müller et al., "Hydroxyapatite growth on anodic TiO_2 nanotubes," *Journal of Biomedical Materials Research A*, vol. 77, no. 3, pp. 534–541, 2006.

[149] Y. C. Xin, J. Jiang, K. F. Huo, G. Y. Tang, X. B. Tian, and P. K. Chu, "Corrosion resistance and cytocompatibility of biodegradable surgical magnesium alloy coated with hydrogenated amorphous silicon," *Journal of Biomedical Materials Research A*, vol. 89, pp. 717–726, 2009.

[150] X. N. Gu, W. Zheng, Y. Cheng, and Y. F. Zheng, "A study on alkaline heat treated Mg-Ca alloy for the control of the biocorrosion rate," *Acta Biomaterialia*, vol. 5, no. 7, pp. 2790–2799, 2009.

[151] Y. Al-Abdullat, S. Tsutsumi, N. Nakajima, M. Ohta, H. Kuwahara, and K. Ikeuchi, "Surface modification of magnesium by $NaHCO_3$ and corrosion behavior in Hank's solution for new biomaterial applications," *Materials Transactions*, vol. 42, no. 8, pp. 1777–1780, 2001.

[152] K. Y. Chiu, M. H. Wong, F. T. Cheng, and H. C. Man, "Characterization and corrosion studies of fluoride conversion coating on degradable Mg implants," *Surface and Coatings Technology*, vol. 202, no. 3, pp. 590–598, 2007.

[153] T. Yan, L. Tan, D. Xiong, X. Liu, B. Zhang, and K. Yang, "Fluoride treatment and in vitro corrosion behavior of an AZ31B magnesium alloy," *Materials Science and Engineering C*, vol. 30, no. 5, pp. 740–748, 2010.

[154] A. Drynda, T. Hassel, R. Hoehn, A. Perz, F.-W. Bach, and M. Peuster, "Development and biocompatibility of a novel corrodible fluoride-coated magnesium-calcium alloy with improved degradation kinetics and adequate mechanical properties for cardiovascular applications," *Journal of Biomedical Materials Research A*, vol. 93, no. 2, pp. 763–775, 2010.

[155] M. D. Pereda, C. Alonso, L. Burgos-Asperilla et al., "Corrosion inhibition of powder metallurgy Mg by fluoride treatments," *Acta Biomaterialia*, vol. 6, no. 5, pp. 1772–1782, 2010.

[156] F. Witte, J. Fischer, J. Nellesen et al., "In vivo corrosion and corrosion protection of magnesium alloy LAE442," *Acta Biomaterialia*, vol. 6, no. 5, pp. 1792–1799, 2010.

[157] X. Y. Ye, M.-F. Chen, C. You, and D.-B. Liu, "The influence of HF treatment on corrosion resistance and in vitro biocompatibility of Mg-Zn-Zr alloy," *Frontiers of Materials Science in China*, vol. 4, pp. 132–138, 2010.

[158] J. E. Gray-Munro, C. Seguin, and M. Strong, "Influence of surface modification on the in vitro corrosion rate of magnesium alloy AZ31," *Journal of Biomedical Materials Research A*, vol. 91, pp. 221–230, 2009.

[159] H. M. Wong, K. W. K. Yeung, K. O. Lam et al., "A biodegradable polymer-based coating to control the performance of magnesium alloy orthopaedic implants," *Biomaterials*, vol. 31, no. 8, pp. 2084–2096, 2010.

[160] X. N. Gu, Y. F. Zheng, Q. X. Lan et al., "Surface modification of an Mg-1Ca alloy to slow down its biocorrosion by chitosan," *Biomedical Materials*, vol. 4, Article ID 044109, 2009.

[161] K. Bleek and A. Taubert, "New developments in polymer-controlled, bioinspired calcium phosphate mineralization from aqueous solution," *Acta Biomaterialia*, vol. 9, pp. 6283–6321, 2013.

[162] J. Zhang, C. Dai, J. Wei, Z. Wen, S. Zhang, and C. Chen, "Degradable behavior and bioactivity of micro-arc oxidized AZ91D Mg alloy with calcium phosphate/chitosan composite coating in m-SBF," *Colloids and Surfaces B*, vol. 111, pp. 179–187, 2013.

[163] J. Zhao, X. Lu, and J. Weng, "Macroporous Ti-based composite scaffold prepared by polymer impregnating method with calcium phosphate coatings," *Materials Letters*, vol. 62, no. 17-18, pp. 2921–2924, 2008.

[164] A. Scott and J. E. Gray-Munro, "The surface chemistry of 3-mercaptopropyltrimethoxysilane films deposited on magnesium alloy AZ91," *Thin Solid Films*, vol. 517, no. 24, pp. 6809–6816, 2009.

[165] A. F. Scott, J. E. Gray-Munro, and J. L. Shepherd, "Influence of coating bath chemistry on the deposition of 3-mercaptopropyl trimethoxysilane films deposited on magnesium alloy," *Journal of Colloid and Interface Science*, vol. 343, no. 2, pp. 474–483, 2010.

[166] M. S. Killian, V. Wagener, P. Schmuki, and S. Virtanen, "Functionalization of metallic magnesium with protein layers via linker molecules," *Langmuir*, vol. 26, no. 14, pp. 12044–12048, 2010.

[167] L. H. Chiu, C. C. Chen, and C. F. Yang, "Improvement of corrosion properties in an aluminum-sprayed AZ31 magnesium alloy by a post-hot pressing and anodizing treatment," *Surface and Coatings Technology*, vol. 191, pp. 181–187, 2005.

[168] W. Mertz, "The essential trace elements," *Science*, vol. 213, no. 4514, pp. 1332–1338, 1981.

[169] C. Palmer and S. H. Wolfe, "Position of the American Dietetic Association: the impact of fluoride on health," *Journal of the American Dietetic Association*, vol. 105, pp. 1620–1628, 2005.

[170] T. P. Rucdi and W. M. Murphy, *Principle of Fracture Management*, AO Publishing, Dupendorf, Switzerland, 2002.

[171] S. T. Xu, B. F. Ge, and Y. K. Xu, *Pratical Orthopaedic*, Military Medical Press, Beijing, China, 3rd edition, 2005.

[172] A. W. Lloyd, "Interfacial bioengineering to enhance surface biocompatibility," *Medical Device Technology*, vol. 13, no. 1, pp. 18–21, 2002.

[173] N. Winzer, A. Atrens, G. Song et al., "A critical review of the Stress Corrosion Cracking (SCC) of magnesium alloys," *Advanced Engineering Materials*, vol. 7, no. 8, pp. 659–693, 2005.

[174] N. Winzer, A. Atrens, W. Dietzel, V. S. Raja, G. Song, and K. U. Kainer, "Characterisation of stress corrosion cracking (SCC) of Mg-Al alloys," *Materials Science and Engineering A*, vol. 488, no. 1-2, pp. 339–351, 2008.

Research Article

Characterisation and Properties of Lithium Disilicate Glass Ceramics in the SiO$_2$-Li$_2$O-K$_2$O-Al$_2$O$_3$ System for Dental Applications

Naruporn Monmaturapoj, Pornchanok Lawita, and Witoon Thepsuwan

National Metal and Materials Technology Center, 114 Thailand Science Park, Pathumthani 12120, Thailand

Correspondence should be addressed to Naruporn Monmaturapoj; narupork@mtec.or.th

This work proposes four different glass formulas derived from the SiO$_2$-Li$_2$O-K$_2$O-Al$_2$O$_3$ system to investigate the effect of glass composition on their crystal formations and properties. Glass LD1 was SiO$_2$-Li$_2$O-K$_2$O-Al$_2$O$_3$ system with the addition of P$_2$O$_5$ and CaF$_2$ as nucleating agents. In Glass LD2, a slight amount of MgO was mixed in order to increase the viscosity of the melting glass. Finally, the important factor of Si : Li ratio was increased in Glasses LD3 and LD4 with compositions otherwise the same as LD1 and LD2. The results found that P$_2$O$_5$ and CaF$_2$ served as a nucleating site for lithium phosphate and fluorapatite to encourage heterogenous nucleation and produce a fine-grained interlocking microstructure of lithium disilicate glass ceramics. MgO content in this system seemed to increase the viscosity of the melting glass and thermal expansion coefficient including the chemical solubility. Increasing the Si : Li ratio in glass compositions resulted in the change of the microstructure of Li$_2$Si$_2$O$_5$ crystals.

1. Introduction

All-ceramic systems for dental restoration have been extensively used over recent years due to substantial developments meeting dental requirements, particularly in terms of their mechanical properties and the opaque, presently accessible appearance of all-ceramic materials [1]. Lithium disilicate glass ceramic (Li$_2$Si$_2$O$_5$) is one such all-ceramic system, currently used in the fabrication of single and multiunit dental restorations mainly for dental crowns, bridges, and veneers because of its color being similar to natural teeth and its excellent mechanical properties [2].

In general, glass ceramics can be produced by melting glass and converting the substance into a uniform nucleation and growth of fine-grained ceramics by controlled crystallization process, in which the crystalline phases are nucleated and grown in glass via heat treatment [3–5]. Lithium disilicate glass ceramic, in particular the Li$_2$O-SiO$_2$ system, is the first material classified as glass ceramic discovered by Stookey as having better mechanical properties over base glass [6]. Since then, many comprehensive studies have paid attention to the

binary Li$_2$O-SiO$_2$ system [7–13]. However, this binary system lacks chemical durability for use as a restorative material in dentistry. Therefore, nonstoichiometric compositions or multicomponent glass ceramics were carried out to improve the chemical durability, especially the addition of Al$_2$O$_3$ and K$_2$O to the stoichiometric composition reported to enhance the chemical durability of this glass ceramic [14–16]. Several constituents, for example, ZnO, ZrO$_2$, CaO, and P$_2$O$_5$, were introduced to improve the properties of the final material [4, 17–20]. Also, it is noted that P$_2$O$_5$ as a nucleating agent plays an important role in phase formation and crystallization for lithium disilicate glass ceramic [16, 21, 22]. For that reason, a slight P$_2$O$_5$ content in glass composition could produce a fine-grained interlocking microstructure resulting in high mechanical strength [21].

Fluorine in glass affect its crystallization mechanism and the phases formation due to the fact that fluorine is a network modifier which could rearrange the glass network by forming nonbridging fluorine to replace nonbridging oxygens [6]. Fluorine in calcium phosphate glasses produces a fluorapatite phase which has less solubility characteristics; therefore, it

could improve the chemical solubility of the glass ceramic [23]. In addition, Beall [24] and Echeverria and Beall [18] suggested that the $SiO_2 : Li_2O$ ratio is also a key success factor in the formation of the main crystal phase in a new lithium disilicate glass ceramic system. In order to optimize the viscous properties of lithium disilicate glass to have better pressing ability, components such as La_2O_3 and MgO were added to the main composition [25, 26].

In fact, studies of lithium disilicate glass ceramics have focused mainly on the phase formation and crystallization of $Li_2Si_2O_5$, as affected by variations of temperature during the heat treatment cycle and of minor compositional changes in the main glass composition. These factors influence the microstructure of the glass ceramic and consequently affect the properties of the final products.

In this study, four different glass formulas derived from the SiO_2-Li_2O-K_2O-Al_2O_3 system were prepared to investigate the effect of glass compositions on their crystal formations, microstructures, and properties through the conventional glass melting process. P_2O_5 and CaF_2 as nucleating agents were introduced to induce heterogeneous nucleation and then produce a fine-grained interlocking microstructure after heat treatment. MgO was added in the glass system to increase the viscous properties, and, finally, the $SiO_2 : Li_2O$ ratio in the glass composition was increased. The experimental results and their discussion are addressed as concerns the crystallization behavior of the glasses, the microstructures, and properties of the glass ceramics with the potential to be used as dental restorations.

2. Materials and Methods

2.1. Glass Preparation. Glass batches were prepared by mixing appropriate amounts of SiO_2, Li_2CO_3, $MgCO_3$ (Sigma-Aldrich Company, Belgium), Al_2O_3 (Fluka Analytical, Germany), P_2O_5 (Acros organics, USA), K_2CO_3 (Fluka chemika, France), and CaF_2 (Merck chemicals, Germany). All starting materials were reagent grade. Glass batches according to glass compositions as shown in Table 1 were melted in a covered Pt-10%Rh crucible at 1500°C for 2 hrs and then quenched in cold water to make frit. To achieve homogeneity, glass frit was milled before being remelted at the same temperature for 2 hrs. The melting glass was cast into warm graphite molds to obtain glass rods with a dimension of 14 mm in diameter × 100 mm long. Graphite molds were annealed in a muffle furnace at 400–500°C for 2 hrs to reduce the internal stress in the glasses followed by cooling to room temperature at 1°C/min.

2.2. Heat Treatment. Samples were cut into several disks of 14 mm × 5 mm long and then heat-treated in a Lenton furnace (Lenton Ltd., Hope Valley, UK). A two-stage heat-treatment schedule was performed in which the glasses were heated to a nucleating temperature of 500°C with a heating rate of 5°C/min, held for 2 hrs, and then ramped up to various crystal growth temperatures (e.g., 700°C). The heating rate was 5°C/min, and samples were held for 2 hrs followed by furnace cooling with 5°C/min to room temperature. Following heat treatment, samples were referred to as glass ceramics LD1–LD4.

TABLE 1: Glass compositions (% mol).

Oxides	LD1	LD2	LD3	LD4
SiO_2	60.0	59.0	63.0	62.0
Li_2O	32.0	31.0	29.0	28.0
K_2O	1.0	1.0	1.0	1.0
Al_2O_3	2.0	2.0	2.0	2.0
P_2O_5	2.0	2.0	2.0	2.0
CaF_2	3.0	3.0	3.0	3.0
MgO	—	2.0	—	2.0
Total	100.0	100.0	100.0	100.0
$SiO_2 : Li_2O$	1.88	1.90	2.17	2.21

2.3. Thermal Analysis

2.3.1. Differential Thermal Analysis. A Netzsch thermal analysis (NETZSCH STA 449 F3, Germany) was used to determine T_g and T_c by heating to 1000°C with a heating rate of 10°C/min. Fine glass samples (6–10 μm) were analyzed under flowing nitrogen with a Pt crucible filled with alumina as reference and then heated together at the set up heating rate. The results were used as a guide for determining the heat treatment temperatures applied to induce crystallization.

2.3.2. Thermal Expansion Measurement. The coefficient of thermal expansion using a Netzsch thermal analysis (NETZSCH DIL 402 PC, Germany) dilatometer with a heating rate of 5°C/min was applied on the glass ceramic bars (5 mm × 5 mm × 25 mm) measuring from room temperature up to 600°C. The linear thermal expansion coefficient (α) was calculated using the general equation: $\alpha = (\Delta L / L) \cdot (1/\Delta T)$, where ($\Delta L$) is the increase in length, (ΔT) is the temperature interval over which the sample is heated, and (L) is the original length of the specimen.

2.4. X-Ray Diffraction Analysis. Phase analyses of the glasses and glass ceramics were performed by X-ray diffraction (XRD, Rigaku TTRAX III) operating from 10° to 70° 2θ at a scan speed of 2° 2θ/min and a step size of 0.02° 2θ with CuK_α radiation (K_α = 1.5406 nm) at 300 mA and 50 kV. Identification of phases was achieved by comparing the result diffraction patterns with the ICDD (JCPDS) standard.

2.5. Scanning Electron Microscopy. Microstructure of the glass ceramics was investigated by scanning electron microscope (SEM: Hitachi S-3400N). After heat treatment, the samples were polished with SiC paper (nos. 400, 800, 1000, 1200, and 2500) and finally with diamond paste (sizes 6, 3, and 1 μm). Then, the samples were edged by chemical etching process with hydrofluoric acid (4% vol) for 1 minute and cleaned afterwards with a high-frequency vibration. The samples were coated with gold by ion sputtering device (JEOL JFC-1200) at a current generation of 15 mA for 200 seconds.

2.6. Mechanical Properties Testing

2.6.1. Indentation Fracture Toughness (IFT). Glass specimens (Ø14 mm × 5 mm) were initially cut from the glass rod with

a diamond saw blade machine (IsoMet 4000, Buehler, Ltd., USA) to create parallel faces. After heat treatment, they were polished down using SiC paper and finally with diamond paste. Indentations were obtained using Vickers hardness testing machine (Vickers-Armstrong, Ltd., Crayford, UK) for loads of 1 kg, 2 kg, 3 kg, 5 kg, and 7.5 kg. The used loads were restricted to a range over which the indentation patterns remained well defined, at the lower end by the minimum requirement $c \geq 2a$, where c is the radial crack length and a is the indentation half-diagonal length, and at the upper end by chipping or by the limitation of specimen thickness. For each load, at least 15–20 indentations were made, and at least ten to fifteen readings were taken using an optical microscopy (ZEISS Model Axiotech) equipped with a digital camera and computer. Fracture toughness was calculated using the formula $K_{Ic} = 0.0824\ P/C^{3/2}$, where K_{Ic} is indentation fracture toughness (IFT), P is the indentation load, and C is the radial crack size.

2.6.2. Biaxial Flexural Strength. Glass specimens (Ø14 mm × 4 mm) were cut from the glass rods to obtain at least six disks. After two-stage heat treatment, they were ground and polished using SiC paper and diamond paste. Test geometry of three-ball supported test-jig equipped with a universal testing machine (Model 8872, Instron Instruments, Ltd., Fareham, Hampshire, UK) with a ring support of 10 mm at a cross-head speed of 1 mm/min was performed on the samples (Figure 1). A sheet of paper was placed between the samples and support ring to eliminate any additional flatness and reduce friction [27]. The center of each disk was marked as the correct place for the loading ball before testing. The maximum stress, σ_{max} at the center was calculated applying the following equation [27]:

$$\sigma_{max} = \frac{3\,(1+\nu)\,P}{4\pi t^2} \left[1 + 2\ln\frac{a}{b} + \frac{(1-\nu)}{(1+\nu)} \left\{ 1 - \frac{b^2}{2a^2} \right\} \frac{a^2}{R^2} \right], \tag{1}$$

where P is load, t is disk thickness, a is the radius of the circle of the support ring, b is the radius of the region of uniform loading at the center $b = t/3$, R is the radius of the disk sample, and ν is Poisson's ratio, $\nu = 0.25$.

2.7. Chemical Solubility Testing. After two-stage heat treatment, the glass specimens (Ø14 mm × 2 mm) were polished to create parallel faces. Glass ceramic specimens were washed and dried at 150°C for 4 hrs followed by being weighed to the nearest 0.1 mg (W_b). The total surface area of the specimens was determined to the nearest 0.1 cm². Specimens were then individually immersed in a 250 mL glass bottle with 100 mL acetic acid, 4% solution in water. The bottles were closed with their caps and then placed in an oven at 80°C for 16 hrs. Next, the specimens were washed and dried at 150°C for 4 hrs to achieve a constant mass. Finally, the specimens were reweighed to obtain the mass after immersion (W_a). The chemical solubility was determined by the following equation:

$$\text{Chemical solubility} = \frac{(W_b - W_a)}{\text{surface area of the specimen}}. \tag{2}$$
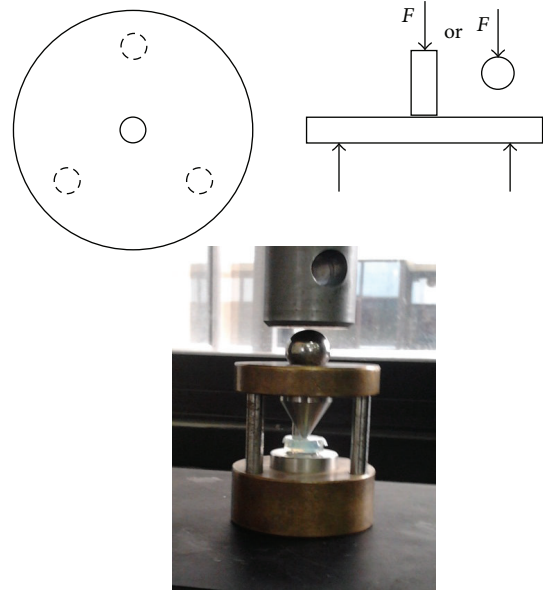
Figure 1: Test geometry of biaxial flexural strength.

Table 2: Summary of transition and crystallization temperatures of glasses.

Glasses	T_g (°C)	1st T_c (°C)	2nd T_c (°C)	3rd T_c (°C)
LD1	520	650	870	910
LD2	530	645	860	910
LD3	505	650	910	—
LD4	500	650	770	885

The chemical solubility test method in this study was referred to the ISO 6872 [28].

3. Results and Discussion

3.1. Differential Thermal Analysis. The DTA traces for glasses LD1–LD4 in Figure 2 and the summary of the exothermic and endothermic peaks in Table 2 show the exothermic and endothermic anomalies for all glasses attributed to either the glass transition (T_g) or crystallization temperatures (T_c).

The DTA traces of Glass LD1 exhibited triple exothermic peaks at 650°C, 860°C, and 910°C. A similar trend of three crystallization peaks at 650°C, 860°C, and 910°C was observed in Glass LD2. The study by Schweiger et al. [29] reported that the first crystallization of SiO_2-Li_2O system founds at 589°C corresponding to Li_2SiO_3 and the second crystallization peak at 770°C associated to $Li_2Si_2O_5$. The first and second crystallization temperatures of Li_2O-Al_2O_3-SiO_2 system in this study were at a higher temperature than the stoichiometric composition. This might be because of the addition of P_2O_5 and CaF_2 into glass compositions. Then, the third exothermic peak was observed. The addition of the MgO may not result in any significant changes in the T_g and T_c of the Glasses LD1 and LD2.

In Glass LD3, T_cs were observed at 650°C and 910°C. Two exothermic peaks associated with the crystallization

FIGURE 2: DTA traces of Glasses LD1–LD4.

FIGURE 3: The coefficient of thermal expansion of LD1, LD2, LD3, and LD4 which were heat-treated at 750–850°C for 2 hrs.

temperatures were observed by increasing the Si : Li ratio in LD3. Differently, in Glass LD4, three exothermic peaks were observed: firstly, a small peak at about 650°C and two broadening peaks at 770°C and 885°C. It seems that the second crystallization temperature decreased to 770°C in this composition. The addition of MgO in LD4 was behind the decrease of the second crystallization down to a lower temperature than that of LD1 and LD2 which had lower $SiO_2 : Li_2O$ ratios. Moreover, the crystallization of fluorapatite, Li_3PO_4, and aluminosilicate is the minor crystallization in the system, so that it is difficult to identify the exothermic peaks related to these minor phases.

3.2. The Coefficient of Thermal Expansion. Figure 3 presents the changes in thermal expansion coefficients of glass ceramics as a function of heat treatment temperatures. The coefficients of thermal expansion for LD1–LD4 decreased with increasing heat treatment temperature in all glass ceramic samples except LD2, of which the thermal expansion coefficient rose following heat treatment at 850°C.

The increasing in thermal expansion coefficient value of LD2 after heat treatment at 850°C was possibly due to the addition of MgO. It is well known that MgO is not a glass former; therefore, the addition of MgO causes a weakening of the glass network structure and, consequently, a higher coefficient of thermal expansion 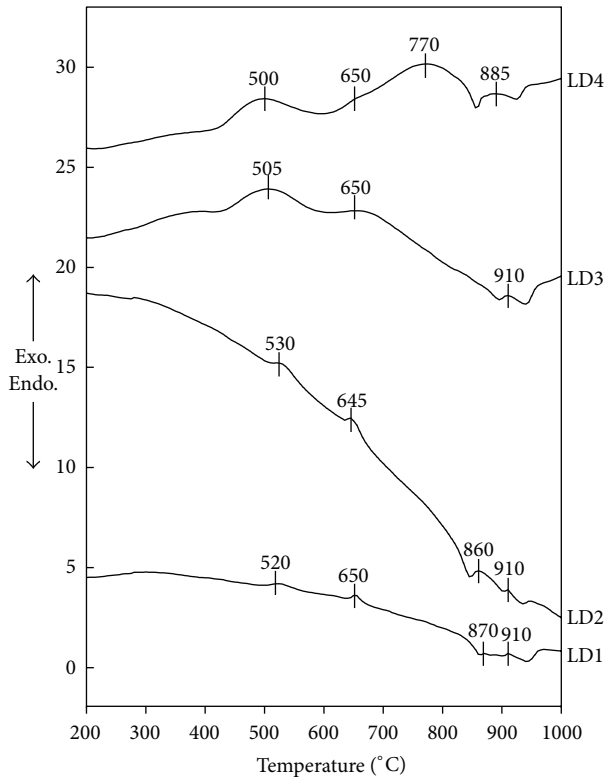[30]. Even though MgO was also added in LD4, the thermal expansion coefficient of LD4 after heat treatment at 850°C was decreased. The possible reason to explain this phenomenon is the different in

$SiO_2 : Li_2O$ ratio. The $SiO_2 : Li_2O$ ratio of LD4 was 2.21, which was higher than that of LD2 (1.90).

In general, the thermal expansion coefficients of the glass ceramics mainly depend on the crystalline phases present at different temperatures and volume content in the matrix glass. Not only crystal types affect the thermal expansion coefficient but also the glass composition which is related to the structure of the glass [31]. The different crystal types have different thermal expansion coefficients [32]. The explanation behind the high thermal expansion coefficient of all glass ceramics in this study is the presence of several crystalline phases such as fluorapatite (10.0×10^{-6}/°C [33]), lithium phosphate, lithium metasilicate (13.0×10^{-6}/°C [34]) and lithium disilicate (11.4×10^{-6}/°C [34]), which have a high thermal expansion coefficient in the glass composition. The decrease of the thermal expansion coefficient as the temperature rise can be explained by the β-quartz solid solution changes into lithium aluminium silicate: virgilite (a stuffed β-quartz), having a low or negative thermal expansion coefficient with the temperature increasing [35].

3.3. Summary of the Phase Evolution. Figure 4 shows XRD patterns of all glass ceramics heat treated at 700–850°C for 2 hrs, and the crystalline phases are summarized in Table 3. The crystal structures found in LD1 heat treated at 700°C were lithium disilicate (LD, $Li_2Si_2O_5$: ICDD no. 40-0376), lithium metasilicate (LS, Li_2SiO_3: ICDD no. 29-0829), lithium aluminium silicate (virgilite, $Li_{0.6}Al_{0.6}Si_{2.4}O_6$: ICDD no. 21-0503 and spodumene ($LiAlSi_2O_6$: ICDD no. 033-0786), fluorapatite ($Ca_5(PO_4)_3F$: ICDD no. 15-0876), lithium phosphate (Li_3PO_4: 015-0760), and SiO_2: high quartz ($2\theta = 20.26°$, ICDD no. 11-0252). At higher temperatures, the intensity of LS and virgilite peaks decreased while the intensity of lithium disilicate peaks increased. This exhibited higher in lithium disilicate crystallization. In addition, the peaks of β-quartz decreased until disappeared when heat treated at 850°C.

(a)

(b)

(c)

(d)
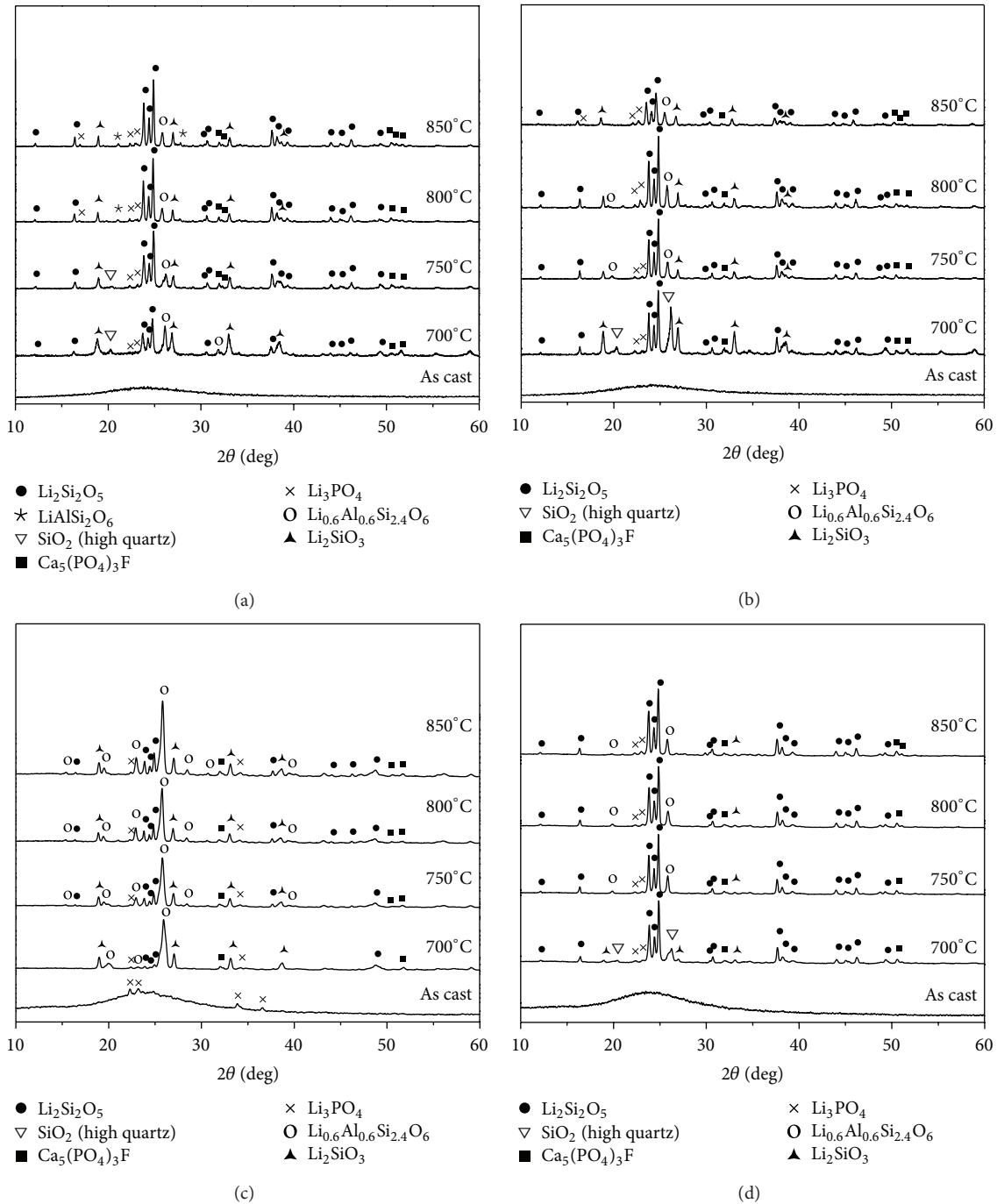
Figure 4: X-ray diffraction patterns of (a) LD1, (b) LD2, (c) LD3, and (d) LD4 after heat treatment at 700–850°C for 2 hrs.

A similar phase formation was also observed in LD2 with the addition of MgO. The small discrepancy was the crystal peaks associated to β-quartz solid solution ($2\theta = 26.26°$) when heat treatment at 700°C transformed into virgilite ($2\theta = 25.88°$) after heat treatment at 750°C. And this phase remained when heat treatment was at 800°C and 850°C.

Generally, the β-quartz could be stabilized by Li^+ or Mg^{2+}, Zn^+, and Al^{3+} called quartz-solid-solution which normally does not transform into the low-quartz-solid-solution while cooling down to room temperature resulting of a small

thermal expansion coefficient [36]. Meanwhile, virgilite is the naturally occurring representative of the solid-solution series between β-quartz and $LiAlSi_2O_6$ with a stuffed β-quartz structure [34]. However, the possible explanation of the virgilite formation in laboratory experiment was that the sluggish reaction rates in the system Li_2O-Al_2O_3-SiO_2 require high pressure and temperature. Then reaction rate could be increased by the presence of Fe, alkalis, and volatiles, thus promoting the formation of virgilite at lower pressure within its stability field [34].

TABLE 3: Summary of crystalline phases.

Glasses	Heat treatment temperature (°C)	Crystalline phases
LD1	700	$Li_2Si_2O_5$, Li_2SiO_3, $Li_{0.6}Al_{0.6}Si_{2.4}O_6$, Li_3PO_4, $Ca_5(PO_4)_3F$, SiO_2
	750	$Li_2Si_2O_5$, Li_2SiO_3, $Li_{0.6}Al_{0.6}Si_{2.4}O_6$, Li_3PO_4, $Ca_5(PO_4)_3F$, SiO_2
	800	$Li_2Si_2O_5$, Li_2SiO_3, $Li_{0.6}Al_{0.6}Si_{2.4}O_6$, Li_3PO_4, $Ca_5(PO_4)_3F$
	850	$Li_2Si_2O_5$, Li_2SiO_3, $Li_{0.6}Al_{0.6}Si_{2.4}O_6$, $LiAlSi_2O_5$, Li_3PO_4, $Ca_5(PO_4)_3F$
LD2	700	$Li_2Si_2O_5$, Li_2SiO_3, $Li_{0.6}Al_{0.6}Si_{2.4}O_6$, Li_3PO_4, $Ca_5(PO_4)_3F$, SiO_2
	750	$Li_2Si_2O_5$, Li_2SiO_3, $Li_{0.6}Al_{0.6}Si_{2.4}O_6$, Li_3PO_4, $Ca_5(PO_4)_3F$
	800	$Li_2Si_2O_5$, Li_2SiO_3, $Li_{0.6}Al_{0.6}Si_{2.4}O_6$, Li_3PO_4, $Ca_5(PO_4)_3F$
	850	$Li_2Si_2O_5$, Li_2SiO_3, $Li_{0.6}Al_{0.6}Si_{2.4}O_6$, Li_3PO_4, $Ca_5(PO_4)_3F$
LD3	700	$Li_2Si_2O_5$, Li_2SiO_3, $Li_{0.6}Al_{0.6}Si_{2.4}O_6$, Li_3PO_4, $Ca_5(PO_4)_3F$, SiO_2
	750	$Li_2Si_2O_5$, Li_2SiO_3, $Li_{0.6}Al_{0.6}Si_{2.4}O_6$, Li_3PO_4, $Ca_5(PO_4)_3F$
	800	$Li_2Si_2O_5$, Li_2SiO_3, $Li_{0.6}Al_{0.6}Si_{2.4}O_6$, Li_3PO_4, $Ca_5(PO_4)_3F$
	850	$Li_2Si_2O_5$, Li_2SiO_3, $Li_{0.6}Al_{0.6}Si_{2.4}O_6$, Li_3PO_4, $Ca_5(PO_4)_3F$
LD4	700	$Li_2Si_2O_5$, Li_2SiO_3, $Li_{0.6}Al_{0.6}Si_{2.4}O_6$, Li_3PO_4, $Ca_5(PO_4)_3F$, SiO_2
	750	$Li_2Si_2O_5$, Li_2SiO_3, $Li_{0.6}Al_{0.6}Si_{2.4}O_6$, Li_3PO_4, $Ca_5(PO_4)_3F$
	800	$Li_2Si_2O_5$, Li_2SiO_3, $Li_{0.6}Al_{0.6}Si_{2.4}O_6$, Li_3PO_4, $Ca_5(PO_4)_3F$
	850	$Li_2Si_2O_5$, Li_2SiO_3, $Li_{0.6}Al_{0.6}Si_{2.4}O_6$, Li_3PO_4, $Ca_5(PO_4)_3F$

Figure 4(c) presents XRD pattern of LD3 heat treatment at different temperatures. By increasing the $SiO_2 : Li_2O$ ratio, in the glass composition, phase separation occurred due to the white and semiopaque appearance observed in LD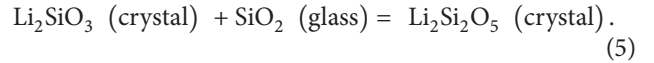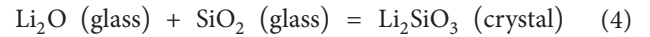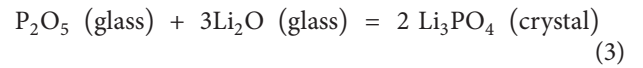3. Therefore, the crystal structures found in the as-cast glass were Li_3PO_4. At 700°C, XRD patterns showed the phase formation of Li_2SiO_3, lithium aluminium silicate, $Li_2Si_2O_5$, $Ca_5(PO_4)_3F$, and SiO_2: high quartz. The small peaks of Li_3PO_4 decreased when heat treated at higher temperatures. With increasing temperature, the intensity of $Li_2Si_2O_5$ increased as well as the retention of Li_2SiO_3, lithium aluminium silicate (virgilite), and $Ca_5(PO_4)_3F$. By increasing the $SiO_2 : Li_2O$ ratio, the more lithium aluminium silicate crystal peaks were observed compared to LD1 which has low $SiO_2 : Li_2O$ ratio.

The phase formation of LD4 is presented in Figure 4(d). The as-cast glass appearance looks clearer than that of LD3, implying that no phase separation occurred in this glass. At 700°C, the peaks corresponded to Li_2SiO_3, Li_3PO_4, $Li_2Si_2O_5$, $Ca_5(PO_4)_3F$, lithium aluminium silicate, and SiO_2 in the form of high quartz observed. Then after heat treatment at higher temperature, the crystal peaks associated to β-quartz solid solution ($2\theta = 26.26°$) when heat-treated at 700°C transformed into virgilite ($2\theta = 25.88°$) after heat treatment at 750°C; this is similar to LD2. The difference from LD2 was the number of Li_2SiO_3 peaks observed in LD4 wich was less than that in LD2.

The growth of lithium disilicate could be initiated by the primary crystallization of the precursor lithium metasilicate, in particular, lithium disilicate glass ceramic containing Al_2O_3 [36]. Glass ceramic containing P_2O_5 may be nucleated by the initiation of the phase separation process, such as Li_3PO_4 nuclei [4, 37, 38]. P_2O_5 can react with Li_2O in Li_2O-rich regions to form the Li_3PO_4 crystal nuclei which act as nucleating sites shown in reaction(3). Some Li_2O was consumed in the Li_2O-rich regions to form Li_3PO_4 phase (reaction (3)) which can induce the precipitation of Li_2SiO_3 crystal (reaction(4)). It is reasonable to assume that Li_2SiO_3 precipitated on the Li_3PO_4 crystal nuclei in Li-rich regions, and the growth of $Li_2Si_2O_5$ was at the expense of consuming Li_2SiO_3 as shown in reaction (5)

$$P_2O_5 \text{ (glass)} + 3Li_2O \text{ (glass)} = 2\ Li_3PO_4 \text{ (crystal)} \tag{3}$$

$$Li_2O \text{ (glass)} + SiO_2 \text{ (glass)} = Li_2SiO_3 \text{ (crystal)} \tag{4}$$

$$Li_2SiO_3 \text{ (crystal)} + SiO_2 \text{ (glass)} = Li_2Si_2O_5 \text{ (crystal)}. \tag{5}$$

Therefore, the sequence of the primary crystal phase formation as Li_3PO_4, Li_2SiO_3, and $Li_2Si_2O_5$ was proposed [4]. On the other hand, the investigation on complex simultaneous and sequential solid-state reactions in an Al_2O_3-free lithium disilicate glass ceramic found that Li_3PO_4 crystals were formed after the crystallization of Li_2SiO_3 and $Li_2Si_2O_5$ [13]. Hence, they [13] concluded that Li_3PO_4 does not nucleate lithium disilicate crystals, as previously studied for the glasses of similar composition [17].

However, in this case a different early phase formation was observed. Due to CaF_2 added in this system, the peaks were associated with the crystal of fluorapatite indexed in the XRD pattern in parallel with Li_3PO_4. Subsequently, at an early stage, the incorporation of fluorine in phosphate glasses leads to P-F bonds at the expense of P-O-P bonds to possibly form fluorapatite: $Ca_5(PO_4)_3F$ crystals [39]. Therefore, it is reasonable to conclude that the formation of $Li_2Si_2O_5$ crystals in this case occurred from the heterogeneous nucleation of Li_3PO_4 and $Ca_5(PO_4)_3F$ caused from the addition of CaF_2 and P_2O_5 in glass compositions. Hence, P_2O_5 also act as a nucleating agent in this system.

Furthermore, the investigation on spodumene, $Li_2O \cdot Al_2O_3 \cdot 4SiO_2$ glass ceramics adding ZrO_2 suggested that Al_2O_3 content should not exceed 30% wt to achieve

a low coefficient of thermal expansion and highly thermal shock resistant [40], as a result of detritions of mechanical strength [35]. In this study only 2% wt of Al_2O_3 was added in the glass compositions, in the range to produce a low thermal expansion coefficient glass ceramic.

3.4. Microstructure.

The morphology of the system was studied, and SEM micrographs of the sample surfaces are shown in Figure 5. At 700°C, SEM images of glass ceramic LD1 illustrate the spherical-like crystals of both Li_2SiO_3 and Li_3PO_4. Normally, Li_2SiO_3 and Li_3PO_4 crystals could dissolve in HF solution if one-stage treatment applied due to the precipitate crystals was not stable [4]. In this study, two-stage treatment was applied, thus, Li_2SiO_3 and Li_3PO_4 crystals could be seen by SEM consistent with XRD pattern which indicated the formation of both crystals. XRD patterns also indicated the formation of the lithium aluminium silicate: virgilite and fluorapatite crystals. Both crystals have a rounded or spherical-like shape similar to Li_2SiO_3 and Li_3PO_4 but smaller in size, which is hardly to find by either SEM technique or energy dispersive spectroscopy (EDS) [41]. Transmission electron microscopy could be a better technique to show these spherical shapes of the virgilite and fluorapatite crystals [42, 43].

After heat treatment at 800°C, several lath-like crystals of lithium disilicate were observed. With increasing heat treatment temperature, the more and the coarser the lath-like crystals occurred, in close consistency with XRD results. A similar microstructure was also observed in LD2. A small discrepancy appeared at 750°C for LD2 in which no lath-like crystal of $Li_2Si_2O_5$ was noticed but the lath-like crystals can be observed in samples after heat treatment at 800°C and 850°C.

SEM images of LD3 and LD4 shown in Figures 5(c) and 5(d) reveal that the spherical-shaped crystals of both Li_2SiO_3 and Li_3PO_4 occurred at 700°C and 750°C followed by the appearance of needle-like crystals or plate-like crystals of $Li_2Si_2O_5$ in a glassy matrix at 800°C and 850°C. This needle-like crystal looked very long with a narrow diameter. The higher the temperature of heat treatment, the larger the aspect ratio and greater interlocking of the needle-like crystal was observed. The increase in the Si : Li ratio in LD3 and LD4 compositions seems to have induced the change in the microstructure of the $Li_2Si_2O_5$ crystal from the fine lath-like crystal to the needle-like or plate-like crystal. The addition of a slight amount of MgO content in glass composition showed no significant changes in the microstructure of the glass ceramics. This phenomenon was also observed in LD1 and LD2.

3.5. Mechanical Properties

3.5.1. Indentation Fracture Toughness (IFT).

The IFT values of the glass ceramics LD1–LD4 at different temperatures are shown in Figure 6. The highest IFT for all samples was obtained at 800°C with glass ceramics LD1, LD2, and LD4, 3.59 ± 0.01, 3.72 ± 0.03, and 3.58 ± 0.01 MPa m$^{1/2}$, respectively, which suggests that this heat-treatment temperature is close to the optimum, probably caused by the finer and more highly interlocked crystals. Of exceptional note was that the highest IFT value of LD3, 7.88 ± 0.01 MPa m$^{1/2}$ was found in samples at a heat treatment of 850°C at which a finer microstructure with a high aspect ratio might be occurring. It was reported that the finer the microstructure, the more twisted the path for fracture and, therefore, the higher the fracture toughness [42]. Consequently, LD1, LD2, and LD4 at 850°C and LD3 at 800°C, which illustrated a coarser microstructure, obtained lower IFT values. As shown in (Figure 4(c)), XRD pattern of LD3 indicated the more numbers of lithium aluminium silicate: virgilite crystals with a high intensity compared to that of other glasses, particularly at 800°C and 850°C. Therefore, the thermal expansion mismatch between $Li_2Si_2O_5$ and virgilite resulted in residual stresses or microcracks on cooling, which create crack tip shielding and enhanced toughness of LD3 at 800C° and 850°C.

3.5.2. Biaxial Flexural Strength (BFS).

Figure 7 presents the BFS values of the glass ceramics LD1-LD4 at different temperatures. For LD1, the BFS was at its maximum (396.24 ± 79 MPa) at 750°C which didnot significantly decrease after heat treatment at 800°C (388.05 ± 38 MPa) followed by drastical change to 256.06 ± 29 MPa at 850°C. In LD2, the maximum BFS was 471.39 ± 42 MPa at 800°C which increased from 383.62 ± 28 MPa at 750°C followed by a decrease to 295.55 ± 23 MPa at 850°C. In LD3, an increase in BFS was observed from 353.17 ± 81 MPa in samples heat-treated at 750°C to 404.94 ± 26 MPa at 800°C followed by a decrease to 317.01 ± 13 MPa at 850°C. For LD4, the maximum BFS was 489.73 ± 47 MPa at 800°C which sharply increased from 251.82 ± 20 MPa at 750°C followed by a decrease to 388.78 ± 39 MPa at 850°C. Overall, the highest BFS of the studied glass ceramics was found at 800°C in which a finer microstructure was noted. Another reason is that the thermal expansion mismatch between lithium disilicate and other phases, including glass matrix, probably caused tangential compressive stresses around the crystals, which was responsible for crack deflection and enhanced strength [1].

Irwin, as with Griffith approach, introduced stress intensity factors as a quantitative indicator on the effect of dimension and shape [44] on the magnitude of the stresses near a crack tip [45]. This is expressed in a general formula for an infinite plate with crack length = $2a$ at its center,

$$\sigma = \frac{K_{IC}}{\sqrt{\pi c}}, \tag{6}$$

where σ is the nominal stress or biaxial flexural strength, K_{IC} is the fracture toughness, and C is the flaw size.

With this formula, it is possible to find the correlation between strength and the stress field (fracture toughness) in the terms of a critical flaw size, as shown in Table 4 since both strength and fracture toughness are known. It is worth noting that Mencik [44] and Green [45] suggested that if the crack length or flaw size is smaller than the pore or crystal size, a high K_{IC} but low strength value may occur. This could explain the situation of the high fracture toughness but low in strength of LD3 at 800°C and 850°C due to the largest critical

(a)

(b)

(c)

(d)
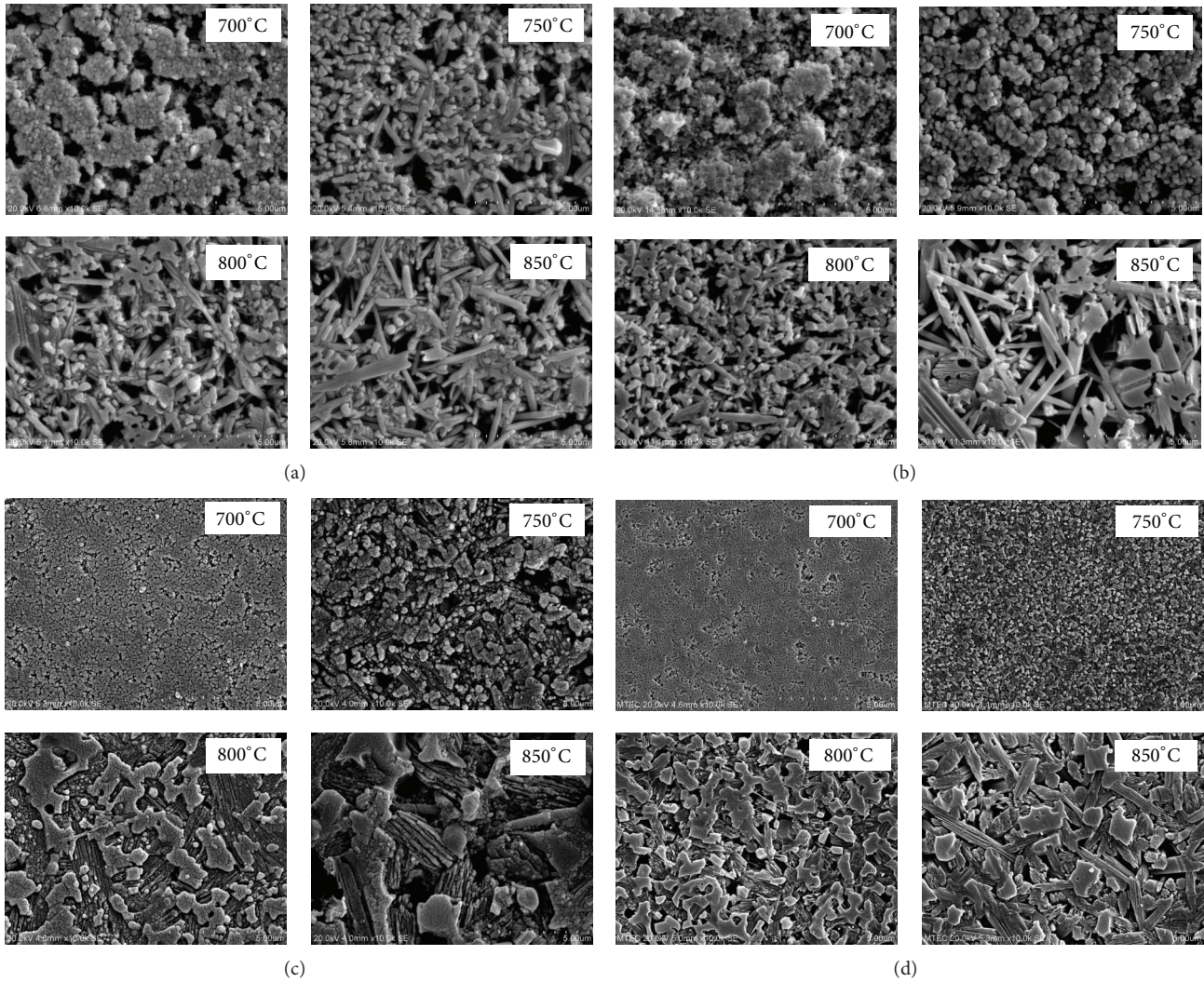
FIGURE 5: SEM micrographs of (a) LD1, (b) LD2, (c) LD3, and (d) LD4 after heat treatment at different temperatures for 2 hrs.

TABLE 4: The comparison on calculated flaw sizes of Glasses LD1–LD4 after being heat-treated at 750°C, 800°C, and 850°C.

Glasses	750°C			800°C			850°C		
	K_{IC} (MPa m$^{1/2}$)	σ (MPa)	C (μm)	K_{IC} (MPa m$^{1/2}$)	σ (MPa)	C (μm)	K_{IC} (MPa m$^{1/2}$)	σ (MPa)	C (μm)
LD1	1.80	396.24	6.56	3.59	388.05	27.25	2.69	256.06	35.21
LD2	1.91	383.62	7.86	3.72	471.39	19.81	2.30	295.55	19.31
LD3	1.44	353.17	5.26	7.25	404.94	102.17	7.88	317.01	196.87
LD4	1.19	251.82	7.10	3.58	489.73	16.98	2.76	388.78	16.03

flaw size (~102 μm for 800°C and ~197 μm for 850°C) which was found in these samples.

3.6. Chemical Solubility. Chemical solubility is an important property for dental restoration since a high solubility or low resistance to erosion will strictly limit the effective lifetime of the restoration. Moreover, the chemical solubility property also directly affects the strength of the glass ceramic material. Figure 8 shows the chemical solubility value of all glass ceramics at different temperatures. It was found that the chemical solubility of all glass ceramics slightly decreased with increasing temperature, except that of LD2 which had

MgO content. The addition of alkaline earth such as CaO and MgO in glass composition could increase chemical solubility in glass ceramics owing to the increased volume of crystalline phase [6]. Considerably, the microstructure of LD2 at 850°C (Figure 5(d)) shows a high aspect ratio of needle-like crystals which are loosely interlocking compared to other glasses. This kind of microstructure might be easy for the acid to attack on the surface of the sample. Therefore, the microstructure could also be responsible for high chemical solubility of LD2.

In fact, the chemical solubility of the core ceramic materials must be less than 2000 μg/cm^2, and that of the body ceramic materials directly in contact with the oral
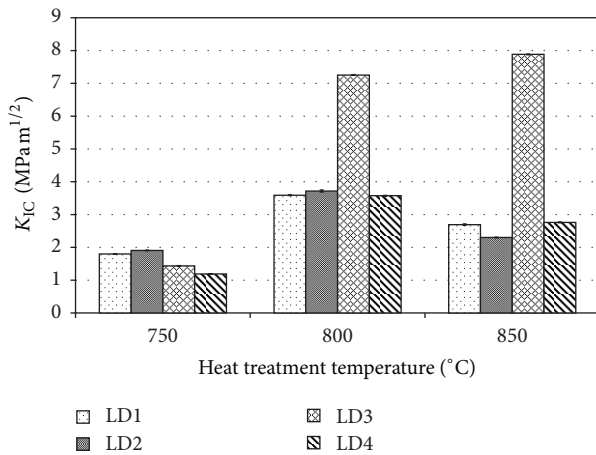
FIGURE 6: The fracture toughness of LD1, LD2, LD3, and LD4 heat treated at different temperatures for 2 hrs.
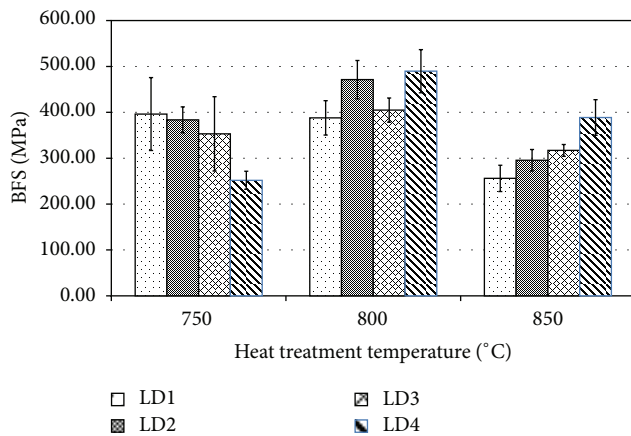
FIGURE 7: The biaxial flexural strength of LD1, LD2, LD3, and LD4 at different heat-treated temperatures for 2 hrs.
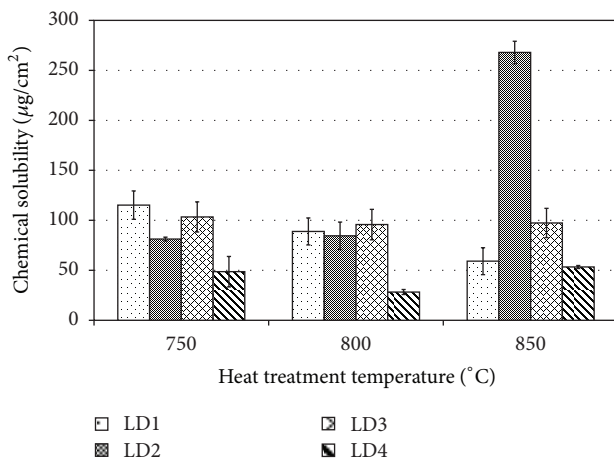
FIGURE 8: The chemical solubility of LD1, LD2, LD3, and LD4 at different heat-treated temperatures for 2 hrs.

environment should be less than $100\,\mu g/cm^2$ according to ISO 6872 [28]. Generally, the chemical solubility of the glass ceramic in this study was in the acceptable range according to ISO 6872 for core ceramic material. The lowest chemical durability was LD4, at $\sim 28\,\mu g/cm^2$, heat-treated at 800°C.

4. Conclusions

All glass ceramics were identified by X–ray diffraction method, and it was found that P_2O_5 and CaF_2 served as a nucleating site for lithium phosphate, Li_3PO_4, and fluorapatite, $Ca_5(PO_4)_3F$, to induce heterogeneous nucleation and then produce a fine-grained interlocking microstructure of lithium disilicate glass ceramics. MgO content in this system seems to have played less of a role in changing the phase formation and microstructure of the glasses but enhanced the viscosity of the melting glass and thermal expansion coefficient including the chemical solubility. The increase in the Si : Li ratio in glass compositions resulted from the change in the microstructure of $Li_2Si_2O_5$ crystal from fine lath-like crystals to needle-like or plate-like crystals. In this study, LD3 heat-treated at 850°C exhibited the best fracture toughness of $\sim 8\,MPa\,m^{1/2}$. In addition, LD4 heat-treated at 800°C had the best biaxial flexural strength and chemical solubility of $\sim 490\,MPa$ and $\sim 28\,\mu g/cm^2$, respectively. These glass compositions are promising for potential use as dental crowns.

Conflict of Interests

There is no financial or other relationship that might be perceived as leading to a conflict of interests. The authors declare that there is no conflict of interests.

Acknowledgment

References

[1] I. Denry and J. A. Holloway, "Ceramics for dental applications: a review," *Materials*, vol. 3, no. 1, pp. 351–368, 2010.

[2] E. El-Meliegy and R. van Noort, *Glasses and Glass Ceramics for Medical Applications*, Springer, New York, NY, USA, 2012.

[3] C. C. Gonzagaa, P. F. Cesara, C. Y. Okadaa, C. Fredericcib, F. B. Netob, and H. N. Yoshimurab, "Mechanical properties and porosity of dental glass-ceramics hot-pressed at different temperatures," *Materials Research*, vol. 11, no. 3, pp. 301–306, 2008.

[4] X. Zheng, G. Wen, L. Song, and X. X. Huang, "Effects of P_2O_5 and heat treatment on crystallization and microstructure in lithium disilicate glass ceramics," *Acta Materialia*, vol. 56, no. 3, pp. 549–558, 2008.

[5] G. H. Beall and R. C. Doman, *Glass-Ceramics in Corning Research*, Corning Glass Works Scientists, New York, NY, USA, 1987.

[6] P. W. McMillan, *Glass-Ceramics*, Academic Press, London, UK, 1979.

[7] P. Hing and P. W. McMillan, "A transmission electron microscope study of glass-ceramics," *Journal of Materials Science*, vol. 8, no. 3, pp. 340–348, 1973.

[8] P. F. James, "Kinetics of crystal nucleation in silicate glasses," *Journal of Non-Crystalline Solids*, vol. 73, no. 1-3, pp. 517–540, 1985.

[9] R. Ota, N. Mishima, T. Wakasugi, and J. Fukunaga, "Nucleation of Li$_2$O-SiO$_2$ glass and its interpretation based on a new liquid model," *Journal of Non-Crystalline Solids*, vol. 219, pp. 70–74, 1997.

[10] E. D. Zanotto, "Metastable phases in lithium disilicate glasses," *Journal of Non-Crystalline Solids*, vol. 219, pp. 42–48, 1997.

[11] L. L. Burgner, P. Lucas, M. C. Weinberg, P. C. Soares Jr., and E. D. Zanotto, "On the persistence of metastable crystal phases in lithium disilicate glass," *Journal of Non-Crystalline Solids*, vol. 274, no. 1, pp. 188–194, 2000.

[12] L. L. Burgner and M. C. Weinberg, "Assessment of crystal growth behavior in lithium disilicate glass," *Journal of Non-Crystalline Solids*, vol. 279, no. 1, pp. 28–43, 2001.

[13] W. Höland, V. Rheinberger, and M. Schweiger, "Control of nucleation in glass ceramics," *Philosophical Transactions of the Royal Society A*, vol. 361, no. 1804, pp. 575–589, 2003.

[14] J. M. Barrett, D. E. Clark, and L. L. Hench, "Glass-ceramic dental restoration," U.S. Patent 4,189,325, 1980.

[15] J. M. Wu, W. R. Cannon, and C. Panzera, "Castable glass-ceramic composition useful as dental restorative," U.S. Patent 4,515,634, 1985.

[16] D. U. Thlyaganov, S. Agathopoulos, I. Kansal, and P. Valerio, "Synthesis and properties of lithium disilicate glass-ceramics in the system SiO$_2$-Al$_2$O$_3$-K$_2$O-Li$_2$O," *Ceramics International*, vol. 35, no. 8, pp. 3013–3019, 2009.

[17] D. Holland, Y. Iqbal, P. James, and B. Lee, "Early stages of crystallisation of lithium disilicate glasses containing P$_2$O$_5$—an NMR study," *Journal of Non-Crystalline Solids*, vol. 232–234, pp. 140–146, 1998.

[18] L. M. Echeverria and G. H. Beall, "New lithium disilicate glass-ceramics," *Boletin de la Sociedad Espanola de Ceramica y Vidrio*, vol. 5, pp. 183–188, 1999.

[19] G. H. Beall, "Glass-ceramics: recent development and application," *Ceramic Transactions*, vol. 30, pp. 241–266, 1993.

[20] G. N. Beall, "Design of glass-ceramics," *Solid State Sciences*, vol. 3, pp. 333–354, 1989.

[21] S. C. von Clausbruch, M. Schweiger, W. Höland, and V. Rheinberger, "The effect of P$_2$O$_5$ on the crystallization and microstructure of glass-ceramics in the SiC$_2$-Li$_2$O-K$_2$O-ZnO-P$_2$O$_5$ system," *Journal of Non-Crystalline Solids*, vol. 263-264, pp. 388–394, 2000.

[22] Y. Iqbal, W. E. Lee, D. Holland, and P. F. James, "Crystal nucleation in P$_2$O$_5$-doped lithium disilicate glasses," *Journal of Materials Science*, vol. 34, no. 18, pp. 4399–4411, 1999.

[23] T. Kasuga, T. Kimata, and A. Obata, "Preparation of a calcium titanium phosphate glass-ceramic with improved chemical durability," *Journal of the American Ceramic Society*, vol. 92, no. 8, pp. 1709–1712, 2009.

[24] G. H. Beall, "Glass-ceramics: recent development and application," in *Nucleation and Crystallization in Glasses and Liquids. Ceramic Transactions*, M. C. Weinberg, Ed., vol. 30, pp. 241–266, American Ceramics Society, Westerville, Ohio, USA, 1993.

[25] M. Schweiger, M. Frank, S. Cramer von Clausbruch, W. Holand, and V. Rheinberger, "Microstructure and properties of presses glass-ceramic core to zirconia post," *Quintessence of Dental Technology*, vol. 22, pp. 143–152, 1998.

[26] M. Frank, M. Schweiger, V. Rheinberger, and W. Holand, "High strength translucent sintered glass-ceramic for dental application," *Glasstech. Ber. Glass Science Technology*, vol. 71C, pp. 345–348, 1998.

[27] R. Morrell, *Biaxial Flexural Strength Testing of Ceramic Materials*, National Physical Laboratory, Teddington, Middlesex, UK, 1998.

[28] "Dentistry—Ceramic materials," Part 4, types, classes and their identification, ISO 6872:2008.

[29] M. Schweiger, W. Holand, M. Frank, H. Drescher, and V. Rheinberger, "IPS Empress®2: a new pressable high strength glass-ceramic for esthetic all ceramic restoration," *Quintessence of Dental Technology*, vol. 22, pp. 143–152, 1999.

[30] S. M. Salman and S. N. Salama, "Crystallization and thermal expansion characteristics of In$_2$O$_3$-containing lithium iron silicate-diopside glasses," *Ceramics—Silikaty*, vol. 55, no. 2, pp. 114–122, 2011.

[31] H. Darwish, S. N. Salama, and S. M. Salman, "Contribution of germanium dioxide to the thermal expansion characteristics of some borosilicate glasses and their corresponding glass-ceramics," *Thermochimica Acta*, vol. 374, no. 2, pp. 129–135, 2001.

[32] R. H. Hopkins, D. H. Damon, P. Piotrowski, M. S. Walker, and J. H. Uphoff, "Thermal properties of synthetic fluorapatite crystals," *Journal of Applied Physics*, vol. 42, no. 1, pp. 272–275, 1971.

[33] P. McAlinn, D. E. Clark, and L. L. Hench, "High expansion glass-cermaic articles," U.S. Patent 4,480,044, 1984.

[34] B. M. French, P. A. Jezek, and D. E. Appleman, "Virgilite: a new lithium aluminum silicate mineral from the Macusani glass, Peru," *American Mineralogist*, vol. 63, pp. 461–465, 1978.

[35] Z. Strnad, *Glass-Ceramic Materials in Glass Science and Technology*, Elsevier, Amsterdam, The Netherlands, 1986.

[36] W. Höland and G. H. Beall, *Glass-Ceramic Technology*, The American Ceramic Society, Westerville, Ohio, USA, 2002.

[37] P. Goharian, A. Nemati, M. Shabanian, and A. Afshar, "Properties, crystallization mechanism and microstructure of lithium disilicate glass-ceramic," *Journal of Non-Crystalline Solids*, vol. 356, no. 4-5, pp. 208–214, 2010.

[38] G. Wen, X. Zheng, and L. Song, "Effects of P$_2$O$_5$ and sintering temperature on microstructure and mechanical properties of lithium disilicate glass-ceramics," *Acta Materialia*, vol. 55, no. 10, pp. 3583–3591, 2007.

[39] A. W. A. El-Shennawi, A. A. Omar, and E. M. A. Hamzawy, "Role of fluorine and phosphorus in the crystallisation of K-fluorricherite glass," in *Proceedings of the 18th International Congress on Glass*, American Ceramic Society, San Francisco, Calif, USA, 1998.

[40] A.-X. Lu, M. Jia, and S.-J. Liu, "Effects of heat treatment temperature on crystallization and thermal expansion coefficient of Li$_2$O-Al$_2$O$_3$-SiO$_2$," *Journal of Central South University of Technology*, vol. 11, no. 3, pp. 235–238, 2004.

[41] Z. Xiao, J. Zhou, Y. Wang, and M. Luo, "Microstructure and properties of Li$_2$O-Al$_2$O$_3$-SiO$_2$-P$_2$O$_5$ glass-ceramics," *Open Materials Science Journal*, vol. 5, pp. 45–50, 2011.

[42] M. Mirsaneh, I. M. Reaney, P. V. Hatton, and P. F. James, "Characterization of high-fracture toughness K-fluorrichterite-fluorapatite glass ceramics," *Journal of the American Ceramic Society*, vol. 87, no. 2, pp. 240–246, 2004.

[43] N. Kanchanarat, S. Bandyopadhyay-Ghosh, I. M. Reaney, I. M. Brook, and P. V. Hatton, "Microstructure and mechanical

properties of fluorcanasite glass-ceramics for biomedical applications," *Journal of Materials Science*, vol. 43, no. 2, pp. 759–765, 2008.

[44] J. Mencik, *Strength and Fracture of Glass and Ceramics*, Elsevier, Amsterdam, The Netherlands, 1992.

[45] D. J. Green, *An Introduction to the Mechanical Properties of Ceramics*, Cambridge University Press, Cambridge, UK, 1998.

Research Article

White-Ceramic Conversion on Ti-29Nb-13Ta-4.6Zr Surface for Dental Applications

Akiko Obata,[1] Eri Miura-Fujiwara,[2] Akimitsu Shimizu,[1] Hirotaka Maeda,[3] Masaaki Nakai,[4] Yoshimi Watanabe,[1] Mitsuo Niinomi,[4] and Toshihiro Kasuga[1]

[1] *Graduate School of Engineering, Nagoya Institute of Technology, Gokiso-cho, Showa-ku, Nagoya 466-8555, Japan*

[2] *Graduate School of Engineering, University of Hyogo, 2167 Shosha, Himeji, Hyogo 671-2280, Japan*

[3] *Center for Fostering Young and Innovative Researchers, Nagoya Institute of Technology, Gokiso-cho, Showa-ku, Nagoya 466-8555, Japan*

[4] *Institute for Materials Research, Tohoku University, 2-1-1 Katahira, Aoba-ku, Sendai 980-8577, Japan*

Correspondence should be addressed to Akiko Obata; obata.akiko@nitech.ac.jp

Ti-29Nb-13Ta-4.6Zr (TNTZ) alloy has excellent mechanical properties and bone conductivity. For dental application, TNTZ surfaces were converted to white oxidized layer by a simple heat treatment in air to achieve the formation of aesthetic surfaces. The oxidized layer formed by the heat treatment at 1000°C for 0.5 or 1 hr was whiter and joined to TNTZ substrate more strongly than that formed by the treatment at 900°C. The layer consisted of TiO_2 (rutile), $TiNb_2O_7$, and $TiTa_2O_7$ and possessed ~30 μm in thickness for the sample heat-treated at 1000°C and ~10 μm for that heat-treated at 900°C. The surface average roughness and the wettability increased after the heat treatment. The spreading and proliferation level of mouse osteoblast-like cell (MC3T3-E1 cell) on the heat-treated sample were almost the same as those on as-prepared one. The cell spreading on TNTZ was better than those on pure titanium (CP Ti) regardless of the heat treatment for the samples. There was no deterioration in the *in vitro* cell compatibility of TNTZ after the oxidized layer coating by the heat treatment.

1. Introduction

Titanium (Ti) and its alloys have been developed for the use in orthopedic and dental fields, such as joints, plates, screws, and tooth roots. Ti materials show better corrosion resistance than stainless steel and Co-Cr alloys, which are used for biomedical applications, due to the stable titanium oxide films formed on their surfaces. Ti alloys are categorized as α-type, $\alpha+\beta$-type, and β-type, according to the quantities and types of their alloying elements. Various types of Ti alloys have been developed, particularly $\alpha+\beta$-type and β-type alloys, which have nontoxic and nonallergic elements, and are expected to be useful for biomedical application [1–4]. Ti-6Al-4V ELI alloy has been registered in ASTM standardizations and used as bone fixation plates and the stems of artificial hip joints. The ELI alloy shows significant toughness: an extremely high 0.2% offset yield strength of 895 MPa, which is higher than those of stainless steel and Co-Cr-Mo alloys [3].

Ti-29Nb-13Ta-4.6Zr (TNTZ) was developed as a low rigidity β-type alloy composed of non-toxic and non-allergic elements [1, 2]. The mechanical properties such as tensile properties and fatigue strength of TNTZ are equal to or greater than those of Ti-6Al-4V ELI alloy. Young's modulus of TNTZ is much lower than that of the ELI alloy, which makes it the preferred material for use in bone fixators. The bone conduction ability of TNTZ is better than that of stainless steel or the Ti-6Al-4V alloy [1]. Differences in mechanical properties between implant materials and natural bone lead to negative effects, such as stress shielding [2]. The properties of TNTZ have been found to be close to those of bone and expected in medical and dental fields.

Some dental materials, for example, artificial tooth and orthodontics devices such as arch wire or bracket, are required to exhibit natural sensuousness to make teeth healthy and beautiful. There is therefore concern that TNTZ

(a)

(b)

(c)

(d)

(e)

(f)

Figure 1: Appearances of TNTZ samples. (a) As-prepared, (b) heated at 900°C for 0.5 hr, (c) heated at 900°C for 1 hr, (d) heated at 1000°C for 0.5 hr, and (e) heated at 1000°C for 1 hr. Spectral reflectances of TNTZ samples before and after heat-treatment at 1000°C for 0.5 hr (f).

has disadvantages of aesthetic sensuousness due to its metallic colour. We believe that natural bone- or tooth-coloured coating (white-coloured coating) on TNTZ surface should be effective to solve this problem. The white-coloured coating should exhibit biocompatibility as well as or better than that of TNTZ.

Several surface modifications for Ti and Ti alloys have been performed to enhance their biocompatibilities [3, 5]. Many pyroprocessing methods of coating hydroxyapatite (HAp), which is the main inorganic component of bone and shows an excellent biocompatibility, on the metal surfaces have been reported [6]. There is, however, concern that the prepared HAp has lower adhesion ability with the metal

substrate and the coating method has limit to achieve complex-shaped metals. In addition, the HAp coating prepared by the pyroprocessing method, such as plasma spraying, exhibits lower chemical durability in body than the stoichiometric one, which attributes to an unexpected dissolution of the coating after implantation.

Calcium phosphate invert glass-ceramic ($60CaO$-$30P_2O_5$-$7Na_2O$-$3TiO_2$ in mol%) coating, which exhibits biocompatibility, for TNTZ has been reported in our previous research [7, 8]. The coating was prepared with the following method: dipping the alloy disc into the glass-powder slurry, drying the resulting disc at 100°C, and heating it in air at 800°C for 0.5~2 hr. Tensile test demonstrated
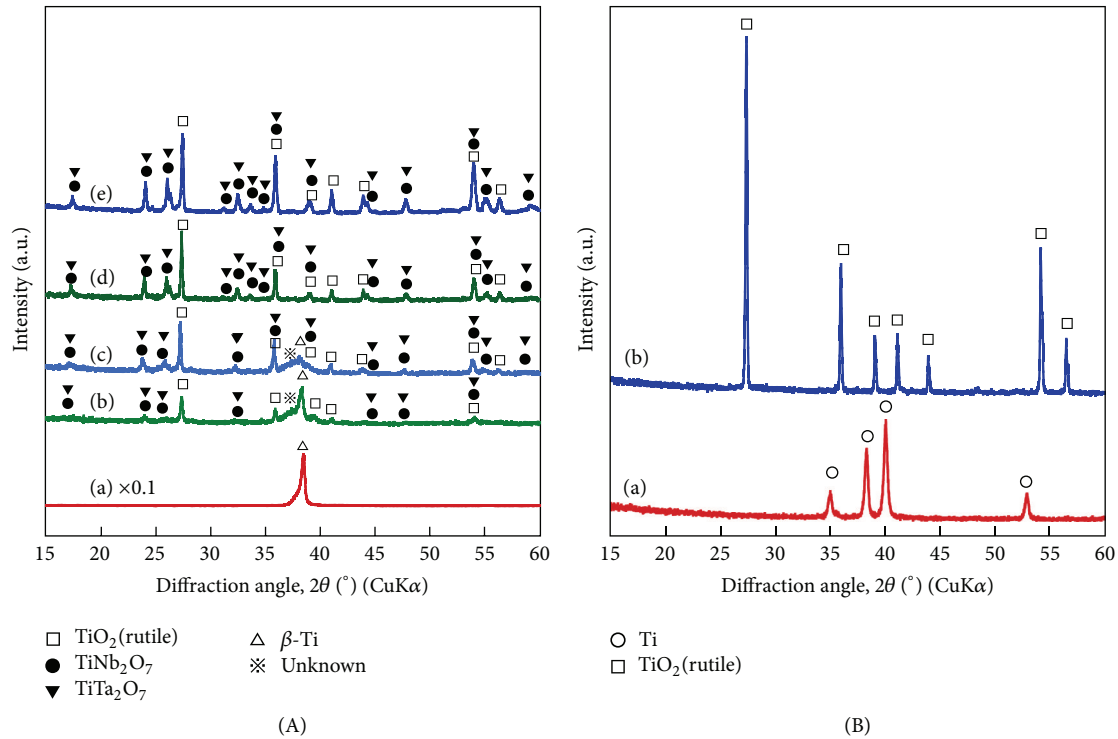
FIGURE 2: XRD patterns of (A) TNTZ and (B) CP Ti. (A-a) As-prepared, (A-b) heated at 900°C for 0.5 hr, (A-c) heated at 900°C for 1 hr, (A-d) heated at 1000°C for 0.5 hr, (A-e) heated at 1000°C for 1 hr, (B-a) as-prepared, and (B-b) heated at 1000°C for 1 hr.

that the bonding strength of the coating with TNTZ was higher than that with Ti-6Al-4V or pure Ti (CP Ti) and the strength value (~25 MPa) was relatively higher than that of the plasma-sprayed HAp coating on CP Ti ($\leq$7 MPa) [6]. It was also found that an intermediate layer consisting of a thin oxidized-TNTZ layer formed between the coating and the substrate. They fractured in the glass-ceramic coating after the tensile test. This means that the bonding strength value of the oxidized layer and TNTZ substrate was higher than the measured one, which may indicate that the layer bonds to the substrate more strongly than the plasma-sprayed HAp. The oxidized layer was white because light scattering takes place at grain boundaries in its crystals. Thus, we considered that the oxidized layer can contribute the aesthetic sensuousness to TNTZ sample and the layer is able to be prepared by a simple heat treatment on the sample surface even if it has a complex shape.

The aim of the present work was to prepare white-coloured layer by oxidization of TNTZ surfaces using a simple dry method, that is, heating TNTZ sample in air, and to evaluate its cell compatibility, particularly initial cell adhesion and proliferation, by *in vitro* test, using CP Ti or TiO_2 as a comparative sample. Initial cell adhesion to substrates has been reported to influence subsequent cell events, such as proliferation, differentiation, and mineralization (in case of osteoblastic cells) [9]. The adhesion is influenced by substrate's surface properties, such as chemical component, wettability, roughness (nano~micro), and topography, [9–14]. TNTZ has already been found to be excellent tissue-compatible by the results of *in vivo* tests [1, 2]. The oxidized

layer was required to be tissue-compatible as well as or better than TNTZ for the dental application, while the aforementioned surface properties would be changed from as-prepared one. In the present work, the initial adhesion, spreading, and proliferation of mouse osteoblast-like cell (MC3T3-E1 cell) on the oxidized layer on TNTZ and CP Ti were assessed and discussed with the layer's properties.

2. Materials and Methods

2.1. Sample Preparation. Hot rolled Ti-29Nb-13Ta-4.6Zr bars with a diameter of 10 mm were used as a substrate material. A solution treatment was done for the prepared TNTZ bar; that is, the material was heated to 795°C with a rate of temperature rising of 50°C·min^{-1} and then to 800°C with the rate of 1°C·min^{-1} and kept for 3 hr at 800°C in Ar gas with an electrical furnace. TNTZ discs with 10 mm in diameter and 0.2 mm in thickness were prepared from the bar using a cutter (Accutom-50, Marumoto Struers, Japan) followed by polishing with an emery cloth (number 1500). To prepare an oxidized layer on the discs, they were set on an Al_2O_3 board, heated in air using an electrical furnace to 900 or 1000°C with a rate of temperature rising of 5°C·min^{-1}, and kept at each temperature for 0.5 or 1 hr. Ti (CP Ti) plate with the dimension of $10 \times 10 \times 0.3$ mm was polished and heated at 1000°C for 1 hr by the same conditions as those for TNTZ.

2.2. Material Characterization. Spectral reflectance of the sample surface was measured with a spectrophotometric

(a)

(b)

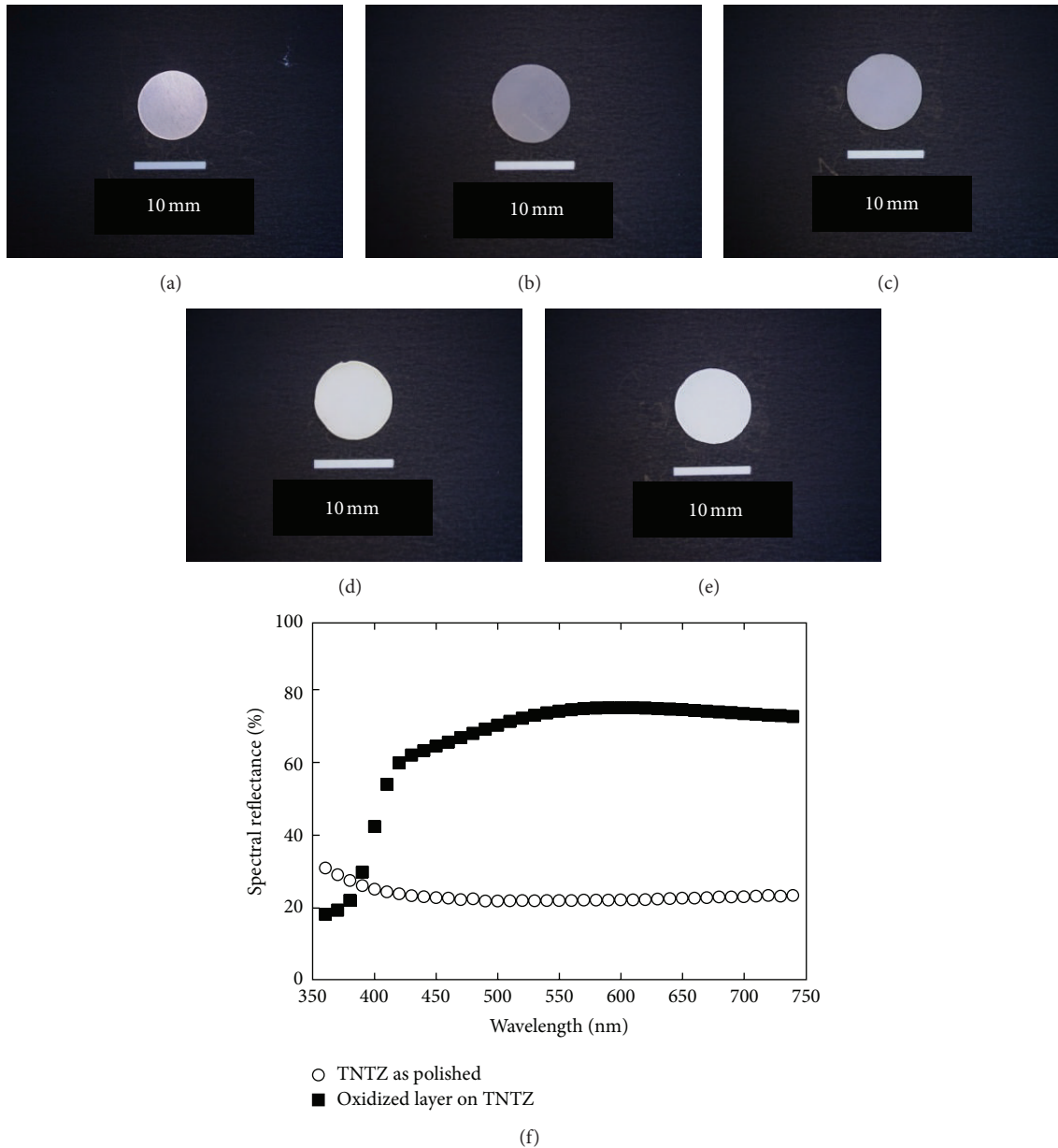(c)

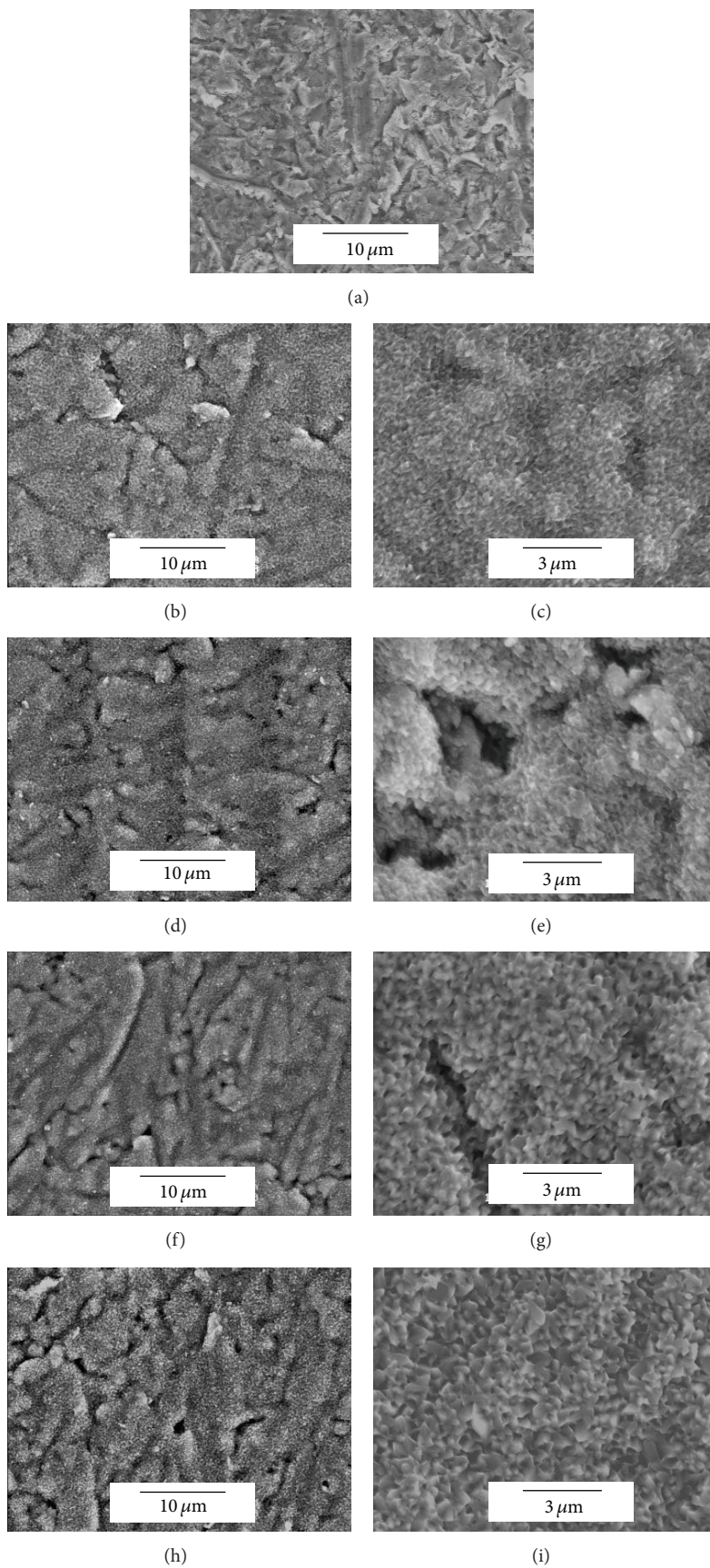(d)

(e)

(f)

(g)

(h)

(i)

FIGURE 3: SEM images of TNTZ surfaces. (a) As-prepared, (b)-(c) heated at 900°C for 0.5 hr, (d)-(e) heated at 900°C for 1 hr, (f)-(g) heated at 1000°C for 0.5 hr, (h)-(i) heated at 1000°C for 1 hr, and (c)–(i) magnified images of (b)–(h).
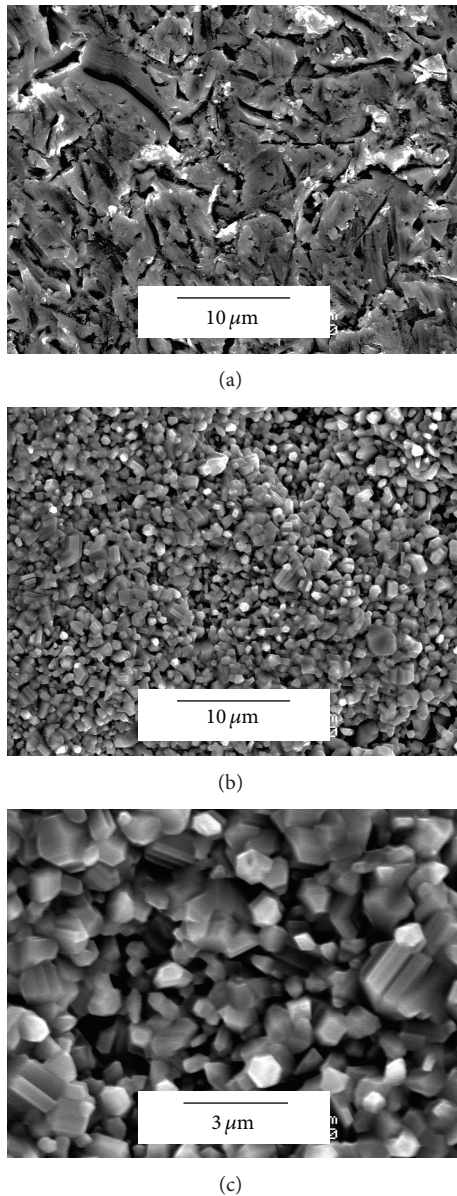
(a)

(b)

(c)

Figure 4: SEM images of CP Ti surfaces. (a) As-prepared, (b)-(c) heated at 1000°C for 1 hr, and (c) magnified image of (b).

colorimeter (CM-700, Konica Minolta). Surface morphology and cross-section of the disc were observed with scanning electron microscope (SEM, JSM-6301F, JEOL, Japan) incorporating an energy dispersive spectrometer (EDS) after coating the samples with amorphous osmium layer using a vapor deposition method (Neoc, Meiwafosis Co. Ltd., Japan). The cross-section of the samples was observed by mounting in methyl methacrylate (Technovit 4004, Okenshoji Co., Ltd., Japan) and then cut by a diamond saw. The cross-section of the samples was polished, coated with amorphous osmium, and then observed by SEM. Surface roughness was measured with a roughness measure (Surftest 401, Mitutoyo, Japan) followed by calculating an average roughness (Ra). X-ray diffractometry (XRD) was performed on the PANalytical

(Holland) X'pert-MPD using a step size of 2θ: 0.017° with Cu Kα radiation, at 45 kV and 40 mA, with a count rate of 15 sec per step, from 2θ values of 15° to 60°. Wettability measurement was performed with a contact angle meter (DM 300, Kyowa, Japan). 10 samples were used for the measurement.

2.3. Ion Release and Cell Compatibility. The discs for cell culture tests were sterilized by heat treatment at 180°C for 1.5 hr and then placed in a 24-well plate. The culture medium used was αMEM containing 10% fetal bovine serum (FBS). 1 mL of αMEM was added to each well followed by incubation at 37°C in a humidified atmosphere of 95% air, 5% CO$_2$ for 7 days. The culture medium was changed after 1 day of incubation and then changed every other day. Ion concentration (Ti, Nb, Ta, and Zr) in the replaced medium was measured by inductively coupled plasma atomic emission spectroscopy (ICP-AES, ICPS-500, Shimadzu, Japan). Three samples of each sample were tested.

MC3T3-E1 cells were seeded on the disc placed in a 24-well plate at a density of 50,000 cells/well and then incubated at 37°C in a humidified atmosphere of 95% air, 5% CO$_2$ for 1 day. SEM was used to monitor cell attachment and morphology. The discs after culturing were rinsed twice with phosphate buffered saline (PBS). The cells were fixed in 2.5% glutaraldehyde for 40 min at 4°C. The cells were dehydrated through a series of increasing concentrations of ethanol and dried using hexamethyldisilazane (HMDS). Samples were coated with amorphous osmium and observed with SEM. The GNU image manipulation program (GIMP2) and ImageJ software were used to calculate an individual cell area on each sample. The cell proliferation was examined after culturing for 5 days. The culture condition was aforementioned. The cell number on the sample was measured with a microplate reader (SUNRISE Remote, TECAN, Switzerland) using a Cell Counting Kit-8 (Dojindo, Japan), following its instruction. The number was counted by measuring the absorbance of the resulting medium at 450 nm. Results represent the mean values of three samples. Thermanox was used as a control sample. Differences between groups were determined by Student t-test with values of $P < 0.05$ considered statistically significant.

3. Results and Discussion

3.1. Surface Characterization. Figures 1(a)~1(e) show appearances of TNTZ before and after the heat treatments. The samples heat-treated at 1000°C exhibited white colour, while that heat-treated at 900°C showed gray colour. The results of colorimeter analysis followed this; Figure 1(f) is a typical spectral reflectance of the TNTZ before and after the heattreatment at 1000°C for 0.5 hr against wavelength within the range of visible light (400–800 nm). Reflectance value of the oxidized surface was within 60–80% in the entire visible light range, whereas the metal surface was around 20%. Generally, the higher the reflectance, the higher brightness can be obtained. Thus, the oxidized layer is much brighter than the metal surface. In addition, reflectance curve of the

(a)

(b)

(c)

(d)
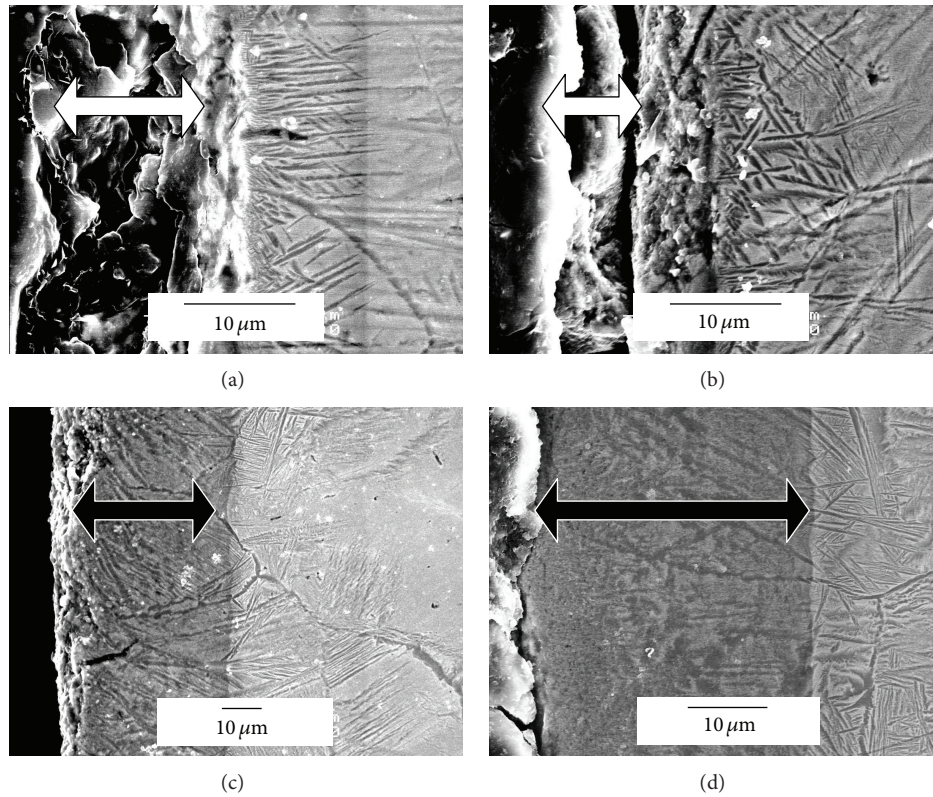
FIGURE 5: Cross-sectional SEM images of TNTZ. (a) Heated at 900°C for 0.5 hr, (b) heated at 900°C for 1 hr, (c) heated at 1000°C for 0.5 hr, and (d) heated at 1000°C for 1 hr. Black arrow: oxidized layer. White arrow: gap formed after the elimination of oxidized layer through sample preparation.

oxidized surface was smooth convex upward and the maximum reflectance appeared at around 550~600 nm, where it includes wavelength component of green-yellow-orange colour. This indicates that oxidized surface colour is slightly yellowish white.

XRD patterns (Figure 2) demonstrated that the oxidized layers were formed on TNTZ and CP Ti samples after the heat treatments. The oxidized layers formed on TNTZ consisted of TiO_2 (rutile), $TiNb_2O_7$, and $TiTa_2O_7$. The peak intensities corresponding to these oxidized phases increased with the increase in the treatment temperature and time; especially no β-Ti peak, which comes from the original TNTZ, was observed on the patterns of the samples heated at 1000°C. This should be due to the change in the oxidized layer thickness. TiO_2 (rutile) was predominantly formed on CP Ti after the heat treatment at 1000°C for 1 hr. It is difficult to identify $TiTa_2O_7$ phase formation on TNTZ by XRD, since both $TiNb_2O_7$ and $TiTa_2O_7$ have similar crystal structure and Ta amount in the alloy is small. However, Ta was not detected by EDS in the oxidized layer. Thus, we are in doubt about $TiTa_2O_7$ formation. If any, Ta could exist as $Ti(Nb, Ta)_2O_7$ phase since Nb and Ta form complete solid solution [15].

Figure 3 shows SEM images of TNTZ surfaces before and after the heat treatments. Linear grooves with ~1 μm in size formed by polishing were observed on all samples. Particles with several hundreds nm in size were formed on the whole surface (in the grooves as well) of all samples after

the heat treatment. Their sizes increased with the increase in the treatment temperature and time. As shown in Figure 4, in the case of CP Ti sample, rod-shaped particles with ~1 μm in size were formed on the whole surface after the heat treatment at 1000°C for 1 hr. The difference in the particle size between TNTZ and CP Ti was contributed by chemical components; $TiNb_2O_7$ and $TiTa_2O_7$ precipitation suppressed the growth of main phase (rutile) during the heat treatment in the case of TNTZ.

The cross-sectional SEM images (Figure 5) demonstrated that the oxidized layers remained on the TNTZ substrate heat-treated at 1000°C, while they were eliminated from the surfaces heat-treated at 900°C through the sample preparation for the SEM observation. The reason why the layers on the samples heat-treated at 900°C were eliminated was unclear; however, thermal stress at the interface due to difference in their coefficients of thermal expansion is probably concerned with it. On the other hand, the elimination was suggested to be caused by the processing of SEM observation, such as cutting, polishing, and keeping in vacuum. In any case, the oxidized layer formed by the heat-treatment at 1000°C was found to possess better adhesion than that formed at 900°C. Elimination behavior of the oxidized layer during oxidation, its bonding strength, and hardness will be discussed in another paper. The oxidized layer thicknesses were found to be ~10 μm for the samples heat-treated at 900°C and ~30 μm for one heat-treated at 1000°C, respectively.

(a)

(b)

(c)

(d)

(e)
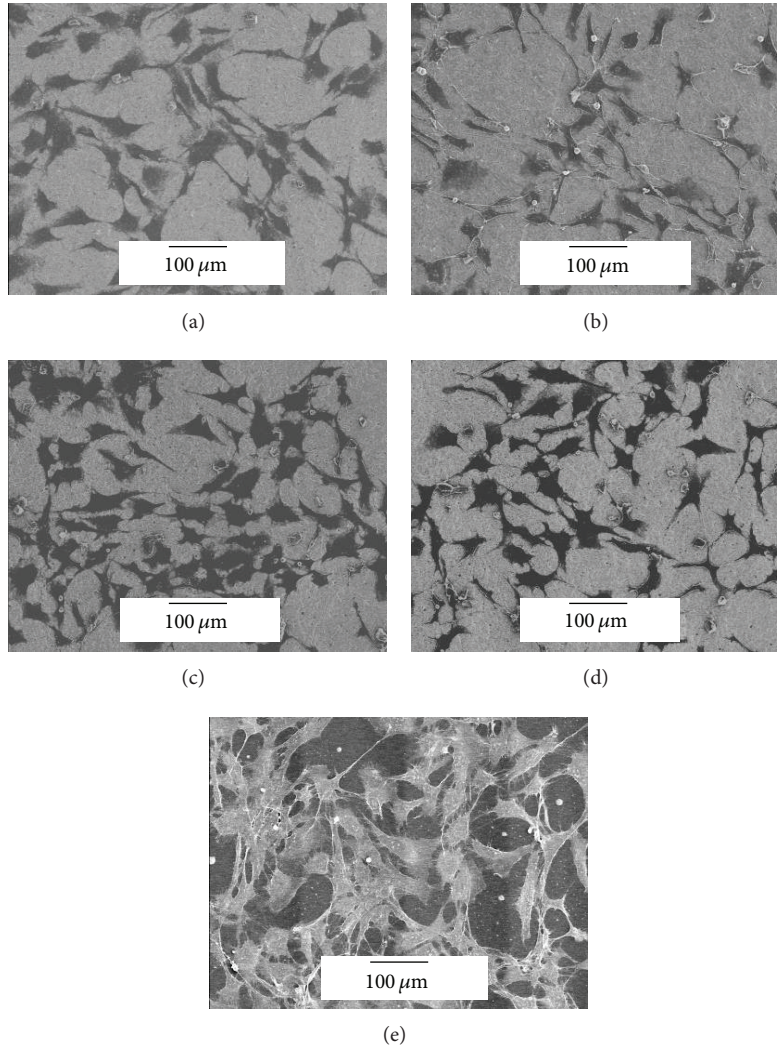
FIGURE 6: SEM images of cells cultured on TNTZ or CP Ti surfaces. (a) As-prepared TNTZ, (b) as-prepared CP Ti, (c) TNTZ heated at 1000°C for 1 hr, (d) CP Ti heated at 1000°C for 1 hr, and (e) control sample (Thermanox).

This difference in the layer thickness may contribute to the change in the appearance colour (Figure 1). Thus, TNTZ heat-treated at 1000°C for 1 hr was used for the subsequent surface characterization and cell culture tests.

Table 1 shows the surface properties, average roughness, and wettability of TNTZ and CP Ti samples before and after the heat treatment at 1000°C for 1 hr. The roughness increased and the contact angle decreased after the heat treatment in both cases of TNTZ and CP Ti. It was reported that contact angle of rutile powder was about 4~5° [16]. The increased wettability may be due to the increased roughness and TiO_2 contained in the oxidized layer. Surface wettability largely depends on surface energy [17]. According to the literatures [18], hydrophilic Ti has higher surface energy than the hydrophobic one and resulted in more rapid cell activation and differentiation.

3.2. Cell Attachment and Morphology. Some metallic ions released from implant materials have been reported to

TABLE 1: Average roughness (Ra) and wettability of TNTZ and CP Ti before and after heat treatment.

Sample	Ra (μm)	Contact angle (°)
TNTZ	0.62	53.7
CP Ti	0.58	50.3
Heat-treated TNTZ (1000°C 1 hr)	1.97	3.7
Heat-treated CP Ti (1000°C 1 hr)	1.74	5.9

influence cell functions [19–22]. The results of ICP-AES demonstrated that no ions were released from the heat-treated TNTZ in the cell culture medium. The SEM images of the cells (Figure 6) demonstrated that they spread on all sample surfaces in 1-day culture and possessed spindle and branched shapes. More spindle-shaped cells were observed on as-prepared CP Ti surface than the other samples. Figure 7 shows the individual cell area calculated using the SEM images. The area of TNTZ was larger than that of CP Ti
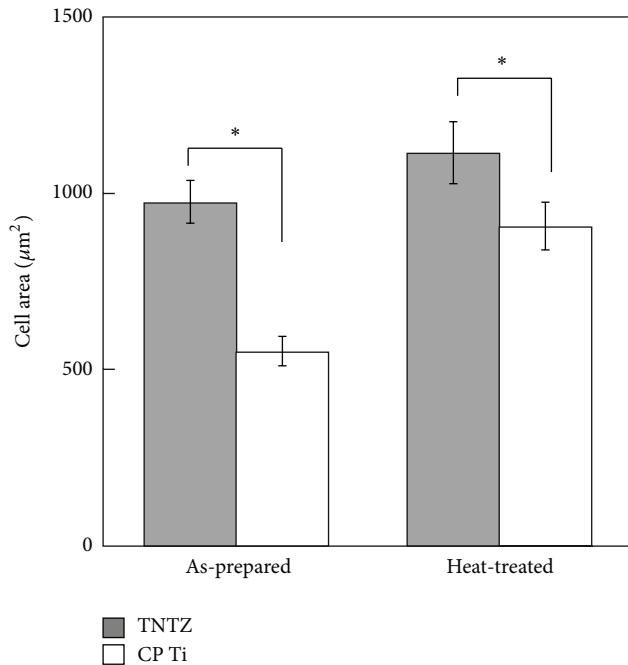
FIGURE 7: Individual cell area after culturing on TNTZ or CP Ti surface for 1 day. Heat treatment condition: 1000°C, 1 hr.
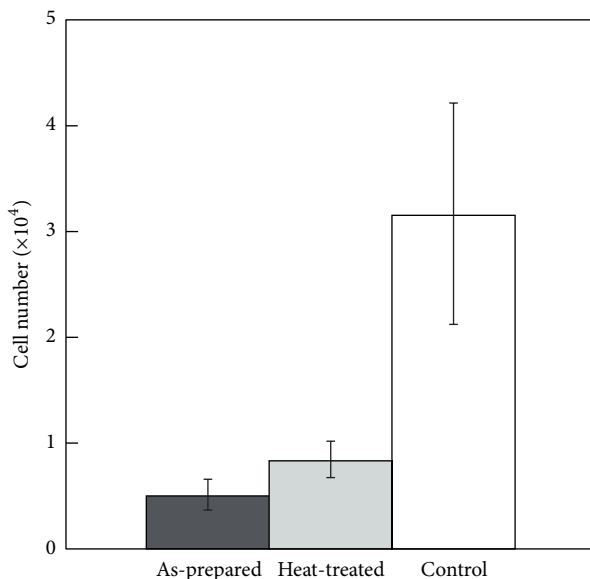
FIGURE 8: Live cell numbers on TNTZ samples after 5-day culture. Control: Thermanox. Heat treatment condition: 1000°C, 1 hr.

regardless of the heat treatment for the samples, which indicates that the cells will spread on TNTZ. The area of the heat-treated samples was larger than that of the as-prepared one in both cases of TNTZ and CP Ti samples, while there was no significant difference in the values in the case of TNTZ. The cells on TNTZ surface maintained higher performance than that on CP Ti even after the oxidized layer coating. Figure 8 shows the live cell numbers on TNTZ samples after 5-day culture. The number of the heat-treated sample

was slightly larger, while there was no significant difference in the numbers between the as-prepared and heat-treated samples. Hence, there was no deterioration in the *in vitro* cell compatibility of TNTZ after the oxidized layer coating by the heat treatment. In future work, human osteogenic cells will be used for the cell compatibility test instead of MC3T3-E1 cells to simulate *in vivo* conditions better.

The slight increase in the cell spreading area (Figure 7) and the live cell number (Figure 8) on the heat-treated samples may be due to their larger roughness and higher wettability. The cell morphology and cytoskeletal formation have been reported to relate to subsequent events, such as proliferation and differentiation [9–14]. This could be regulated by the activity and interaction of protein associated with cytoskeleton and focal adhesion. For example, the adsorption of fibronectin, which is one of extracellular matrix proteins, was reported to be favoured on hydrophobic surfaces and influenced by the substrate surface roughness [11]. Changes in cell morphology were reported to be significant in the regulation of the Hippo pathway which plays an important role in regulation of cell proliferation [23]. Stress fibers inhibit the Hippo pathway upstream of or at Lats which is one of the protein kinases in cell membrane, resulting in the upregulation of cell proliferation. The flat and spread morphology of cells promotes the formation of stress fibers (F-actin). The cell activity on the oxidized layer formed on TNTZ will be investigated in detail in future work.

4. Conclusion

The white-coloured coating consisting of the oxidized layer was prepared on TNTZ discs by heat treatment in air to achieve the formation of aesthetic surface on them for dental application. TNTZ has excellent mechanical properties and biocompatibility. The oxidized layer formed by the heat treatment at 1000°C was white-coloured and joined to TNTZ substrate more strongly than that formed by the treatment at 900°C. The particles with the size of several hundreds nm containing TiO_2 (rutile), $TiNb_2O_7$, and $TiTa_2O_7$ were formed during the treatment. The layer thickness was ~30 μm for the sample heat-treated at 1000°C. The surface average roughness and the wettability increased after the heat treatment. The spreading and proliferation level of MC3T3-E1 cells on the heat-treated sample were almost the same as those on as-prepared one. Hence, there was no deterioration in the *in vitro* cell compatibility of TNTZ after the oxidized layer coating by the simple heat treatment.

Conflict of Interests

No potential conflict of interests was disclosed.

Acknowledgment

References

[1] M. Niinomi, T. Hattori, K. Morikawa et al., "Development of low rigidity β-type titanium alloy for biomedical applications," *Materials Transactions*, vol. 43, no. 12, pp. 2970–2977, 2002.

[2] M. Niinomi, M. Nakai, and J. Hieda, "Development of new metallic alloys for biomedical applications," *Acta Biomaterialia*, vol. 8, no. 11, pp. 3888–3903, 2012.

[3] T. Hanawa, "Research and development of metals for medical devices based on clinical needs," *Science and Technology of Advanced Materials*, vol. 13, no. 6, Article ID 064102, 2012.

[4] C. Veiga, J. P. Davim, and A. J. R. Loureiro, "Properties and applications of titanium alloys: a brief review," *Reviews on Advanced Materials Science*, vol. 32, no. 2, pp. 133–148, 2012.

[5] K. Kuroda and M. Okido, "Hydroxyapatite coating of titanium implants using hydroprocessing and evaluation of their osteoconductivity," *Bioinorganic Chemistry and Applications*, vol. 2012, Article ID 730693, 2012.

[6] Y. C. Tsui, C. Doyle, and T. W. Clyne, "Plasma sprayed hydroxyapatite coatings on titanium substrates. Part 1: mechanical properties and residual stress levels," *Biomaterials*, vol. 19, no. 22, pp. 2015–2029, 1998.

[7] T. Kasuga, M. Nogami, M. Niinomi, and T. Hattori, "Bioactive calcium phosphate invert glass-ceramic coating on β-type Ti-29Nb-13Ta-4.6Zr alloy," *Biomaterials*, vol. 24, no. 2, pp. 283–290, 2003.

[8] T. Kasuga, M. Nogami, and M. Niinomi, "Joining of calcium phosphate invert glass-ceramics on a β-type titanium alloy," *Journal of the American Ceramic Society*, vol. 86, no. 6, pp. 1031–1033, 2003.

[9] S. Lavenus, P. Pilet, J. Guicheux, P. Weiss, G. Louarn, and P. Layrolle, "Behaviour of mesenchymal stem cells, fibroblasts and osteoblasts on smooth surfaces," *Acta Biomaterialia*, vol. 7, no. 4, pp. 1525–1534, 2011.

[10] S. Faghihi, F. Azari, A. P. Zhilyaev, J. A. Szpunar, H. Vali, and M. Tabrizian, "Cellular and molecular interactions between MC3T3-E1 pre-osteoblasts and nanostructured titanium produced by high-pressure torsion," *Biomaterials*, vol. 28, no. 27, pp. 3887–3895, 2007.

[11] G. Zhao, A. L. Raines, M. Wieland, Z. Schwartz, and B. D. Boyan, "Requirement for both micron- and submicron scale structure for synergistic responses of osteoblasts to substrate surface energy and topography," *Biomaterials*, vol. 28, no. 18, pp. 2821–2829, 2007.

[12] H. M. Kowalczyńska and M. Nowak-Wyrzykowska, "Modulation of adhesion, spreading and cytoskeleton organization of 3T3 fibroblasts by sulfonic groups present on polymer surfaces," *Cell Biology International*, vol. 27, no. 2, pp. 101–114, 2003.

[13] A. Diener, B. Nebe, F. Lüthen et al., "Control of focal adhesion dynamics by material surface characteristics," *Biomaterials*, vol. 26, no. 4, pp. 383–392, 2005.

[14] A. Okumura, M. Goto, T. Goto et al., "Substrate affects the initial attachment and subsequent behavior of human osteoblastic cells (Saos-2)," *Biomaterials*, vol. 22, no. 16, pp. 2263–2271, 2001.

[15] T. B. Massalski, J. L. Murray, L. H. Bennett, and H. Baker, *Binary Alloy Phase Diagram*, 2nd edition, 1986.

[16] T. Mitsui and S. Takada, "On factors influencing dispersibility and wettability of powder in water," *Journal of the Society of Cosmetic Chemists*, vol. 20, pp. 335–351, 1969.

[17] D. V. Kilpadi and J. E. Lemons, "Surface energy characterization of unalloyed titanium implants," *Journal of Biomedical Materials Research*, vol. 28, no. 12, pp. 1419–1425, 1994.

[18] C. Eriksson, H. Nygren, and K. Ohlson, "Implantation of hydrophilic and hydrophobic titanium discs in rat tibia: cellular reactions on the surfaces during the first 3 weeks in bone," *Biomaterials*, vol. 25, no. 19, pp. 4759–4766, 2004.

[19] A. Yamamoto, R. Honma, and M. Sumita, "Cytotoxicity evaluation of 43 metal salts using murine fibroblasts and osteoblastic cells," *Journal of Biomedical Materials Research*, vol. 39, no. 2, pp. 331–340, 1998.

[20] M. Ikeuchi, A. Ito, Y. Dohi et al., "Osteogenic differentiation of cultured rat and human bone marrow cells on the surface of zinc-releasing calcium phosphate ceramics," *Journal of Biomedical Materials Research A*, vol. 67, no. 4, pp. 1115–1122, 2003.

[21] X. Wang, L. Yuan, J. Huang, T.-L. Zhang, and K. Wang, "Lanthanum enhances in vitro osteoblast differentiation via pertussis toxin-sensitive Gi protein and ERK signaling pathway," *Journal of Cellular Biochemistry*, vol. 105, no. 5, pp. 1307–1315, 2008.

[22] A. Hoppe, N. S. Güldal, and A. R. Boccaccini, "A review of the biological response to ionic dissolution products from bioactive glasses and glass-ceramics," *Biomaterials*, vol. 32, no. 11, pp. 2757–2774, 2011.

[23] K.-I. Wada, K. Itoga, T. Okano, S. Yonemura, and H. Sasaki, "Hippo pathway regulation by cell morphology and stress fibers," *Development*, vol. 138, no. 18, pp. 3907–3914, 2011.

Research Article

Interpenetrating Polymer Network Hydrogels Based on Gelatin and PVA by Biocompatible Approaches: Synthesis and Characterization

Eltjani-Eltahir Hago[1] and Xinsong Li[2]

[1] *Department of Chemistry and Chemical Engineering, Southeast University, Nanjing 210096, China*
[2] *School of Chemistry and Chemical Engineering, Southeast University, Nanjing 211189, China*

Correspondence should be addressed to Eltjani-Eltahir Hago; eltjanihago@gmail.com

In this work, a new approach was introduced to prepare interpenetrating polymer network PVA/GE hydrogels by cross-linking of various concentration gelatin in the presence of transglutaminase enzyme by using the freezing-thawing cycles technique. The effects of freezing-thawing cycles on the properties of morphological characterization, gel fraction, swelling, mechanical, and MTT assay were investigated. The IPN PVA/GE hydrogels showed excellent physical and mechanical Properties. MTT assay data and the fibroblasts culture also showed excellent biocompatibility and good proliferation. This indicates that the IPN hydrogels are stable enough for various biomedical applications.

1. Introduction

Polyvinyl alcohol (PVA) hydrogels are a gel polymer known for the quality of biocompatibility that have been used in many biomedical applications, for example, as implants [1], artificial devices [2], contact lenses [3], drug delivery devices [4], and also wound dressings [5–7]. The following methods were used on a large scale: chemical cross-linking [8]; glutaraldehyde as the cross-linking agent [9]; cross-linking through γ radiation [10, 11], ultraviolet radiation [12], and by using cycles of freezing-thawing of successive [13, 14]. The last one is very convenient and biocompatible, while the molecular bonds (hydrogen bonds), which form through the freezing-thawing process of aqueous solutions of PVA, act as an efficient crosslinks [15].

The extent of poly(vinyl alcohol) (PVA) hydrogels for various biomedical applications has been realized because of their excellent biocompatibility and chemical stability. The freezing-thawing techniques used in the preparation of the PVA hydrogels showed good mechanical strength and have been examined for use as intervertebrate disk intended [16], artificial meniscus [17], and a contact lens [18, 19]. However, manufactured polymers, due to the lack of bioactive moieties, have no biological activity compared with natural polymers. The concept of integrating artificial materials with cell locations approved sites of naturally derived materials is very attractive. To achieve this result, efforts were made to incorporate cell adhesion of synthetic biomaterials [20].

Gelatin (GE) is a protein produced by partial denaturalization of collagen extracted from the bones, connective tissues, organs, and some intestines of animals such as domesticated cattle, porcine, and horses. Gelatin presents biological activities because of the natural origin, which makes it suitable for use of an ingredient of wound dressing, scaffolds for tissue engineering, and drug delivery carriers. Gelatin hydrogels are common for the applications in medical areas [21]. Hydrogels are insoluble hydrophilic polymers having a high-water content and tissue like mechanical properties that make them highly attractive scaffolds for implantation in empty tubular nerve prosthesis or for direct injection at the lesion site to enhance cell attachment and growth. Gelatin hydrogels have often crossed-linked by chemical approach using crosslinks, such as glutaraldehyde, to improve elasticity, consistency, and stability. However, the chemical cross-linker may lead to toxic effect on physiological environment, due to the presence of residual crosslinks. Therefore, it is highly

demanded to develop biocompatible mild cross-linking methods to prepare hydrogels [20].

Transglutaminases are widely distributed in various organisms, including vertebrates, invertebrates, plants, and microorganism, and are reportedly responsible for certain biological events such as epidermal keratinization, blood coagulation, and regulation of erythrocyte membranes. A microbial transglutaminase isolated from the culture medium of *Streptoverticillium mobaraense* has become commercially available [22]. Unlike TGases from many sources, the mTG possesses many features, including Ca^{2+} independence, a broader substrate specificity for acyl donors, a smaller molecule size, and a higher reaction rate, which makes them suitable for industrial applications. Currently, this mTG has been successfully applied in the food industry for improving the physical properties and texture of protein-related foods [23]. More recently, the use of mTG to modify gelatin has also been reported [24, 25]. The enzymatic cross-linking is a biocompatible approach to enhance the mechanical properties of gelatin hydrogels. An interpenetrating polymer network (IPN) is a composite of polymers, exhibiting varied characteristics, which is obtained when one polymer network is synthesized or cross-linked independently in the instantaneous presence on the other [26]. The IPN is a combination of at least two polymer chains each in network form, which is synthesized and/or cross-linked in the immediate presence on the other without any covalent bonds between them [27] or the two or more networks can be envisioned to be entangled in such a way that they are concatenated and cannot be pulled apart but not bonded to each other by any chemical bond [28]. Many researchers have been focusing on the development of polymer blends with IPN structure. Recently, hydrogels with IPN structure have attracted much attention because of their potential application in the biomedical area. Kurokawa et al. invented double network hydrogels with superior toughness [29].

In this paper, a new approach was introduced to prepare interpenetrating polymer network PVA/GE hydrogels by a combination of enzymatic and physical methods, used freezing-thawing process, and in situ with synthesis of gelatin/mTG in PVA solution. The influence on the contents and dispersed condition of gelatin in PVA matrixes on the hydrogels mechanical strength was investigated in order to obtain applicable hydrogels. The morphology and crystalline structures of interpenetrating polymer network PVA/GE were also observed by some experimental analysis techniques, such as scanning electronic microscope (SEM). Moreover, in order to understand the initial behavior of fibroblasts cells, proliferation was assessed in vitro using fibroblast like L 929 cell culture.

2. Experimental

2.1. Materials. PVA with a degree of polymerization of 1750 ± 50 and hydrolysis degree values of greater than 99% was purchased from Beijing Organic Chemical Plant, China. Gelatin (GE) (type A, 300 bloom from porcine) was obtained

Table 1: Composition of IPN PVA/GE hydrogels.

Hydrogels	IPN-1	IPN-2	IPN-3	IPN-4
Gelatin %w/v	0	2	5	7
PVA %w/v	15	15	15	15

The concentration of mTG at a range of 5–20 U/mL.

(Sigma-Aldrich, St. Louis, MO, USA). The source of transglutaminase was the commercial product obtained from Yiming Biological Products Co., Ltd. (Jiangsu, China). As determined by a colorimetric hydroxamate method [30], the enzyme activity of mTG was 102 (U/g) of powder. All other regents used in the paper were of analytical grade.

2.2. Moisture Determination of Gelatin. In order to know the accurate concentration of the gelatin solution prepared subsequently, it is necessary to know the moisture content of the gelatin. The moisture of gelatin was determined according to Chinese standards GB/T 5009.3-2003 [31].

2.3. Preparation of Gelatin and mTG Blends. A concentrated gelatin solution was prepared by adding 50 gm of gelatin to 100 mL of warm deionized water and mixing at 50°C until the protein was dissolved. Aliquots from this concentrated gelatin solution were then mixed with deionized water to prepare solutions with differing gelatin concentrations (0%, 2%, 5%, and 7% w/v). The gelatin solutions were stored at 4°C. A concentrated enzyme solution was prepared for each experiment by mixing 0.5 gm of mTG per 5 mL of deionized water at room temperature. This enzyme solution was stored at 4°C until it was ready for use.

2.4. Preparation of IPN PVA/Gelatin Hydrogels. IPN PVA/GE hydrogels were prepared by cyclic freezing-thawing method. For this purpose, aqueous solutions containing 15% by weight PVA with different amounts of gelatin, (i.e., 0%, 2%, 5%, and 7%) by weight, were used. The (15% w/v) of PVA solution was prepared at 95°C. A varying amount of solution's gelatin and mTG was mixed slowly to the PVA solution at room temperature to induce cross-linking. The mixture was cast between glass slides with 3 mm thick spacers then incubated at 45°C for 4 h to achieve complete cross-linking. Then, they were physically cross-linked by three freeze-thaw cycles, which consisted of freezing at −20°C for 24 h and thawing at room temperature 21°C for 24 h, respectively, to produce IPN hydrogels. The IPN hydrogels films had a thickness of 3 mm. Table 1 shows the composition of IPN PVA/GE hydrogels.

2.5. Morphological Characterization. For morphological characterization, hydrogels after swelling (equilibrium) in water were freeze-dried using a freeze drier (Christ, Germany, Alpha 1-2) at −52°C for 12 h. Transverse sections were cut from freeze-dried film samples using a cold knife. Samples were then examined by a scanning electron microscope (SEM JSM-6360LV, a voltage of 20 KV, China). The working face of the samples was sprayed with gold in advance. The observed morphologies for each SEM fractograph were analyzed using

Sigma Scan Pro software. Quantitative analysis of the pore size was obtained from structural indices measured from scaffold samples. The density of the solid material (film) was calculated according to the mass fractions (M_x where x refers to the constituent material) and densities of the constituent materials (ρ_x), by assuming that the total mass and volume remain the same before and after reaction [32], using (1)

$$\rho_s = \left[\frac{(M_{PVA} + M_{GE} + M_{mTG})}{[(M_{PVA}/\rho_{PVA}) + (M_{GE}/\rho_{GE}) + (M_{mTG}/\rho_{mTG})]} \right]. \quad (1)$$

2.6. Gel Fraction.
The weight ratio of the dried hydrangeas in rinsed and unrinsed conditions or gel fraction can be assumed as an index of the degree of cross-linking. Therefore, the gel fraction of samples can be calculated as follows (2):

$$\text{Gel fraction (\%)} = \left(\frac{W_f}{W_i} \right) \times 100, \quad (2)$$

where W_f and W_i are the weights of the dried hydrogel after and before rinsing and extraction. To perform gel fraction measurement, preweighed slice of each sample was dried under vacuum at room temperature until observing no change in its mass. Nearly identical weight of another slice of the same sample was immersed into excess of distilled water for 4 days to rinse away amorphous or soluble part. Subsequently, the immersed sample was removed from distilled water and dried at room temperature under vacuum until the dried mass showed constant weight.

2.7. Equilibrium Degree of Swelling and Equilibrium Water Content.
For swelling experiments, the vacuum-dried films were immersed in excess distilled water at room temperature ($\sim 30^\circ$C) until reaching to an equilibrium state. Then, the swelled samples were withdrawn from distilled water and weighed after gentle surface wiping using absorbent paper. The equilibrium degree of swelling (EDS) and equilibrium water contents (EWC) were calculated, respectively, as follows [33]:

$$
\begin{aligned}
\text{EDS (\%)} &= \left[\frac{(W_s - W_d)}{W_d} \right] \times 100, \\
\text{EWC (\%)} &= \left[\frac{(W_s - W_d)}{W_s} \right] \times 100,
\end{aligned}
\quad (3)
$$

where W_s is the swollen weight of the sample of the equilibrium state and W_d is the final dry weight of the extracted sample.

2.8. Mechanical Properties.
The samples were cut into a slice shape with a thickness of 3 mm and their mechanical properties, including tensile strength at break, were determined. The mechanical properties were measured at a temperature of 17°C and humidity of 60%, at a crosshead speed of 50.000 (mm/min) using Instron tester—4466, type: 42/43/4400. The elastic moduli of the IPN PVA/GE hydrogels were determined by performing constant strain-rate compression measurements on an Instron 4466 mechanical tester at room

temperature. The hydrogel sample, 15 mm in diameter and 10 mm in height, was tested at a rate of 5.000 (pts/secs) and humidity of 40%, at a crosshead speed of 1.5000 mm/min. The results are expressed as mean value ± standard deviation with the confidence level of 95%.

2.9. Cell Viability Assay.
Cellular survivability evaluation against cross-linked PVA, GE, and IPN PVA/GE blend has been evaluated by MTT (3-[4,[5-dimethylthiazol-2-yl]-2,5-diphenyl tetrazolium bromide) assay [34]. This standard test method is based on exposing L929 cells to the fluid extract of the test materials and control materials. The extract solution of the PVA, GE, or cross-linked IPN PVA/GE blend was prepared according to the protocol as outlined in ISO 10993 [35]. In brief, to determine the cytotoxicity of osteoblast-like L929 cells on the IPN hydrogels samples, samples were incubated with DMEM media at 37°C for 72 h in an incubator. The extract solutions were diluted serially with the media (0%, 12.5%, 25%, 50%, and 100%). For the control, 100% media were used to compare among the dilution, and then, 200 mL of extracting and diluted solution was added in a 96-well plate. The 96-well plate was previously (24 h before adding the extract solutions) incubated and coated with fibroblasts cells (1×10^4 cells/well). The plate was then incubated in a CO_2 incubator at 37°C for 1 day, 3 days, and 5 days. In MTT, assay cell survivability is measured through the production of purple colors by the reaction of dehydrogenase enzymes of living cells and MTT. Metabolically active and viable cells produce mitochondrial dehydrogenase enzymes during incubation in media, which can be read out through the change of color intensity by a spectrophotometer. The optical density (OD) corresponds to the viable cell numbers. Therefore, cell survival and proliferation at the different dilutions and time points were quantified by adding 100 μL of the MTT solution (20 μg/100 mL) to each of the wells. After 4 h of incubation, the OD values of the solution were measured using an BIORAD reader (Model 680, Microplate reader) at a wavelength of 595 nm.

2.10. Optical Microscope Study.
In order to observe directly whether the viable cell numbers increases after treating the osteoblast like L929 cells with sample extracts after three freezing-thawing cycles and day 5, an inverted light microscope (Olympus, 1×71) attached with LCD monitor was used. After 70–80% confluent growth in the subculture flask, cells were trypsinized (0.25% Trypsin-EDTA), detached, and counted. Approximately, 1×10^3 cells/mL media was pipette into the wells of a Microtiter plate containing 24 wells. The plate was then incubated in a CO_2 incubator (5% CO_2, 37°C) for 24 h. after seeding cells into the wells of Microtiter plates, media were removed carefully and replaced with the extract solution of the samples, and the Microtiter plate was kept back into the CO_2 incubator either for 5 days. After finishing each of the incubation periods, cell growth in the Microtiter plate was observed using an inverted light microscope.

2.11. Statistical Analysis.
All experiments were done in triplicate, and the results were expressed as mean ± SD, and the means were analyzed by one-way ANOVA at a P value of 0.05.

3. Results and Discussion

3.1. Moisture of Gelatin. The result of moisture in gelatin used in the study is 11.51%. As the gelatin solutions were prepared, the moisture content of the gelatin was taken into account.

3.2. Morphological Characterization. In applied freezing-thawing process, the structure of the PVA and PVA/GE IPN hydrogels was determined by SEM. The densities of the cross-linked IPN hydrogels containing gelatin contents from 0 wt.% to 7 wt.% were investigated by density measurement, SEM. Tables 2 and 3 show the densities of IPN PVA/gelatin-mTG films (ρ_s) calculated by (1). The density of the IPN PVA/gelatin-mTG hydrogels was found to increase monotonously with increasing the gelatin content, namely, from 1.45 Mg m^{-3} to 1.49 Mg m^{-3}. Figure 1 shows the scanning electron micrographs of transversal sections of the films after 1 (Figures 1(a1), 1(a2), 1(a3), and 1(a4))) and 3 (Figures 1(b1), 1(b2), 1(b3), and 1(b4)) freezing-thawing cycles. These micrographs show that increasing the concentration of gelatin blends and number of freezing-thawing cycles results in higher network arrangement, which leads to porous structure on the surface of IPN hydrogels. The internal porosity of samples shows significant correlation between number of freezing-thawing cycles, the chemical structure of additive and the pore size, and arrangement. Before adding the gelatin/mTG blends as modifying agent to PVA blend, the PVA hydrogel produced smooth structured films and exhibits a few irregular pores, and the morphology is not significantly changed as compared to the IPN PVA hydrogel Figures 1(a1) and 1(b1). As illustrated in Figures 1(b2), 1(b3), and 1(b4), IPN hydrogels after 3 freezing-thawing cycles shows highly irregular porous structure with the large pores size in the range of 50–100 μm. Figures 1(a1) and 1(b1) after 1 and 3 cycles showed a fewer and smaller pore size in the range of 5–10 μm, as a consequence of the preparation technique. In the freeze-thaw process, pore size is in fact controlled by the size of the ice crystals, which could be adjusted by varying the rate of freezing. In Figures 1(a2), 1(a3), and 1(a4), IPN hydrogels after 1 cycle showed lower and smaller irregular porous size structure in the range of 20–40 μm than those obtained with Figures 1(b2), 1(b3), and 1(b4). More significant change in sample morphology is observed after introducing the gelatin/mTG and increased the cycles as cross-linking agent. Therefore, it might be an optimum candidate for biomedical applications. In the films produced with PVA/GE mixtures, the presence of cracks and empty spaces increased with an increasing proportion of gelatin in the mixture.

3.3. Gel Fraction. Enzymatic cross-linking of gelatin and cyclic freezing-thawing of pure PVA leads to the formation of insoluble and entangled polymeric network in the IPN PVA/GE hydrogels. A typical dependency of the gel fractions to the quantity of gelatin incorporated into hydrogels is given in Tables 2 and 3 using (2). As seen, the gel fraction of samples is increased by increasing the number of freezing-thawing cycles and amounts of gelatin up to 7 (%) by weight after (1 and 3) cycles. For example, the gel fraction of IPN hydrogel increases to 74 (%) by adding 7% weight of gelatin after three

cycles compared with the other IPN hydrogels after one cycle. On the other hand, Tables 2 and 3 exhibit a semilinear relationship between gel fraction, number of freezing-thawing cycles, and gelatin weight fraction in mixture hydrogels. The increase of the gel fraction may be attributed to the enzymatic cross-linked gelatin and the additional interactions between PVA and gelatin; besides, the bonds existed between PVA long neighboring chains induced crystallization, which caused an increase in gel fraction.

3.4. Degrees of Swelling and Water Content. In this work, the equilibrium degree of swelling (EDS) and equilibrium water content (EWC), as important swelling characteristics of hydrogels, were calculated using (3). These characteristics indicated the ability of absorption of fluids and exudates. Tables 2 and 3 demonstrate EDS and EWC of IPN PVA/GE hydrogels as a function of the amount of gelatin and the number of freezing-thawing cycles. Both parameters showed nearly similar decreasing trends by increasing the quantity of the gelatin content and the number of freezing-thawing cycles. The samples treated for three freeze-thaw cycles showed a much more swollen structure than others treated with one freeze-thaw cycle. The highly swollen hydrogel represents a high tight structure and a higher degree of cross-linking when compared with the hydrogels with lower swelling ratio. The comparison of the EDS and EWC data for the gel fraction values indicates that there is a logic relationship between these swelling characteristics and gel fraction, that is, more gel fractions lead to less EDS or EWC. Although the swelling characteristics of IPN PVA/GE hydrogels decrease due to presence of gelatin in comparison with pure PVA hydrogel, it seems that there have been high enough swelling capacity to be used as a suitable dressing even for healing exudative wounds.

3.5. Mechanical Properties. As mentioned before, the main interest in the production of IPN PVA/gelatin hydrogels is to achieve the materials with better mechanical properties. The investigated mechanical properties, that is, tensile strength, as well as strain at break were found to depend on the amount of gelatin and number of freezing-thawing cycles. As expected, cross-linking led to an improvement in the tensile strength. Based on these analyses, the composition of IPN hydrogels and three freezing-thawing cycles was considered the optimum conditions for the preparation of IPN hydrogels. The irregular arrangement within PVA hydrogel modified with gelatin/mTG after 3 freezing-thawing process (Table 3) has strong influence on mechanical properties. Independent of the enzymatic modification, the values for tensile strength of the films produced from IPN PVA/GE mixtures was significantly different varied as a function of the gelatin concentrations and number of freezing-thawing cycles in the mixture Tables 2 and 3. Table 3 shows that the highest values of compressive stress and tensile strength increases with increasing the concentration of gelatin and number of freezing-thawing cycles. It is observed that the tensile strength for pure PVA is (0.41 ± 0.07 MPa) and the elastic modulus is (0.45 ± 0.60 MPa). By addition of 2% w/v gelatin into PVA blend, the tensile strength increases to (0.66 ± 0.12 MPa)

TABLE 2: The properties of IPN PVA/GE hydrogels after one freezing-thawing cycle.

Samples	IPN-1	IPN-2	IPN-3	IPN-4
Gel fraction (%)	25 ± 1.20	36 ± 1.35	49 ± 1.50	58 ± 1.65
EDS (%)	135 ± 4.50	132 ± 3.75	130 ± 3.45	130 ± 3.50
EWC (%)	45 ± 2.00	44.5 ± 2.25	42.5 ± 2.50	42 ± 2.75
Stress (MPa)	0.11 ± 0.14	0.15 ± 0.18	0.25 ± 0.24	0.28 ± 0.22
Strain (%)	18.23 ± 4.60	25.67 ± 7.80	34.56 ± 12.90	47.78 ± 14.65
Elastic modulus (MPa)	0.35 ± 0.45	0.41 ± 0.49	0.56 ± 0.62	0.65 ± 0.64
Tensile strength (MPa)	0.30 ± 0.05	0.42 ± 0.09	0.52 ± 0.15	0.58 ± 0.19
Solid density (ρ_s) (Mg m^{-3})	1.13	1.20	1.29	1.34

TABLE 3: The properties of IPN PVA/GE hydrogels after three freezing-thawing cycles.

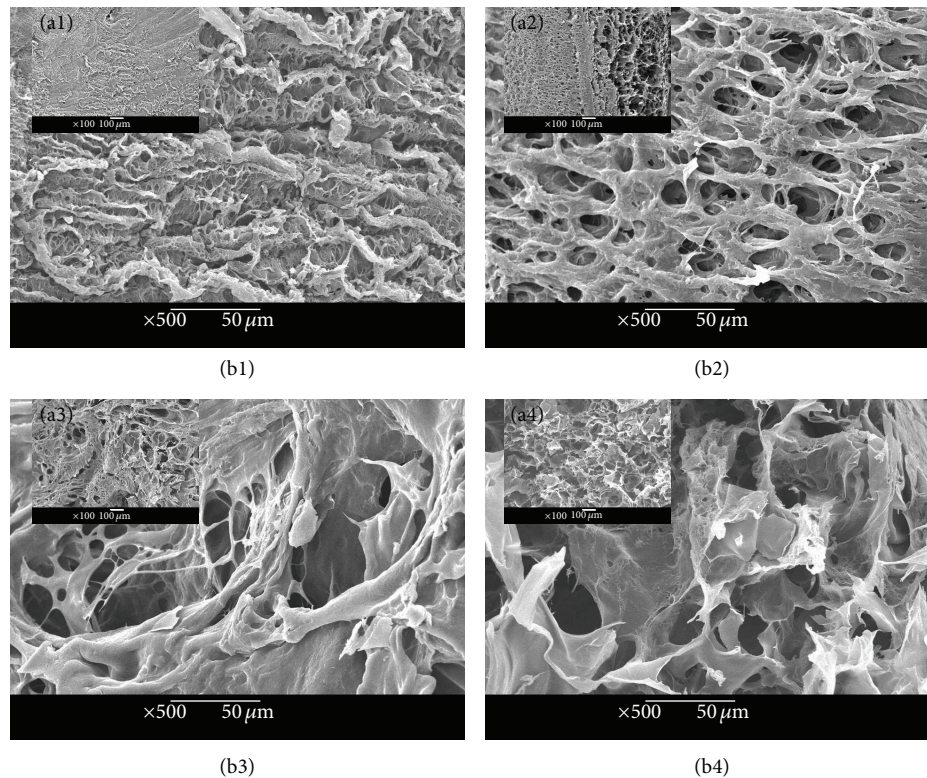| Samples	IPN-1	IPN-2	IPN-3	IPN-4
Gel fraction (%)	44 ± 1.30	58 ± 1.60	67 ± 1.70	74 ± 1.90
EDS (%)	165 ± 3.50	158 ± 3.10	149 ± 2.80	142 ± 2.40
EWC (%)	62 ± 1.98	61 ± 1.92	60 ± 1.87	59 ± 1.82
Stress (MPa)	0.25 ± 0.12	0.43 ± 0.20	0.64 ± 0.34	0.67 ± 0.38
Strain (%)	25.50 ± 6.40	31.85 ± 10.50	48.64 ± 14.00	68.70 ± 17.50
Elastic modulus (MPa)	0.45 ± 0.60	0.45 ± 0.60	0.87 ± 1.75	0.98 ± 2.45
Tensile strength (MPa)	0.41 ± 0.07	0.66 ± 0.12	0.74 ± 0.16	0.75 ± 0.18
Solid density (ρ_s) (Mg m^{-3})	1.27	1.45	1.47	1.49

FIGURE 1: SEM micrographs of the surface sections of PVA hydrogel and PVA with additives: ((a1), (b1)) IPN-1 with 15% w/v PVA; ((a2), (b2)) IPN-2 with 2% w/v gelatin; ((a3), (b3)) IPN-3 with 5% w/v gelatin; ((a4), (b4)) IPN-4 with 7% w/v gelatin; after 1 and 3 of freezing-thawing cycles, respectively. Scale bar (a1)–(a4): 100 (μm); (b1)–(b4): 50 (μm).

with an elastic modulus of (0.80 ± 1.50 MPa). The IPN hydrogels containing 7% w/v gelatin display the highest tensile strength compared to the other samples. Table 2 shows a tensile strength of (0.75 ± 0.18 MPa) and the elastic modulus is (0.98 ± 2.45 MPa). The increment of elastic modulus and tensile strength is attributed to an increase in rigidity, because the IPN hydrogels a hard inorganic component. The extraordinary asset value of strength at break for IPN hydrogels is undoubtedly due to the presence of gelatin, which shows higher gel fraction and more entangled structure in comparison with pure gel. To examine the correlation between mechanical property changes and IPN hydrogels, constant strain-rate compression tests were performed on the IPN hydrogel in order to determine their elastic moduli. Representative stress-strain curves of the IPN hydrogels are presented in Tables 2 and 3. These results displayed the ability of gelatin concentration and number of cycles to individually affect the compressive modulus of hydrogels. Based on the mechanical property results for our biocomposite IPN hydrogels which are able to attain high tensile strength, it is concluded that there is an opportunity for applications as potential candidate for scaffolds tissue engineering.

3.6. Cytotoxicity of Photocrosslinked IPN PVA/GE Hydrogels. The MTT assay, which is a rapid, standardized, sensitive, and inexpensive method to determine cell viability and proliferation or whether a material contains significant quantities of biologically harmful extracts, is the first step used to screen the biocompatibility of a biomaterials. The effect of PVA, GE, uncross PVA/GE, and cross-linked PVA/GE IPN hydrogels on viability (cytotoxicity) and proliferation of L929 cells was examined using the MTT assay, which is a colorimetric assay that measures the metabolic activity of viable cells. The cytotoxicities of L929 cells on the PVA, GE, uncross PVA/GE, and cross-linked PVA/GE are shown in Figure 2. Based on cytotoxicity results, a fairly acceptable viability of the cells was observed on PVA (>88% at 100% extract solution), uncross PVA/GE (>94% at 100% extract solution), and cross-linked PVA/GE (>98% at 100% extract solution), while GE membrane showed a slightly higher viability (109% at 100% extract solution). Although the biocompatibility of GE was high, the general survival rate of the cells for photocrosslinked PVA/GE scaffold was satisfactory; therefore, the IPN photocrosslinked PVA/GE scaffolds were not toxic to the L929 cells and could be used for tissue engineering scaffolds.

3.7. Proliferation of Fibroblast Cells L 929 on IPN PVA/GE Blend. The proliferation of fibroblasts on PVA, GE, uncross PVA/GE, and cross-linked IPN PVA/GE blend was evaluated using MTT assay after 1, 3, and 5 days of incubation as shown in Figure 3. A significantly higher cell proliferation (day 5) in GE and PVA/GE blend compared to PVA was exhibited in Figure 3. After 1 day, the number of cells had exceeded the number of cells initially seeded (10^4 cells/well). As clearly shown in Figure 3, the number of fibroblasts that grew was greater than the number of cells initially seeded even after only 3 days in culture. From 1 day to 5 days in culture, the L 929 cells continually proliferated on including the cross-linked IPN PVA/GE.
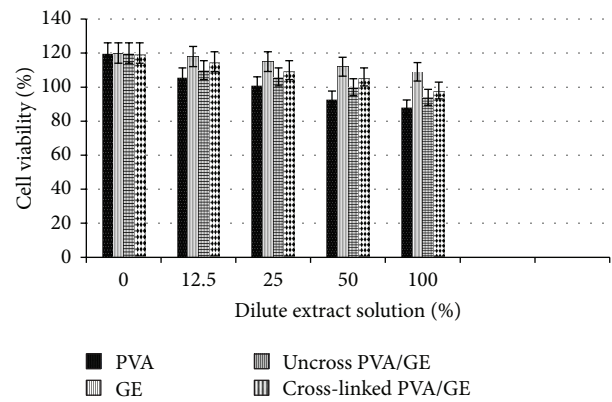

FIGURE 2: Cell viability of PVA, GE, uncross PVA/GE, and cross-linked PVA/GE IPN blend. The MTT assay was used to measure the viability of L929 cells at various dilute extract solution concentrations. Media at 100% were used as a control. Standard errors were expressed as bar diagram.
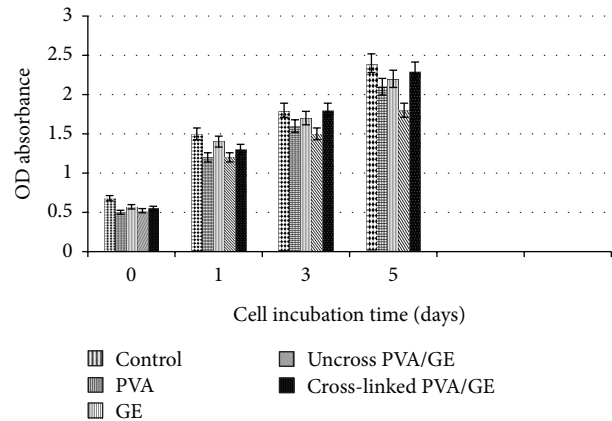
FIGURE 3: Fibroblast cellular proliferation of PVA, GE, uncross PVA/GE, and cross-linked IPN PVA/GE blend after 3 cycles and 1, 3, and 5 days using the MTT assay. Standard errors were expressed in the bar diagram. Media at 100% were used as a control and optical density (OD) corresponded to the cell survivability after 1, 3, and 5 days.

Cellular viability assay by MTT was used to find out the percentage of viable cell numbers per extract dilutions after certain periods. However, to observe the increased cell numbers and their real time morphologies, light microscopic studies were conducted. Observation of the morphological changes of cells is a very important means for predicting post-cellular responses: spreading, proliferation, and survival. An ideal scaffold must provide the contact guidance for controlling cell adhesion and directing cell migration that influences cell proliferation [36, 37]. Figure 4 shows the light microscopic images of cells treated with extract solutions for day 5. For the morphologies' fibroblasts at day 1, only a little amount of cells was observed. However, the amount of cell numbers was found to increase gradually at day 5 for all samples. Especially, at day 5, cellular growth was almost confluent. However, in case of cross-linked PVA/GE composed of cells, growth pattern was better than that of the
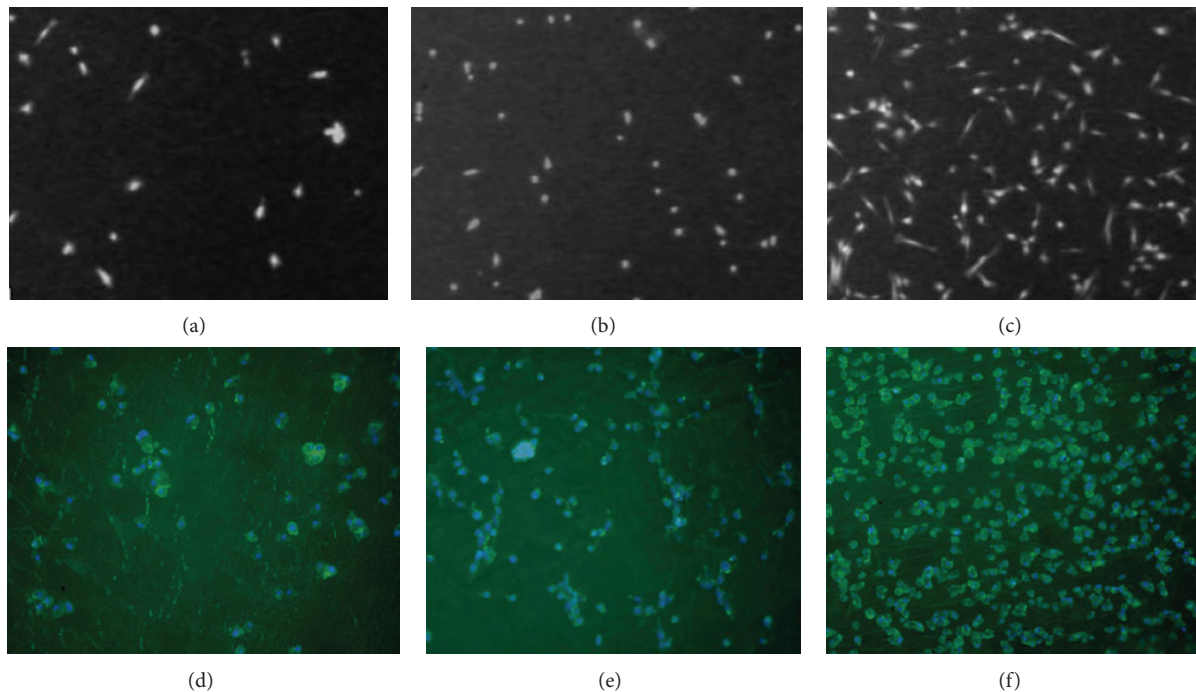
(a)

(b)

(c)

(d)

(e)

(f)

FIGURE 4: Fibroblast cellular proliferation of uncross PVA/GE and cross-linked IPN PVA/GE blend after 1 ((a), (d)), 3 ((b), (e)), and 5 ((c), (f)) days using the optical microscope observation.

uncrossing PVA/GE. In fact, this result corresponds with the cell viability and proliferation results very well.

4. Conclusion

PVA/GE hydrogels with IPN structure were prepared successfully by enzymatic and cyclic freezing-thawing method. The size and arrangement of these pores are the result of number of freezing-thawing cycles and the presence of cross-linking agents. The IPN PVA/GE hydrogels have the highest values of mechanical properties as evaluated from compression tests, also the cross-linking density showed the highest values. The SEM micrographs of these hydrogels show that the majority of the pores is opened and irregular. These interactions become stronger with increasing number of freezing-thawing cycles and results in more regular internal structure. The quantity of gelatin was the key factor to obtain IPN PVA/GE hydrogels with desirable properties. The IPN PVA/GE hydrogels showed excellent physical and mechanical properties, which met the essential requirements for ideal medical applications. Based on swelling measurements, they exhibited high capability in absorbing fluid, so recommended for exudative wounds. In addition, fibroblasts that grew over the cells treated with extract solutions exhibited the appropriate morphology and displayed good proliferation; this indicates that the cross-linked network structure of obtained gels is stable enough, suggesting that developer scaffolds might be used for tissue engineering applications.

Acknowledgment

References

[1] J.-H. Juang, S. Bonner-Weir, Y. Ogawa, J. P. Vacanti, and G. C. Weir, "Outcome of subcutaneous islet transplantation improved by polymer device," *Transplantation*, vol. 61, no. 11, pp. 1557–1561, 1996.

[2] D.-H. Chen, J.-C. Leu, and T.-C. Huang, "Transport and hydrolysis of urea in a reactor-separator combining an anion-exchange membrane and immobilized urease," *Journal of Chemical Technology and Biotechnology*, vol. 61, no. 4, pp. 351–357, 1994.

[3] S. H. Hyon, W. I. Cha, Y. Ikada, M. Kita, Y. Ogura, and Y. Honda, "Poly(vinyl alcohol) hydrogels as soft contact lens material," *Journal of Biomaterials Science*, vol. 5, no. 5, pp. 397–406, 1994.

[4] J. K. Li, N. Wang, and X. S. Wu, "Poly(vinyl alcohol) nanoparticles prepared by freezing-thawing process for protein/peptide drug delivery," *Journal of Controlled Release*, vol. 56, no. 1–3, pp. 117–126, 1998.

[5] M. T. Razzak, D. Darwis, Z. Zainuddin, and S. Sukirno, "Irradiation of polyvinyl alcohol and polyvinyl pyrrolidone blended hydrogel for wound dressing," *Radiation Physics and Chemistry*, vol. 62, no. 1, pp. 107–113, 2001.

[6] F. Yoshii, Y. Zhanshan, K. Isobe, K. Shinozaki, and K. Makuuchi, "Electron beam crosslinked PEO and PEO/PVA hydrogels for wound dressing," *Radiation Physics and Chemistry*, vol. 55, no. 2, pp. 133–138, 1999.

[7] F. Yoshii, K. Makuuchi, D. Darwis, T. Iriawan, M. T. Razzak, and J. M. Rosiak, "Heat resistance poly(vinyl alcohol) hydrogel," *Radiation Physics and Chemistry*, vol. 46, no. 2, pp. 169–174, 1995.

[8] D. A. Ossipov and J. Hilborn, "Poly(vinyl alcohol)-based hydrogels formed by 'click chemistry'," *Macromolecules*, vol. 39, no. 5, pp. 1709–1718, 2006.

[9] H. K. Purss, G. G. Qiao, and D. H. Solomon, "Effect of "glutaraldehyde" functionality on network formation in poly(vinyl

alcohol) membranes," *Journal of Applied Polymer Science*, vol. 96, no. 3, pp. 780–792, 2005.

[10] Z. Ajji, "Preparation of poly(vinyl alcohol) hydrogels containing citric or succinic acid using gamma radiation," *Radiation Physics and Chemistry*, vol. 74, no. 1, pp. 36–41, 2005.

[11] S. Benamer, M. Mahlous, A. Boukrif, B. Mansouri, and S. L. Youcef, "Synthesis and characterisation of hydrogels based on poly(vinyl pyrrolidone)," *Nuclear Instruments and Methods in Physics Research B*, vol. 248, no. 2, pp. 284–290, 2006.

[12] P. Martens and K. S. Anseth, "Characterization of hydrogels formed from acrylate modified poly(vinyl alcohol) macromers," *Polymer*, vol. 41, no. 21, pp. 7715–7722, 2000.

[13] N. A. Peppas and N. K. Mongia, "Ultrapure poly(vinyl alcohol) hydrogels with mucoadhesive drug delivery characteristics," *European Journal of Pharmaceutics and Biopharmaceutics*, vol. 43, no. 1, pp. 51–58, 1997.

[14] T. Hatakeyema, J. Uno, C. Yamada, A. Kishi, and H. Hatakeyama, "Gel-sol transition of poly(vinyl alcohol) hydrogels formed by freezing and thawing," *Thermochimica Acta*, vol. 431, no. 1-2, pp. 144–148, 2005.

[15] R. Ricciardi, C. Gaillet, G. Ducouret, F. Lafuma, and F. Lauprêtre, "Investigation of the relationships between the chain organization and rheological properties of atactic poly(vinyl alcohol) hydrogels," *Polymer*, vol. 44, no. 11, pp. 3375–3380, 2003.

[16] T. Koyano, N. Koshizaki, H. Umehara, M. Nagura, and N. Minoura, "Surface states of PVA/chitosan blended hydrogels," *Polymer*, vol. 41, no. 12, pp. 4461–4465, 2000.

[17] W.-Y. Chuang, T.-H. Young, C.-H. Yao, and W.-Y. Chiu, "Properties of the poly(vinyl alcohol)/chitosan blend and its effect on the culture of fibroblast in vitro," *Biomaterials*, vol. 20, no. 16, pp. 1479–1487, 1999.

[18] T. Chandy and C. P. Sharma, "Prostaglandin E1-immobilized poly(vinyl alcohol)-blended chitosan membranes. Blood compatibility and permeability properties," *Journal of Applied Polymer Science*, vol. 44, no. 12, pp. 2145–2156, 1992.

[19] J. M. H. Yang, M. J. Huang, and T. S. Yeh, "Preparation of poly (acrylic acid) modified polyurethane membrane for biomaterial by UV radiation without degassing," *Journal of Biomedical Materials Research*, vol. 45, pp. 133–139, 1999.

[20] H. S. Koh, T. Yong, C. K. Chan, and S. Ramakrishna, "Enhancement of neurite outgrowth using nano-structured scaffolds coupled with laminin," *Biomaterials*, vol. 29, no. 26, pp. 3574–3582, 2008.

[21] H.G.l, "United States Patent," 4055554, 1977.

[22] U. Gerber, U. Jucknischke, S. Putzien, and H.-L. Fuchsbauer, "A rapid and simple method for the purification of transglutaminase from Streptoverticillium mobaraense," *Biochemical Journal*, vol. 299, no. 3, pp. 825–829, 1994.

[23] K. Yokoyama, N. Nio, and Y. Kikuchi, "Properties and applications of microbial transglutaminase," *Applied Microbiology and Biotechnology*, vol. 64, no. 4, pp. 447–454, 2004.

[24] C. W. Yung, L. Q. Wu, J. A. Tullman, G. F. Payne, W. E. Bentley, and T. A. Barbari, "Transglutaminase crosslinked gelatin as a tissue engineering scaffold," *Journal of Biomedical Materials Research A*, vol. 83, no. 4, pp. 1039–1046, 2007.

[25] M. Carmen Go'mez-Guillén, A. Isabel Sarabia, M. Teresa Solas, and P. Montero, "Effect of microbial transglutaminase on the functional properties of megrim (*Lepidorhombus boscii*) skin gelatin," *Journal of the Science of Food and Agriculture*, vol. 81, no. 7, pp. 665–673, 2001.

[26] A. P. Rokhade, S. A. Agnihotri, S. A. Patil, N. N. Mallikarjuna, P. V. Kulkarni, and T. M. Aminabhavi, "Semi-interpenetrating polymer network microspheres of gelatin and sodium carboxymethyl cellulose for controlled release of ketorolac tromethamine," *Carbohydrate Polymers*, vol. 65, no. 3, pp. 243–252, 2006.

[27] A. P. Rokhade, S. A. Patil, and T. M. Aminabhavi, "Synthesis and characterization of semi-interpenetrating polymer network microspheres of acrylamide grafted dextran and chitosan for controlled release of acyclovir," *Carbohydrate Polymers*, vol. 67, no. 4, pp. 605–613, 2007.

[28] L. H. Sperling, "Interpenetrating polymer networks and related materials," *Journal of Polymer Science Macromolecular Reviews*, vol. 12, pp. 141–180, 1977.

[29] T. Kurokawa, H. Furukawa, W. Wang, Y. Tanaka, and J. P. Gong, "Formation of a strong hydrogel-porous solid interface via the double-network principle," *Acta Biomaterialia*, vol. 6, no. 4, pp. 1353–1359, 2010.

[30] J. E. Folk, "[127] Transglutaminase (guinea pig liver)," *Methods in Enzymology*, vol. 17, pp. 889–894, 1970.

[31] Chinese standards GB/T, 5009. 3-2003, D.o.m.i.f.

[32] M. Frydrych, C. Wan, R. Stengler, K. U. O'Kelly, and B. Chen, "Structure and mechanical properties of gelatin/sepiolite nanocomposite foams," *Journal of Materials Chemistry*, vol. 21, no. 25, pp. 9103–9111, 2011.

[33] P. R. Hari and K. Sreenivasan, "Preparation of polyvinyl alcohol hydrogel through the selective complexation of amorphous phase," *Journal of Applied Polymer Science*, vol. 82, no. 1, pp. 143–149, 2001.

[34] G. Mickisch, S. Fajta, G. Keilhauer, E. Schlick, R. Tschada, and P. A lken, "Chemosensitivity testing of primary human renal cell carcinoma by a tetrazolium based microculture assay (MTT)," *Urological Research*, vol. 18, no. 2, pp. 131–136, 1990.

[35] American National Standard, *Biological Evaluation of Medical Devices-Part 5: Tests for Cytotoxicity*, 1999.

[36] J. Fukuda, A. Khademhosseini, Y. Yeo et al., "Micromolding of photocrosslinkable chitosan hydrogel for spheroid microarray and co-cultures," *Biomaterials*, vol. 27, no. 30, pp. 5259–5267, 2006.

[37] A. J. Horobin, K. M. Shakesheff, and D. I. Pritchard, "Promotion of human dermal fibroblast migration, matrix remodelling and modification of fibroblast morphology within a novel *3D* model by *Lucilia sericata* larval secretions," *Journal of Investigative Dermatology*, vol. 126, pp. 1410–1418, 2006.

Research Article

Susceptibility to Stress Corrosion of Laser-Welded Composite Arch Wire in Acid Artificial Saliva

Chao Zhang and Xinhua Sun

Orthodontic Department, Jilin University, No. 1500 Qinghua Street, Changchun 130021, China

Correspondence should be addressed to Xinhua Sun; wojiushiwo0723@126.com

The corrosion resistance of laser-welded composite arch wire (CoAW) with Cu interlayer between NiTi shape memory alloy and stainless steel wire in artificial saliva with different acidities and loads was studied. It was found that both the solution pH and the stress had a significant influence on the corrosion behaviors of the CoAW samples. Decreasing the solution pH or increasing the loading stress caused the increase of Cu release and weight loss. The corroded morphology formed on the surfaces of the CoAW was the consequence under the combined effect of corrosion and stress.

1. Introduction

NiTi shape memory (Nitinol) alloy and stainless steel (SS) are widely and successfully used as orthodontic wires, self-expanding cardiovascular and urological stents, and so forth [1–3]. However, Nitinol and stainless steel arch wires have been used, respectively, in orthodontic clinical treatment all along. Nitinol wire has a superelastic property after placement in orthodontic bracket slot leading to less pain feeling of patients and being less prone to root absorption, whereas its stiffness is small causing the anchorage teeth move which has a negative impact on orthodontic treatment. Though the stiffness of SS wire could provide adequate anchorage, it is difficult to be put into brackets with the addition of causing significant pain and alveolar bone latent excavation of absorption due to its small flexibility [3–5].

Composite arch wire (CoAW) is an arch wire solder connection made by Nitinol and SS wires. CoAW combines the advantages of both materials by virtue of correcting malposed teeth during the teeth alignment stage and at the same time maintaining the stability of the antitooth. The application of CoAW could not only effectively reduce the suffering of patients and simplify therapeutic operation, but it can also reduce the number of subsequent visits. However, successful application of any advanced material depends not only on its inherent properties, but also on the development of joining technology for itself or other dissimilar materials [6]. Therefore, laser welding was carried out to join Nitinol and SS wires with pure Cu interlayer. The joint tensile strength (>520 MPa) and shape recovery ratio of Nitinol alloy HAZ (>98%) could meet the requirements of clinical performance [7]. The excellent mechanical properties of the new type CoAW provide more and more possibility on orthodontic application. However, there is still no clinical evidence to indicate the potential carcinogenicity of orthodontic CoAW. Therefore, the biocompatibility of orthodontic CoAW is very important and worth further investigation.

The corrosion resistance of orthodontic wire is an important factor determining its biocompatibility [8]. Previously, there are many studies separately reported the corrosion behaviors of Nitinol and stainless steel [9–11]. Huang found that the SS wire showed higher pitting potential and wider passive range than Nitinol wire [12]. Huang found that decreasing the solution pH led to an increase in corrosion potential, corrosion rate, and passive current of the Nitinol wires [13]. The acidity changes can alter chemistry environment and biological processes around arch wires leading to the variation of corrosion resistance. However, studies on corrosion behavior of the new type orthodontic CoAW laser welded by Nitinol and SS wires with Cu interlayer are still missing.
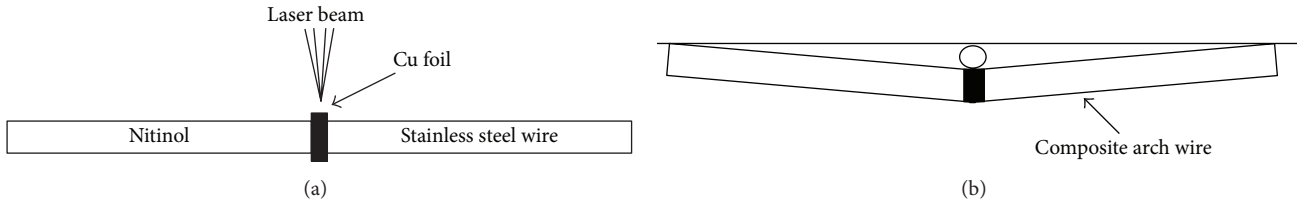
FIGURE 1: (a) Schematic diagram of laser welding; (b) device for applying 3-point bending forces to composite arch wire.

As a biomaterial like arch wire, the resistance to general and localized corrosion, as well as the resistance of harmful metal ions, is prerequisite for in-oral applications [14]. From the dental application point of view, the load plays important roles in the corrosion resistance of CoAW. Orthodontic arch wires are often working under continuous loading conditions, especially when correcting the malposed teeth. The applied forces might induce damage of the oxide film on the wire surface, and the loss of protection could allow active metal to react with the surrounding environment [15]. Wang et al. studied the stress corrosion cracking (SCC) mechanism of Nitinol wires in artificial saliva [16]. Liu et al. suggested that the passive film was not stable under loading conditions, and cracking of the passive film of Nitinol wires would occur under continuous bending stress [17]. However, studies of the corrosion behavior of CoAW which contains relatively frail copper interlayer under stress are still missing.

Therefore, in this paper, the stress corrosion behaviors of the CoAW laser welded by Nitinol and SS wires with Cu interlayer in artificial saliva with different acidities and loading force were studied.

2. Experimental Details

2.1. Materials and Samples Preparation. Ti-44.73 wt. % Ni SMA wire (purchased from Smart Co., Beijing), Fe-18Cr-8Ni stainless steel (Grikin Advanced Materials Co., Ltd.), and pure Cu foil were used as base metals in this investigation. The dimensions of the wires are 30 mm (length) × 0.64 mm (width) × 0.48 mm (thickness). The pure Cu interlayer is 0.2 mm of thickness. The base metal was ground using SiC papers of nos. 800, 1200, and 2000 grit to remove oxide layer and then ultrasonically degreased in acetone. The Nitinol and stainless steel wire were fixed on a self-constructed fixture by wire-to-wire butt with the pure Cu interlayer as shown in Figure 1(a). An Nd : YAG laser welding system (JHM-1GY 300B) with the wavelength of 1064 nm was used for the welding. The optimized laser parameters used in the study were 5.23 J (laser power), 6 ms (welding time), and diameter of 0.5 mm.

2.2. Test Solution Preparation and Stress Condition Implement. The common physiological solution of 0.9% NaCl was prepared as the chloride solution. The artificial saliva (AS) was a phosphate buffered saline solution of the composition shown in Table 1, and pH value was set to 6.75 and adjusted to pH 4.0 with lactic acid. A total of 10 groups (2 pH values AS and 5 loading conditions) were investigated for stress tests and each

TABLE 1: Modified Fusayama artificial saliva used in this study.

Composition	mg/L
NaCl	400
KCl	400
$CaCl_2 \cdot 2H_2O$	795
$NaH \cdot PO_4 \cdot H_2O$	690
KSCN	300
$Na_2S \cdot 9H_2O$	5
Urea	1000

group contained 5 specimens. All the wires were mechanically grinded using SiC papers up to no. 2000 grit and ultrasonically cleaned in 95% alcohol and then rinsed with double-distilled water.

The specimens were immersed in modified Fusayama artificial saliva with different acidities and maintained at 37°C for periods up to 28 days. A 3-point flexure fixture, made of ceramic sheet, was used to apply a continuous bending force that deflected the displacement of 1.0, 2.0, 3.0, 5.0 mm as shown in Figure 1(b). The wires were fixed in the solution with a free length of 60 mm. The unbent specimens were also placed in the same designed vessel without applied force.

After 14 days of immersion, the solution was collected and substituted by the new solution, and after 28 days each retrieved sample was cleaned. Precision electronic balance (M2-P, Sartorius, Germany) was used to measure the weight changes after soaking in artificial saliva. The collected solutions were individually analyzed for copper using an inductively coupled plasma-optical emission spectrometer (ICP-OES, Optima 3300DV, Perkin Elmer, Boston, USA). The detection limit of ICP-OES used in this study was 0.01 ppm for copper ion.

2.3. Electrochemical Measurements. All the electrochemical measurements were performed using a CHI 920C electrochemical workstation. The counter electrode was a rectangular platinum plate and the reference electrode was a saturated calomel electrode (SCE). Additionally, the test solutions were not deaerated before the electrochemical measurement. All test samples were mechanically ground using SiC papers up to no. 2000 grit to guarantee consistent surface roughness and then embedded in cold-curing epoxy resin, exposing a sample surface area of 20×0.64 mm^2.

After an initial delay of 60 min to accomplish the equilibrium, the scanning rate was 5 mV/s, starting from-1 V/SCE to remove the surface film heterogeneity. The cyclic
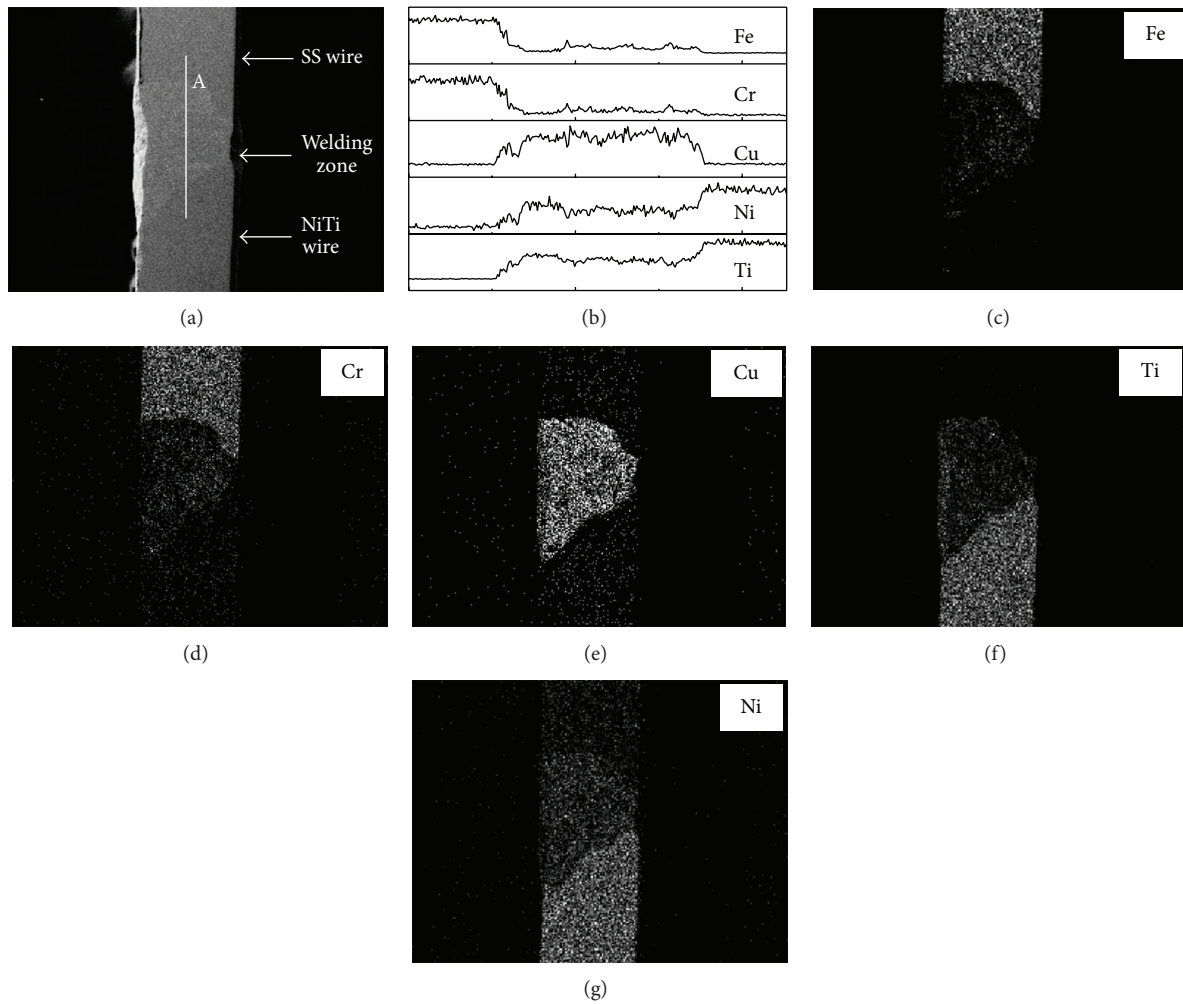
FIGURE 2: (a) SEM surface morphologies of the welded composite arch wire; (b) EDS line analysis of the welded composite arch wire; ((c)–(g)) map EDS analysis of the welded composite arch wire.

potentiodynamic tests were conducted between −1000 and +1500 mV. Each test contained 3 specimens.

2.4. SEM Surface Morphology.
The surface morphologies of composite orthodontic wires were observed using environmental scanning-electron microscopy (SEM, ZEISS EVO18, Germany) equipped with an energy dispersive spectrometer (EDS) analyzer (INCA-X-Max, UK).

3. Results and Discussion

3.1. Microstructure of the CoAW.
Figure 2 shows surface morphologies of the welding zone between the dissimilar materials. It can be seen that the surface of the welding zone was smooth and complete, free of any apparent pores or other defects. According to the map EDS analysis, the welding zone shows a heterogeneous composition. From stainless steel to Nitinol side, the concentrations of Fe and Cr decrease and the concentrations of Ti and Ni have an increased tendency. Furthermore, Cu element distributes homogeneously in the welding zone, Figures 2(b)–2(g).

3.2. Potentiodynamic Polarization Measurement.
The effects of chloride and pH on potentiodynamic polarization behaviors of CoAW are shown in Figure 3, and the detailed electrochemical parameters are listed in Table 2. It can be seen that the cathodic section of the polarization curves comprised two distinct stages. For the anodic polarization curves, the CoAW exhibited a typical passive region up to the pitting potential in the pH = 6.75 AS solution compared the other two solutions. The passive region of the chloride solution polarization curves was much smaller than the section of artificial saliva polarization curves. The corrosion potentials remained very similar as pH increased, whereas the pitting potential (E_{pit}) as well as passive current densities of pH = 6.75 was higher than that in pH = 4.0 solution.

3.3. Cyclic Potentiodynamic Polarization Measurement.
In order to evaluate the repassivation ability of CoAW in the three categories of solutions, cyclic potentiodynamic polarization measurements were carried out. Figure 4 presents typical cyclic polarization curves of CoAWs in PH = 6.75, 4.0 artificial saliva, and 0.9% NaCl solution. In all the three
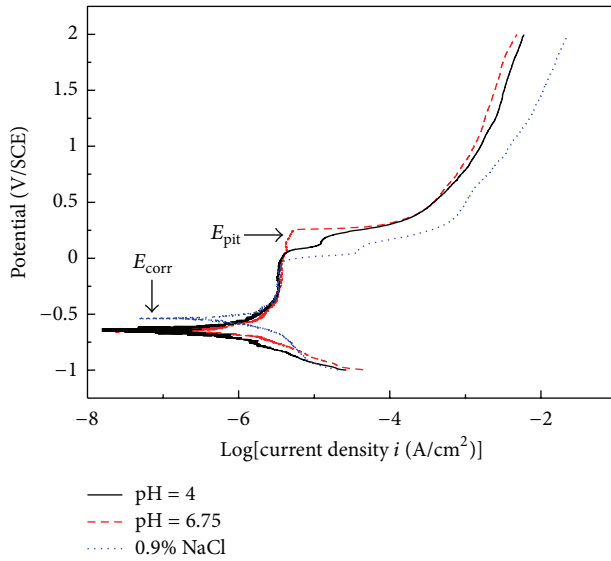
FIGURE 3: Polarization curves for composite arch wires in different solutions.
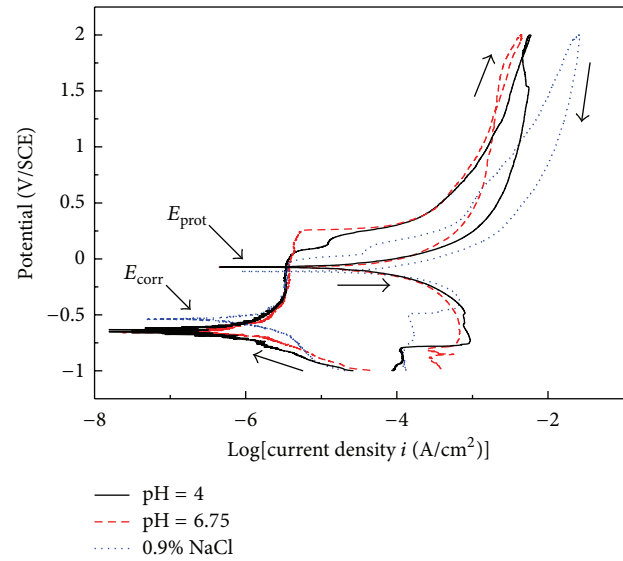

FIGURE 4: Representative cyclic polarization curves of composite arch wires in different solutions.

solutions, no obviously hysteresis loop occurred in the reverse anodic scan. The reprotection potentials (E_{prot}) were much higher than the free corrosion potentials (E_{corr}). Moreover, the reprotection potential of the CoAW in the 0.9% NaCl solution is a little lower than in the acid AS solutions.

The SEM images of the CoAWs after the cyclic potentiodynamic polarization measurement are shown in Figure 5. It can be seen that the CoAWs in the 0.9% NaCl solution were easily corroded compared to these in the artificial saliva solutions.

3.4. Corrosion Tests with Applied Stress. After soaking in AS at both pH 4.0 and 6.75 with different stresses, the typical surface morphologies of CoAWs are shown in Figure 6. Copper element release and weight loss are shown in Figure 7. It can be seen that under both unstressed and stressed circumstances, no obvious degradation occurred after 28 days of immersion in artificial saliva, regardless of the pH value. Furthermore, the interlayer part of stressed wires showed more irregular surfaces than unstressed wires. With the increase of applied loading force, the corrosive surface performed rougher. The Cu release and weight loss increase with the decrease in pH and increase in applied loading force.

3.5. Discussion. The biocompatibility of orthodontic arch wire is thought to depend mainly on the host reaction induced by the degradation of the material in bodily environment. The biologic response to metal is directly related to its corrosion performance, which is associated with the protective oxide film on the surface [15]. CoAWs are subject to mechanical stresses and deformation for tooth movement, which might induce damage of the oxide film on the wire surface and allow active metal to react with the surrounding environment. Therefore, in this study, we investigated the

effect of bending stress and pH values on corrosion performance of CoAW in vitro.

As indicated, different environments have important effect on the corrosion performance of CoAW. The standard and cyclic potentiodynamic tests were used to estimate the corrosion behaviors in different solutions. The results of standard potentiodynamic polarization test are shown in Figure 3 and Table 2. The pitting potential (E_{pit}) is used to evaluate the corrosion resistance. E_{pit} represents conservative measures of anodic pitting tendency because it shows minimum potential below which pitting cannot be sustained [18]. The nearly vertical stage at lower potential corresponds to the hydrogen generation process, whereas the sloped region represents the oxygen consumption process. The E_{pit} of two acidities artificial saliva solution was higher than that of NaCl solution, which may be due to the inhibitory effect of other ions in artificial saliva [19]. The explanation of this phenomenon is based on research showing that natural calcium phosphate layers will naturally form in complex simulated physiological solutions due to certain inhibiting ions, such as $CaCl_2$ and phosphate which would possibly act as further protective barriers against the corrosion process [20]. Although the pitting potential (E_{pit}) in pH = 6.75 was extended to higher potential value compared with pH = 4.0, the pitting potentials in both solutions were large. Therefore, the pitting corrosion is not easy to occur. Decreasing the pH value leading to a decrease in the E_{pit} and passive range for composite arch wire indicated that the pitting corrosion resistance and passivity breakdown resistance of CoAW were more susceptible to the pH variation. With the increase in potential, the movement of ions was controlled by the electronic potential rather than by diffusion, where CoAW exhibited increase in current density at the same point of pitting potential, indicating the abrupt damage of the protective film was compatible with a passivity
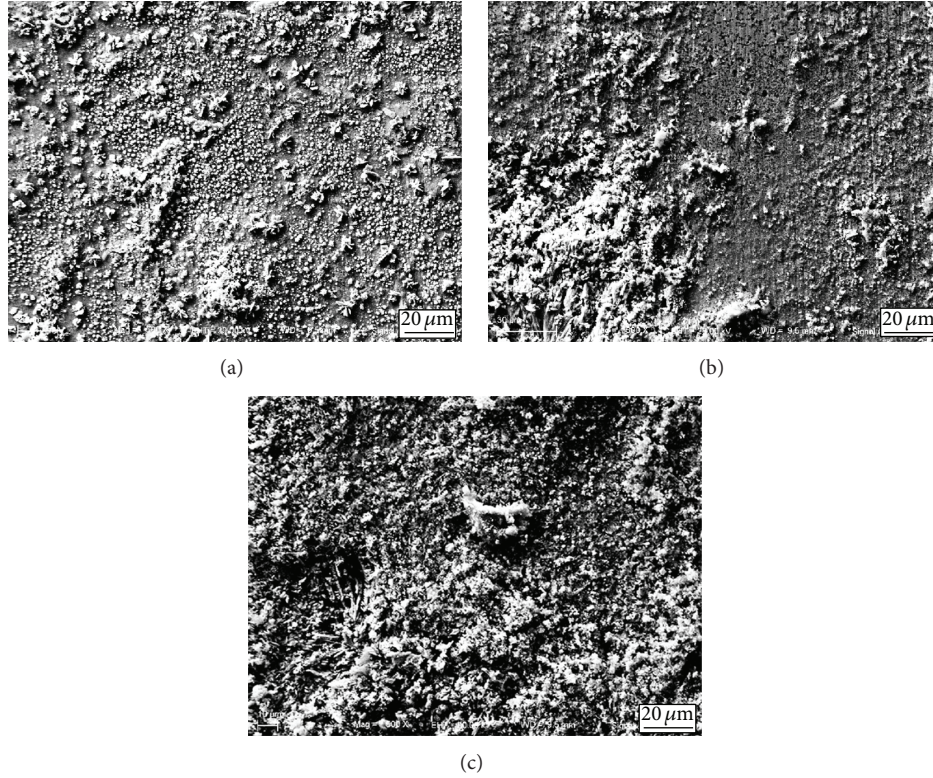
(a)

(b)

(c)

FIGURE 5: SEM surface morphologies of potentiodynamic polarized composite arch wires: (a) pH 4.0; (b) pH 6.75; (c) 0.9% NaCl.

TABLE 2: The pitting potential (E_{pit}), corrosion potential (E_{corr}) with respect to SCE, and corrosion current density (I_{corr}) extracted from potentiodynamic polarization curve.

Solution type	E_{pit} (V)	E_{corr} (V)	I_{corr} ($\mu A/cm^2$)
pH = 4.0	0.121 (0.010)	−0.628 (0.011)	1.38 (0.014)
pH = 6.75	0.260 (0.012)	−0.641 (0.014)	1.02 (0.006)
NaCl	0.052 (0.008)	−0.534 (0.016)	1.58 (0.011)

regime occurring before the breakdown potential. Additionally, the corrosion current densities and passivation current densities in the three solutions are similar, which means that the value of corrosion current density attacking the entire material rapidly is the same [21].

In Figure 4, there was a smaller hysteresis loop in the polarization curve, which suggested that the CoAW did not experience true localized corrosion in the experimental solutions. Although it appears that there was an initial small degree of pitting, this did not develop into large pitting because the surrounding corrosion quickly eliminated it. The reverse of the anodic potential in cyclic potentindynamic test was scanned down to interact with the passive region. The interaction at the passive region defined protection potential (E_{prot}). Wilde reported that the difference between E_{pit} and E_{prot} can be correlated with the resistance to crevice corrosion. The higher difference between E_{pit} and E_{prot} means the higher susceptibility of an alloy to crevice corrosion [22]. In our study, the difference between E_{pit} and E_{prot} is small which

means lower susceptibility to crevice corrosion. Therefore, regardless of the solution type, the transpassive region in the polarization curves for composite wires was a result of uniform corrosion. On the other hand, the E_{prot} above the corresponding E_{corr} indicates that the specimens are capable of repassivation when the passive film is damaged [23]. Transpassivation takes place with the generation of oxygen gas accompanied by the anodic dissolution of a metallic ion, which was copper ion in this study. The corrosion resistance of copper in the interlayer is mainly dependent on the oxidation product formed on the surface after the initial corrosion. The copper corrosion kinetics, with the increased coverage of the surface of the corrosion product, is mainly decided by the surface concentration of adsorbed oxygen. Generally, the corrosion process of Cu causes the increase of pH value of solution, which would reduce the corrosion rate. As a result, the corrosion performance of CoAW in pH = 4.0 artificial saliva is almost the same as the neutral saliva in electrochemical and SEM results. However, more severely damaged surface and spongy morphology were observed on tested interlayer surfaces of composite wire in chloric solution. The reason was stated in the proceeding part and supported by the study of Kim and Johnson which showed that Nitinol wire revealed extensive pitting and localized corrosion after potentiodynamic polarization tests in 0.9% NaCl solution [24].

Another important aspect of the biocompatibility behavior of CoAWs is their corrosion performance under stress condition in applications. Bending stress used in this study,
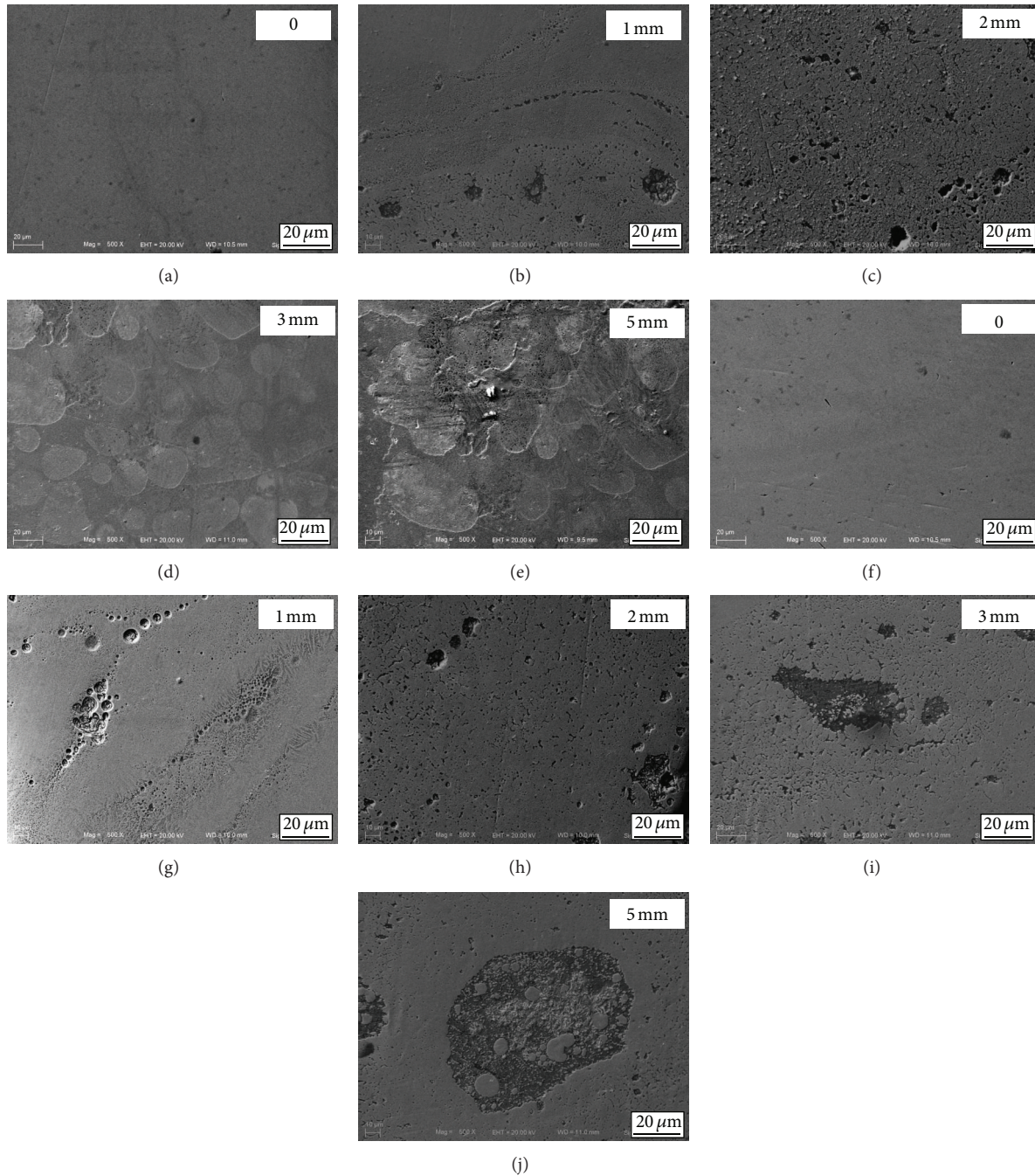
(a)

(b)

(c)

(d)

(e)

(f)

(g)

(h)

(i)

(j)

FIGURE 6: SEM surface morphologies of unstressed and stressed composite arch wires immersed in artificial saliva with different pH: ((a)–(e)) pH = 4.0; ((f)–(j)) pH = 6.75.

unlike tensile stress, could cause homogenous deformation of orthodontic wires which would start at an initial point and propagate along the wires then allow body fluids and tissues to touch the wire surface under the damaged oxide layer. Rondelli and Vicentini found no effect of 4% strain on the localized corrosion behavior of Nitinol wires [25]. Huang mentioned that the applied tensile stress would not change the corrosion resistance of as-received Nitinol wires in artificial saliva at both pH values 2 and 5 [12]. It was suggested that

the passive film of specimens would be damaged under bending condition more than under tensile stress. In this study we simulate the real corrosion conditions to evaluate the corrosion behavior of CoAW in orthodontic applications. An electrolytic cell is formed between the stressed and unstressed metal portions and grain boundaries of stressed metal are most vulnerable to corrosion. The failure of the soldered joint or the flaking away of a thin margin of metal would occur due to stress corrosion [26]. As previously discussed,
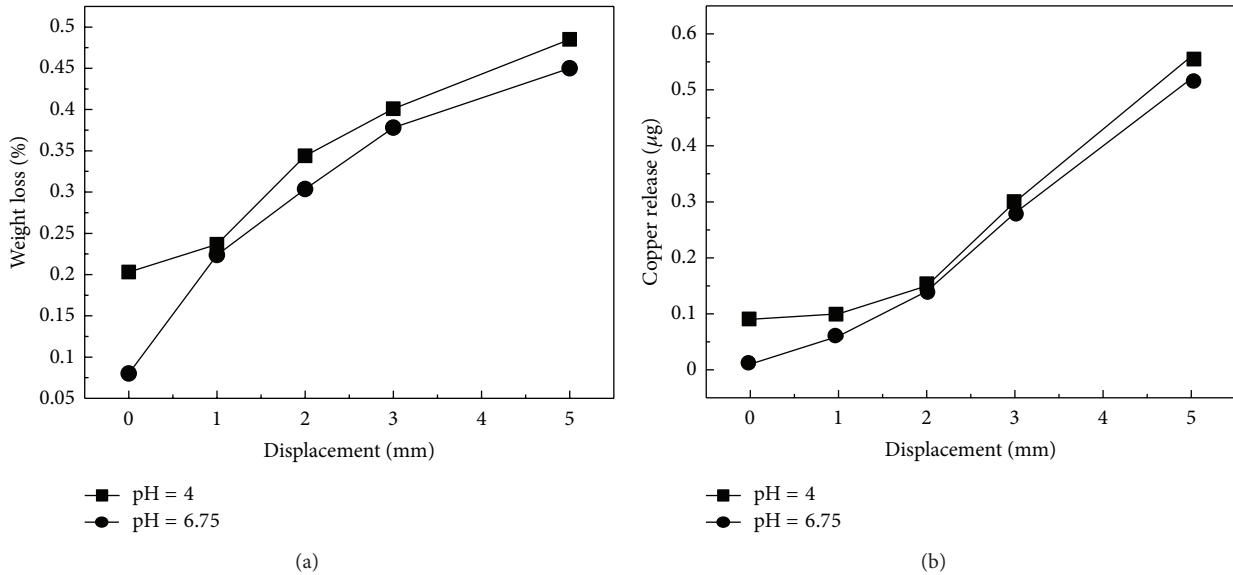
FIGURE 7: (a) Weight loss and (b) copper release of the composite arch wires in artificial saliva with different pH values.

the acid solution is easier to react with the CoAW than the neutral solution. The Cu release and weight loss in the pH = 4.0 solution is larger than that in the pH = 6.75 solution. On the other hand, for the static corrosion test in which the force displacement is 0, the Cu release and weight loss is low. The reason is that the surface is protected by the oxide layer. For the stress corrosion, the 3-point bending method would induce buckling or cracking of the oxide layer of interlayer part, and loss of this protection allows the active metal to react with surrounding environment. With the increase of the applied loading force, more Cu release and larger weight loss occurred in both pH = 4.0 and 6.75 artificial saliva solutions. The utmost weight losses and copper element release of CoAW were under the condition of pH = 4.0 and force displacement 5 mm. The results come to an agreement with conclusion of Liu et al. that the stressed Nitinol wires exhibited substantial increase in nickel release compared with the unbent specimens at different pH values AS [17].

As shown in Figure 6, both stressed and unstressed specimens showed uniform corrosion but relative intact surface in longer period of artificial saliva immersion. Under the same applied force, the CoAW is more corrodible to the acid artificial saliva. With the increase of the applied loading force, the surface of the CoAW becomes rougher due to the break of the oxide film under the bending force.

For clinical applications, the orthodontic arch wires have dynamic conditions rather than static conditions, which possibly damage the passive film. The open metal surface would react with the aggressive solution and release metal ions into the surrounding environment. We must understand the stress on corrosion behavior and ion release to ensure the stable surface properties of CoAW in clinical use and reexamine the loading conditions with respect to corrosion behavior. In clinical applications, orthodontic wires would be used for more than 1 month, and the continuous bending stress and acidity variation would affect the properties of the passive

film of the composite wires. Therefore, the factor of stress and acidity should be considered on the corrosion behavior in the design and clinical use of CoAW and related-alloy wires. The clinical application and performance improvements of CoAW must refer to the results of pH and stress corrosion.

4. Conclusions

Under the different experimental conditions of this study, the following conclusions were drawn.

(1) Through the polarization test, the CoAW seems easily occurred with uniform corrosion in the artificial saliva solution. With the decrease of the pH, the corrosion resistance becomes worse.

(2) The applied bending stress would break the oxide film on the surface of the CoAW which leads to more Cu release and larger weight loss. The most serious corrosion occurred under the largest stress and lowest pH value.

(3) The factor of stress and acidity must be considered on the corrosion behavior in the design and clinical use of CoAW and related-alloy wires.

References

[1] C. W. Chan, H. C. Man, and T. M. Yue, "Effect of post-weld heat-treatment on the oxide film and corrosion behaviour of laser-welded shape memory NiTi wires," *Corrosion Science*, vol. 56, pp. 158–167, 2012.

[2] N. B. Morgan, "Medical shape memory alloy applications—the market and its products," *Materials Science and Engineering A*, vol. 378, no. 1-2, pp. 16–23, 2004.

[3] W. A. Brantley, *Orthodontic Materials: Scientific and Clinical Aspects*, Thieme, New York, NY, USA, 2001.

[4] R. P. Kusy, "A review of contemporary archwires: their properties and characteristics," *Angle Orthodontist*, vol. 67, no. 3, pp. 197–207, 1997.

[5] S. A. Thompson, "An overview of nickel-titanium alloys used in dentistry," *International Endodontic Journal*, vol. 33, no. 4, pp. 297–310, 2000.

[6] N. J. Noolu, H. W. Kerr, Y. Zhou, and J. Xie, "Laser weldability of Pt and Ti alloys," *Materials Science and Engineering A*, vol. 397, no. 1-2, pp. 8–15, 2005.

[7] D. Q. Sun and H. M. Li, "A new method of TINi shape memory alloy and austenitic stainless steel different Kind of material connection," CN Patent, CNIO2152017, 2011.

[8] N. Schiff, B. Grosgogeat, M. Lissac, and F. Dalard, "Influence of fluoridated mouthwashes on corrosion resistance of orthodontics wires," *Biomaterials*, vol. 25, no. 19, pp. 4535–4542, 2004.

[9] G. Rondelli, "Corrosion resistance tests on NiTi shape memory alloy," *Biomaterials*, vol. 17, no. 20, pp. 2003–2008, 1996.

[10] Y. Okazaki and E. Gotoh, "Metal release from stainless steel, Co-Cr-Mo-Ni-Fe and Ni-Ti alloys in vascular implants," *Corrosion Science*, vol. 50, no. 12, pp. 3429–3438, 2008.

[11] C. Liu, P. K. Chu, G. Lin, and D. Yang, "Effects of Ti/TiN multilayer on corrosion resistance of nickel-titanium orthodontic brackets in artificial saliva," *Corrosion Science*, vol. 49, no. 10, pp. 3783–3796, 2007.

[12] H.-H. Huang, "Corrosion resistance of stressed NiTi and stainless steel orthodontic wires in acid artificial saliva," *Journal of Biomedical Materials Research A*, vol. 66, no. 4, pp. 829–839, 2003.

[13] H.-H. Huang, "Surface characterizations and corrosion resistance of nickel-titanium orthodontic archwires in artificial saliva of various degrees of acidity," *Journal of Biomedical Materials Research A*, vol. 74, no. 4, pp. 629–639, 2005.

[14] J. C. Wataha, "Biocompatibility of dental casting alloys: a review," *Journal of Prosthetic Dentistry*, vol. 83, no. 2, pp. 223–234, 2000.

[15] J. C. Setcos, A. Babaei-Mahani, L. D. Silvio, I. A. Mjör, and N. H. F. Wilson, "The safety of nickel containing dental alloys," *Dental Materials*, vol. 22, no. 12, pp. 1163–1168, 2006.

[16] J. Wang, N. Li, G. Rao, E.-H. Han, and W. Ke, "Stress corrosion cracking of NiTi in artificial saliva," *Dental Materials*, vol. 23, no. 2, pp. 133–137, 2007.

[17] J.-K. Liu, T.-M. Lee, and I.-H. Liu, "Effect of loading force on the dissolution behavior and surface properties of nickel-titanium orthodontic archwires in artificial saliva," *The American Journal of Orthodontics and Dentofacial Orthopedics*, vol. 140, no. 2, pp. 166–176, 2011.

[18] M. D. Ralph, T. D. Bold, and M. J. Johnson, *Corrosion of Stainless Steel*, Materials Park, Ohio, OH, USA, 1987.

[19] K. Y. Chiu, F. T. Cheng, and H. C. Man, "Corrosion behavior of AISI 316L stainless steel surface-modified with NiTi," *Surface and Coatings Technology*, vol. 200, no. 20-21, pp. 6054–6061, 2006.

[20] D. J. Wever, A. G. Veldhuizen, J. de Vries, H. J. Busscher, D. R. A. Uges, and J. R. van Horn, "Electrochemical and surface characterization of a nickel-titanium alloy," *Biomaterials*, vol. 19, no. 7–9, pp. 761–769, 1998.

[21] K.-T. Oh, C.-J. Hwang, Y.-S. Park, and K.-N. Kim, "In vitro corrosion resistance of orthodontic super stainless steel wire. The effects of stress relieving heat-treatment," *Journal of the Electrochemical Society*, vol. 149, no. 9, pp. B414–B421, 2002.

[22] B. E. Wilde, "A critical appraisal of some popular laboratory electron chemical tests for predicting the localized corrosion resistance of stainless alloys in seawater," *Corrosion*, vol. 28, no. 8, pp. 283–291, 1972.

[23] A. Anderko, N. Sridhar, and D. S. Dunn, "A general model for the repassivation potential as a function of multiple aqueous solution species," *Corrosion Science*, vol. 46, no. 7, pp. 1583–1612, 2004.

[24] H. Kim and J. W. Johnson, "Corrosion of stainless steel, nickel-titanium, coated nickel-titanium, and titanium orthodontic wires," *Angle Orthodontist*, vol. 69, no. 1, pp. 39–44, 1999.

[25] G. Rondelli and B. Vicentini, "Evaluation by electrochemical tests of the passive film stability of equiatomic Ni-Ti alloy also in presence of stress-induced martensite," *Journal of Biomedical Materials Research*, vol. 51, no. 1, pp. 47–54, 2000.

[26] D. Upadhyay, M. A. Panchal, R. S. Dubey, and V. K. Srivastava, "Corrosion of alloys used in dentistry: a review," *Materials Science and Engineering A*, vol. 432, no. 1-2, pp. 1–11, 2006.

Research Article

The Production of Nickel-Chromium-Molybdenum Alloy with Open Pore Structure as an Implant and the Investigation of Its Biocompatibility In Vivo

Yusuf Er[1] and Emine Unsaldi[2]

[1] *Department of Metallurgy Education, Gazi Vocational High School, Directorate of National Education, 23100 Elazig, Turkey*
[2] *Department of Surgery, Faculty of Veterinary, Firat University, 23119 Elazig, Turkey*

Correspondence should be addressed to Yusuf Er; yusufer23@hotmail.com

A dental crown material, Nickel-Chrome-Molybdenum alloy, is manufactured using precision casting method from a polyurethane foam model in a regular and open-pore form, as a hard tissue implant for orthopedic applications. The samples produced have 10, 20, and 30 ($\pm$3) pores per inch of pore densities and 0.0008, 0.0017, and 0.0027 g/mm^3 densities, respectively. Samples were implanted in six dogs and observed for a period of two, four, and six months for the histopathological examinations. The dogs were examined radiologically in 15-day intervals and clinically in certain intervals. The implants were taken out with surrounding tissue at the end of these periods. Implants and surrounding tissues were examined histopathologically in terms of biocompatibility. As a result, it is seen that new bone tissue was formed, in pores of the porous implant at the head of the tibia in dogs implanted. Any pathology, inflammation, and reaction in old and new tissues were not observed. It was concluded that a dental alloy (Ni-Cr-Mo alloy) could also be used as a biocompatible hard tissue implant material for orthopedics.

1. Introduction

In recent years, many developments have taken place in the field of orthopedics; the most important developments, without doubt, are in the field of implantology. The materials used in implantology are subjected to very hard conditions in vivo [1, 2]. The properties of the material, design, and method of fixation of the implant determine the performance. Strength, fatigue, surface corrosion, allergic reactions caused, and totally biocompatibility of the biomaterials used are the main research subjects today [2–4].

Many different materials have been used as bone implants. An ideal hard tissue implant must be fully compatible and biologically inert, be easy to be found, have strength close to the bone strength, and should be accepted or rejected by the patient's tissue without infection. Biocompatible implants, because of their open-cellular structure, permit the ingrowths of the new bone and transport of the body fluids [5–7]. Serious problems are due to implant-bone interphase in the field of implantology [4]. Therefore, there is

a need to develop high biocompatible new implant materials. Porous materials enable osseous tissue into the implant. Investigations have shown that the average pore size of the porous bone substitute material implanted must have pore size to allow the advancement of the bone tissue ingrowth. This size should be approximately 200 to 500 μm [6–8]. Metallic foams are new class of materials with extremely low densities and unique combination of excellent mechanical, thermal, electrical, and acoustic properties [7, 9]. It is especially attractive that the strength and the Young's modulus of the cellular materials can be adjusted through the adjustment of the porosity to match the strength and the Young's modulus of the natural bone. Hence it is indispensable to develop new bone-substitute materials with high strength and appropriate Young's modulus to ensure the biomechanical properties of the natural bones [7].

In the present study, a Nickel-based a Ni-Cr-Mo alloy widely used in the construction of dental prostheses was used to produce the samples by precision casting method [9–13] with different open pore sizes. Furthermore, the usability as

an orthopedic implant material and biocompatibility in vivo conditions were investigated.

2. Materials and Methods

2.1. The Production of Implant Samples. Nickel-based alloys are used as implant materials. The alloy which was used in this study is commercially produced by the German company Böhler. In Table 1, the chemical composition is given by the manufacturer. In the production of the samples, a two-stage casting method was used. In this method, the open cell metal foams are produced by using polymeric foams. Here, polyurethane foams with open pores in three different sizes were used as a sample model. The produced sample models have 10, 20, and 30 (± 3) pores per inch (ppi) and 0.0008, 0.0017, and 0.0027 g/mm^3 densities, respectively. Molds were prepared by pouring precision casting plaster into the mold cavities. Prepared molds were heated for 1 hour at 1000°C in a thermocouple equipped oven for the preparation of precast. In this way, the cast cavity has been created in the mold by burning out polyurethane foams. Then the alloy is heated up to 1410°C and poured into molds by using a centrifugal casting device. Molds were left to cool down and then were broken and cleaned to remove the case. A sufficient number of samples (Figures 1(a) and 1(b)) were produced in this way.

2.2. Preparation of Experimental Subject Materials. Six healthy dogs were used as an experimental subject material of different breed, age, sex, and weight 27 to 35 kg. Preventative rabies vaccines, endo- and ectoparasitic drug applications were performed prior to the operation. Soft tissue operation sets, orthopedic sets, drill bit, and the curette were used for operations.

2.3. Method. The anesthesia was performed with i.m. injection of 15 mg/kg ketamine hydrochloride 10 minutes after administration of i.m. 1.5 mL/10 Xylazine hydrochloride (Rompun, Bayer). The implants produced for the study were applied to the proximal metaphysis of the tibia. A maximum care was paid to asepsis and antisepsis procedures during the study. The implants were applied to randomly selected tibias. The skin incision was extended from the tuberosity of the tibia to the crista tibialis. Following exclusion of the skin and underlying tissues, the periosteum was elevated performing a 2-3 cm incision. After lifting the periosteum with an elevator, the bone cortex was perforated with an aid of a 5 diameter Steinmann pin. The holes established in the bones were readjusted to the implants' sizes using different size drills and bone curettes. For insertion the implants, some spongiosis bone graft was removed from the window established in the cortex with a curette and then they were carefully placed in the defects performed (Figures 2(a) and 2(b)).

2.4. Postoperative Applications. Operation wound was closed by the conventional operational techniques. All cases were examined radiographically immediately after the operations. Antibiotics were parenterally administered for five days in order to prevent possible postoperative infections. The dogs

TABLE 1: Alloy chemical composition.

Content	Mixing ratio
Nickel	Bal.
Chromium	26.0
Molybdenum	11.0
Silicon	1.5
Carbon	<0.05

TABLE 2: Average porosities of the samples by groups.

Samples groups	(1) Sample porous average (%)	(2) Sample porous average (%)	(3) Sample porous average (%)	General porous average (%)
A	89.6	91	91.5	90.7
B	78.9	80.3	83.8	81
C	66.8	68.1	72.8	68.8

TABLE 3: General porosities by the pore sizes.

Samples groups	Pore sizes (ppi)	Solid densities (g/mm^3) (ρ_{solid})	Porous densities (g/mm^3) (ρ_{porous})	General porosities in percent (ε) (%)
A	10 (± 3)	0.0088	0.0008	90.7
B	20 (± 3)	0.0088	0.0017	81
C	30 (± 3)	0.0088	0.0027	68.8

were investigated radiographically and clinically checked in fifteen-day intervals. The implants and surrounding tissue were taken out with all tibias second, fourth, and sixth months after the implantation, respectively. Implants with surrounding tissue were fixed in 10% paraformaldehyde for 48 hours and then for decalcified were kept in 10% formic acid for 15 days, dehydrated for one hour with water, and embedded in wax. 4 micrometer thick sections were cut by microtom and stained with haematoxylin-eosin. The sections were viewed and photographed using a Kyowa-Tokyo microscope.

3. Results

3.1. Materials Characterization. In this study, the densities and average porosities of the samples produced in the dimensions of $\phi 12 \times 14$ mm with three different pore sizes were calculated (Table 2). Pore size was determined by the porous per inch (ppi). Since the samples have open pores, the volume was found by liquid weighing method. Porous densities (ρ_{porous}) were found from the relation between mass (m) and volume (v) given in (a). Then porosities in percent (ε) were calculated by the formulae given in (b) by full densities and porous densities of the samples. The solid density of the alloy used, the pore sizes, porous densities, and average
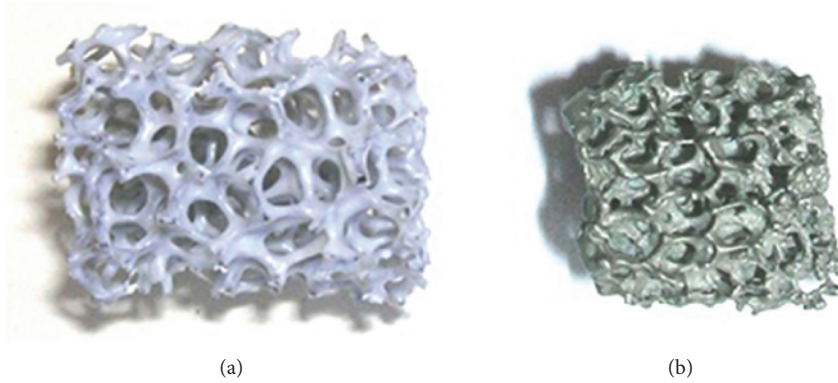
(a)   (b)

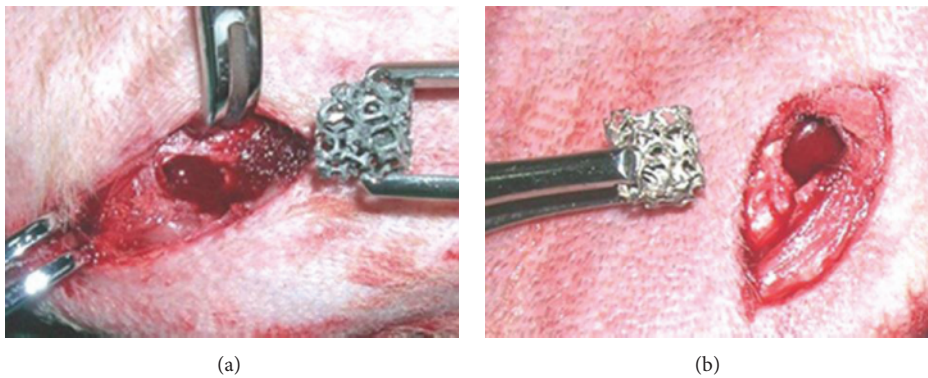FIGURE 1: (a) Polyurethane foam model. (b) Produced sample.

(a)   (b)

FIGURE 2: Placement of the sample.

percent porosities of the samples were given in Table 3 as follows:

$$\rho_{\text{porous}} = \frac{m}{v}, \qquad (a)$$

$$\varepsilon = \left(1 - \frac{\rho_p}{\rho_s}\right) \times 100. \qquad (b)$$

When percent porosity, densities, and porosity ratios given in Table 3 were evaluated together, it is seen that group A samples have maximum pore size and average pore amount. The number of pore in inch in this group is 10 (±3). These properties were adjusted by changing the diameter of the wires connecting pores in polyurethane model before casting. The samples in group B having a pore number of 20 (±3), the amount of pores decreases with regard to the one of the group A samples. It is quite natural that porous densities of the samples in the same dimensions decrease proportional to the pore rates. The reason for the irregular change in the average porosity of the samples in three different groups is due to the difference in the branches of the wires among the pores in models.

3.2. Radiography.
Implants in vivo were radiographically examined in 2th, 4th, and 6th postoperative months and the graphs are given in Figures 3(a)–3(c). No pathologic symptoms and reaction were observed within the implanted area.

3.3. Macroscopy.
In macroscopic examination of tibias in postoperative 2, 4, and 6 months just immediately after euthanasia, it was seen that the implant area and the pores of the implant were covered by the bone tissue completely. Figure 4 shows the pores full of bone tissue in the cross sectional area of the implant.

3.4. Microscopy.
In the light microscopy of all tissue examples taken from all the groups in postoperative periods, no immunological reaction and inflammatory cell infiltration were observed. Osteoblastic activity increased and osteocytes became increasingly evident from 2nd month to 6th month and gained normal bone tissue appearance in the end of the 6th month. Not one of the bone examples taken from all the samples had active inflammation, chronic infection, osteomyelitis, foreign object granuloma, giant cell reactions, benign or malign tumor, and definite tissue necrosis observed. In Figure 5(a), the number of osteocyte is low and no clear osteoblastic activity is seen. Similarly both the number of the osteocytes is low and osteoblast activity is poor at the end of the 2nd postoperative month. No immunological reaction is seen in periosteum in Figure 5(b) but osteoblast activity. More osteocytes are seen in comparison to the 2nd
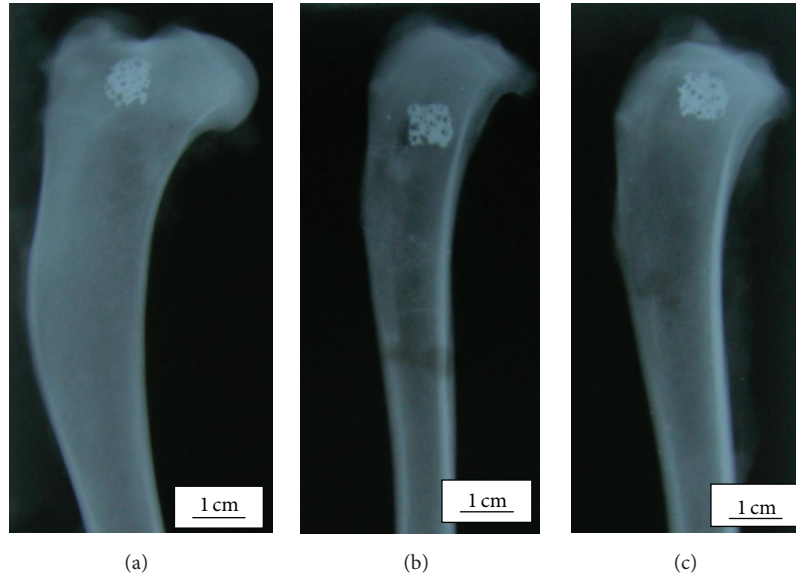
Figure 3: (a, b, c) 2nd, 4th, and 6th month radiography.

Table 4: Mechanic properties of some different alloys and bone.

| Material	Form	Solid density (g/cm^3)	Elastic modulus (GPa)	Yield strength (MPa)	General porosities in percent (%)	References
Co-Cr-Mo	Solid	8.3–8.6	200–230	275–1585	—	[14]
316L	Solid	8	200	170–750	—	[14]
Ti-6Al-4V	Solid	—	110	850–900	—	[14]
Hidroksiyapatit	Solid	3.2	—	279	—	[2]
Ni-21Cr-9Mo-4Nb	Porous	—	0.77–1.87	1.28–3.48	6.84–10.71	[13]
Ni-Cr-Mo	Porous	8.8	0.078–0.54	2.05–13.54	68.8–90.7	This study
Bone	Porous	2.1	10–40	20	5–95	[14]
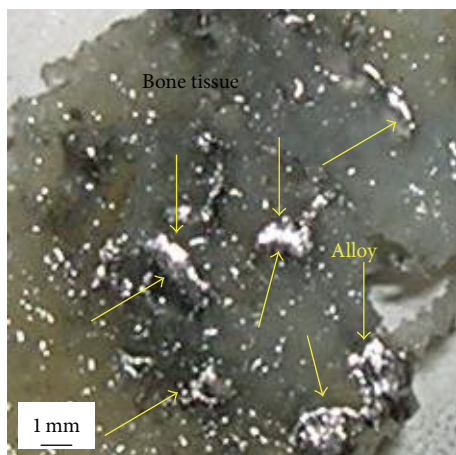
Figure 4: View of the sample in the bone tissue.

month. At the end of the 4th month osteoblasts are observed clearly as seen in Figures 5(c) and 5(d). Figure 5(e) shows normal bone tissue, osteoblast activity, and healthy periosteum with no immunological reaction at the end of the

6th postoperative month. Normal periosteum and spongiosis bone structure are seen in Figure 5(f). No immunological reaction and inflammatory cell infiltration are seen in the periosteal region (Figure 5(g)).

4. Discussion and Conclusion

In this study, a Ni-based Ni-Cr-Mo alloy which is commonly used in the orthopedic and dental field was used to produce the samples as an implant material and was composed with the precision cast method. The samples had an open porosity structure, various pore sizes, and filamentary gauges. The produced samples were implanted in dogs for various periods, the biocompatible process was examined in vivo conditions, and the following results were obtained.

The material used for the production method was according to Curran, [15]; the endurance of the foams obtained with metal powder and the powder metallurgy method was related with the tiniest spots between the metal or granules. He has noted that the specific endurance of foams produced by powder metallurgy would be low in accordance with
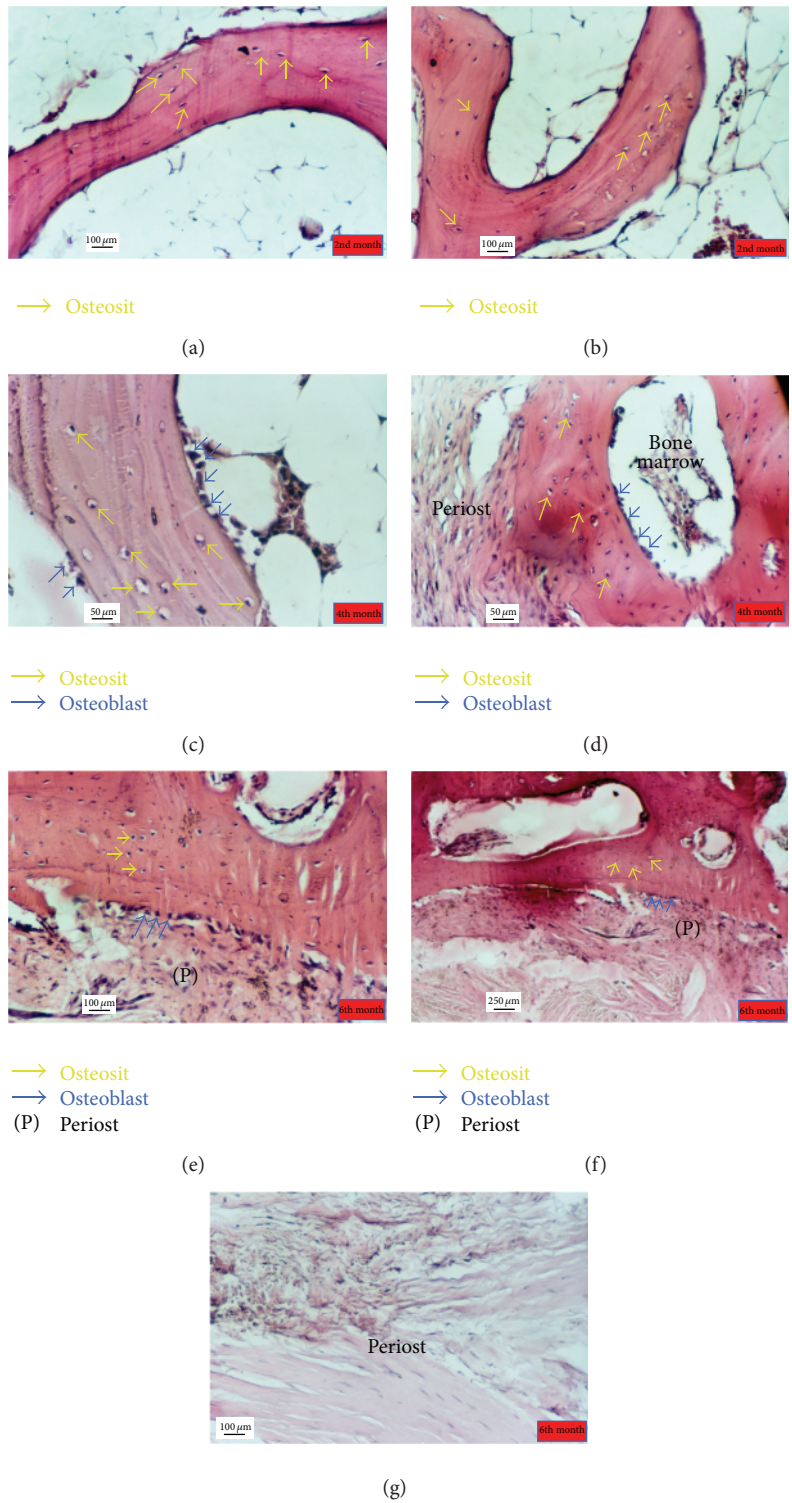
FIGURE 5: (a, b) Poor osteoblast activity at the end of the 2nd postoperative month. (c, d) At the end of the 4th month osteoblasts are clearly observed. (e, f) More osteoblast activity and healthy periosteum with no immunological reaction at the end of the 6th postoperative month. (g) Normal periosteum and spongiosis bone structure.

their production method. Yamada et al. [12] reported that a casting with an open pore structure was materialized with the infiltration method using a polyurethane foam model, and it was noted that the materials used for the production were of high quality and reliable, and the porosity rate can climb up to 98%. Yamada et al. also reported that any alloy or metal could be cast by this method. Yamada et al. [12] used Al and Mg materials to produce samples with a polyurethane foam model in their study. They derived relative density ratios as Al; 0.0446–0.0653, Mg; 0.0282–0.0306. A centrifugal casting device was used in this study alternatively for the infiltration casting of Yamada et al. [12]. Bone growth into porous metal surfaces depends on several factors including the porosity of the surface [16–18]. The controllability of the pore sizes and the filamentary sections of the samples which were produced with the precision casting method can be observed in the centrifugal casting device. Pores with uniform structure were obtained by using the polyurethane foam model. All the pores resemble the polyurethane foam pores used as model. Porous implants having densities between 0.0008 g/mm^3 and 0.0027 g/mm^3 were obtained from an alloy of Ni-Cr-Mo with a solid density of 0.0088 g/mm^3. Solid and porous densities and Young's modulus of some biomaterials and bone itself are given together with the results of this study in Table 4 for comparison.

There are big differences between Young's modulus and compressive strengths of solid and porous materials as seen in Table 4. Human bone has much less density (2.1 g/cm^3) than porous metallic implant materials but higher Young's modulus and compressive strength indicating a tougher structure. The porosity of human bone changes in different parts of body. The locations where bone is subjected to excessive, compressive, or impact loads are less porous and consequently have higher compression strength and Young's modulus.

The materials, which were produced porous, it is observed that they display a relative attitude to the bone attitudes in terms of the density, elasticity, and stress values in accordance with the materials produced nonporous. The density values of the samples were examined; the pore size and the filamentary section caused the increase of the relative density. These values show that porous structures are more proper in terms of using biomaterial. The Ni-Cr-Mo and Ni-21Cr-9Mo-4Nb alloys were produced by applying the polyurethane foam model method, and these were examined as porous elements; it was reported that the compressive stress and the elasticity module of the materials related with the rate of the porosity amount and the filamentary sections were controllable and their features were relevant to the mechanic behaviors of the bone. This result reveals with this study that the alloy which is commonly used in tooth implantation in fact can also be utilized in orthopedic implants.

In the macroscopic examination of the samples taken from tibias after euthanasia, it was seen that bone tissue covered the pores within the implant and implant region itself. Although Clemow et al. [6] state that for a good bone ingrowth, the pore size of the implant material must be between 200 and 500 μm, the pore sizes of the implant

material chosen as 85–127 and 254 μm in our study were also seen to be proper for bone ingrowth.

No immunological reaction or inflammatory cell infiltration was observed in the periosteum of the tissue samples extracted in postoperative periods. Osteoblastic activity increased, osteocytes appeared clearly in time, and at the end of observation period mature bone formation was seen in the samples. No active and chronic infection, osteitis, extraneous granules, giant cell reactions, and benign or malign neoplasm with evident tissue necrosis were reported from the bone samples taken from all cases. The results obtained showed that the Ni-Cr-Mo alloy generally was biocompatible.

Acknowledgments

References

[1] R. Murugan and S. Ramakrishna, "Bioresorbable composite bone paste using polysaccharide based nano hydroxyapatite," *Biomaterials*, vol. 25, no. 17, pp. 3829–3835, 2004.

[2] F. Sarsilmaz, N. Orhan, E. Unsaldi, A. S. Durmus, and N. Colakoglu, "A polyethylene-high proportion hydroxyapatite implant and its investigation *in vivo*," *Acta of Bioengineering and Biomechanics*, vol. 9, no. 2, pp. 9–16, 2007.

[3] R. Murugan and S. Ramakrishna, "Development of nanocomposites for bone grafting," *Composites Science and Technology*, vol. 65, no. 15-16, pp. 2385–2406, 2005.

[4] K. Anselme, "Osteoblast adhesion on biomaterials," *Biomaterials*, vol. 21, no. 7, pp. 667–681, 2000.

[5] L. D. Zardiackas, L. D. Dillon, D. W. Mitchell, L. A. Nunnery, and R. Poggie, "Structure, metallurgy, and mechanical properties of a porous tantalum foam," *Journal of Biomedical Materials Research*, vol. 58, no. 2, pp. 180–187, 2001.

[6] A. J. T. Clemow, A. M. Weinstein, J. J. Klawitter, J. J. Koeneman, and J. J. Anderson, "Interface mechanics of porous titanium implants," *Journal of Biomedical Materials Research*, vol. 15, no. 1, pp. 73–82, 1981.

[7] C. E. Wen, M. Mabuchi, Y. Yamada, K. Shimojima, Y. Chino, and T. Asahina, "Processing of biocompatible porous Ti and Mg," *Scripta Materialia*, vol. 45, no. 10, pp. 1147–1153, 2001.

[8] E. Tsuruga, H. Takita, H. Itoh, Y. Wakisaka, and Y. Kuboki, "Pore size of porous hydroxyapatite as the cell-substratum controls BMP-induced osteogenesis," *Journal of Biochemistry*, vol. 121, no. 2, pp. 317–324, 1997.

[9] L. J. Gibson and M. F. Ashby, *Cellular Solids: Structure and Properties*, Cambridge University Press, Cambridge, UK, 1997.

[10] M. W. Christopher, M. S. Richard, J. P. F. Garry, and J. D. Alison, "Dental materials," *Dental*, vol. 982, p. 10, 2006.

[11] Y. Yamada, K. Shimojima, Y. Sakaguchi et al., "Processing of an open-cellular AZ91 magnesium alloy with a low density of 0.05 g/cm^3," *Journal of Materials Science Letters*, vol. 18, no. 18, pp. 1477–1480, 1999.

[12] Y. Yamada, K. Shimojima, Y. Sakaguchi et al., "Effects of heat treatment on compressive properties of AZ91 Mg and SG91A Al foams with open-cell structure," *Materials Science and Engineering A*, vol. 280, no. 1, pp. 225–228, 2000.

[13] D. T. Queheillalt, Y. Katsumura, and H. N. G. Wadley, "Synthesis of stochastic open cell Ni-based foams," *Scripta Materialia*, vol. 50, no. 3, pp. 313–317, 2004.

[14] M. Long and H. J. Rack, "Titanium alloys in total joint replacement—a materials science perspective," *Biomaterials*, vol. 19, no. 18, pp. 1621–1639, 1998.

[15] D. Curran, *Metal Foams*, Cambridge University Press, Cambridge, UK, 2001.

[16] B. Y. Li, L. J. Rong, Y. Y. Li, and V. E. Gjunter, "Synthesis of porous Ni-Ti shape-memory alloys by self-propagating high-temperature synthesis: reaction mechanism and anisotropy in pore structure," *Acta Materialia*, vol. 48, no. 15, pp. 3895–3904, 2000.

[17] S. Kujala, J. Ryhänen, A. Danilov, and J. Tuukkanen, "Effect of porosity on the osteointegration and bone ingrowth of a weight-bearing nickel-titanium bone graft substitute," *Biomaterials*, vol. 24, no. 25, pp. 4691–4697, 2003.

[18] C. N. Cornell and J. M. Lane, "Current understanding of osteo-conduction in bone regeneration," *Clinical Orthopaedics and Related Research*, no. 355, pp. S267–S273, 1998.